Università di Bologna

Dipartimento di Fisica e Astronomia

Dottorato in Geofisica - XXX ciclo

Settore concorsuale: 02/C1

Settore scientifico disciplinare: FIS/06

Inversion of remote sensing measurements of Middle and Upper Planetary Atmospheres under non-equilibrium conditions

Dottorando: Federico Fabiano

Supervisore:
prof. Marco Ridolfi
Co-supervisore:
dott. Bianca Maria Dinelli

Coordinatore dottorato:
prof.ssa Nadia Pinardi

Esame finale anno 2018

Contents

Constants and acronyms

Constants

- $h = 6.62607\ erg\,s$
- $c = 2.99792 \times 10^{10}\ cm\,s^{-1}$
- $k = 1.38065 \times 10^{-16}\ erg\,K^{-1}$
- $c_2 = hc/k = 1.43878\ erg\,cm\,K$

Acronyms-1

- LTE = Local Thermodynamic Equilibrium
- non-LTE = non-Local Thermodynamic Equilibrium
- VMR = Volume Mixing Ratio
- LOS = Line Of Sight
- SZA = Solar Zenith Angle

Acronyms-2

- HITRAN = HIgh-resolution TRANsmission molecular absorption database (spectroscopic database)
- GBB = Geofit Broad Band (code)
- SR = SpectRobot (code)
- GRANADA = Generic RAdiative traNsfer AnD non-LTE population Algorithm (code)
- VIMS = Visual and Infrared iMaging Spectrometer (instrument)

- JIRAM = Jovian InfraRed Auroral Mapper (instrument)

Introduction

Since the first glimpses of atmospheric sciences and until the mid 19th century, the only laboratory for the study of planetary atmospheres has been the atmosphere of our planet. In the last 50 years, space missions have headed towards the other planets in our solar system, allowing to study their atmospheres close-by. The current picture - with thousands of planetary systems discovered around other stars - shows a great variability of conditions, stellar illumination, sizes and orbital parameters and thus represents a revolution in the field of planetary atmospheres.

Developing a more general picture might help in better understanding the physical processes that govern planetary atmospheres and their climates and learn new lessons about the Earth's atmosphere as well. This is the case for Titan, the largest satellite of Saturn, which possesses a thick atmosphere made mainly of nitrogen and methane that shows a complex organic chemistry, possibly similar to the one at work in the primordial Earth. Even a giant gaseous planet like Jupiter - with its evident patterns of atmospheric dynamics, like jet streams and anticyclones - has taught much about the dynamics of geophysical fluids.

This thesis treats the inversion of remote sensing measurements (infrared spectra) of middle and upper planetary atmospheres. The term remote sensing refers to plenty of different techniques that are used to gain information about some environment without making direct *in situ* measurements. In this work, the measurements consist in infrared atmospheric spectra and the information is extracted through bayesian inversion strategy.

The main part of the work done during my PhD regards the middle and upper atmosphere of Titan, through inversion of VIMS measurements, a spectrometer aboard the Cassini mission. VIMS measured emission from CO, CH_4, HCN and C_2H_2 in the 3-5 μm region, in conditions of non-Local Thermodynamic Equilibrium (non-LTE). Under non-LTE conditions, the vibrational levels of molecules are over-

or underpopulated with respect to their equilibrium value, because local molecular collisions are not frequent enough to restore equilibrium. During day-time, the pumping of solar radiation produces overpopulation of the excited levels and the emission may be strongly enhanced. These emissions depend on the local position of the Sun, given by the Solar Zenith Angle (SZA).

A bias observed in the results of the inversion of CH_4, brought to the development of SpectRobot, a new code for radiative transfer modeling and inversion of atmospheric quantities, that considers the full 3D geometry of the problem.

Beside the work on Titan, during my PhD I had the opportunity to join the Juno-JIRAM team. JIRAM is an infrared imager/spectrometer aboard the Juno mission to Jupiter and one of its goals is the analysis of Jupiter's aurorae. Although referring to a different planet, the work on Jupiter shares some of the problematics encountered in the Titan case. The inversion technique is similar, though dealt with a simpler model. JIRAM measurements sound the upper auroral atmosphere of Jupiter, where particle precipitation alters the local chemical equilibrium, producing non-equilibrium species such as H_3^+, or pumps molecules in their excited states. As in the Titan case, the emission depends on an external forcing and the analysis may benefit of a 3D approach, as the one developed in SpectRobot.

The thesis is organized as follows. Chapter 1 and 2 recall the fundamentals of radiative transfer theory - specialized to the infrared region - and of the bayesian inversion strategy. After this introductory material, the thesis is split into two parts.

Part I is dedicated to the study of the middle and upper atmosphere of Titan, introduced in Chapter 3. Chapter 4 treats the inversion of the abundance of carbon monoxide (CO) in the upper stratosphere and mesosphere from Cassini-VIMS measurements. Chapter 5 regards the inversion of CH_4, HCN and C_2H_2 in the mesosphere and thermosphere and the study of their seasonal and latitudinal variations also from Cassini-VIMS measurements. Chapter 6 treats the development of SpectRobot, with a description of the code and its validation and a study of the bias produced by ignoring the 3D configuration of the observation geometry. This bias is significant in Titan's atmosphere for large SZAs. More technical details on the code structure can be found in Appendix A.

Part II of the thesis is dedicated to the study of Jupiter's aurorae. Some fundamental results regarding the configuration of Jupiter's magnetosphere and the physics that drives the aurorae are recalled in Chapter 7. Chapter 8 reports the results of the analysis done on the first JIRAM measurements at the two polar regions

of Jupiter, with the inversion of H_3^+ and CH_4.

Finally, the overall conclusions are drawn in Chapter 9 and possible future evolutions are identified.

Chapter 1

Radiative transfer theory

This Chapter recalls the fundamentals of radiative transfer theory. A fundamental quantity in the theory of radiative transfer is the *specific intensity* I_w, often called *radiance*. The specific intensity in direction $\hat{\boldsymbol{n}}$ is the energy flux - per unit time, wavenumber and solid angle - through a surface dA perpendicular to $\hat{\boldsymbol{n}}$. For a general surface dA:

$$dE = I_w(\boldsymbol{x}, \hat{\boldsymbol{n}}) \cos\theta \; dw \; dt \; d\Omega \; dA \tag{1.1}$$

where θ is the angle between the vector $\hat{\boldsymbol{n}}$ and the normal to the surface dA, and dE is the infinitesimal energy that is flowing through dA in the time dt. In this Chapter, the units of the specific intensity are $erg/(s\, cm^2\, cm^{-1}\, sr)$ and we will always deal with stationary conditions, so the intensity has no dependence on time. We consider here the specific intensity per unit wavenumber $w = 1/\lambda$, but it could be defined also as a function of wavelength $\lambda = 1/w$ or frequency $\nu = cw$.

We define some related quantities which are useful in what follows and are essentially the consecutive moments of the specific intensity with respect to the angle θ. The *mean intensity* at a point is the zero-th order moment and is given by:

$$J_w(\boldsymbol{x}) = 1/4\pi \int I_w(\boldsymbol{x}, \hat{\boldsymbol{n}}) d\Omega \tag{1.2}$$

This quantity is related to the energy density of the electromagnetic field by the simple relation $u_w = 4\pi/c \; J_w$.

At thermodynamic equilibrium, the specific intensity is isotropic and the mean intensity is expressed by the Planck function at temperature T. In function of

wavenumber w:

$$B_w(T) = \frac{2hc^2w^3}{e^{c_2 w/T} - 1} \tag{1.3}$$

Let us now define the *net radiative flux* $\boldsymbol{F}_w$, the first order moment of the specific intensity with respect to θ. The radiative flux is a vector quantity such that the net energy that is passing through a surface with normal vector $\boldsymbol{dA}$ is given by $\boldsymbol{F}_w \cdot \boldsymbol{dA}$.

$$\boldsymbol{F}_w(\boldsymbol{x}) = \int I_w(\boldsymbol{x}, \hat{\boldsymbol{n}})\hat{\boldsymbol{n}}\, d\Omega \tag{1.4}$$

Note that, as required, $\boldsymbol{F}_w \cdot \boldsymbol{dA} = \int I_w(\boldsymbol{x}, \hat{\boldsymbol{n}}) \cos\theta \; dA \; d\Omega$ is indeed the net energy passing through our surface. Like the mean intensity, which is a scalar quantity, is related to the energy density, so the net flux can be related to the momentum density of the electromagnetic field $\boldsymbol{g}_w = 1/c^2 \; \boldsymbol{F}_w$.

1.1 The radiative transfer equation

The fundamental problem in the theory of radiative transfer is to understand how a light packet evolves when it propagates in a medium composed by particles that can absorb, emit or scatter photons. We focus here on the theory regarding unpolarized light: in this case, the specific intensity $I_w(\boldsymbol{n})$ is the quantity completely describing the radiation field at a point $\boldsymbol{x}$[1].

Let us now consider the specific intensity at a certain point in the atmosphere and in a particular direction $\boldsymbol{n}$. To simplify the notation we will consider a point x in a coordinate system in the axis of propagation $\boldsymbol{n}$. If we know the specific intensity $I_w(x)$ and want to find out the specific intensity at the point $x + ds$ along the ray path, we have to take into consideration the absorption, emission and scattering of radiation by the material contained in the infinitesimal volume $dV = dA\, ds$ crossed by the light ray. Neglecting scattering for a while, the difference between the energy going out and the one entering this volume per unit time is equal to the difference between the energy emitted and absorbed per unit time inside that volume. We can write:

$$dA \cdot [I_w(x + ds) - I_w(x)] = \; dV \cdot (\textit{emission - absorption})$$

If we consider also scattering processes, we have to add the radiation deviated

[1] For a more general treatment, needed in the case of polarized light, one would need to introduce the four Stokes parameters. See [Bohren and Huffman, 1983].

in the direction $\boldsymbol{n}$ considered from other directions and to subtract the radiation deviated from $\boldsymbol{n}$ to other directions. Writing this more explicitly we obtain:

Fundamental equation of radiative transfer

$$\frac{dI_w(x,\boldsymbol{n})}{ds} = \varepsilon_w(x,\boldsymbol{n}) - \alpha_w(x,\boldsymbol{n})I_w(x,\boldsymbol{n}) \tag{1.5}$$

The first term appearing on the right-hand side of this equation is called *emissivity*. Dimensionally, this is an intensity emitted per unit length of ray path. The other term corresponds to extinction and is proportional to the incoming radiation. The constant of proportionality α_w is the extinction coefficient, also called *opacity*, which is the inverse of a length. Both these coefficients can be divided in two parts:

- a thermal part, in which the photons are effectively destroyed or created in the interaction with matter
- a scattering part, in which the photons are just deviated in other directions

$$\varepsilon_w = \eta_w + \int \sigma_w(\boldsymbol{n}',\boldsymbol{n})I_w(\boldsymbol{n}')\,d\Omega' \qquad \alpha_w = \chi_w + \int \sigma_w(\boldsymbol{n},\boldsymbol{n}')\,d\Omega' \tag{1.6}$$

Where η_w and χ_w represent the thermal parts of emission and absorption respectively, and $\sigma_w(\boldsymbol{n},\boldsymbol{n}')$ is the scattering opacity for an incoming direction $\boldsymbol{n}$ and outgoing direction $\boldsymbol{n}'$. This is the most general form of the extinction and emission coefficients. However, in our case we will only deal with scattering in a simple case in which single scattering of solar radiation is taken into account (see Section 4.5). For the remaining part of this section we will consider the situation without scattering. Neglecting scattering, Equation 1.5 reads:

$$\frac{dI_w(x)}{ds} = \eta_w(x) - \chi_w(x)I_w(x) \tag{1.7}$$

$\eta_w(x)$ and $\chi_w(x)$ are the thermal emission and absorption coefficient, which are isotropic and depend on the local conditions of the atmosphere. Equation (1.7) can be rewritten in a different form that requires the definition of two quantities of primary importance, the *source function* $\mathcal{S}_w$ and the *optical depth* τ_w. Let us first rewrite the equation, dividing by the thermal absorption coefficient χ_w and substituting the new quantities:

$$\frac{d\,I_w(x)}{d\tau_w} = I_w(x) - \mathcal{S}_w(x) \tag{1.8}$$

$$\text{where} \quad \mathcal{S}_w = \frac{\eta_w}{\chi_w} \qquad \text{and} \qquad \tau_w(x, x+s) = \int_0^s \chi_w(x+\zeta)\, d\zeta$$

The source function is simply the ratio between emission and absorption coefficient. In the absence of scattering and if Local Thermodynamic Equilibrium (LTE) holds (see Section 1.2.1), the source function reduces to the Planck function at the local temperature. The most general case is much more complicated, since the source function could contain scattering terms proportional to the intensity in other directions.

The optical depth is a dimensionless number and measures the light path in unit of the mean free path of photons. When $\tau_w \ll 1$ we speak of optically thin conditions, when $\tau_w > 1$ of optically thick conditions.

1.1.1 Formal solution of the equation

We recall here the formal solution of Equation 1.5 and look at its behaviour in the optically thin and optically thick limiting cases. In the most general case (with scattering or non-LTE processes), the so-called formal solution is just a step in the iteration procedure, since the source function contains the intensity itself. Using the optical depth as the independent variable along the line of sight and considering the form in Equation 1.7, the solution can be written as:

$$I_w(0) = I_w(\tau_w)\, e^{-\tau_w} + \int_0^{\tau_w} \mathcal{S}_w(\zeta_w)\, e^{-\zeta_w}\, d\zeta_w \tag{1.9}$$

Where τ_w is the total optical depth along the line of sight and the point at zero optical depth is our observation point. The meaning of eq. 1.9 is clear: we have a first part which is the original intensity, attenuated by the exponential of the total optical depth of the atmospheric slab crossed, and a second which is the radiation emitted at each point ζ_w along the line of sight, attenuated by the absorption in the remaining path before reaching the observer.

1.1.2 Limiting cases

It is worth having a look at the solution 1.9 in the optically thin and optically thick limits. Since we are most interested in the study of limb emission spectra of planetary atmospheres, we consider the case in which the original intensity $I_w(\tau_w)$ is zero. In the first case we obtain:

$$\lim_{\tau_w \to 0} \quad \rightsquigarrow \quad I_w(0) = \tau_w \cdot \mathcal{S}_w^* \tag{1.10}$$

$\mathcal{S}_w^*$ is an appropriate mean of the source function in the thin slab. So in the optically thin limit the signal is proportional to the total optical depth and to the source function.

The opposite situation is obtained setting the limit for large optical depth:

$$\lim_{\tau_w \to \infty} \quad \rightsquigarrow \quad I_w(0) = \int_0^{\tau_w \sim 1} \mathcal{S}_w(\zeta_w) e^{-\zeta_w} d\zeta_w \;\; \hookrightarrow \;\; \mathcal{S}_w^* \tag{1.11}$$

In this case we see only the photons emitted in the part of the atmospheric slab nearer to the observer, till ζ_w is of order unity; again $\mathcal{S}_w^*$ is some appropriate mean of the source function for $\zeta_w < 1$. Any contribution further than this is suppressed by a factor $e^{-\zeta_w}$ with $\zeta_w > 1$ and is usually almost negligible[2].

As we can see, in the optically thin case the observed radiation is proportional to the optical depth and to the number density n_g of the emitters, whereas in the optically thick case it is not: if we double the gas concentration in the atmosphere, we see a doubly strong signal in the first case and exactly the same in the second.

1.1.3 Discretization of the radiative transfer equation

The formal solution 1.9 is computed numerically in the radiative transfer code. In the following we will consider all quantities at a fixed wavenumber and omit the subscript w.

The line of sight is divided in discrete steps, such that the atmospheric parameters (pressure, temperature, ..) can be considered constant inside each step. The smaller the steps the more accurate the calculation is. For a single step i along the ray path,

[2]But the source function may vary greatly along the line of sight, so still some contribution from further points is possible.

we define a transmittance factor $\Gamma_i \equiv e^{-\tau_i}$, where $\tau_i = \tau(x_{i,0}, x_{i,f})$ is the optical depth between the beginning $x_{i,0}$ and the end $x_{i,f}$ of the step. The total optical depth is simply $\tau = \sum_i \tau_i$ and the total transmittance factor becomes $e^{-\tau} = \prod_i \Gamma_i$. The second term in Equation 1.9 is modified in the following way:

$$\int_0^\tau \mathcal{S}(\tau) e^{-\tau} d\tau = \sum_i \mathcal{S}_i \left[\int_0^{\tau_i} e^{-\zeta} d\zeta \right] \prod_{\ell=0}^{i-1} \Gamma_\ell \tag{1.12}$$

The remaining integral is simply solved:

$$\int_0^{\tau_i} e^{-\zeta} d\zeta = 1 - e^{-\tau_i} = 1 - \Gamma_i$$

Therefore, the complete solution in the discrete form can be written as:

$$I(0) = I(\tau) \prod_{i=0}^{n} \Gamma_i + \sum_i \mathcal{S}_i \left[1 - \Gamma_i\right] \prod_{\ell=0}^{i-1} \Gamma_\ell \tag{1.13}$$

This equation is the computational solution of the radiative transfer problem for each wavenumber, once the source function and the optical depth at each step are known. In the line-by-line approach, which is used throughout this work, the spectral dependence is treated discretizing the wavenumber spectra and solving for each discrete component separately. The step used here is 0.0005 cm^{-1}, which allows to resolve even the thinner lines in the cold and rarefied upper atmosphere of Titan.

1.2 Vibrational and rotational levels of molecules

Since we focus here on the infrared part of the electromagnetic spectrum, between 2000 and 5000 cm^{-1}, all radiative transitions considered involve roto-vibrational levels of some molecule. Here and in the following we will speak of energies in terms of wavenumber, measured in cm^{-1}; this convention is widely used in atmospheric physics and is equivalent to expressing the energy in units of hc ($E = hcw$). Transitions between vibrational levels of molecules usually have energies of hundreds to thousands of cm^{-1}, while rotational transitions have energies of some cm^{-1} to tens of cm^{-1} up to hundreds of cm^{-1}.

For a vibrational transition, the rotational quantum number J may vary as well, but at most by unity, due to the selection rule on the angular momentum at the dipole order. A roto-vibrational band can thus be divided in three branches: P branch ($\Delta J = +1$), Q branch ($\Delta J = 0$) and R branch ($\Delta J = -1$). For all diatomic

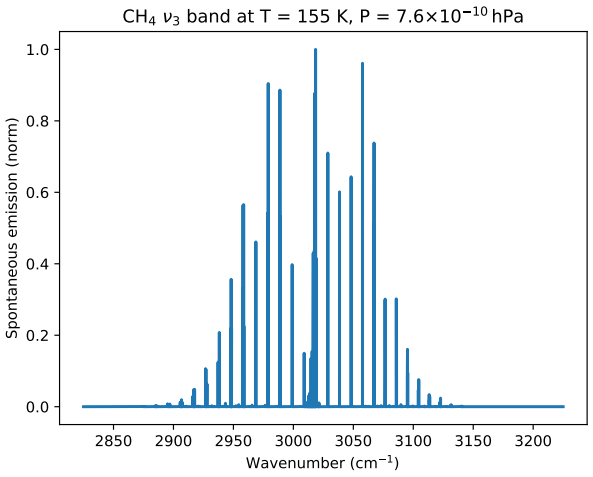

Figure 1.1: CH_4 $\nu_3 \rightarrow 0$ roto-vibrational band.

molecules and many linear molecules[3] the Q branch is not present, because the transition with $\Delta J = 0$ is not allowed. Figure 1.1 shows the ν_3 band of CH_4 in which one can clearly identify the three branches.

Let us call $f_\nu = n_{X,\nu}/n_X$ the population fraction of the excited level ν of molecule X with respect to the number density of the molecule. At thermal equilibrium, f_ν is given by the Boltzmann factor:

$$f_\nu = \frac{g_\nu e^{-c_2 E_\nu / T}}{Q_X(T)} \tag{1.14}$$

Where g_ν is the degeneracy factor of level ν, c_2 is a constant, $Q_X(T)$ is the partition sum of molecule X at temperature T.

1.2.1 LTE vs non-LTE populations

Equation 1.14 above holds only in case of Local Thermodynamic Equilibrium (LTE). In the more general case of vibrational non-LTE considered here, the populations of the vibrational levels may depart from their equilibrium population due to external forcing. This usually happens in the more rarefied regions of the atmosphere and is produced by the unbalance between excitation produced by absorption of solar radiation and the rare collisional thermalization processes. More details about the problem of vibrational non-LTE can be found in Section 3.3.

The population fractions of the molecular levels are usually written in the fol-

[3]For linear polyatomic molecules this is true only if the projection of the electronic angular momentum on the molecular axis - usually denoted as Λ - is zero.

lowing form in the vibrational non-LTE case:

$$f_\nu = \frac{g_\nu e^{-c_2(E_\nu - E_{\rm vib})/T}}{Q_X(T)} e^{-c_2 E_{\rm vib}/T_{\rm vib}} \tag{1.15}$$

Where E_ν is the total level energy, $E_{\rm vib}$ is the vibrational energy alone (taken as the energy of the fundamental rotational level in that vibrational state) and $T_{\rm vib}$ is the vibrational temperature of the level. The vibrational temperature is a useful artifact to write the level population fraction in the form above, that reduces to the LTE form when $T_{\rm vib} = T$.

1.3 Absorption coefficient and emissivity

The terms χ_w and η_w in Equation 1.6 constitute the thermal part of the total extinction and emission coefficients in Equation 1.5. We will focus here on their calculation starting from the properties of the single radiative transitions that couple matter with radiation. The full discussion that follows is specialized to the case of molecular roto-vibrational bands, which is representative for the study of planetary atmospheres in the infrared.

1.3.1 Einstein coefficients

The interaction of light with matter in bound-bound transitions can be described in terms of the Einstein coefficients. Let us consider a simple two-level molecule X, denoting the upper level with label 2 and the lower level with label 1. The upper level has energy E_2 and degeneracy g_2, the lower level E_1 and g_1. The energy difference between the two levels is $E_2 - E_1 = w_{21}$ which corresponds to the energy of the electromagnetic transition.

The radiative transition between the two levels is governed by three processes. If the molecule is in the upper level 2, it may spontaneously emit a photon w_{21} and de-excite to the lower level. This is called the *spontaneous emission* and the rate of this process per unit time is described by the Einstein coefficient $\mathcal{A}_{21}$, expressed in units of s^{-1}. The interaction of molecule X with a transiting photon w_{21} may produce two effects: the *absorption* of a photon in the lower state 1 that excites the molecule to the upper state, or the *induced emission* of another photon and the de-excitation from the upper to the lower level. These two processes are described by the Einstein coefficients $\mathcal{B}_{12}$ for absorption and $\mathcal{B}_{21}$ for induced emission. The

rate per unit time for absorption of a photon is given by $\mathcal{B}_{12} \cdot J_{21}$, where J_{21} is the local mean radiance at the transition energy w_{21}. Analogously the rate for induced emission is given by $\mathcal{B}_{12} \cdot J_{21}$. Another possible definition for B is in terms of number of photons instead of mean radiance, but we will never use it here. The Einstein coefficients $\mathcal{B}_{12}$ and $\mathcal{B}_{21}$ are expressed here in units of $\mathrm{cm}^3\ \mathrm{erg}^{-1}\ \mathrm{cm}^{-2}$ and the mean radiance in units of $\mathrm{erg}\ \mathrm{cm}^{-2}\ \mathrm{s}^{-1}\ \mathrm{cm}$.

The relation between the three coefficients can be obtained using an elegant statistical approach first proposed by Einstein. Let us consider an ensemble of molecules X at equilibrium at temperature T with radiation. The ratio of the population of the two levels is, considering Equation 1.14:

$$\frac{n_2}{n_1} = \frac{g_2}{g_1} e^{-c_2 w_{21}/T}$$

At the same time, if the radiation is at equilibrium as well, J_{21} is equal to the Planck function at temperature T, given by Equation 1.3. Since we are at equilibrium, the number of transitions from the upper to the lower level is equal to those from the lower to the upper level[4], giving:

$$n_2 \left[B_{21} J_{21} + A_{21}\right] = n_1 B_{12} J_{21}$$

Combining this with the Boltzmann expression for the levels' population ratios and expressing the mean radiance with the Planck function at temperature T, we obtain the relations between the three Einstein coefficients:

$$A_{21} = 2hc^2 w_{21}^3 B_{21} \qquad B_{12} = \frac{g_2}{g_1} B_{21} \tag{1.16}$$

Although they have been obtained in an equilibrium configuration, the validity of the relations above is universal, since they reflect the radiative properties of a single molecule.

1.3.2 Line strength

The Einstein coefficients defined above describe a particular radiative transition involving two molecular levels. In Section 1.1 we instead defined the thermal emission η_w and absorption χ_w coefficients, that are needed in the radiative transfer equation.

[4]The principle of detailed balance ensures that this approach is valid also if more than two states are possible.

χ_w has dimensions of an inverse length, while η_w is an intensity per length. Here we want to relate the Einstein coefficients of a single transition to the contribution of that transition to the overall absorption and emission coefficients. The contribution of a single transition to the absorption coefficient, integrated in wavenumbers, is called the *line strength* or *line intensity*. Denoting again the lower level of the transition as 1 and the upper level as 2, with w_{21} being the energy difference between the two levels, the line strength S is defined as follows:

$$S = \frac{hcw_{21}}{4\pi} \left[f_1 \mathcal{B}_{12} - f_2 \mathcal{B}_{21} \right] \tag{1.17}$$

Where f_1 and f_2 are the two population ratios defined as in Equation 1.14 for the LTE case, or as in Equation 1.15 for the case of vibrational non-LTE. The line strength defined in this way has dimensions of $\mathrm{cm}^{-1}/\mathrm{cm}^{-2}$, often written as $\mathrm{cm}^{-1}/(\mathrm{mol\,cm}^{-2})$ to stress the fact that this is the contribution of a single transition.

The line strength gives the total contribution of the transition considered to the absorption coefficient. The induced emission, being proportional to the radiative intensity, is considered as negative absorption and is expressed in the equation above by the term $f_2\mathcal{B}_{21}$.

We can define a similar term $\mathcal{E}$ for the emission process, that expresses the contribution of the single transition to the emission coefficient. So we can write:

$$\mathcal{E} = \frac{hcw_{21}}{4\pi} f_2 \mathcal{A}_{21} \tag{1.18}$$

It is worth noting that, in case of LTE, the ratio of $\mathcal{E}$ to S is indeed equal to the Planck function $B(w_{21}, T)$, as expected for the source function in LTE.

In most spectroscopic databases the line strength of each transition is listed at some reference temperature T_{ref} - which is usually $296\,K$ - and in LTE conditions. The ratio between the line strength at a different temperature T and the reference temperature T_{ref} in LTE conditions can be calculated starting from Equation 1.17 and Equation 1.14, and gives:

$$S(T) = S(T_{\mathrm{ref}}) \frac{Q(T_{\mathrm{ref}})}{Q(T)} \frac{e^{-c_2 E_1/T} \left[1 - e^{-c_2 w_{21}/T}\right]}{e^{-c_2 E_1/T_{\mathrm{ref}}} \left[1 - e^{-c_2 w_{21}/T_{\mathrm{ref}}}\right]} \tag{1.19}$$

In LTE the emission term is simply: $\mathcal{E}(T) = B(w_{21}, T) S(T)$.

Let us consider now the more general case of vibrational non-LTE, assuming a vibrational temperature T_{v1} for the lower vibrational level and T_{v2} for the upper

vibrational level. In this case, the two population ratios f_1 and f_2 in Equation 1.17 are given by Equation 1.15 and the line strength is given by:

$$S_{\text{non-LTE}}(T_{v1}, T_{v2}, T) = S_{\text{LTE}}(T)\alpha(T_{v1}, T_{v2}, T) \quad \text{with} \quad \alpha = r_1 \frac{1 - (r_2/r_1)e^{-c_2 w_{21}/T}}{1 - e^{-c_2 w_{21}/T}} \tag{1.20}$$

Where $r_1(T_{v1}, T) = e^{-c_2 E_1(1/T_{v1} - 1/T)}$ and $r_2(T_{v2}, T) = e^{-c_2 E_2(1/T_{v2} - 1/T)}$ are the two non-LTE ratios of the populations with respect to their LTE values. The alpha factor corrects for the fact that the populations of the two levels are different from their equilibrium values.

The emission term depends only on the population of the upper level and is modified in this way:

$$\mathcal{E}_{\text{non-LTE}}(T_{v2}, T) = r_2(T_{v2}, T)\mathcal{E}_{\text{LTE}}(T) \tag{1.21}$$

More details on the derivation of line strengths from the Einstein coefficients and on the calculation of the statistical weights for many molecules can be found in [Simeckova et al., 2006].

1.3.3 Line shape

A radiative transition does not happen always exactly at the same frequency but there is a significant probability of absorption in a small interval of wavenumbers around the exact energy difference between the two levels. This is due to two broadening mechanisms that take place in an ensemble of molecules at temperature T and pressure P:

- the *Doppler* or *thermal* broadening, which is due to the thermal motion of molecules ("observers") with respect to the light source;
- the *pressure* broadening, often called also *Stark* or *collision* broadening, which is produced by the distortion of energy levels through the effect of molecular collisions.

There is a third mechanism called *natural* broadening, which is due to a quantum effect linked to the time-energy uncertainty relation, but is completely negligible with respect to the other two in basically all real situations. The *Doppler* broadening produces a gaussian profile:

$$\phi(w,T) = \sqrt{\frac{1}{\pi\sigma_D^2}} e^{-(w-w_0)^2/\sigma_D^2} \quad \text{whit} \quad \sigma_D = \frac{w_0}{c}\sqrt{\frac{2N_a kT}{M_m}} \tag{1.22}$$

Where N_a is the Avogadro number, M_m the molecular mass in atomic mass units and all other constants are expressed in cgs units. w_0 is called the vacuum wavenumber of the transition, which is the one reported in spectroscopic databases. The Doppler width of the line σ_D is proportional to the square root of temperature.

The *pressure* broadening produces a Lorentzian profile whose central wavenumber is shifted due to a process called *pressure shift*, also linked to molecular collisions.

$$\phi(w,P,T) = \frac{1}{\pi}\frac{\sigma_L(P,T)}{\sigma_L(P,T)^2 + (w-w_{0s})^2)} \tag{1.23}$$

Where $\sigma_L(P,T)$ is the pressure broadening coefficient, which represents the half width at half maximum (HWHM) of the Lorentzian function, and $w_{0s} = w_0 - \delta(P_{\text{ref}})P/P_{\text{ref}}$ is the central wavenumber due to the pressure shift. $\sigma_L(P,T)$ is usually divided in σ_{self} - which takes into account the collision with other molecules of the same gas - and σ_{air} - the broadening produced by all other molecules. At first order $\sigma_L(P,T)$ has the following behaviour with respect to a reference pressure P_{ref} and temperature T_{ref}:

$$\sigma_L(P,T) = \left(\frac{T_{\text{ref}}}{T}\right)^{\alpha}\left[\sigma_{\text{air}}(P_{\text{ref}},T_{\text{ref}})\frac{P-P_{\text{self}}}{P_{\text{ref}}} + \sigma_{\text{self}}(P_{\text{ref}},T_{\text{ref}})\frac{P_{\text{self}}}{P_{\text{ref}}}\right] \tag{1.24}$$

The quantities $\sigma_{\text{air}}(P_{\text{ref}},T_{\text{ref}})$, $\sigma_{\text{self}}(P_{\text{ref}},T_{\text{ref}})$, α and $\delta(P_{\text{ref}})$ are measured in laboratory and tabulated in the spectroscopic databases. For the HITRAN spectroscopic database [Rothman et al., 2013], $P_{\text{ref}} = 1\,atm$ and $T_{\text{ref}} = 296\,K$.

The assumption of a Lorentz profile for the pressure broadening is a simplification of the actual situation, which can be very complicated, but still the Lorentz profile is a good approximation at least if not interested in the ultra-high resolution spectrum. In the simplest approximation, the line shape resulting from the combined effect of the Doppler and pressure broadening is a convolution of the two, known as the Voigt profile. Parameterizations for the Voigt profile are available [Humlicek, 1982; Tran et al., 2013].

The line shape is normalized in the wavenumber domain, such that $\int \phi(w)dw = 1$. So $\phi(w)$ has dimension of $1/cm^{-1}$.

1.3.4 Total absorption and emission coefficients

The total absorption and emission coefficients are the sum of the contribution of all transitions and all gases in the atmosphere. Both coefficients are linear in the gas number density n_g, which can be factorized.

$$\chi(w) = \sum_{g=1}^{N_{gas}} n_g \, \chi_g(w) \qquad \eta(w) = \sum_{g=1}^{N_{gas}} n_g \, \eta_g(w) \tag{1.25}$$

$\chi_g(w)$ has dimensions of an area and can be thought of as a cross section. For each gas we have to sum over all possible transitions, to obtain:

$$\begin{aligned} \chi_g(w, T, P, T_{v1}, T_{v2}) =& \frac{hcw}{4\pi} \sum_{\ell} \left(f_1(T, T_{v1}) - \frac{g_1}{g_2} f_2(T, T_{v2}) \right) \mathcal{B}_{12} \phi_\ell(w, P, T) \\ =& \sum_{\ell} S_\ell(T, T_{v1}, T_{v2}) \phi_\ell(w, P, T) \end{aligned} \tag{1.26}$$

Where all quantities in the summation term are referred to the ℓ transition. The formula above is valid in the general situation of vibrational non-LTE, where the f's are given by Equation 1.15 and S is in the form of Equation 1.20. The case of LTE is equivalent to simply setting T_{v1} and T_{v2} equal to T.

Turning to the emission coefficient, the situation is completely analogous, with the exception that we have now to consider the Einstein coefficient for spontaneous emission $\mathcal{A}_{21}$.

$$\begin{aligned} \eta_g(w, T, P, T_{v2}) =& \frac{hcw}{4\pi} \sum_{\ell} f_2(T, T_{v2}) \mathcal{A}_{21} \phi_e ll(w, P, T) \\ =& \sum_{\ell} \mathcal{E}_\ell(T, T_{v2}) \phi_\ell(w, P, T) \end{aligned} \tag{1.27}$$

As above, this expression is valid in the case of vibrational non-LTE.

1.3.5 Level-specific coefficients for the non-LTE case

The coefficients defined above, although valid in case of vibrational non-LTE, do not allow the tabulation of the absorption coefficient for different pressures and temperatures, because the upper and lower levels are coupled in Equation 1.26 and have generally different behaviour in non-LTE. To avoid the problem, one possibility is

the tabulation of level-specific coefficients for each molecule that consider separately the absorption, induced emission or spontaneous emission processes, leaving outside the vibrational non-LTE factor.

For each transition, we can define the following G-coefficients, derived from the Einstein coefficients, that already take into account a the rotational population of the level.

$$\begin{aligned} \text{absorption} \ &\rightarrow \ G_a(T) = \frac{hcw}{4\pi}\rho_1^{rot}(T)\mathcal{B}_{12} \\ \text{ind. emiss.} \ &\rightarrow \ G_i(T) = \frac{hcw}{4\pi}\rho_2^{rot}(T)\mathcal{B}_{21} \\ \text{sp. emiss.} \ &\rightarrow \ G_s(T) = \frac{hcw}{4\pi}\rho_2^{rot}(T)\mathcal{A}_{21} \end{aligned} \tag{1.28}$$

where 1 and 2 indicate the lower and upper level of the transition, and the rotational population is $\rho_\nu^{rot}(T) = g_\nu e^{-hc(E_\nu - E_{\text{vib}})/T}$.

Now, for each level ν we can define level-specific absorption, induced emission and spontaneous emission coefficients, leaving outside the vibrational population factor:

$$\begin{aligned} \mathcal{G}_\nu^a(P,T,w) &= \sum_{\ell:1=\nu} G_a(T,\ell)\phi_\ell(P,T,w) \\ \mathcal{G}_\nu^i(P,T,w) &= \sum_{\ell:2=\nu} G_i(T,\ell)\phi_\ell(P,T,w) \\ \mathcal{G}_\nu^s(P,T,w) &= \sum_{\ell:2=\nu} G_s(T,\ell)\phi_\ell(P,T,w) \end{aligned} \tag{1.29}$$

The sum on $\ell : 1 = \nu$ means that the summation takes place on all lines for which level ν is the lower level of the transition; if $\ell : 2 = \nu$ is specified the summation is done only on the lines for which level ν is the upper level. With the new level-specific coefficients defined in this way we can build up the total gas coefficients:

$$\begin{aligned} \chi_g(P,T,w,T_\nu) &= \sum_\nu e^{-c_2 E_\nu/T_\nu}\left[\mathcal{G}_\nu^a(P,T,w) - \mathcal{G}_\nu^s(P,T,w)\right] \\ \eta_g(P,T,w,T_\nu) &= \sum_\nu e^{-c_2 E_\nu/T_\nu}\mathcal{G}_\nu^s(P,T,w) \end{aligned} \tag{1.30}$$

In this way, the vibrational factor is left outside the coefficients that can be calculated beforehand and tabulated for different pressures and temperatures. This strategy will be adopted in the forward model developed as part of this thesis work

(see Section 6.1.1).

1.4 GBB forward model

The radiative transfer equation is solved numerically through radiative transfer codes. The one widely used in Part I of this work is the Geofit Broad Band code (GBB in the following), which is the self-standing version of the forward model inside the Geofit Multi-Target Retrieval (GMTR) code [Carlotti et al., 2006], updated to perform simulations over broad frequency grids. The GBB code performs line-by-line calculations of the absorption and emission coefficients with a high-resolution frequency grid ($5 \times 10^{-4}\,\mathrm{cm}^{-1}$). The atmosphere is discretized in a two-dimensional set of cloves, produced by the intersections of radii (with correction for elliptical geometry) and altitude levels, as shown in Figure 1.2.

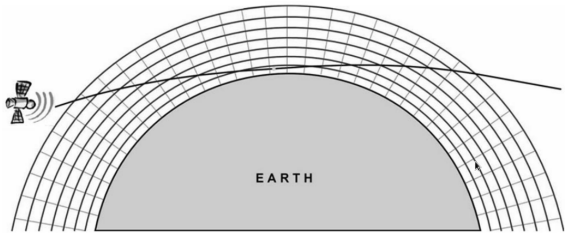

Figure 1.2: Scheme of the 2D discretization of the atmosphere and the ray-tracing used in the GBB code.

The ray tracing calculates for a given Line Of Sight (LOS) all the intersections with radii and levels encountered. Refraction is computed at each intersection. For each segment between two intersections, the atmospheric quantities are calculated using Curtis-Godson (CG) averages. In the Curtis-Godson approach, all quantities are weighted with the abundance of the gas considered:

$$n_{\mathrm{col,\,g}} = \int_{x_1}^{x_2} n(x) X_g(x) dx \qquad Q_{\mathrm{eq,\,g}} = \frac{\int_{x_1}^{x_2} Q(x) n(x) X_g(x) dx}{n_{\mathrm{col,\,g}}} \tag{1.31}$$

Where $n(x)$ is the total number density of the atmosphere, X_g is the VMR of gas g, $n_{\mathrm{col,\,g}}$ is the column abundance of gas g in the portion of the LOS between x_1 and x_2 and $Q_{\mathrm{eq,\,g}}$ is the Curtis-Godson average of a generic quantity Q relative to gas g in the same portion of the LOS.

The GBB code has been upgraded to compute non-LTE radiances as described in [Edwards et al., 1993]. The code has been validated with the non-LTE computations

made with KOPRA [Stiller et al., 2002]. The GBB forward model is coupled to a retrieval module performing optimal estimation of atmospheric quantities through a bayesian approach, adopting a Levenberg-Marquardt iterative procedure (see next Chapter and Section 2.3). The code is able to perform simultaneous inversion of atmospheric quantities like temperature, pressure and gas concentration on the 2D grid.

Chapter 2

Retrieval method

In the previous Chapter we recalled some basic concepts of the radiative transfer theory, which allows to simulate the radiation emitted by the atmosphere assuming known thermodynamic state and concentration of different molecular species. This is what builds the *forward model* of a radiative transfer code. When studying planetary atmospheres, we usually face the opposite situation, that is we measure a radiance and we want to derive the concentration of a particular molecule or the temperature profile. This is known as the *inverse* or *retrieval problem*.

Let us assume that we have a set of radiance measurements $\boldsymbol{y}$ (measurements vector) - whose measurement error is expressed by the covariance matrix $\boldsymbol{S}_y$ - and we want to derive from those a set of atmospheric parameters $\boldsymbol{x}$ (state vector). When using spectral measurements, as it is done in this work, each spectral point is an element of vector $\boldsymbol{y}$, and one usually uses a set of spectra acquired at slightly different positions in the atmosphere, to gain enough information. So the length of vector $\boldsymbol{y}$ is the product of the number of spectra (n_{spet}) in the set and the number spectral points (n_{wl}) in each spectrum $n_y = n_{\mathrm{spet}} \cdot n_{\mathrm{wl}}$. The atmosphere may be sounded with different observational configurations. One speaks of a *limb* observation if the line of sight (LOS) does not encounter the planetary surface and the altitude of the point in the LOS closer to the surface is called *tangent altitude*. If the LOS encounters the surface one speaks of a *nadir* observation[1]. For the works in Chapter 4 and 5 sets of limb spectra of Titan atmosphere at different tangent altitudes are used. For the work in Chapter 8 a set of nadir spectra is used.

In the cases treated in Chapters 4 and 5, the set of parameters $\boldsymbol{x}$ to be estimated

[1]Strictly speaking, the term *nadir* refers to an observation with a LOS normal to the surface in downward direction, while inclined geometries are called *slant*. However, the term nadir is broadly used to include both configurations.

is the abundance of some gases at a number of fixed altitudes in the atmosphere. For a one-dimensional problem, the VMR X_g of the molecule can be approximated by its decomposition in a set of triangular functions centered at the fixed altitudes z_i of the retrieval grid:

$$\begin{aligned} X_g(z) = \sum_i \alpha_i \mathcal{T}_i(z) \qquad \mathcal{T}_i(z) &= \frac{|z - z_i|}{|z_{i+1} - z_i|} \quad \text{if } z_i \leq z \leq z_{i+1} \\ &= \frac{|z - z_i|}{|z_i - z_{i-1}|} \quad \text{if } z_{i-1} \leq z \leq z_i \\ &= 0 \quad \text{otherwise} \end{aligned} \tag{2.1}$$

We also assume that some information on the state vector $\boldsymbol{x}$ is available in form of an *a priori* state vector $\boldsymbol{x}_a$, whose error is represented by a covariance matrix $\boldsymbol{S}_a$.

2.1 Bayes' theorem and formal solution of the inverse problem

We recall here some basic concepts from the Bayesian theory of probability. In the Bayesian view, both the measurement and the state are represented by two probability distributions $P(\boldsymbol{y})$ and $P(\boldsymbol{x})$, which tell our prior knowledge of the problem. The inverse problem consists in finding the conditional probability of the state vector $\boldsymbol{x}$ if the result of the measurement is $\boldsymbol{y}$, that is we are looking for $P(\boldsymbol{x}|\boldsymbol{y})$. This conditional probability is linked to the other conditional probability $P(\boldsymbol{y}|\boldsymbol{x})$ by the Bayes' theorem, which states:

$$P(\boldsymbol{x}|\boldsymbol{y}) = \frac{P(\boldsymbol{y}|\boldsymbol{x})P(\boldsymbol{x})}{P(\boldsymbol{y})} \tag{2.2}$$

Let us assume a measurement space with dimension n and a state space with dimension m. To solve the inverse problem we need a model for the direct problem, that is a function $\boldsymbol{f}\colon \mathbb{R}^m \to \mathbb{R}^n$ which allows us to compute a simulated measurement, starting from the state vector:

$$\boldsymbol{y} = \boldsymbol{f}(\boldsymbol{x}) + \boldsymbol{e} \tag{2.3}$$

Where $\boldsymbol{f}(\boldsymbol{x})$ is the solution of the direct problem and $\boldsymbol{e}$ is the measurement error. Assuming that the error $\boldsymbol{e}$ is gaussian and assuming that its covariance is given by $\boldsymbol{S}_y$, we have an expression for the conditional probability $P(\boldsymbol{y}|\boldsymbol{x})$:

$$P(\boldsymbol{y}|\boldsymbol{x}) = c_n e^{-(\boldsymbol{y}-\boldsymbol{f}(\boldsymbol{x}))^T \boldsymbol{S}_y^{-1}(\boldsymbol{y}-\boldsymbol{f}(\boldsymbol{x}))/2} \tag{2.4}$$

Where c_n is a normalization constant: $c_n = (2\pi)^{-n/2}|\boldsymbol{S}_y|^{-1/2}$. Since we assumed we have an *a priori* estimate of the state vector $\boldsymbol{x}$, we can write the a priori probability $P(\boldsymbol{x})$:

$$P(\boldsymbol{x}) = c_m e^{-(\boldsymbol{x}-\boldsymbol{x}_a)^T \boldsymbol{S}_a^{-1}(\boldsymbol{x}-\boldsymbol{x}_a)/2} \tag{2.5}$$

$P(\boldsymbol{y})$ could be calculated from $P(\boldsymbol{y}) = \int P(\boldsymbol{y}|\boldsymbol{x})P(\boldsymbol{x})d^n x$, but it is not needed since it does not depend on $\boldsymbol{x}$ and is just a normalization factor.

We may then write the expression for $P(\boldsymbol{x}|\boldsymbol{y})$ as:

$$P(\boldsymbol{x}|\boldsymbol{y}) = c_3 e^{-\left[(\boldsymbol{y}-\boldsymbol{f}(\boldsymbol{x}))^T \boldsymbol{S}_y^{-1}(\boldsymbol{y}-\boldsymbol{f}(\boldsymbol{x})) + (\boldsymbol{x}-\boldsymbol{x}_a)^T \boldsymbol{S}_a^{-1}(\boldsymbol{x}-\boldsymbol{x}_a)\right]/2} \tag{2.6}$$

Where c_3 is a normalization constant.

2.2 The maximum likelihood method

Once we have written the expression for the conditional probability in Equation 2.6, we may want to extract the *best* estimate of the state vector given the measurements. The usual way is to assume the value of $\boldsymbol{x}$ for which $P(\boldsymbol{x}|\boldsymbol{y})$ is maximum as our best estimate and solution of the inverse problem. This is called the *maximum likelihood method* or *maximum a posteriori solution.*

In order to maximize the conditional probability, we have to minimize the cost function χ^2, given by:

$$\chi^2 = (\boldsymbol{x}-\boldsymbol{x}_a)^T \boldsymbol{S}_a^{-1}(\boldsymbol{x}-\boldsymbol{x}_a) + (\boldsymbol{y}-\boldsymbol{f}(\boldsymbol{x}))^T \boldsymbol{S}_y^{-1}(\boldsymbol{y}-\boldsymbol{f}(\boldsymbol{x})) \tag{2.7}$$

The maximum likelihood solution to the inverse problem is the value of $\boldsymbol{x}$ for which the χ^2 function is at a minimum. We then look for the points in which $\nabla_x \chi^2 = 0$. that is:

$$\boldsymbol{g}(\boldsymbol{x}) = \nabla_{\mathrm{x}} \chi^2 = -2\boldsymbol{K}^T \boldsymbol{S}_y^{-1}(\boldsymbol{y}-\boldsymbol{f}(\boldsymbol{x})) - 2\boldsymbol{S}_a^{-1}(\boldsymbol{x}-\boldsymbol{x}_a) = 0 \tag{2.8}$$

Where $\boldsymbol{g}(\boldsymbol{x})$ is the gradient of the cost function χ^2 and $\boldsymbol{K}$ is the Jacobian matrix of the function $\boldsymbol{f}$, the direct model, with respect to each of the parameters; that is $K_{i,j} = \frac{\partial f_i}{\partial x_j}$. Equation 2.8 does not have an analytic solution in the great majority of

cases, depending on the complexity of the function $\boldsymbol{f}$.

2.3 Numerical procedures: the Gauss-Newton and Levenberg-Marquardt methods

The equation $\nabla_{\mathrm{x}}\,\chi^2 = 0$ can be solved numerically with an iterative procedure. The success of such iteration will depend on the degree of non-linearity of function $\boldsymbol{f}$, so that a procedure that is successful in one case may not be equally adequate for a different situation. An approach is called the Gauss-Newton method.

If we have a scalar function $g(x)$ of which we want to find the closest zero to our starting point x_1, one way is to use Newton's method, whose iterative procedure at point x_i is:

- calculate the tangent at x_i;
- follow the tangent till it intersects the x axis at the new point x_{i+1};

Generalized to the many variables case where $\boldsymbol{g}$ is a vectorial function depending on the vector $\boldsymbol{x}$, the Newton's method can be written:

$$\boldsymbol{x}_{\mathrm{i}+1} = \boldsymbol{x}_{\mathrm{i}} - \left[\nabla_{\mathrm{x}}\boldsymbol{g}(\boldsymbol{x}_{\mathrm{i}})\right]^{-1}\boldsymbol{g}(\boldsymbol{x}_{\mathrm{i}}) \tag{2.9}$$

The quantity in squared parenthesis is the Hessian of the χ^2 function and we can write it explicitly starting from Equation 2.8, obtaining:

$$\nabla_{\mathrm{x}}\boldsymbol{g}(\boldsymbol{x}_{\mathrm{i}}) = 2\boldsymbol{K}^{\mathrm{T}}\boldsymbol{S}_{\mathrm{y}}^{-1}\boldsymbol{K} - 2\left[\nabla_{\mathrm{x}}\boldsymbol{K}^{\mathrm{T}}\right]\boldsymbol{S}_{\mathrm{y}}^{-1}\big(\boldsymbol{y} - \boldsymbol{f}(\boldsymbol{x})\big) + 2\boldsymbol{S}_{\mathrm{a}}^{-1} \tag{2.10}$$

The second term in the expression above is related to the second derivatives of the function $\boldsymbol{f}$. The calculation of this term requires a significant effort in terms of computational time. The approximation known as Gauss-Newton method consists in neglecting this term, which is often small. In this approximation, the iterative step reads:

$$\boldsymbol{x}_{\mathrm{i}+1} = \boldsymbol{x}_{\mathrm{i}} + \left(\boldsymbol{K}_{\mathrm{i}}^{\mathrm{T}}\boldsymbol{S}_{\mathrm{y}}^{-1}\boldsymbol{K}_{\mathrm{i}} + \boldsymbol{S}_{\mathrm{a}}^{-1}\right)^{-1}\left[\boldsymbol{K}_{\mathrm{i}}^{\mathrm{T}}\boldsymbol{S}_{\mathrm{y}}^{-1}\big(\boldsymbol{y} - \boldsymbol{f}(\boldsymbol{x}_{\mathrm{i}})\big) - \boldsymbol{S}_{\mathrm{a}}^{-1}(\boldsymbol{x}_{\mathrm{i}} - \boldsymbol{x}_a)\right] \tag{2.11}$$

Where $\boldsymbol{K}_i$ is the Jacobian calculated at $\boldsymbol{x} = \boldsymbol{x}_i$. The *a priori* estimate $\boldsymbol{x}_a$ ensures the invertibility of matrix $\boldsymbol{K}_{\mathrm{i}}^{\mathrm{T}}\boldsymbol{S}_{\mathrm{y}}^{-1}\boldsymbol{K}_{\mathrm{i}} + \boldsymbol{S}_{\mathrm{a}}^{-1}$. The error on the retrieved parameters

$\boldsymbol{x}_{\mathrm{f}}$ can be expressed in form of the covariance matrix:

$$\boldsymbol{S}_{\mathrm{x}} = \left(\boldsymbol{K}_{\mathrm{f\text{-}1}}^{\mathrm{T}} \boldsymbol{S}_{\mathrm{y}}^{-1} \boldsymbol{K}_{\mathrm{f\text{-}1}} + \boldsymbol{S}_{\mathrm{a}}^{-1}\right)^{-1} \tag{2.12}$$

The Gauss-Newton method may fail in case of strongly non-linear problems, in which the step might be too large and project the state vector $x_{\mathrm{i+1}}$ out of the forward model linearity region.

An optimization of the Gauss-Newton method is the Levenberg-Marquardt method, also known as the *damped least squares method*. The main problem with the Gauss-Newton method is that it may fail convergence due too large steps. The idea is then to reduce the single steps, to guarantee that the χ^2 function is still decreasing. This result is obtained by adding a new term to equation 2.11:

$$\boldsymbol{x}_{\mathrm{i+1}} = \boldsymbol{x}_{\mathrm{i}} + \left(\boldsymbol{K}_{\mathrm{i}}^{\mathrm{T}} \boldsymbol{S}_{\mathrm{y}}^{-1} \boldsymbol{K}_{\mathrm{i}} + \boldsymbol{S}_{\mathrm{a}}^{-1} + \lambda_{\mathrm{LM}} \boldsymbol{D}_{\mathrm{i}}\right)^{-1} \left[\boldsymbol{K}_{\mathrm{i}}^{\mathrm{T}} \boldsymbol{S}_{\mathrm{y}}^{-1} \left(\boldsymbol{y} - \boldsymbol{f}(\boldsymbol{x}_{\mathrm{i}})\right) - \boldsymbol{S}_{\mathrm{a}}^{-1} (\boldsymbol{x}_{\mathrm{i}} - \boldsymbol{x}_{a})\right] \tag{2.13}$$

Where $\boldsymbol{D}_{\mathrm{i}}$ is a diagonal matrix which is usually taken equal to the diagonal elements of $\boldsymbol{K}_{\mathrm{i}}^{\mathrm{T}} \boldsymbol{S}_{\mathrm{y}}^{-1} \boldsymbol{K}_{\mathrm{i}} + \boldsymbol{S}_{\mathrm{a}}^{-1}$; λ_{LM} is a positive scalar parameter. The λ_{LM} at each has to be chosen so that the χ^2 decreases.

The strategy used in this work is to start from a small λ_{LM} (equal to 0.1) and then eventually raise it if the χ^2 increases.

2.4 Averaging Kernel and degrees of freedom

A test of the sensitivity of the retrieval to the atmospheric parameters can be performed though the use of the Averaging Kernel matrix. The Averaging Kernel is a measure of the sensitivity of the final retrieved state $\tilde{\boldsymbol{x}}$ produced by a change in the true atmospheric state: $A_{ij} = \partial \tilde{x}_i / \partial x_j$, where $\boldsymbol{A}$ is the averaging kernel matrix, $\tilde{x}_i$ is the i-th component of the final retrieved state $\tilde{\boldsymbol{x}}$ and x_j is the j-th component of the true atmospheric state.

The expression for the averaging kernel is obtained deriving Equation 2.11 with respect to $\boldsymbol{x}_{i-1}$ at the last iteration, which results in:

$$\boldsymbol{A} = (\boldsymbol{K}^T \boldsymbol{S}_y \boldsymbol{K} + \boldsymbol{S}_a^{-1})^{-1} \boldsymbol{K}^T \boldsymbol{S}_y \boldsymbol{K} \tag{2.14}$$

In the ideal situation of perfectly constrained retrieval and full information (where the contribution of the a-priori is negligible), $\boldsymbol{A}$ is equal to the identity

matrix. The i-th row of matrix $\boldsymbol{A}$ ($\boldsymbol{a}_i$) indicates how much is the i-th component of the retrieval sensitive to the different components of the atmospheric state. For a well constrained retrieval, the i-th row $\boldsymbol{a}_i$ has a sharp peak close to one at its i-th component (that is, the element on the diagonal of $\boldsymbol{A}$). The width of $\boldsymbol{a}_i$ at the two sides is a measure of the actual resolution of the retrieval. For an ill-posed problem, the peak value and the sum of all components of $\boldsymbol{a}_i$ tends to zero. In general, $\boldsymbol{A}$ is not symmetrical and the j-th column ($\boldsymbol{b}_j$) indicates instead the effect of a perturbation of the j-th component of the true state on all retrieved parameters.

A useful scalar metrics of the sensitivity of the retrieval is the number of degrees of freedom of the retrieval, defined as the trace of matrix $\boldsymbol{A}$: $n_{\mathrm{DOF}} = \sum_i A_{ii}$. For a well constrained problem the number of degrees of freedom is close to the number of retrieved parameters.

Part I

Titan's middle and upper atmosphere

Chapter 3

Introduction: Titan

Titan is the largest satellite of Saturn, orbiting the planet at a mean distance of about 1.2×10^6 km. With a mean radius of about 2575 km, it is the second largest satellite of the solar system after Ganymede and even slightly larger than planet Mercury. Titan shows a dense atmosphere, with a surface pressure about 1.5 times the Earth's and a molecular number density at the surface about 5 times larger. No other satellite in the Solar system shows such a massive atmosphere. Since the gravitational acceleration on Titan's surface is about $1.5\,m/s^2$, Titan's atmosphere is much more expanded than the Earth's, with a pressure scale height ranging from about 15 km to 50 km [Müller-Wodarg et al., 2014]. The 1 μbar level on Titan is reached at about 500 km altitude, while it lies at about 100 km on the Earth. Titan's upper atmosphere is yet more expanded due to the large atmospheric thickness to planetary radius ratio, which makes the gravitational acceleration decrease substantially. Due to the large distance from the Sun, which varies between about 9.0 and 10.1 AU, the solar flux is approximately one percent the Earth's and the mean surface temperature is therefore very cold, around 90 K.

Being tidally locked, Titan rotates around its axis in about two weeks and always exposes the same hemisphere to Saturn. For the same reason, the rotation axis has zero tilt with respect to the perpendicular to the satellite orbital plane and is almost perfectly aligned with Saturn's rotation axis. The axial tilt is about 26.7° with respect to the perpendicular to the ecliptic plane. This means that Titan does show seasonal variations of its atmosphere and climate, much like the Earth. The axial tilt is similar, somewhat larger, and one Titan year lasts 29.46 Earth years. Titan's last northern winter solstice took place in October 2002, last spring equinox in August 2009 and the last summer solstice in May 2017.

3.1 The Cassini mission

The Cassini mission was a planetary exploration mission dedicated to the Saturn system, that has been operating around the ring planet from July 2004 until September 2017, when it was sent inside Saturn and thus destroyed. It's worth introducing here the Cassini mission, because many of its instruments changed radically out knowledge of Titan's atmosphere and are the key to the current picture.

Figure 3.1 shows Titan's orbit around the sun and its position in the different phases of the Cassini mission. Cassini reached Saturn system during northern winter, less than two years after the winter solstice, and saw the arrival of northern spring till the summer solstice in May 2017. So the instruments onboard Cassini have been collecting data for about half a Titan's year.

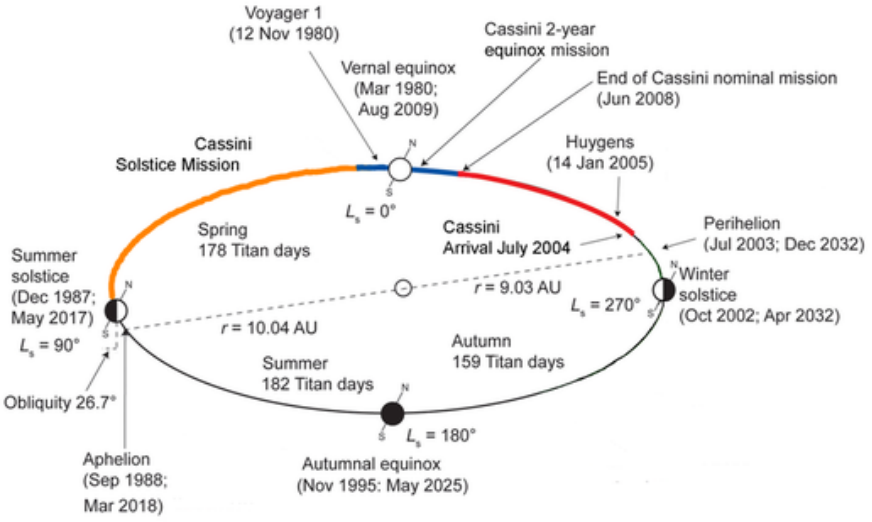

Figure 3.1: Orientation of Titan relative to the sun during the Cassini mission.

Cassini carried 12 instruments onboard dedicated to optical remote sensing, direct measurement of particles and magnetic field and radio science. This work exploits the measurements made by VIMS (Visual and Infrared iMaging Spectrometer) [Brown et al., 2004], described in the next subsection. Here follows a brief description of the instrument whose results are used in the discussion in the next chapters:

- **UVIS**: UltraViolet Imaging Spectrograph, a set of detectors that measured ultraviolet light reflected or emitted from the atmosphere in the spectral range between 55.8 and 190 nm [Esposito et al., 2004];

- **INMS**: Ion and Neutral Mass Spectrometer (INMS), a mass spectrometer sensible both to ions and neutral particles, which measured number and weight of molecules collected in situ, during the closest approaches to Titan [Waite et al., 2004];
- **CIRS**: Composite InfraRed Spectrometer, a spectrometer active in the middle and far infrared from 10 to 1400 cm^{-1}, which measured temperature and composition in the stratosphere and mesosphere of Titan [Flasar et al., 2004].

3.1.1 VIMS

VIMS (Visual and Infrared iMaging Spectrometer) is an imaging spectrometer aboard Cassini working at visible and near-infrared wavelengths from 0.3 to 5.1 μm [Brown et al., 2004]. The spectral resolution in the infrared region ranges between 15 and 20 nm, depending on the band considered. The instrumental line shape (ILS) is gaussian, with a slight deviation consisting in two small lobes beside the gaussian, accounting for less than 2% of the main window. VIMS takes hyper-spectral images, organised in cubes with two spatial and one spectral dimension: each cube contains a maximum of 64×64 pixels with 256 spectral bands; each pixel has a field of view of 0.5 by 0.5 mrad, in the nominal mode. Figure 3.2 shows a typical VIMS spectrum of Titan acquired on a limb LOS tangent at 300 km. The spectral range from 2 to 5μm is shown. The signatures of CH_4, HCN+C_2H_2, CO and CH_3D can be clearly identified, as well as a continuum signal due to scattering of solar radiation produced by Titan aerosols.

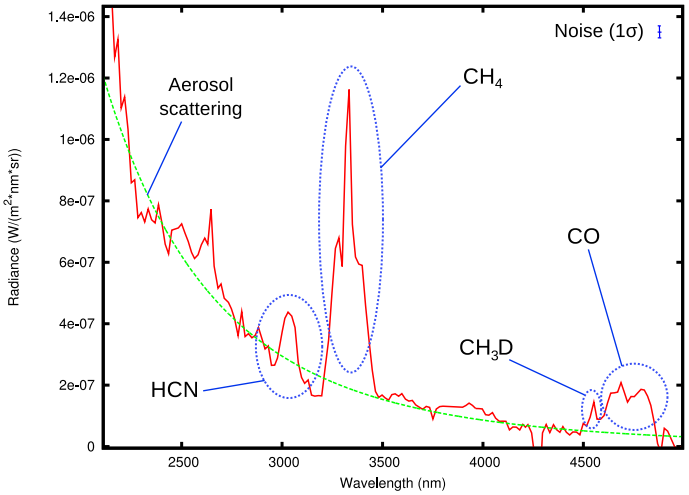

Figure 3.2: VIMS spectrum acquired on the dayside of Titan with a limb LOS tangent at 300 km.

3.2 Titan's atmosphere

3.2.1 Thermal structure

In January 2005 the Huygens probe detached from Cassini and descended into the Titan's atmosphere, taking precious *in situ* measurements of temperature, pressure and molecular abundances. The landing point was situated at a latitude of 20° S. The direct measurement of temperature and pressure was possible only below 150 km, while the upper atmosphere density profile was determined indirectly from data on the deceleration of the probe [Fulchignoni et al., 2005].

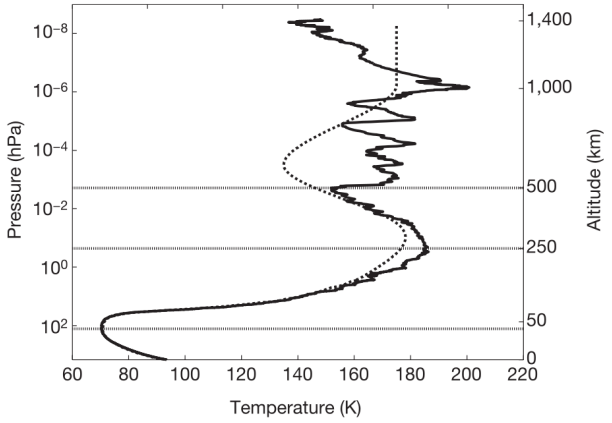

Figure 3.3: Comparison between the temperature profile measured by HASI (onboard Cassini) and the empirical model temperature profile by Yelle (after [Fulchignoni et al., 2005].

In Figure 3.3 we can see the comparison between the measured HASI profile (solid line) and the Yelle empirical model of Titan's atmosphere (dotted) [Yelle et al., 1997]. We can see that Titan atmospheric structure presents similarities with the Earth's, with a first temperature inversion at the tropopause about 40 km, with a minimum value of 70 K, a second one at the stratopause around 270 km, with a maximum of 185 K, and a third one at the mesopause about 500 km. The two profiles in figure 3.3 are in quite good agreement below 500 km; in the upper atmosphere instead large fluctuations are seen in the HASI measurement and are probably due to a gravity wave with an amplitude of 10-20 K and a wavelength varying between 100 km and 150 km.

More recently, new data on the temperature profile on Titan and a first evaluation of the latitude and seasonal variations came from analysis of the CIRS, UVIS and INMS data onboard Cassini. The CIRS data focus on the stratosphere, up to about 450-500 km. The temperature inversion makes use of the CH_4 ν_4 band at 7.7 μm

and has been done routinely on all CIRS data, which allowed the production of detailed latitude/pressure maps of temperature and the monitoring of the evolution in time of the thermal structure [Achterberg et al., 2008, 2011; Vinatier et al., 2015]. In Figure 3.4 some of these maps are shown, showing the variation form Northern winter to early spring. The minimum pressure in the graphs corresponds to about 500 km. shows an evident signature of the formation of a northern polar vortex, The first image, result of the analysis during northern winter, shows colder temperatures in the northern polar troposphere and lower stratosphere and heating in the corresponding upper stratosphere and mesosphere. This is a signature of the subsidence of the air column above the winter pole, accompanied by the formation of a polar vortex [Flasar et al., 2014; Teanby et al., 2012, 2008, 2009]. In the other panels, relative to years 2009 and 2010, the vortex slowly disappears, leaving an almost perfectly symmetric structure at the equinox in 2009. In the last image, a small heating in the mesosphere above the South Pole is seen, which proves the beginning of the formation of the winter polar structure.

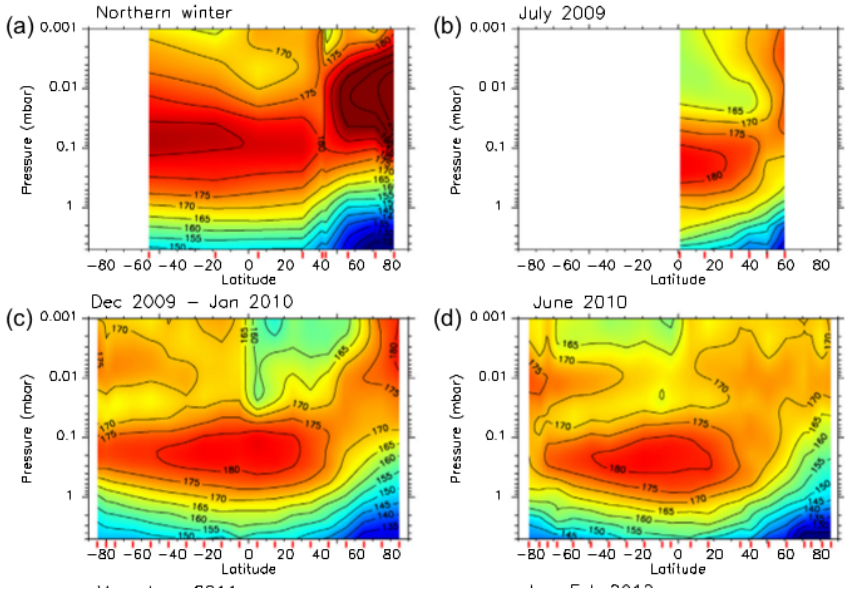

Figure 3.4: CIRS temperature maps for different year of observation, after [Vinatier et al., 2015].

Above 500 km less data are available. However, some works have been published based on data taken by UVIS - from about 600 to 1000 km - and INMS - from 950 to 1400 km.

Figure 3.5 reports the thermal structure measured by UVIS above 600 km, which shows a behaviour similar to the measurements made by the HASI instrument on-

board the Huygens probe: the average temperature is between 170 and 180 K, but fluctuations most probably produced by gravity waves are ubiquitous. Since UVIS observations are mainly in occultation, the sampling of UVIS data is sparse and does not allow the determination of seasonal/latitudinal variations [Capalbo et al., 2015; Koskinen et al., 2011; Yelle et al., 2014].

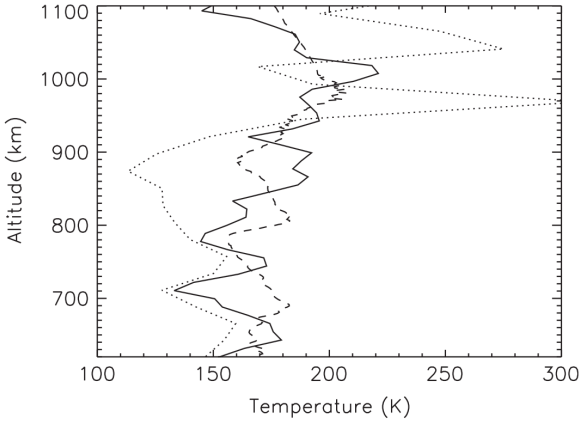

Figure 3.5: Comparison of the HASI temperature profile (dashed line) and two temperature profiles retrieved from UVIS, relative to flybys T41 (solid line) and T53 (dotted line). After [Koskinen et al., 2011].

INMS has been able to retrieve indirectly the temperature profile in the upper regions of Titan's atmosphere from about 950 km to 1400 km, integrating the hydrostatic equation with the measured N_2 density profile [Yelle et al., 2006; Cui et al., 2009; Snowden et al., 2013; Yelle et al., 2014]. The mean retrieved profile is shown in Figure 3.6. As can be seen from the shaded area in the Figure, which represents the standard deviation of the retrieved profiles, the temperature in the upper atmosphere shows a very large variability.

3.2.2 Composition and chemistry

Titan's atmosphere is composed mainly by molecular nitrogen ($X_{N_2} \sim 95\%$) and methane ($X_{CH_4} \sim 5\%$). Methane sources are at the surface of the planet, where it is found in the liquid phase, and its abundance is thus larger in the troposphere, decreasing to about 1% in the stratosphere, due to a cold trap mechanism that takes place at the extremely cold tropopause. Methane on Titan follows a cycle much like water on Earth, evaporating from the lakes, forming clouds and then precipitating again to the surface [Müller-Wodarg et al., 2014].

Titan atmospheric chemistry is very rich and in fact many trace gases are found.

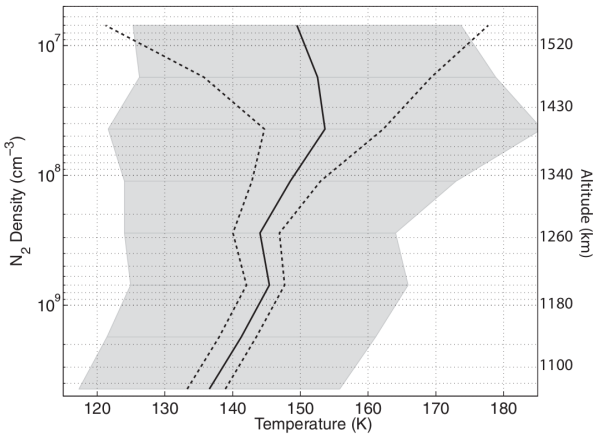

Figure 3.6: Mean temperature profile inferred from INMS data, after [Snowden et al., 2013].

The production of minor species is initiated in the upper atmosphere from the dissociation or ionization of CH_4 and N_2. The main energy source for these processes are solar UV photons, but also energetic photoelectrons produced by solar X-ray and EUV radiation and saturnian magnetospheric electrons contribute [Wilson and Atreya, 2004; Krasnopolsky, 2009; Vuitton et al., 2014; Dobrijevic et al., 2014]. CH_4 absorbs significantly UV photons with $h\nu > 8.6\,\mathrm{eV}$ and is much more easily dissociated than N_2, which absorbs photons with $h\nu > 12.4\,\mathrm{eV}$. The products of CH_4 photolysis are CH_2, CH_3 and CH, which initiate a rich hydrocarbon chemistry. Among the most abundant trace species there are HCN, C_2H_2, C_2H_4, C_6H_6. A very active Nitrogen-Carbon chemistry gives rise to much more complex molecules, which precipitate in the atmosphere and aggregate in particles to build Titan's ubiquitous organic aerosols [Lavvas et al., 2008a,b].

The main reaction of production of acetylene (C_2H_2) takes place in the upper atmosphere from the primary products of CH_4 dissociation:

$$^3CH_2 + \ ^3CH_2 \rightarrow C_2H_2 + 2H \ (H_2)$$

The main losses for C_2H_2 in the upper atmosphere is through reaction with another product of CH_4 dissociation:

$$^1CH_2 + C_2H_2 \rightarrow C_3H_3 + H$$

while in the lower atmosphere main losses take place due to photolysis and reaction with H atoms. $C_2H_2$is very important in the photochemistry of Titan's atmosphere

since it is photolized by photons with lower energies ($h\nu > 5.17\,\mathrm{eV}$) which are not absorbed by CH_4 or N_2. Moreover it is a catalyst of CH_4 dissociation through the intermediate species C_2H, produced in the C_2H_2 photodissociation.

Another important constituent of Titan's atmosphere is HCN, produced in the upper atmosphere in a couple of reactions that involve atomic nitrogen and the products of CH_4 dissociation:

$$N(^4S) + CH_3 \rightarrow H_2CN + H$$

$$H_2CN + H \rightarrow HCN + H_2$$

The first reaction is the source of more than 70% of all nitriles in Titan's atmosphere [Krasnopolsky, 2009]. Photolysis of HCN produces CN that leads mostly to HCN recycling in reactions with hydrocarbons and partly to HCN losses. Other losses take place in reactions with CH, C_2H_3, C_3N and ions. Anyway the net balance for HCN is positive and about 13% of the HCN produced condenses at the cold tropopause and is deposited on the surface.

Few molecular species containing oxygen are found in the atmosphere. The main oxygen bearing molecule is CO, with an abundance of about 50 ppm. More details on the production and loss of CO are in Chapter 4.

3.2.3 Dynamics of the middle atmosphere

One of the most interesting things with Titan's atmosphere is that we can study its climate and understand more about the dynamical patterns in planetary atmospheres.

Titan's insolation shows large variation during Titan's year due to the 26.7° inclination of the orbit with respect to the sun, but just 10% of the direct incoming sunlight reaches the surface, which is screened by a thick haze. Due to the low temperatures of Titan's troposphere, the radiative losses are also slow and the timescale for energetic variation of the troposphere end up to be much longer than a Titan's year [Lebonnois et al., 2014; Flasar et al., 2014]. This is shown by the estimate of the radiative damping time, the typical time for energy loss and temperature variation through radiative emission, represented in Figure 3.7. Below about 100 km this timescale is longer than Titan's year and no seasonal variation is seen in the atmospheric structure. Above that level, in the stratosphere and mesosphere, the radiative damping time is short enough and seasonal variations are expected.

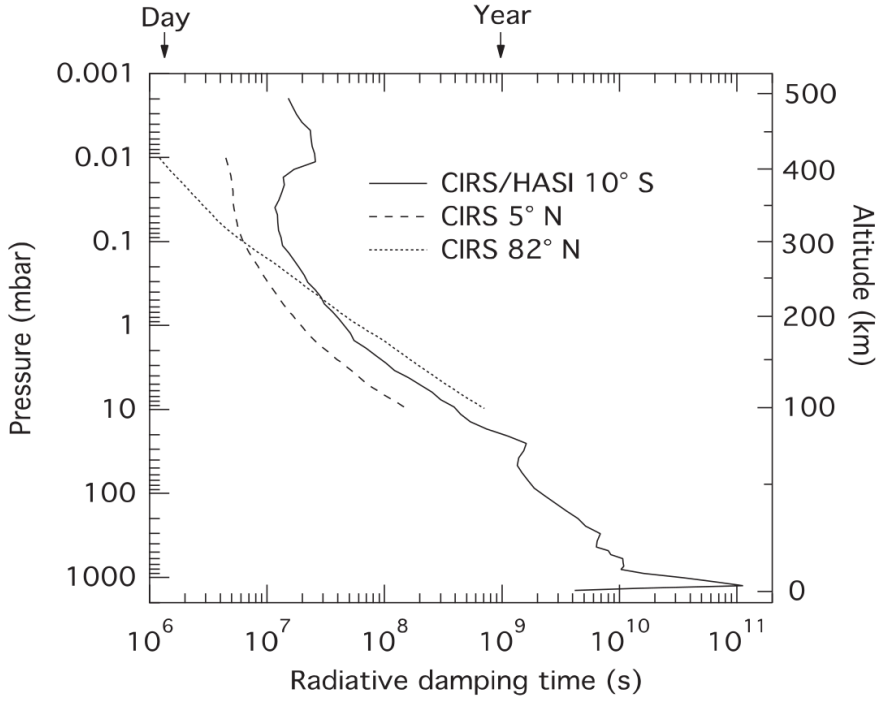

Figure 3.7: Estimate of the radiative damping time in Titan's atmosphere through CIRS measurements. After [Flasar et al., 2014].

The main characteristics of Titan's middle atmospheric circulation is the so called *superrotation*, that is the whole atmosphere rotates much faster than the planet itself, which rotates slowly in about 16 days due to the tidal locking with Saturn. Another planet in the solar system which shows a similar behaviour is Venus. The wind peak intensity is found in the upper stratosphere, at about 300 km, around the winter pole. In this strong circumpolar jet winds can reach 200 m/s, while the circulation around the summer pole is much slower (a few m/s) [Lebonnois et al., 2014]. The source of the circumpolar jet is in the meridional circulation, which transports energy and angular momentum from lower to higher latitudes. The slow planetary rotation and consequently small Coriolis force enable the meridional cells that redistribute energy to reach the polar latitudes, making Titan's circulation substantially different from the Earth's.

Current models of the meridional circulation predict the existence of a single cell that goes from the summer hemisphere to the winter pole, with ascending motions in the first and subsidence in the latter. Some models also predict the existence of a second smaller and weaker cell from the summer hemisphere to the the summer pole, but there is no agreement nor observational evidence on this [Lebonnois et al., 2014; Teanby et al., 2008]. The subsidence on the winter pole is instead both confirmed

by all existing models and by observation of the concentrations of some tracers in the CIRS measurements.

The tracers used are gases like HCN, C_2H_2 and other hydrocarbons which are produced in the upper atmosphere and have abundance profiles that increase with altitude. In case of subsidence, air parcels from the upper atmosphere - with larger concentration of the tracer - are moved towards lower altitudes and a larger VMR of the tracer is seen at a fixed altitude. In case of ascending motions the opposite occurs.

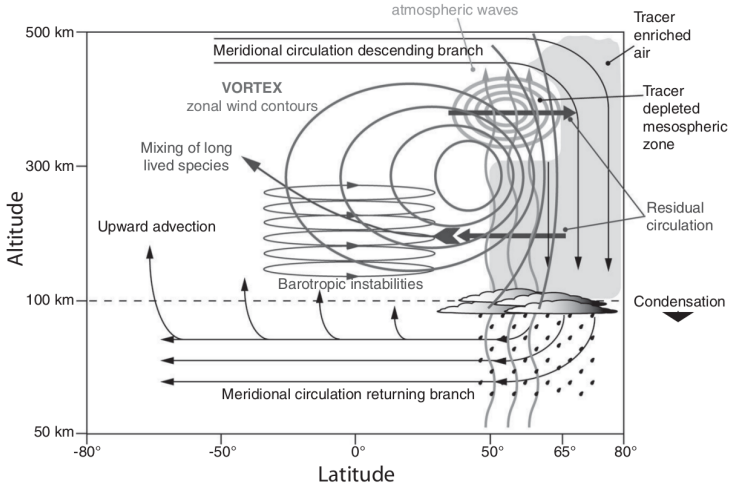

Figure 3.8: Schematic model of the circulation at the winter pole, with the formation of the circumpolar jet and the subsidence of tracer-rich air inside the polar vortex. After [Teanby et al., 2008].

In Figure 3.8, a scheme of the dynamical processes taking place at the winter pole is shown. The upper branch of the meridional circulation brings air from the summer hemisphere towards the winter pole, which then subsides in the polar vortex with a large concentration of tracers. Some gases condense at the cold polar tropopause, forming stratospheric ice clouds in the so called *polar cap* and then precipitating towards the surface. CIRS measurements have given an unprecedented picture of the dynamical processes in the middle atmosphere of Titan, evidencing the passage from the late northern winter to northern spring [Teanby et al., 2009, 2012, 2010, 2008; Vinatier et al., 2015]. Figure 3.9 shows the average of the retrieved temperatures before 2009, during the northern winter (left panel, and in 2011, during early spring (right panel). Main achievements of CIRS analysis are:

- during northern winter a vortex structure is seen at the North pole (left panel of Figure 3.9, with a strong heating in the polar mesosphere and cooling in

the lower stratosphere, sign of a subsidence process taking place in the polar region. The subsidence velocities have been estimated to be in the range 0.5-2 mm/s to explain the observed adiabatic heating in the mesosphere [Teanby et al., 2012].

- in the early spring in 2009-2010, the heating in the northern polar mesosphere ceases and leaves an almost symmetrical temperature pattern, indicating the onset of a two cells dynamics, with ascending motions at low latitudes and descending motions at the poles.

- in 2011 a first clear sign of circulation reversal is seen, with heating in the southern polar mesosphere (right panel in Figure 3.9).

- in 2012 unexpected low temperatures are found in the southern polar mesosphere, indicating a negative feedback due to trace gases radiative cooling that competes with the adiabatic heating.

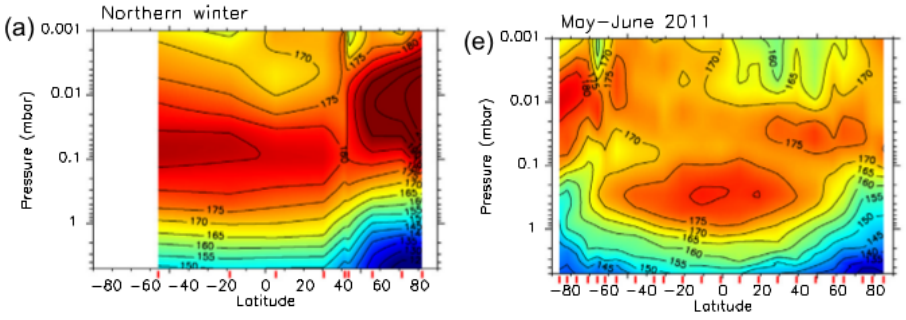

Figure 3.9: Temperature maps retrieved by CIRS measurements relative to northern winter (average before 2009) and early spring (2011). After [Vinatier et al., 2015].

Figures 3.10 and 3.11 show respectively the HCN and C_2H_2 abundance maps retrieved through CIRS measurements. Main results obtained by CIRS analysis are:

- during northern winter a sign of enrichment of trace gases is seen in the northern polar mesosphere, but CIRS maps miss the highest latitudes (¿ 80°) due to partial coverage. The enrichments are confined very close to the polar region at latitudes higher than 70-75°.

- few months after the equinox in August 2009, the peak in the tracer enrichments - the red region in the left panels of Figures 3.10 and 3.11 - lies in the northern polar mesosphere between 300 and 500 km, but is much more expanded at lower latitudes till 50°N; a moderate enrichment - the yellow-green

region - is also seen at lower latitudes, covering the whole northern hemisphere mesosphere, and at lower altitudes in the polar stratosphere. No enrichment is seen in the southern hemisphere.

- in early 2012, well inside northern spring (right panels of Figures 3.10 and 3.11), the first sign of enrichment is seen in the upper south polar mesosphere. This enrichment is thought to be responsible for the mesosphere cooling seen in this period [Vinatier et al., 2015].

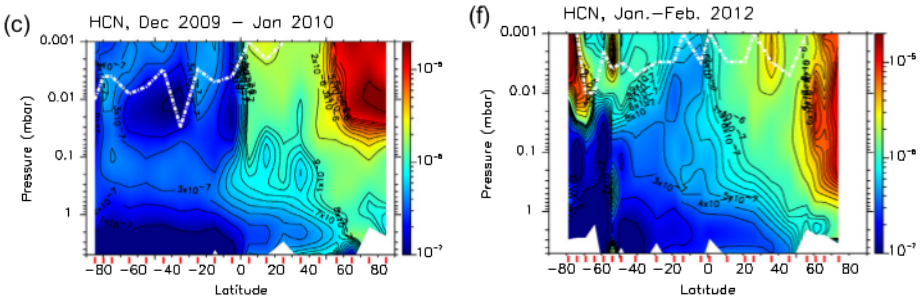

Figure 3.10: HCN abundance maps retrieved by CIRS measurements relative to years 2009/10 and 2012. After [Vinatier et al., 2015].

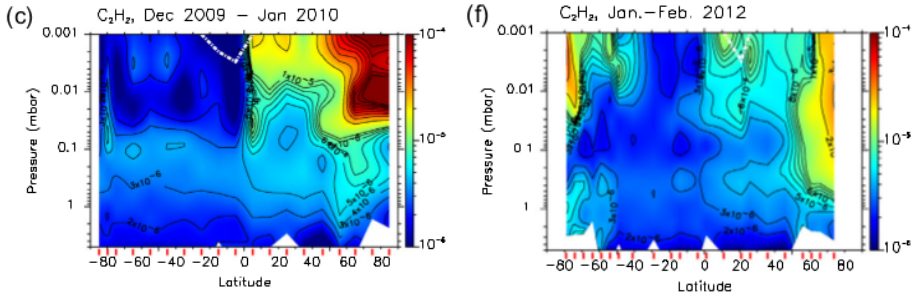

Figure 3.11: C_2H_2 abundance maps retrieved by CIRS measurements relative to years 2009/10 and 2012. After [Vinatier et al., 2015].

Although CIRS retrievals extend only up to 500 km altitude, Teanby et al. [2012] estimate that the top of the middle atmosphere circulation has to extend at least up to 600 km, inside the photochemical source region, in order to explain the observed enrichment in trace gases. As for the dynamical models, currently the top of the atmosphere for such models is set at 400 or 500 km, but higher altitude levels are needed to fully understand Titan's middle atmosphere dynamics.

3.2.4 Dynamics and variability of the upper atmosphere

The current knowledge of Titan's upper atmosphere is puzzling [Yelle et al., 2014]. On the observational side, the only dataset with some statistics and coverage are the measurements of INMS at altitudes above 950 km, while UVIS occultation data in the 600-1000 km range are sparse.

INMS data measure the N_2 and CH_4 densities during close passes of Titan by Cassini. From those data the temperature profile in the upper atmosphere (higher than about 950-1000 km) is inferred integrating the hydrostatic equation and using the ideal gas law [Yelle et al., 2006; Cui et al., 2009; Snowden et al., 2013; Yelle et al., 2014].

Müller-Wodarg et al. [2008] developed an empirical model of the temperature structure in the upper atmosphere fitting a linear combination of Legendre polynomials to the INMS temperatures. They considered only data before T32 flyby of Cassini that took place in 2007 and all data are relative to the northern hemisphere [Yelle et al., 2006]. The result of the fit shows a large temperature gradient (from 170 to 130 K) at 1000 km from low latitudes to the pole, which is shown in Figure 3.12. From this model temperature and through the thermal wind equation, they derived wind estimates for the dynamics of the upper atmosphere. The model shows zonal winds of 50 m/s with a peak at 70° latitude, meridional winds up to 150 m/s directed towards the pole and a strong subsidence at the pole.

With these estimates of the horizontal winds, the authors predict an accumulation of lighter gases in the northern polar thermosphere. For the case of CH_4, the dynamical time constant at 1000 km is of the order of 10^4s, which is much lower than the time constant for $Ly\alpha$ absorption of CH_4 (2×10^7 s) and molecular diffusion (2×10^6 s). Following this picture, Titan's thermosphere would be dominated by dynamics. However, the authors point out that an energetic problem exists in driving the dynamics apparent in the empirical model, that can't be explained with solar EUV input alone, and that the influence from the lower atmosphere might be determinant [Müller-Wodarg et al., 2008; Yelle et al., 2014].

A serious limitation of the model in Müller-Wodarg et al. [2008] is the small statistics (only 13 passes of INMS till T32 were available at the time of the analysis) and the poor fit of the observations, which show a large variability.

Analyzing a more complete INMS dataset, Snowden et al. [2013] made a thorough check for the existence of correlations between the retrieved temperature profiles and a set of geophysical variables, which include latitude, longitude, solar zenith angle,

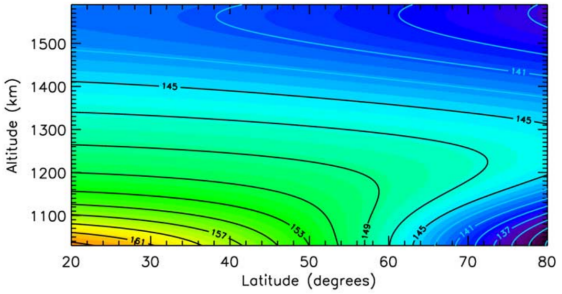

Figure 3.12: Inferred temperature map in the model of [Müller-Wodarg et al., 2008].

local time, position of Titan in Saturn's magnetospheric enviroment and solar EUV flux. They conclude that no clear correlation exists with latitude, longitude, solar zenith angle and local time. However, the sparse coverage of INMS data (32 passes in close flybys) does not allow to distinguish seasonal variations, thus muting any eventual latitude dependence of temperature. The temperatures retrieved at a N_2 density of $5 \times 10^9\,\mathrm{cm}^{-3}$, which corresponds on average to 1000 km altitude, are shown in Figure 3.13 in function of latitude. The variability of the retrieved temperatures is large and the statistics too low to try to assess any latitudinal dependence of temperature.

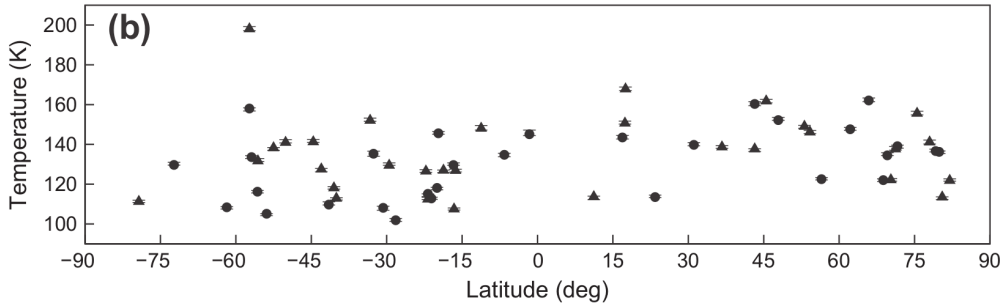

Figure 3.13: Temperatures retrieved from INMS data around 1000 km altitude. After [Snowden et al., 2013].

The authors conclude that there is an important influence of gravity waves propagating from the lower atmosphere in determining the thermal structure of the upper atmosphere. Snowden and Yelle [2014] assessed all possible thermal energy sources in Titan's upper atmosphere. The main source is solar EUV radiation with a flux of 3 to $5 \times 10^9\,\mathrm{eV\,cm^{-2}\,s^{-1}}$ (global average) in the thermosphere, followed by wave dissipation that could account for a flux up to $3 \times 10^9\,\mathrm{eV\,cm^{-2}\,s^{-1}}$ at 1200 km. Peak energy deposition due to magnetospheric sources is estimated to be smaller than EUV input, but constitutes an important fraction of the EUV (from 10 to 100%

between 1000 and 1300 km). However, the magnetospheric particle precipitation is highly variable and not uniform globally.

On the other side, the cooling is expected to be produced mostly by HCN rotational lines above 800 km and by the vibrational bands of HCN, CH_4, C_2H_2, C_4H_2 and C_6H_6 below 800 km. The authors point out that a larger HCN abundance than that measured by UVIS would be needed to explain the observed low temperatures in the thermosphere.

Müller-Wodarg et al. [2003] presented a general circulation model (GCM) of Titan's upper atmosphere. The model included as energy source only the solar EUV radiation, with no contribution from waves or particle precipitation. The predicted temperature field showed a strong day-night difference at 1300 km altitude (about 20 K), with the development of day-night winds of about 50 m/s. However, the regular pattern predicted by the model finds no observational confirmation in the measurements, which show no clear pattern [Snowden et al., 2013].

3.3 non-LTE processes in planetary atmospheres

The next chapters focus on the inversion of molecular abundances from the middle and upper atmosphere of Titan, through measurement of their IR emission in conditions of vibrational non-LTE. In this works we will always assume that translational and rotational degrees of freedom of molecule are well represented by LTE and only vibrational excited states may run out their equilibrium value. This is usually a good approximation in planetary atmospheres, apart from the very upper part, and suited to the case under study.

This Section is dedicated to introduce to the problem of the calculation of vibrational levels populations under non-LTE conditions. The modeling and calculation of non-LTE populations used in this work have been performed by the group of planetary atmospheres at the Instituto de Astrofisica de Andalucia (IAA) of Granada (Spain). Since this is a necessary ingredient of all subsequent analysis, it needs at least a brief introduction.

In case of non-Local Thermodynamic Equilibrium (non-LTE), the population of the excited levels of molecules is not known a priori once known the local kinetic temperature, as is done in the case of LTE. Instead one needs to explicitly take into account the balance between forces that tend to drive the system out of equilibrium and forces that tend to restore the equilibrium state (thermalization).

This balance is calculated through a set of statistical equilibrium equations that consider all processes that may populate or de-populate the vibrational levels of the molecules considered.

3.3.1 Collisional processes between molecules

Let us consider the following sketch of the processes into play, that might be visualized as the scheme in Figure 3.14.

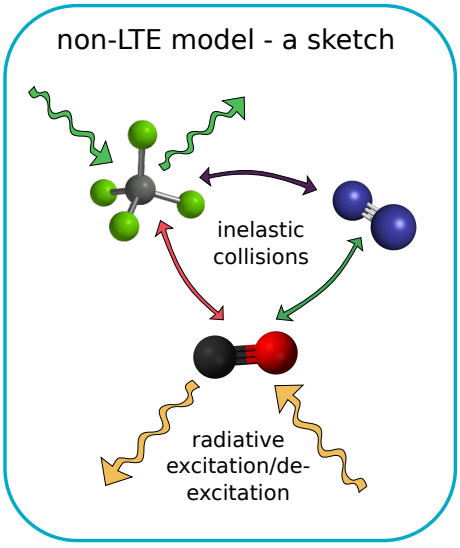

Figure 3.14: Scheme of the collisional and radiative processes that may take place in a typical non-LTE situation.

A molecule X gets excited to the vibrational state v through the absorption of a solar photon. Now it can either re-emit a photon and de-excite to some other vibrational state (the energy of the photon is lost) or collide with another molecule M. In the most common situation nothing happens to the vibrational state (elastic collision), otherwise molecule X may de-excite from the original vibrational state to another one (v'), but now transferring the lost energy to other vibrational levels or to the thermal bath. We can roughly distinguish between two types of de-excitation: we call *vibrational-translational (V-T)* energy transfer the one in which the whole energy difference between v and v' is completely transferred to the thermal bath (translational or rotational degrees of freedom); the other possible situation is the *vibrational-vibrational (V-V)* transfer in which another transition takes place at the same time, exciting molecule M from the initial state α to a higher vibrational state β.

$$X_\upsilon + M_\alpha \rightarrow \begin{cases} X_\upsilon + M_\alpha & \textit{elastic collision} \\ X_{\upsilon'} + M_\alpha & \textit{inelastic collision: V-T transfer} \\ X_{\upsilon'} + M_\beta & \textit{inelastic collision: V-V transfer} \end{cases} \tag{3.1}$$

In the general situation of V-V transfer, the two simultaneous transitions are not exactly resonant ($E_\upsilon - E_{\upsilon'} \neq E_\beta - E_\alpha$) and part of the energy goes to the thermal bath. While V-T processes always lead towards thermalization, V-V processes tend to connect the population of two vibrational levels and may also contribute to drive a level's population out of LTE if the other level is strongly out of equilibrium.

For a particular collision between molecule M in the vibrational state α and molecule X in state υ, with final states β and υ' respectively, we may write the number N of such collisions that take place per unit time and volume as:

$$N^{M-X}_{\alpha,\upsilon;\beta,\upsilon'} = n_{\mathrm{M}} f_\alpha n_{\mathrm{X}} f_\upsilon \, k^{M-X}_{\alpha,\upsilon;\beta,\upsilon'} \tag{3.2}$$

Where n_{M} and n_{X} are the number density of the two species, f_α and f_υ the population fraction of the two levels α and υ and k is the rate constant for the particular process, which has dimensions of $cm^3\, s^{-1}$.

The rate constants for specific processes are either calculated theoretically (molecular collision theory) or, most commonly, determined experimentally. The paucity of data on rate constants and the large error often connected with the measured values is one of the main complications in the modeling of vibrational non-LTE.

3.3.2 The equation of statistical equilibrium

Let us focus on a particular excited vibrational level υ of some molecule X, which we will indicate as $X_{(\upsilon)}$. Molecules in the $X_{(\upsilon)}$ state may relax to lower states through spontaneous emission of a photon or collision with another molecule. On the other side, molecules X may be excited to level υ through collisions or absorption of a photon.

The radiative processes, both absorption and spontaneous emission, play a primary role in bringing vibrational levels out of LTE: absorption of a strong incoming radiative field can significantly raise the excited level population, whereas spontaneous emission in the absence of an intense radiative field and of efficient collisions can lower it compared to LTE.

The statistical equation that rules the evolution of the number density of molecule X in the υ level (indicated as $\left[X_{(\upsilon)}\right]$), can be written as:

$$\frac{d\left[X_{(\upsilon)}\right]}{dt} = -\left[X_{(\upsilon)}\right]\sum_{\upsilon'}\mathcal{R}_{\upsilon,\upsilon'} + \sum_{\upsilon'}\left[X_{(\upsilon')}\right]\mathcal{R}_{\upsilon',\upsilon} - \left[X_{(\upsilon)}\right]\sum_{M,\alpha}k^{M-X}_{\alpha,\upsilon;*}\left[M_{(\alpha)}\right] + \sum_{M,\upsilon',\alpha,\beta}k^{M-X}_{\beta,\upsilon';\alpha,\upsilon}\left[M_{(\beta)}\right]\left[X_{(\upsilon')}\right] \tag{3.3}$$

$$\text{where} \quad \mathcal{R}_{\kappa,\lambda} = \begin{cases} \mathcal{A}_{\kappa,\lambda} & \text{if } \kappa > \lambda \\ \bar{J}(w_{\kappa,\lambda})\,\mathcal{B}_{\kappa,\lambda}\left(1 - \dfrac{g_\kappa\left[X_{(\lambda)}\right]}{g_\lambda\left[X_{(\kappa)}\right]}\right) & \text{if } \kappa < \lambda \end{cases}$$

The meaning of the different part of the above equation is as follows:

$\left[X_{(\upsilon)}\right]\sum_{\upsilon'}\mathcal{R}_{\upsilon,\upsilon'}$ — Losses due to absorption of a photon and radiative excitation to a higher level ($\upsilon' > \upsilon$) or spontaneous emission and relaxation to a lower one ($\upsilon' < \upsilon$).

$\sum_{\upsilon'}\left[X_{(\upsilon')}\right]\mathcal{R}_{\upsilon',\upsilon}$ — Production of X molecules in the (υ) state due to radiative excitation/relaxation from other excited states or from the ground.

$\left[X_{(\upsilon)}\right]\sum_{M,\alpha}k^{M-X}_{\alpha,\upsilon;*}\left[M_{(\alpha)}\right]$ — Overall losses due to collisional relaxation/excitation of the $X_{(\upsilon)}$ level.

$\sum_{M,\upsilon',\alpha,\beta}k^{M-X}_{\beta,\upsilon';\alpha,\upsilon}\left[M_{(\beta)}\right]\left[X_{(\upsilon')}\right]$ — Overall production of X molecules in the (υ) state, through collisional excitation/relaxation.

When studying non-LTE in planetary atmospheres, one looks for the stationary state of the equations above, since the timescales for variation of the external conditions in an atmospheres is usually much larger than the typical time for reaching a stationary state. The time-varying version of the equation of statistical equilibrium

is instead fundamental in other situations, like the experimental determination of rate constants.

The band radiative excitation rate $\mathcal{R}_{\kappa,\lambda}$ that appears in the equation above requires the definition of proper weighted sums of the Einstein coefficients and mean intensity over the rotational sublevels corresponding to the two vibrational states. For their definition and further details see Funke et al. [2012] and López-Puertas and Taylor [2001].

3.3.3 Vibrational temperatures

A common convention is to speak of the population of the vibrational levels in terms of the *vibrational temperature* T_v, different for each excited state. The vibrational temperature is the temperature at which the considered level would have the same population fraction it has in non-LTE. Thus we may write:

$$n_v = n_{\text{tot}} \frac{g_v e^{-c_2 E_v / T_v}}{\mathcal{Z}_{\text{vib}}} \qquad \text{with} \quad \mathcal{Z}_{\text{vib}} = \sum_{\lambda} g_\lambda e^{-c_2 E_\lambda / T_\lambda} \tag{3.4}$$

In the equation above we also defined the non-LTE partition function $\mathcal{Z}_{\text{vib}}$ of the vibrational levels, which in general differs from the equilibrium one [Edwards et al., 1998]; n_{tot} is the total number density of the molecule under consideration. The vibrational temperature is usually defined in function of the ratio of the level population with respect to the ground level:

$$n_v = \frac{n_0 g_v}{g_0} e^{-c_2 E_v / T_v} \quad \rightsquigarrow \quad T_v \equiv -c_2 E_v / \log\left(\frac{n_v g_0}{n_0 g_v}\right) \tag{3.5}$$

Another quantity often used is the ratio $r_v = n_v / n_v^{\text{eq}}$ of the effective population of a vibrational state to its equilibrium value; from the relations above, we obtain:

$$r_v = \frac{\mathcal{Z}_{\text{vib}}^{\text{eq}}}{\mathcal{Z}_{\text{vib}}} \, e^{-c_2 E_v \left(\frac{1}{T_v} - \frac{1}{T}\right)} \tag{3.6}$$

3.3.4 The GRANADA code

Taking into account all relevant vibrational levels of each molecule potentially out of LTE (let us say these are n vibrational levels), one obtains a system of n (in general coupled) equations in the n unknowns of the level populations, for each fixed position $\boldsymbol{x}$ in the atmosphere. Simultaneously with these n statistical equations, one has to consider m equations of radiative transfer, one for each vibrational band involved

(in general $n \neq m$). These m integral equations are coupled to the n statistical ones. The resulting problem is non-local and in general non-linear.

The non-LTE calculations used in the next chapters have been performed through the Generic RAdiative traNsfer AnD non-LTE population Algorithm (GRANADA) - originally developed for the Earth's atmosphere [Funke et al., 2007, 2012] and adapted to the Titan's atmosphere - by the group of planetary atmospheres at the IAA of Granada (Spain). The code makes use of the direct radiative transfer simulations performed by KOPRA (Karlsruhe optimized and precise radiative transfer algorithm, presented in Stiller et al. [2002]). It can work with an arbitrary number of vibrational bands and vibrational excited levels. GRANADA adopts a Lambda iteration scheme, which can optionally be coupled to an algebraical resolution of the linearized system of equation (modified Curtis-Matrix method).

Chapter 4

CO concentration in Titan's middle atmosphere

This chapter focuses on the inversion of carbon monoxide (CO) in the middle atmosphere of Titan, through the analysis of CO non-LTE emission at 4.7 μm measured by VIMS. The chapter is derived from the following publication:

- F. Fabiano, M. López Puertas, A. Adriani, M.L. Moriconi, E. D'Aversa, B. Funke, M.A. López-Valverde, M. Ridolfi, B.M. Dinelli, *CO concentration in the upper stratosphere and mesosphere of Titan from VIMS dayside limb observations at 4.7μm*, In Icarus, Volume 293 (2017), 119-131

4.1 CO abundance in Titan's atmosphere

Since the discovery of carbon monoxide in Titan's atmosphere [Lutz et al., 1983], the determination of its abundance has been the focus of many investigations and has stimulated an intense scientific debate. To date, only three molecules carrying oxygen have been detected in the atmosphere of Titan: CO_2, CO and H_2O. Among them CO is by far the most abundant, with a relative abundance of about 5×10^{-5}, compared with about 1.5×10^{-9} for CO_2 and 4×10^{-10} for H_2O.

The presence of CO in Titan's atmosphere has been a mystery for many years. CO molecule is substantially inert in Titan's environment, with an estimated chemical lifetime of the order of 10 kyr, and it does not condense even at tropospheric temperatures [Wilson and Atreya, 2004]. Its extremely large bond energy of 10.7 eV makes CO difficult to be photolized by radiation, since hard UV photons are absorbed by the much more abundant N_2. Therefore, photodissociation is negligible

with respect to other loss processes [Hörst et al., 2008; Wilson and Atreya, 2004]. The main loss process of CO is the production of CO_2 through the reaction:

$$CO + OH \rightarrow CO_2 + H. \tag{4.1}$$

Most of the CO_2 produced is then photodissociated and essentially recycled back to CO [Wilson and Atreya, 2004]. According to models, a minor part of CO_2 condenses at the cold Titan's tropopause and its deposition on the surface represents a sink for atmospheric oxygen, which is not at equilibrium on Titan. The overall net losses in the atmosphere for CO are due almost exclusively to CO_2 condensation and account for $1.8 \times 10^6\,cm^{-2}\,s^{-1}$ [Hörst et al., 2008]. This loss rate has to be compared with a total CO column of about $1.4 \times 10^{22}\,cm^{-2}$, corresponding to a uniform 50 ppmv CO fraction.

This small net loss of oxygen means that either CO is not in a steady state in the atmosphere and is the remnant of a larger primordial concentration [Wong et al., 2002], or there is some active oxygen source in Titan's atmosphere. This 30-years-old question has been finally addressed by Hörst et al. [2008], who proposed that the observed CO abundance could be explained by the O^+ influx from Saturn's magnetosphere, measured by CAPS [Hartle et al., 2006]. Following Hörst et al. [2008], many photochemical models assume now that CO is produced in the upper atmosphere around 1000 km through the reaction of O atoms with CH_3 [Krasnopolsky, 2009; Lara et al., 2014; Dobrijevic et al., 2014]:

$$O + CH_3 \rightarrow CO + H_2 + H \tag{4.2}$$

However, since the photochemical production and losses of CO are extremely slow and its molecular mass is equal to that of N_2, CO is efficiently diffused throughout the atmosphere by eddy processes. Therefore, photochemical models predict a uniform CO volume mixing ratio (VMR) profile with no significant latitudinal and seasonal variations.

While there is now quite a good agreement on a 50 ppmv CO VMR, at least in the lower stratosphere, some previous Earth-based measurements have led to contradictory results. Observing the absorption of solar reflected radiation in the 4.7 μm region, Noll et al. [1996] concluded that tropospheric CO VMR was about 10 ppmv. More recently, the same absorption has been re-analysed by Lellouch et al. [2003] and López-Valverde et al. [2005], leading to a tropospheric relative abundance of 32 ± 10 ppmv; in the latter a non-LTE model of CO excited states was developed

and the result suggested a larger abundance in the stratosphere, about 60 ppmv.

Rotational transitions of CO on Titan have been observed from Earth by many authors in the past 30 years [Muhleman et al., 1984; Gurwell and Muhleman, 1995; Hidayat et al., 1998; Gurwell and Muhleman, 2000; Gurwell, 2004], and most of these works agree very well with a 50 ppmv value for CO VMR. More recently, Serigano et al. [2016] have analysed ALMA observations of CO rotational lines and confirm the value of 49.6 ± 1.8 ppmv with a low uncertainty. These works were mostly sensitive to the lower stratosphere, between 100 and 300 km, and assumed a uniform CO VMR profile. Some of them, however, also attempted to derive the vertical distribution of CO, even with a low resolution. Hidayat et al. [1998] found a profile varying from 27 ppmv in the lower stratosphere to 5 ppmv at 300 km, while Gurwell and Muhleman [2000], using interferometric observations of the CO 2–1 rotational line, obtained an uniform 52 ± 2 ppmv profile as the best fit. However, their measurements were also compatible with a CO profile ranging from 48 ppmv in the lower stratosphere to 60 ppmv in the upper stratosphere at 300 km.

The beginning of the Cassini era has shed new light on many aspects of Titan's atmosphere and new analysis on CO are now available. The Composite Infrared Spectrometer (CIRS) and the Visual and Infrared Mapping Spectrometer (VIMS) aboard Cassini have both allowed new studies on CO. The former, by observing CO rotational lines in the far infrared $0.1 - 0.5$ mm region and, the latter, by observing IR vibrational emission bands near 4.7 μm. Three results based on limb and nadir observations by CIRS have been reported to date, with CO abundances in the lower stratosphere of 45 ± 15 ppmv, 47 ± 8 ppmv and 55 ± 6 ppmv, respectively [Flasar et al., 2005; De Kok et al., 2007; Teanby et al., 2010]; all assuming that the CO VMR is constant with altitude and with a significant contribution function between about 60 and 140 km.

The 4.7 μm band of CO is situated at the longest wavelength edge of VIMS spectral range, where the noise level and the background produced by the instrument's thermal radiation are larger. Nevertheless, to date, three works have been published based on VIMS measurements, either on the CO extinction during solar occultations [Bellucci et al., 2009; Maltagliati et al., 2015] or on thermal emission in the night side [Baines et al., 2006]. They report a CO abundance in the lower stratosphere of 33 ± 10 ppmv (at 100 ± 30 km), 46 ± 16 ppmv (60-180 km) and 32 ± 15 ppmv (below ~ 200 km), respectively.

Although most recent works do agree on a CO VMR of about 50 ppmv in the

lower stratosphere [Gurwell and Muhleman, 2000; De Kok et al., 2007; Maltagliati et al., 2015; Serigano et al., 2016], the observational confirmation of the predicted well-mixed vertical profile is still awaited, because of contradictory results [Hidayat et al., 1998; López-Valverde et al., 2005].

The aim of this work is to retrieve the vertical distribution of CO from VIMS daytime measurements. The strong non-LTE solar pumping of the CO vibrational levels near 4.7 μm during daytime produces a strong limb radiance at these wavelengths that allows to retrieve CO up to high altitudes. Thus, we aim at measuring CO in the altitude range between 200 and 500 km, where it has not been measured yet, and hence to shed some light on the CO origin in Titan's atmosphere.

In Section 4.2 we describe the selection and calibration of the analysed data; in Sec. 4.4 we describe the non-LTE model for CO; in Secs. 4.5 and 4.7 we describe the analysis method and results; and, finally, in Sec. 4.8 we draw our conclusions.

4.2 VIMS observations of CO 4.7 μm emission

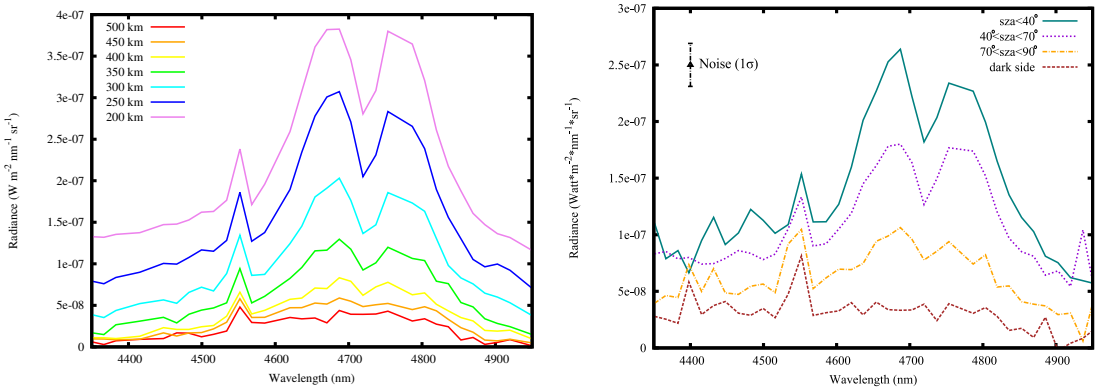

Figure 4.1: Typical VIMS limb daytime spectra near 4.7 μm. Upper panel: spectra taken at an average SZA of 30° and a phase angle of 60° showing the variation of the radiance with the limb tangent altitude. Lower panel: spectra taken at a tangent height of 350 km showing the variation with SZA.

4.2.1 Data overview

In this work we analyse VIMS observations above Titan's limb, focusing on the long wavelength part of VIMS spectral range, from 4.2 μm to 5 μm. Various examples of average spectra are shown in Fig. 4.1 where we can see that the signal depends strongly on both the tangent altitude and the solar zenith angle (SZA) at the tangent

point. Two main molecular emissions contribute to the spectrum: the peak at 4.55 μm is clearly a signature of the Q branch of CH_3D ν_2 band (the $2\nu_6$ band contributes as well), while the emission between 4.6 and 4.9 μm is mainly due to the fundamental, first hot and isotopic bands of CO. The shape of the CO signature changes with the tangent altitude: the hot band (centred at 4.72 μm) is the main responsible of the signal at low altitudes, whereas the fundamental band (centred at 4.67 μm) dominates the spectra above 400 km. We discuss this issue in more detail in Sec. 4.5.1. The continuum-like signal, which is due to the scattering of the solar radiation by Titan's aerosols, gives a non-negligible contribution at tangent altitudes lower than 300 km, thus constituting a major complication in the data analysis.

The vibrational excited states of the CO molecule are strongly out of LTE in Titan's middle atmosphere during daytime. The lower panel of Fig. 4.1 shows the average of a large set of VIMS spectra at 350 ± 25 km tangent altitude, for different SZAs. At smaller SZAs the continuum due to scattering increases and, at the same time, the intensity ratio between the CO and CH_3D bands changes. The CO emission is stronger with the sun higher above the horizon, when the solar radiation produces a larger pumping of the excited levels. This can be better appreciated in Fig. 4.2, where we show the mean of the band-integrated intensity from 4.6 to 4.85 μm, for different altitudes and SZAs. In that integration we corrected the continuum contribution approximately by using a linear interpolation that depends on the SZA. Note that in the retrieval of the CO this contribution is calculated more accurately (see Sec. 4.5). The dependence of the residual integrated signal on SZA is due mainly to non-LTE effects. We discuss further this issue in Sec. 4.4.

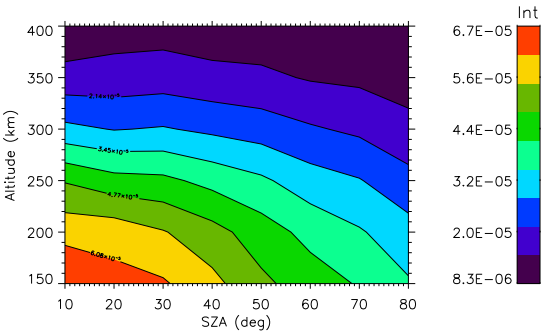

Figure 4.2: Altitude-SZA map of the integrated radiance in the CO band, corrected for solar scattering contribution. Color scale units are in $W\,m^{-2}\,sr^{-1}$. The strong dependence of the radiance on the SZA confirms the non-LTE nature of the CO emission.

4.2.2 Data selection

Extracting information on the CO abundance from these spectra is challenging, especially at the highest tangent altitudes, because of the low signal-to-noise (S/N) ratio. A good data selection is therefore mandatory in order to obtain accurate results on the CO abundance. We considered here only measurements taken along one year between July 2006 and July 2007 (see Sec. 4.3) and selected the cubes with an integration time of 600 ms, which represent a good compromise between the number of measurements available, the altitude coverage and the S/N ratio.

When analysing limb measurements, the precision and stability of the instrument pointing is crucial. In order to avoid important biases in the analysis, the pointing error has to be considerably smaller than the pressure scale height of the atmosphere. On Titan, the scale height in the stratosphere is about 50 km. As reported by Brown et al. [2004], the VIMS' pointing calibration is quite satisfactory, although there is a wavelength-dependent misplacement between the actual and calculated pointing. Quoting [Brown et al., 2004], "the large-scale effect present has a very low frequency (at the scale of the entire spectral range) and likely results from optical aberrations within the IR spectrometer". The measured misplacement has an average value of 0.1 pixels (0.05 mrad) in the 4–5 μm region. The pointing error in terms of tangent altitude is then, in the worst case, $\epsilon_H = 5\,D \cdot 10^{-5}$, where D is the distance from Titan. We found that the best compromise between the number of measurements available, the altitude range covered and the small potential error on pointing requires the distance of the spacecraft from Titan to be smaller than $D_{max} = 1.5 \times 10^5$ km, which corresponds to a maximum 8 km uncertainty in the pointing. This uncertainty is a constant systematic error for measurements belonging to a single cube, but varies in a random way among different cubes, thus reducing the overall effect on the result (see further discussion in Sec. 4.6). For the same reasons, we also checked the effect of long integration time on the actual footprints of VIMS pixels (motion smearing), finding it to contribute for as small as 1 km to the tangent altitude uncertainty, significantly smaller than the assumed pointing bias.

The last selection criterion regards the SZA. It is apparent from Figs. 4.1 and 4.2 that the signal depends strongly on SZA because the population enhancement of the upper molecular levels is supplied essentially by sunlight (see Sec. 4.4). We found that, for SZA greater than 70°, the S/N ratio is very low, due to the fainter solar illumination. Moreover, the SZA varies along the line of sight (LOS). However,

in our forward model we assume that the SZA does not change along the LOS and simulate the emission, for each LOS, at the SZA corresponding to the tangent point. This approximation is very good at the smallest SZA, but becomes progressively less accurate with larger SZAs (see Funke et al. [2009] for a discussion of this approximation in the Earth's atmosphere). For these reasons, we decided to take into account only measurements with SZA at the tangent point smaller than 60°.

Table 4.1: List of VIMS cubes used in the analysis. For each cube, the table lists the cube name, the number of spectra, the time of measurement in years, the distance between the spacecraft and the centre of Titan ('Dist' in units of 10^5 km), the mean phase angle (Pha), and the covered ranges in SZA (degrees) and in latitudes.

#	Cube	# Spectra	Time	Dist	Pha	SZA range	Lat range
1	V1530497617	237	2006.50	1.48	62	30–59	74 S–32 S
2	V1530499395	170	2006.50	1.38	62	27–59	74 S–6 S
3	V1530501191	248	2006.50	1.29	62	26–59	74 S–11 S
4	V1530502987	115	2006.50	1.19	62	26–59	74 S–14 S
5	V1547346754	336	2007.04	1.29	109	20–58	25 S–36 N
6	V1547349422	215	2007.04	1.14	109	20–51	21 S–31 N
7	V1563519758	18	2007.55	1.13	60	49–60	68 S–54 S
8	V1563524168	12	2007.55	1.39	60	50–59	68 S–56 S
9	V1563525149	28	2007.55	1.45	60	40–59	68 S–42 S
10	V1563525638	52	2007.55	1.48	60	32–59	67 S–29 S
11	V1563526309	88	2007.55	1.52	60	28–47	53 S–16 S

The list of the cubes analysed in this study, along with the number of spectra considered, the time of measurement, the distance from Titan and the phase angle, are listed in Table 4.1. The data of each cube have been binned in latitude-SZA boxes. We chose a 10° latitudinal bin where we expect almost uniform thermal conditions and composition. The criterion for SZA binning of the measurements considers that the length of the solar ray path inside the atmosphere, given approximately by $1/\cos(\mathrm{SZA})$ for our SZAs, varies less than 10%. Data belonging to the same latitude-SZA bin inside one VIMS cube constitute a "limb scanning sequence", that is, a collection of spectra at different tangent altitudes that are sounding the same atmospheric region and are similarly illuminated. For latitude-SZA boxes with more than 70 spectra we obtained more sequences. Out of the eleven VIMS cubes considered, we extracted 47 limb scanning sequences (see Table 4.2), each one with a characteristic latitude and SZA. Each limb scanning sequence collects, on average, about 30 spectra.

Table 4.2: Latitude/SZA boxes analysed in this work and obtained from the VIMS cubes in Table 4.1. The number of spectra in each Lat/SZA box (#sp) and the corresponding number of sequences (#limb) are indicated in parenthesis.

Lat. range	Mean SZA (#sp, #limb)
80°S-70°S	57(69, 3)
70°S-60°S	49(53, 2), 54(118, 7)
60°S-50°S	44(74, 2)
50°S-40°S	38(114, 4), 44(54, 3)
40°S-30°S	30(188, 6)
30°S-20°S	30(159, 4)
20°S-10°S	30(237, 6)
10°S-0°S	14(52, 1)
0°S-10°N	14(64, 1)
10°N-20°N	30(123, 2)
20°N-30°N	38(83, 2), 44(63, 2)
30°N-40°N	49(18, 1), 54(14, 1)

4.2.3 Data calibration

Raw VIMS data have been calibrated geometrically, using ad hoc algorithms based on NAIF-SPICE tools [Acton, 1996], and radiometrically, using the RC17 calibration pipeline [McCord et al., 2004; Adriani et al., 2011] by the group at IAPS-INAF in Rome. Both the geometrical and radiometric calibrations are crucial to this work. The first because even a slight mis-pointing would constitute a significant bias in the analysis (see Sec. 4.6 for further discussion). A precise radiometric calibration is important in order to analyse a signal which is close to the noise level at altitudes higher than 400 km.

A known problem with VIMS data is the spectral shift of the actual band centres with respect to the nominal ones. This has been noted by various authors [Maltagliati et al., 2015; Sromovsky et al., 2013]. We applied here the usual recalibration proposed by the VIMS team[1]. The spectral shift is estimated to be smaller than 3 nm for the period considered here.

In addition, we performed a statistical analysis on almost 30 thousand deep space spectra and found systematically negative radiance values between 4.5 and 5 μm, as shown in Fig. 4.3. The bias is significant, being larger than the noise error bars, also shown in the graph, and the cause lies in the overestimation of the dark/background signal subtracted in the calibration pipeline. As reported by McCord et al. [2004], this can be caused by the thermal contribution of the chopper to the measured

[1]See `http://pds-atmospheres.nmsu.edu/data_and_services/atmospheres_data/Cassini/vims.html` for reference.

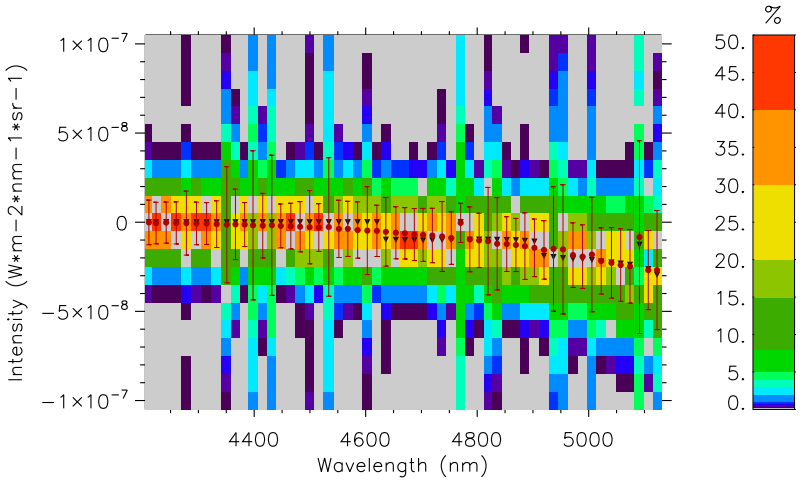

Figure 4.3: Occurrences of radiance values as a function of wavelength in the deep space spectra (color scale). Black points are the median of the data values, the red points with error bars represent the mean and standard deviation. The offset at long wavelengths is apparent and reaches a maximum value of $-3\times10^{-8}\,\mathrm{W\,m^{-2}\,nm^{-1}\,sr^{-1}}$ at $5\,\mu$m, which is larger than the standard deviation. The color scale indicates the percentiles of the distribution.

signal, more important for long integration times at the longest wavelengths. Thus, we re-calibrated all the spectra for the offset calculated on the deep space spectra, separately for each cube. The offsets calculated for the single cubes are consistent, well inside the error bars, with the general one shown in Fig. 4.3.

4.3 Model atmospheres

In order to retrieve the CO abundance from VIMS data, we need to know the thermal structure of the atmosphere. Due to the moderate spectral resolution of VIMS, this information can not be obtained from the measurements themselves. The only reference atmosphere available before the Cassini era was the Titan engineering model by Yelle et al. [1997], based on Voyager I data. Our knowledge of the thermal structure of Titan's atmosphere has been greatly improved in the last years, due to the direct sounding made by the Huygens probe [Fulchignoni et al., 2005] and to the measurements performed by CIRS [Achterberg et al., 2008, 2011; Vinatier et al., 2015].

As mentioned in Sec. 4.2, we focus here on VIMS measurements taken during about one year between July 2006 and July 2007. This period corresponds to a fraction of 1/30 of one Titan's year and is far enough from the transition in the

general atmospheric circulation that happened close to the equinox in 2009 [Teanby et al., 2012]. Thus, the atmospheric temperature and the solar radiation at the top of the atmosphere can be considered constant in time and depending on latitude and SZA only. Therefore, we averaged the available CIRS temperature/pressure latitudinal maps along the period considered [Achterberg et al., 2011] and divided our reference atmosphere in 10° latitudinal bins. Outside the polar regions, temperature variations within 10° of latitude are of the order of 1 K, close to CIRS measurement error. Latitudinal temperature gradients are larger near the Northern winter pole. However, since no measurements at latitudes larger than 40° N fit our selection criteria (see Sec. 4.2.2), the 10° latitudinal averages can be considered adequate.

The obtained zonal reference atmospheres for years 2006-2007 has been used both for the non-LTE calculations (Sec. 4.4) and for the simulation of the synthetic spectra (Sec. 4.5.1). Since CIRS data only provide information on the thermal structure up to $\sim$500 km, we extrapolated the CIRS temperature profiles with a smoothed profile of the measurements taken by the Huygens Atmospheric Structure Instrument (HASI) [Fulchignoni et al., 2005], which was already used in Adriani et al. [2011] (see, e.g., Fig. 4.5). Anyway, the synthetic spectra and the data analysis are not significantly affected by the thermal structure above 500 km. The pressure profile was calculated assuming hydrostatic equilibrium, starting from the ground pressure provided by CIRS [Achterberg et al., 2011] and assuming the mean molecular mass profile measured by the GCMS instrument on the Huygens probe [Niemann et al., 2005].

Regarding the atmospheric composition, abundances for CH_4, HCN, CO_2 and C_2H_2 are taken from Coustenis et al. [2007] and Vinatier et al. [2015]. We assumed terrestrial isotopic ratios for $^{13}CO/^{12}CO$ and $C^{18}O/C^{16}O$, as found recently by Serigano et al. [2016] using ALMA observations.

4.4 The non-LTE modelling

The limb measurements taken by VIMS analysed in this work require an accurate non-LTE model that include weak CO (isotopic and hot) bands which contribute significantly to the limb radiances at stratospheric tangent heights. Actually one of the major systematic error of the retrieved CO VMR is induced by the uncertainties in the non-LTE model (see Sec. 4.6).

Carbon monoxide non-LTE modelling for Titan's atmosphere has been previ-

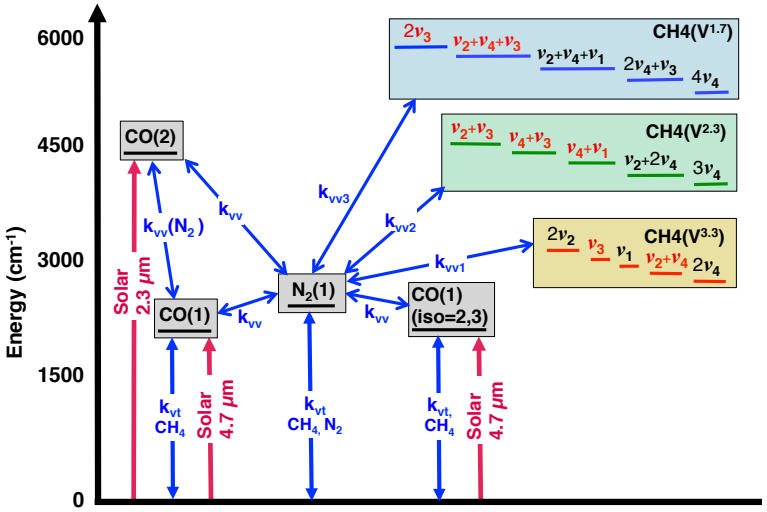

Figure 4.4: Diagram of the energy levels and collisional scheme considered in this work.

ously developed by Lellouch et al. [2003] and López-Valverde et al. [2005] for the analysis of ground-based observations of Titan's atmosphere. Here, the CO non-LTE populations have been calculated through the code GRANADA (see 3.3.4. Thus, the method used here is different from the previous model and several collisional rates (see below) have also been updated.

The setup for the calculation of the CO populations used here is very similar to that described in Funke et al. [2007] and includes the vibrational levels v=1, 2 for $C^{12}O^{16}$ (isotopologue 1), and v=1 for $C^{13}O^{16}$ (isotopologue 2) and $C^{12}O^{18}$ (isotopologue 3) (see Fig. 4.4). The energies of the vibrational levels have been taken from Guelachvili et al. [1983]. These CO vibrational levels are coupled with the first vibrational level of N_2 through collisional processes. All the collisional processes considered are listed in Table 4.3 and discussed below.

The CO levels are connected by five radiative transitions: the fundamental bands of the three isotopologues near 4.7 μm and the overtone (2–0) and first hot (2–1) bands of the main isotopologue. Spectroscopic data for the CO bands were taken from the HITRAN 2012 database [Rothman et al., 2013].

The radiative transfer calculations include the full exchange of radiation between all layers specified in the atmosphere (from the surface up to 1000 km) for all bands. During daytime, CO vibrational populations are largely controlled by absorption of solar radiation at 4.7 and 2.4 μm. Thus, solar incoming fluxes at the top of the atmosphere were included, taking into account modulations due to variations of the Sun-Titan distance. The solar background radiance is expressed as a blackbody with

an effective temperature T_e=5450 + 0.25 · ($\tilde{\nu}$ − 2000), being $\tilde{\nu}$ wavenumber in cm^{-1}. This parametrization agrees with other typical parameterizations within 1% [Jurado-Navarro et al., 2015] and hence we expect similar errors in the calculated non-LTE populations. Solar CO Fraunhofer lines reduce significantly the solar incoming radiation at the CO ro-vibrational line positions [Hase et al., 2006]. Typically, calculated reduction factors of the solar flux are around 0.72-0.73 for the $^{12}C^{16}O(v \rightarrow v–1)$ bands, and 0.95 for the overtone band at 2.4 μm and the fundamental bands of the minor isotopologues. The absorption of solar radiation by CH_4 bands that overlap the CO bands near 2.4 μm were also included. This produces a large depletion on the population of CO(2) (1-4 K in its vibrational temperature in the 300-100 km region), with an important effect on the retrieval of CO performed here. The CH_4 spectroscopic data used are described in García-Comas et al. [2011]. A line-by-line calculation of the upwelling tropospheric flux given by the temperature of the lower boundary (Titan's surface) were included for all bands. Radiative transfer calculations for all transitions were performed with the line-by-line approach by using the Karlsruhe Optimized and Precise Radiative Transfer Algorithm [Funke et al., 2012; Stiller et al., 2002].

Table 4.3: Collisional processes included in the CO non-LTE model.

No.	Process		Rate (cm^{3}s^{-1})
1a	$k_{vv,1a}$:	$CO^i(1) + N_2 \rightleftharpoons CO^i + N_2(1)$; i=1	$5.47\times10^{-15}\times$ $\times\exp(3.82A - 5.47B)^\dagger$
1b	$k_{vv,1b}$:	$CO^i(2) + N_2 \rightleftharpoons CO^i(1) + N_2(1)$; i=1	$k_{vv,1a}/2$
1c	$k_{vv,1c}$:	$CO^i(1) + N_2 \rightleftharpoons CO^i + N_2(1)$; i=2, 3	$k_{vv,1a}/4$
2	k_{vt,CH_4}:	$CO^i(v) + CH_4 \rightarrow CO^i(v\text{-}1) + CH_4$; i=1-3	4.0×10^{-15}
3	k_{vt,N_2-N_2}:	$N_2(1) + N_2 \rightarrow N_2 + N_2$	1.0×10^{-22}
4	k_{vt,N_2-CH_4}:	$N_2(1) + CH_4 \rightarrow N_2 + CH_4$	1.6×10^{-15}
5	$k_{vv,5}$:	$CH_4(V^{3.3}) + N_2 \rightarrow CH_4(v')^\ddagger + N_2(1)$	1.2×10^{-15}
6	$k_{vv,6}$:	$CH_4(V^{2.3}) + N_2 \rightarrow CH_4(v')^\ddagger + N_2(1)$	1.8×10^{-15}, 10^{-13}
7	$k_{vv,7}$:	$CH_4(V^{1.7}) + N_2 \rightarrow CH_4(v')^\ddagger + N_2(1)$	2.4×10^{-15}, 10^{-13}

$^\star i$ run from 1 to 3 for the isotopologues $C^{12}O^{16}$, $C^{13}O^{16}$ and $C^{12}O^{18}$. v takes values of 1 and 2 for isotopologue 1, and 1 for isotopologues 2 and 3. $^\dagger A = (T - 300) \times 10^{-3}$. $B = (T - 300)^2 \times 10^{-5}$. T is temperature in K. ‡ v' is any lower energy level, including the ground state.

4.4.1 Collisional processes

Regarding the collisional processes (see Table 4.3), we have considered the vibrational-vibrational (V–V) (processes 1) collisions between $CO^i(v)$ and N_2. This is one of the

most important collisional parameters controlling the population of the CO levels, as it rules the V–V energy transfer of the solar-pumped $CO^i(1,2)$ levels to $N_2(1)$ which is subsequently thermalized in collisions mainly with CH_4 (process 4) and, to a lesser extent, with N_2 itself (process 3). López-Valverde et al. [2005] also included a direct (vibrational to thermal, V-T) thermalization of $CO(v)$ in collision with N_2 but with a rate coefficient 1000 times smaller than for the V–V process. The rate coefficient of this process is very uncertain and the laboratory measurements have not been able to decipher if the after-collision N_2 is excited or not. The inclusion of that V-T process in our scheme with such a small rate has a negligible effect on the populations of $N_2(1)$ and $CO(v)$. The reason is that the thermal relaxation of $N_2(1)$ in our scheme is much stronger than in López-Valverde et al. [2005]. Two are the major causes. First, we have included the $N_2(1)$ relaxation with N_2 itself with a value of $1.0\times10^{-22}\,cm^3s^{-1}$ at 170 K [Shin, 1981], which is about a factor of 1000 larger than that used by López-Valverde et al. [2005]. Secondly, they did not include the thermalization of $N_2(1)$ by CH_4 which is considered here (process 4) with the rate measured by Gregory et al. [1983] ($1.6\times10^{-15}\,cm^3s^{-1}$ at 170 K, Titan's typical stratospheric temperature). With this value, and given the Titan N_2 and CH_4 abundances, it is clear that this process is much more efficient than collisions with N_2 to relax $N_2(1)$. Actually this is the major thermalization process of $N_2(1)$ and, indirectly, of the $CO(v)$ levels.

Processes 1 also have important effects on coupling of populations of the $CO^i(1)$ levels of the three isotopologues between 200 and 400 km. $N_2(1)$ acts as a reservoir in redistributing the energy between them with the result of decreasing the vibrational temperature of CO(1) of the main isotopologue (i=1), with a maximum change of about 5 K, and increasing those of the minor isotopologues in about 10 K and 5 K for isotopologues i=2 and 3, respectively. The rate for the V-V exchange between $CO^{i=1}(1)$ and $N_2(1)$, $k_{vv,1a}$, is taken from the measurements of Allen and Simpson [1980]. These authors also measured the rate coefficient between CO(1) and other minor N_2 isotopologues ($^{14}N^{15}N$ and $^{15}N_2$) finding important changes in the collisional rates. These differences were explained on the basis of their different energy mismatches. That is, the smaller the energy mismatch, the larger the rate. Although those processes are not the same as processes $k_{vv,1c}$, the molecules involved are the same and, in absence of specific measurements of $k_{vv,1c}$, we estimate these rates from Allen and Simpson [1980] measurements for the isotopic N_2 rates and assuming that the transition probability (in log scale) is proportional to the energy

mismatch. This resulted in a $k_{vv,1c}$ value of ≈4 times smaller than $k_{vv,1a}$. The same procedure was used for deriving the rate of process $k_{vv,1b}$, which has a energy mismatch of 214.2 cm^{-1} versus 187.73 cm^{-1} of process $k_{vv,1a}$, resulting is a value ≈2 times smaller. This factor of 2 has important consequences on the population of CO(2) below around 300 km (see Fig. 4.6) and on the derivation of the CO VMR, since most of the measured radiance below that altitude at 4.7 μm comes from the CO first hot band emission (see Fig. 4.9).

The direct relaxation of CO(v) levels with CH_4 has been included with the rate reported by Gregory et al. [1983] for the most abundant CO isotopologue. A similar rate was found before by Stephenson and Mosburg Jr [1974]. In absence of measurements for the v=2 level and for the minor isotopologues, the same rate has been used for these levels. Thermal relaxation of CO(v) in collisions with H_2 has been found to be negligible in comparison with the direct-CH_4 and indirect through $N_2(1)$ de-activations (see also López-Valverde et al. [2005]). Also, the V–V collisional deactivation of CO(2) by CO itself is about 200 times smaller than in collisions with N_2 and therefore it was neglected.

We have also explored new potential excitation mechanisms that could lead to significantly different CO(v) non-LTE populations. One possible mechanism is the V-V energy transfer from the highly excited levels of the very abundant CH_4. Thus, we have tested processes 5, 6 and 7 in Table 4.3 from the very excited CH_4 levels near 3.3, 2.3 and 1.7 μm [García-Comas et al., 2011]. The problem is the lack of knowledge of these V–V transfer rates. García-Comas et al. [2011] included these processes as a V–T relaxation of CH_4 levels (i.e., regardless the after-collision N_2 resulted vibrationally excited or not), assuming small energy jumps, v_4 or v_2 quanta, and with a value of 3.7×10^{-16} cm^3s^{-1} at 170 K taken from Siddles et al. [1994]. Boursier et al. [2003] has studied in detail the relaxation of CH_4 levels by N_2, but only considered relaxation of v_4 and v_2 quanta. By the way, they reported a value of 1.2×10^{-15} cm^3s^{-1} at 193 K, which is significantly larger than the rate of Siddles et al. [1994]. In the absence of measured or estimated rates in which N_2 results excited, we have estimated the possible range of values. Boursier (priv. comm., 2015) suggested that possibly about half of the energy of CH_4 levels in the process $CH_4(v_2,v_4) + N_2 \rightarrow CH_4 + N_2(1)$ goes into $N_2(1)$. Under this assumption, and considering also the harmonic oscillator approach, a plausible rate for process 5 could be 1.2×10^{-15} cm^3s^{-1}, and 1.8×10^{-15} and 2.4×10^{-15} cm^3s^{-1} for processes 6 and 7, respectively. Maximum values of these rates based on this hypothesis would

be twice as large, i.e., if assuming that all the energy of the CH_4 excited states is transferred to $N_2(1)$. The inclusion of these processes with the estimated values produces a significant change in the population of $N_2(1)$ above ∼450 km but it has no effect on the population of the CO levels (maximum change of –0.2 K in the vibrational temperature of CO(1) at ∼300 km). The non-LTE populations of the CH_4 levels used here were computed with the non-LTE model described by García-Comas et al. [2011] for the conditions analysed here (see below). If assuming the maximum rates, the change is of –0.5 K in the CO(1) at ∼300 km. Note that the change is to decrease instead of increasing the CO(1) T_v because the $CH_4(V^{3.3})$ levels are essentially in LTE below 400 km (see Fig. 3 in García-Comas et al. [2011]). The $CH_4(V^{2.3})$ and $CH_4(V^{1.7})$ levels are significantly overpopulated with respect to LTE but the V–V collisional exchange of $N_2(1)$ with these levels, using those rates, is much smaller than with $CH_4(V^{3.3})$. Thus, these processes have not been included in the nominal retrievals of CO VMR.

4.4.2 Vibrational temperatures of CO energy levels

The non-LTE population of a level v with energy E_v is usually described in terms of its vibrational temperature:

$$T_v = -E_v / \left[k \ln[(n_v g_0)/(n_0 g_v)] \right], \tag{4.3}$$

where n_v and n_0 are the number density of level v and of the ground vibrational state, and g_v and g_0 their respective degeneracies.

Examples of the vibrational temperatures for the CO energy levels for the kinetic temperature profile near the equator (10°S-0°, see Table 4.2) and the collisional rates listed in Table 4.3 (except as noted) are given in Figs. 4.5 and 4.6. A constant CO VMR of 50 ppmv was used for the results presented in this section. Note, however, that they were consistently re-calculated for the retrieved CO abundances (see Sec. 4.7). The figures show the very enhanced population of the v=1 level of the three CO isotopologues due to absorption of solar radiation in their respective fundamental bands. The population of the CO(1) major isotopologue is significantly affected by collisions with N_2 below around 500 km. Those of the minor isotopologues are also affected but at lower altitudes because of the relative less importance of collisions versus radiative processes. The CO(2) level is much more excited because of the absorption of solar radiation in the overtone 2-0 band near 2.35 μm. The photo-absorption coefficient in this band starts being depleted around 400 km and

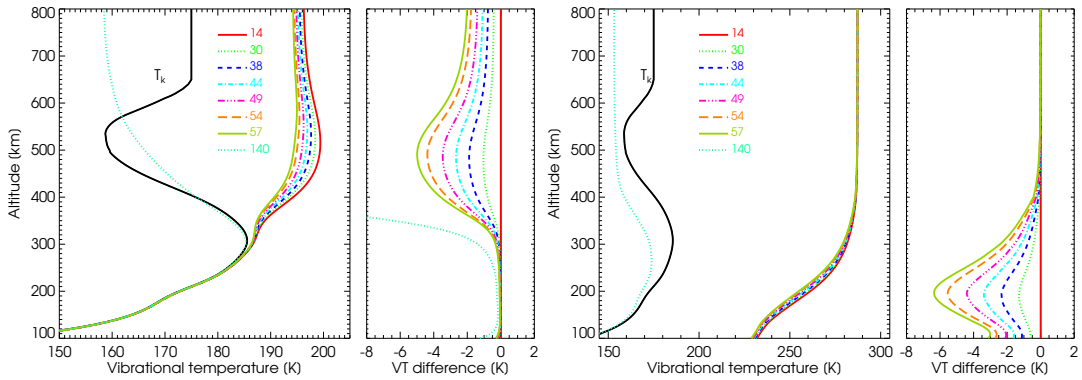

Figure 4.5: Vibrational temperatures for the CO(1) (top) and CO(2) (bottom) energy levels for the kinetic temperature profile (T_k) of 10°S-0°S and several SZAs. The right panels show the differences with respect to the T_v for SZA=14°. The nominal collisional rates in Table 4.3 have been used.

hence the population of CO(2) decreases. As noted above, the absorption of solar radiation in the bands of CH_4 overlapped to that of CO(2-0) near 2.4 μm produces a significant depletion in the T_v of CO(2) below ∼300 km.

As shown in Fig. 4.2, the limb emission in the CO 4.7 μm band depends strongly on SZA. The reason is that the emitting CO(v) levels are mainly pumped by absorption of solar radiation. Fig. 4.5 shows the variation of the vibrational temperature of the CO(1) and CO(2) levels with SZA for the temperature profile mentioned above. As we can see, for CO(1) the change is large above around 350 km and more pronounced at high SZAs. For the CO(2) level, on the contrary, the effects are larger below that altitude. It is also noticeable that in nighttime conditions (SZA=140°) the population of both levels are much smaller, even smaller than the kinetic temperature.

Concerning systematic errors in the non-LTE model, the major inaccuracies are expected to be introduced by uncertainties in the rates of processes 1, particularly 1b. We made a sensitivity test changing the expected value of $k_{vv,1a}$ by ±20% and of $k_{vv,1b,c}$ by ±50%. The results show (see Fig. 4.6) that this variation leads to peak changes in the population of CO(1) of about 1 K near 350 km. A larger rate couples CO(1) with $N_2(1)$ more efficiently producing a stronger thermalization and hence leading to a decrease of the T_v of CO(1). The largest effects in the minor isotopologues and in the CO(2) levels take place at lower altitudes, where collisions with these levels become important and they are still in non-LTE. The change at 200 km is about 1.5 K for the isotopologues and 1.2 K for CO(2). As expected, the change in the population of $N_2(1)$ is of opposite sign to those in the CO levels and takes place only in the region where it is not thermalized.

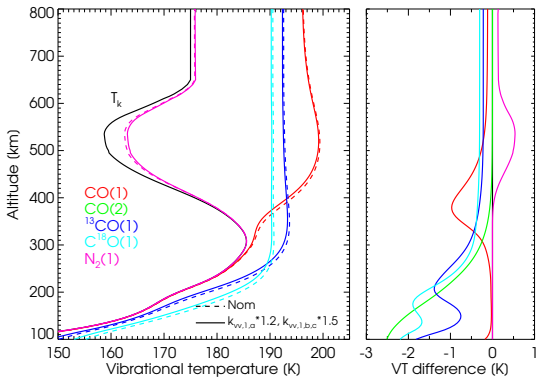

Figure 4.6: The effects of increasing the rate coefficient of processes 1a in Table 4.3 by 20% and of processed 1b and 1c by 50% on the vibrational temperatures of the CO and $N_2(1)$ energy levels. The profiles with the unperturbed rates of Table 4.3 are also shown for comparison (dotted lines). The right panel shows the differences.

We have also estimated the uncertainties of the collisional rates of processes 2, 3 and 4 on the populations of CO(v). Of these processes, process 4 is the most important. We have changed the rate of k_{vt,N_2-CH_4} in Table 4.3 by 50% and found changes (not shown) smaller than 0.1 K in the T_v of CO(1) and negligible in the T_v of CO(2). The T_v of $N_2(1)$ changes by 3-4 K near 500 km but, in the region where it is coupled with CO(v), below 500 km, $N_2(1)$ is completely thermalized already. Thermal relaxation of $N_2(1)$ with N_2 itself is of much less importance than with CH_4 and hence does not introduce any significant error. We have also tested the thermal relaxation of CO(v) with CH_4 (process 2) by changing the rate coefficient by 50% and found maximum changes (not shown) of only 0.15 K in both the T_v of CO(1) near 350-400 km and of CO(2) near 200 km.

The CO(1) populations depend very much on the kinetic temperature profiles below about 450-500 km. We have also estimated the errors produced on the CO non-LTE populations by the uncertainty in the kinetic temperature. The errors of the CIRS temperatures are estimated in 1-2 K [Achterberg et al., 2008]. We show here the results when increasing the temperature profile by 1 K at all altitudes. Pressure has been artificially kept fixed in order to evaluate the potential error produced by the temperature alone. The results on the CO T_v's are shown in Fig. 4.7 for the selected case of 10°S-0°S and SZA=14°. We see significant differences. As expected the differences are small at very high altitudes, where the CO(1) populations are decoupled from T_k, and nearly follow the 1 K enhancement in the lower regions, where they are thermalized. The CO(2) T_v remains practically unchanged in the full atmosphere. The effects of these changes on the retrieved CO abundance are discussed in Sec. 4.6.

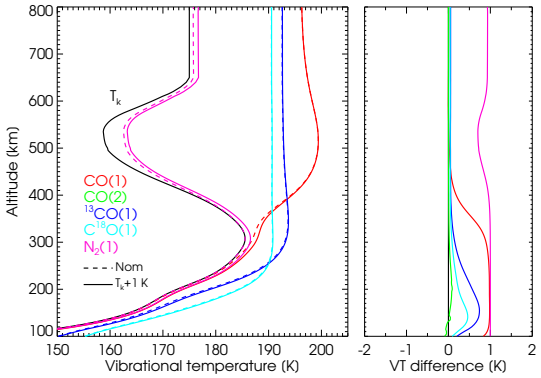

Figure 4.7: The effects of perturbing the kinetic temperature by 1 K on the vibrational temperatures of CO and $N_2(1)$ energy levels. Temperature was increased by 1 K in the whole altitude range. The nominal profiles are also shown (dotted lines). The right panel shows the differences.

4.5 Forward model and retrieval method

4.5.1 Forward model

The atmospheric emission measured by VIMS has been simulated with the code GBB, described in Section 1.4. Given that Titan is almost perfectly spherical [Zebker et al., 2009] and we are sounding the rarefied upper atmosphere, we assume the satellite as a sphere and neglect refraction. Depending on the latitude and SZA of the limb scanning sequence (see Table 4.2), the appropriate reference atmosphere and the corresponding non-LTE populations are used (see Secs. 4.3 and 4.4). The model atmosphere is discretized in 80 vertical layers. As in García-Comas et al. [2011] and Adriani et al. [2011], the atmosphere is assumed horizontally homogeneous and all atmospheric quantities refer to the geolocation of the tangent points.

The gases included in the simulations are CO, ^{13}CO, C^{18}O, CH_4, CH_3D, HCN, CO_2 and C_2H_2. For all these gases, spectroscopic data are taken from the HITRAN 2012 compilation [Rothman et al., 2013]. In order to properly model the narrow line shape at the low pressures of Titan's upper atmosphere, the spectra have been simulated on a wavenumber grid of $0.0005\,\mathrm{cm}^{-1}$.

Since the analysed observations refer to daytime measurements in an altitude region where solar scattering is not negligible, the GBB code used in Adriani et al. [2011] has been improved to include the treatment of the single scattering of the solar radiation. As already discussed in Sec. 4.2.1, the scattering continuum signal produced by aerosols is comparable to the molecular emission. A quantitative analysis of the aerosols concentration is outside the purposes of this work. Here we are only interested in the accurate simulation of their contribution in order to avoid

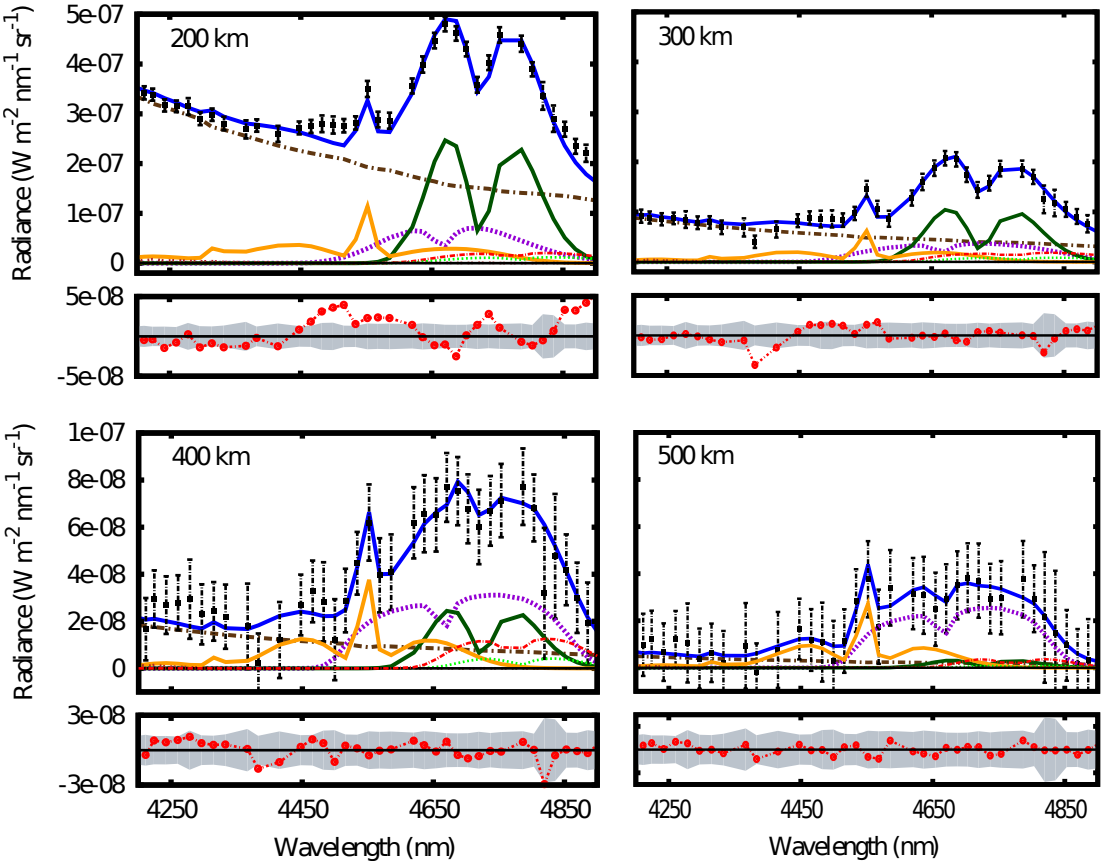

Figure 4.8: Simulated spectra at different tangent altitudes (blue, solid) compared with average VIMS spectra (black points) for the 'limb scanning sequence' of latitude band 10° S–0° S and SZA of 14°(see Table 4.2). The other curves show the contribution of solar scattering (brown, dash-dotted), CO(2→1) band (dark green, solid), CO(1→0) band (purple, dotted), ^{13}CO (red, dash-dotted), C^{16}O (light green, dotted) and CH_3D (yellow, solid). Note the different radiance scale in the upper and lower rows of panels. The lower panels show the residuals (red dots) in comparison with the measurement error at different wavelengths (grey shaded area).

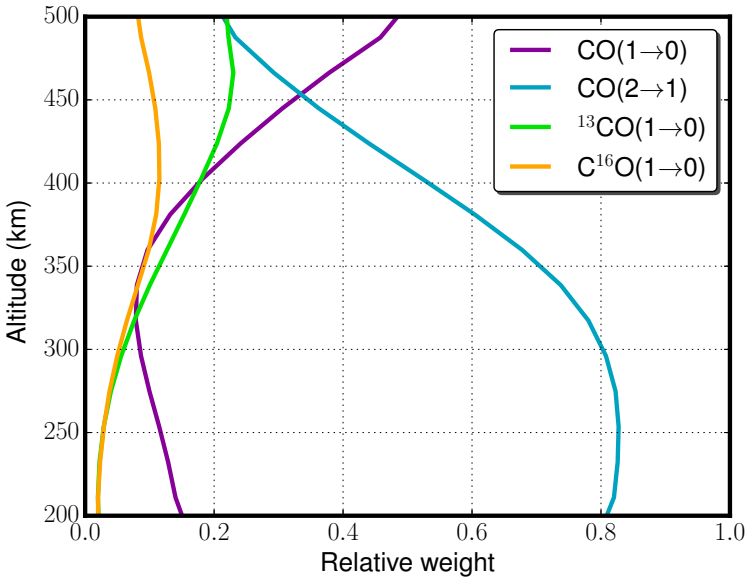

Figure 4.9: Contribution of the different CO bands to the retrieval at different altitudes. Each curve shows the derivative of the total band intensity with respect to the CO VMR at different altitudes, normalized to the sum of the four contributions.

systematic errors in the retrieved CO. Assuming the extinction coefficient and single scattering albedo of Lavvas et al. [2010], the single scattering approximation is sufficient to reproduce the measured spectra, since the aerosol optical depth is always smaller than about 0.07. However, the vertical profile of the scattering extinction of Lavvas et al. [2010] does not have any latitudinal, seasonal or temporal variability. Therefore, in the inversion we keep fixed the spectral response of the aerosols at each altitude as in Lavvas et al. [2010] but fit an altitude-dependent extinction coefficient. The thermal emission and absorption by the aerosols are neglected. For each altitude level, the solar radiation is properly calculated, taking into account the molecular absorption and the aerosol scattering of the layers above and including the SZA dependency.

Figure 4.8 shows the contributions of the different bands of CO as well as the other components for the average spectra corresponding to the latitude band 10° S–0° S and SZA of 14°(see Table 4.2). Spectra have been averaged in seven 50 km wide altitude bins and the simulated radiances are the results of the retrieval done on these average spectra. The total simulated radiance is shown by the blue solid line and the VIMS measurements by the black dots with error bars.

The CO spectral signature is composed by the superimposition of four bands: the main isotopologue fundamental (1-0) and hot (2-1) bands, and the two minor

isotopic fundamental bands. As we noted in Sec. 4.2.1, the shape of the overall CO contribution changes with altitude because of the change in the relative importance of the different bands. Fig. 4.9 indicates how much each band contributes to the retrieval. Each curve shows the derivative of the total band intensity with respect to the CO VMR at different altitudes, normalized to the sum of the four contributions. The (2-1) hot band is optically thin at practically all the tangent heights shown. This feature, together with its high excitation (see Fig. 4.5), makes it dominate in the retrieval at altitudes below around 450 km. The fundamental band of the main isotopologue is optically thick at tangent heights below around 400-450 km and its vibrational temperature starts declining there (see Fig. 4.5), hence its contribution to the retrieval is smaller than that of the first hot band. We also see that the minor isotopic fundamental bands contribute significantly at tangent heights above around 350 km, due to their optically thin regime.

Figure 4.8 also shows the contributions of CH_3D and of the other constituents. As we can see CH_3D has a significant contribution at all tangent heights but the radiance of the rest of the molecules is negligible. The CH_3D emission is superimposed to the R branch of the fundamental and hot CO bands. Thus, an accurate simulation of this emission is very important for the retrieval of CO. We expect the $CH_3D(\nu_2)$ level to be in non-LTE in day-side conditions and, to a first order, to have a vibrational temperature similar to that of CO(1) given their similar energies. Lacking of a detailed non-LTE model for $CH_3D(\nu_2)$, we tested the approach of assigning to $CH_3D(\nu_2)$ the CO(1) vibrational temperature and retrieve an 'equivalent' CH_3D abundance from the measured spectra. We found, however, that this approach introduces a bias in the retrieved CO due to large uncertainties in the retrieved CH_3D. Hence, we decided to mask out the spectral region where CH_3D contributes significantly, between 4450 and 4720 nm. The remaining region, corresponding to the P branch of CO bands, still contains enough information to retrieve CO. In the retrieval we kept the CH_3D abundance fixed at terrestrial isotopic ratio and assumed the vibrational temperature of $CH_3D(\nu_2)$ equal to that of CO(1). The bias produced by this assumption was quantified and found to be almost negligible, as explained in Sec. 4.6.

Between 4450 and 4530 nm we also find a significant and systematic mismatch between the simulated and measured spectra (see the upper left panel of Fig. 4.8). This coincides with previous analysis of VIMS measurements in this spectral region that suggest that some emission/absorption at 4.5 μm is missing [Baines et al., 2006;

Maltagliati et al., 2015]. However, we masked out this spectral region in the retrieval of CO abundance.

4.5.2 Retrieval method

The GBB forward model is coupled to a retrieval module performing optimal estimation of atmospheric quantities through a bayesian approach. The retrieval procedure minimizes the cost function (χ^2) through the Levenberg-Marquardt iterative procedure (see Section 2.3).

The state vector $\boldsymbol{x}$ used for these inversions has 14 elements and consists of the vertical profiles of the CO abundance and the aerosol extinction coefficient. Each vertical profile is discretized with a piecewise linear curve on a vertical grid from 200 to 500 km, at 50 km steps (7 nodes).

We choose for the *a priori* of CO a uniform 50 ppmv profile, as suggested in the works by Gurwell and Muhleman [2000], De Kok et al. [2007] and Maltagliati et al. [2015], with a diagonal *a priori* CM matrix corresponding to a 70% error on the *a priori*. The *a priori* for the aerosol extinction coefficient is taken from the model of Lavvas et al. [2010], with a 90% relative error. The inversion procedure is iterated for each limb scanning sequence until the relative variation of the cost function between two iterations is less than 1%.

4.6 Systematic errors

The analysis of the VIMS data presented here is based on several assumptions that may introduce systematic errors.

The potential sources of errors analysed are the following: a) VIMS pointing error (PE); b) VIMS wavelength calibration (WS); c) *a priori* profiles for CO (ApCO) and aerosol (ApAer); d) temperature profile (Tk); e) collisional rates used in the non-LTE model (Kvv); f) CH_3D non-LTE (CH3D) and g) error of the non-LTE populations of CO -mainly CO(2)- due to the uncertainty in the CO abundance at high altitudes (COab). For a), b) and c) the systematic error has been estimated by perturbing the inquired parameter and performing a test retrieval on the averaged spectra of Fig. 4.8. The difference between the nominal and the perturbed retrievals gives an estimate of the error produced by that parameter. For the other potential error sources, an inversion of the full dataset with the perturbed parameter has been performed instead. Each systematic error source is described below and the results

are summarized in Figure 4.10. Note that, by definition, we do not know the sign of the model parameter errors, therefore also the sign of the resulting profile error is unknown and it is a common convention to take it positive (see e.g.: `http://eodg.atm.ox.ac.uk/MIPAS/err/`). Since the various error components are statistically independent from each other, we sum them quadratically to get an estimate of the total systematic error.

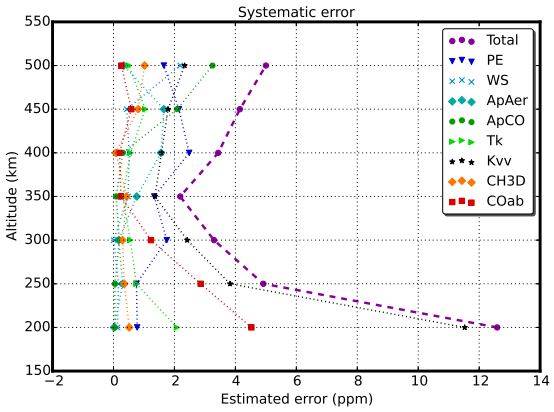

Figure 4.10: Summary of the estimated systematic errors on the retrieved CO VMR expressed in ppmv. The abbreviations are: PE = pointing error, ±8 km; WS = wavelength shift, ±2 nm; ApCO = CO *a priori*, ±15 ppmv; ApAer = aerosol *a priori*, ±90%; Tk = kinetic temperature, ±1 K; Kvv = $k_{vv1,a}$ ±20%, $k_{vv1b,c}$ ±50% (see Table 4.3); CH3D = effect of CH_3D non-LTE (see text); COab = error of the non-LTE populations of CO due to the uncertainty in the CO abundance at high altitudes of ±5 ppmv. The Total error is the quadratic sum of all errors.

We made test retrievals with a PE of ±8 km and with a WS of ±2 nm (see Fig. 4.10). For PE, the actual bias produced on a single retrieval is actually reduced when considering the full dataset. In fact, the bias of the pointing is expected to be uniform inside one VIMS cube, apart from a gradual variation with latitude. However, the pointing biases of different VIMS cubes are completely uncorrelated and thus we divided the single-cube bias by $\sqrt{n_{cub} - 1}$.

The results of the tests performed by varying the *a priori* profile of CO (ApCO) by ±15 ppmv and of the aerosol by ±90% (ApAer) are shown in Fig. 4.10. As expected, the bias produced by the *a priori* is larger when there is less information in the data, i.e. at the highest altitudes.

The error on the temperature profile (see Sec. 4.3) is of the order of 1 K [Achterberg et al., 2011]. The error is considered to be the same when averaging over time and latitude. We performed a test assuming a 1 K variation in the whole temperature profile (Tk), keeping fixed the pressure profile; the change in the vibrational

temperature is described in Sec. 4.4. The induced temperature error is larger in the lower atmosphere, where the vibrational levels are in LTE.

As discussed in Sec. 4.4, the vibrational temperatures of the levels considered here are quite sensitive to the $k_{vv,1a,b,c}$ rates that couple the excited levels of CO with N_2. We estimated the induced error of these rates (Kvv) by assuming an uncertainty of $\pm 20\%$ for $k_{vv,1a}$ and of $\pm 50\%$ for $k_{vv,1b,c}$, which we considered as realistic (see Sec. 4.4). As we can see in Fig. 4.10, the error introduced by this parameter is very important both at the upper altitudes, because it affects to the population of CO(1), and at the lowest altitudes where it largely influences the population of CO(2). At 200 km this represents by far the largest error source.

Another systematic error considered is the effect of CH_3D being in non-LTE (CH3D). As explained in Sec. 4.5.1, we expect the $CH_3D(\nu_2)$ level to be in non-LTE above around 300 km, with a vibrational temperature similar to that of the CO(1) level, which we assumed in the nominal inversion. We repeated the inversion with CH_3D in LTE and conservatively estimated the error produced on CO VMR as being half of the difference between the nominal and LTE inversions. As shown in Fig. 4.10, this error is quite small at all altitudes, because most of the CH_3D emission is outside the retrieval spectral range.

The last error considered is the effect of the uncertainty in the CO abundance itself at high altitudes on the non-LTE populations of CO, mainly CO(2) (COab). A larger abundance makes the solar radiation to be absorbed higher in the atmosphere, lowering the vibrational temperatures in the lower atmosphere, especially that of the CO(2) level. For the nominal inversion a CO abundance of 60 ppmv has been used in the calculations of the non-LTE populations, which is consistent with the result we obtain at the highest altitudes (see Sec. 4.7). To estimate the error produced, we performed the full set of retrievals using the non-LTE populations calculated with a CO profile perturbed with the estimated error found here of 5 ppmv, i.e. 55 ppmv. As shown in Fig. 4.10 this error is quite important below about 300 km.

4.7 Results and discussion

We performed the simultaneous inversion of the CO abundance and of the aerosol extinction coefficient profiles for each of the 47 limb scanning sequences obtained in Sec. 4.2.2 (see Table 4.2). The reduced χ^2 for the full set of simulated spectra is 1.04, which proves the good fit of the measured spectra. To test whether the

measurements contain enough information to retrieve 7 altitude points of the VMR profile, we calculated the averaging kernels for each sequence [Rodgers et al., 2000], and we used them to compute the Degrees Of Freedom (DOF) of the retrieval. On average the DOF is 5.6. A value of 0 would mean that we are getting all information from the *a priori*. A value of 7, the number of altitude layers, would mean that we are extracting all information from the measurements, regardless of the *a priori*. A value of 5.6 is very satisfactory, meaning that we are obtaining most of the information from the measurements and that the 7-nodes retrieved profiles are only slightly dependent on the a-priori.

Table 4.4: Summary of the results shown in Fig. 4.11. Mean, standard error (StE), systematic error (Sys) and standard deviation (StD) for the full set of CO VMR retrievals and the average single retrieval noise error (Nerr1) at all altitudes are listed. All values are given in ppmv.

Alt (km)	Mean	StE	Sys	StD	Nerr1
200	58.1	1.1	12.6	7.5	4.4
250	52.6	1.0	4.9	6.8	4.9
300	60.5	1.6	3.3	11	6.2
350	59.7	2.2	2.2	15	9.4
400	64.4	2.9	3.4	20	14
450	53.9	3.2	4.1	22	19
500	65.2	2.4	5.0	16	17

The mean of the 47 retrieved CO profiles is shown in Fig. 4.11. We also show the standard error (in red) and the total systematic error (in blue), obtained from the quadratic sum of the individual systematic errors (see Sec. 4.6). The results are also listed in Table 4.4, together with the standard deviation of the 47 retrieved profiles and the average single retrieval noise error. As stated in Table 4.4, the standard deviation (StD) and the noise error of a single retrieval (Nerr1) are comparable at all altitudes and are large at the highest altitudes because of the small S/N ratio.

The mean profile takes values from about 53 ppmv at 250 km to 65 ppmv at 500 km. The VMR at 200 km (58 ppmv) is slightly larger than that found by Maltagliati et al. [2015] in the lower stratosphere from VIMS solar occultation measurements but the two results lay within the respective error bars. Our result is however significantly larger than the other results obtained with VIMS in the lower stratosphere [Baines et al., 2006; Bellucci et al., 2009].

Comparing our result at 200 km with CIRS results in the lower stratosphere around 100 km, we find it to be very close to Teanby et al. [2010], well inside the error bars, and slightly larger than Flasar et al. [2005] and De Kok et al. [2007].

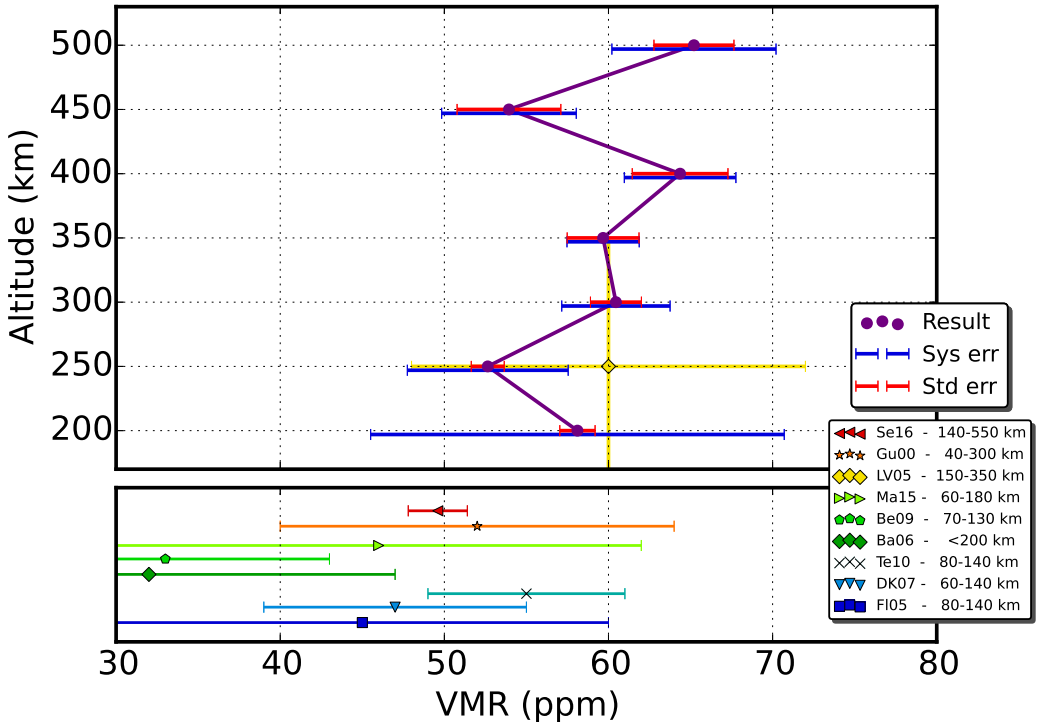

Figure 4.11: Average CO VMR profile obtained in this work (violet line and circles) with standard error (red) and systematic error (blue) (top panel). Results from already published works are also reported for comparison, labels refer to Se16 = Serigano et al. [2016], LV05 = Flasar et al. [2005], Gu00 = Gurwell and Muhleman [2000], Ma15 = Maltagliati et al. [2015], Be09 = Bellucci et al. [2009], Ba06 = Baines et al. [2006], Te10 = Teanby et al. [2010], DK07 = De Kok et al. [2007], Fl05 = Flasar et al. [2005]. Apart from LV05, which is plotted in the top panel, all other points are shown in the bottom panel for ease of viewing and the altitude region they refer to is indicated in the labels.

Finally, we compare our VMR profile with some results of CO abundance on Titan obtained from ground-based observations. The mean abundance recently retrieved with ALMA by Serigano et al. [2016] is at our 1σ level. López-Valverde et al. [2005] found that a CO VMR of 60 ppmv in the stratosphere represented the best fit to their observations, which is well compatible with our VMR profile; the result is shown in the upper panel of Fig. 4.11. One lesson learned from the present NLTE modelling is that the CO(1) vibrational temperatures of López-Valverde et al. [2005] might be overestimated below about 350 km, but their CO(2) populations match very well with our results in the whole stratosphere and above. The hot band contribution to their ground-based observations originates in the 150-350 km region and seemed to require a VMR of 60 ppmv for a good fit. According to our calculations,

such conclusion about the CO first hot band should be valid. The nominal result by Gurwell and Muhleman [2000] is compatible with ours; moreover they indicate that a CO abundance of 60 ppmv in the stratosphere fits their measurements better, which is still closer to what we obtain. Instead, the result found by Hidayat et al. [1998] who claimed a lower abundance of 5 ppmv in the upper stratosphere at 300 km is much lower than our result (not shown in Fig. 4.11).

The main motivation of this work is to retrieve the CO VMR profile between 200 and 500 km, where previous studies did not have enough vertical resolution to assess whether it shows significant vertical variations. Our results are not fully conclusive either. On one hand, considering the estimated systematic and noise errors, we do not observe any significant vertical gradient. This conclusion is in line with the photochemical models prediction (see Sec. 4.1) of a well-mixed vertical profile of CO in Titan's atmosphere. However, if comparing our measurements, with a mean value of 60 ppmv at 400-500 km, with the ground-based mm measurements [Serigano et al., 2016; Gurwell and Muhleman, 2000], which are mainly sounding the 100-300 km region and obtain a value of 50 ± 2 ppmv, we could then infer a slight gradient in the CO profile. A similar gradient was suggested by Gurwell and Muhleman [2000], although the accuracy of their measurements too was not enough to confirm the gradient. New generation of ALMA observations could possibly rule out this ambiguity. If confirmed, this unexpected behaviour of the CO molecule in Titan's atmosphere could not be explained by the current generation of photochemical models. This would rather mean that a still unknown chemical pathway of CO destruction in the lower middle atmosphere is at work. Indeed, an enhanced O influx at the top of the atmosphere [Hörst et al., 2008] would suffice to produce a CO VMR larger than 50 ppm, but a gradient in the profile of about 0.05 ppm/km in the middle atmosphere could only be explained by a new loss process with maximum efficiency around 300-400 km.

4.8 Conclusion

In this work we analyse a set of day-side VIMS limb measurements around 4.7 μm acquired during 2006 and 2007. The dataset consists of 47 limb scanning sequences with tangent altitudes ranging from 200 km to 500 km taken at different latitudes and SZAs. The data studied are extracted from 11 VIMS cubes in the mentioned period.

The atmospheric emission in this spectral region comes mainly from the fundamental and first hot bands of CO, which are in strong non-LTE conditions during day-time. Non-LTE populations were calculated with the Generic RAdiative traNsfer AnD non-LTE population Algorithm (GRANADA) [Funke et al., 2012]. We included in the model the first and second excited levels of the main isotopologue and the first excited levels of ^{13}CO and $C^{18}O$. The main processes controlling the population of the levels are: the solar pumping in the fundamental bands of the three isotopologues and in the overtone and first hot for the main isotopologue; the collisional energy transfer to N_2 and, to a lesser extent, to CH_4. We found the collisional V-V coupling between CO and N_2 to be crucial in determining the excited populations. Lacking experimental values for the rate constant of the V-V processes $CO(2) + N_2 \rightleftharpoons CO(1) + N_2(1)$, $^{13}CO(1) + N_2 \rightleftharpoons {}^{13}CO + N_2(1)$ and $C^{16}O(1) + N_2 \rightleftharpoons C^{16}O + N_2(1)$, we propose, based on the measurements of Allen and Simpson [1980], a quasi-resonant approach to determine these rates using the energy gap between the levels considered.

The non-LTE calculations show that the CO(2) level is strongly pumped by solar radiation in the whole Titan's atmosphere, with a vibrational temperature close to 290 K above around 400 km, which decreases below due to absorption of radiation in the overtone band at 2.3 μm and to energy exchange with N_2. The population of this level is significantly modulated by SZA below around 400 km. The first excited level of the main isotopologue shows a peak excitation at about 500 km, which depends strongly on SZA, due to solar pumping and radiative exchange with the lower layers. Its vibrational temperature then relaxes to the kinetic temperature at about 300 km. The first level of the two minor isotopologues shows a nearly constant excitation above 300 km and slowly relax to the kinetic temperature below. Given the significant errors introduced by the vibrational-vibrational collisional exchange between CO(2) and N_2, laboratory measurements of this collisional rate would be of very high interest.

The results of the non-LTE calculations were used for the simulation of the observed radiance in the 4.7 μm region of VIMS spectra with the Geofit Broad Band (GBB) line-by-line radiative transfer and retrieval code, already used in Adriani et al. [2011], modified to model the scattered solar radiation. Using the VIMS measurements in the spectral region of the P branch of CO, we retrieved CO VMR between 200 and 500 km for a set of 47 limb scanning sequences. These represent the first measurement of the CO VMR profile in the upper stratosphere and mesosphere

of Titan. A comparison of our retrieved VMR at 200 km with previous results focused on the lower stratosphere [Maltagliati et al., 2015; Teanby et al., 2010] shows that it is slightly larger but lays within their error bars.

We tried to assess whether the CO profile is uniform with altitude or not. Assuming we have not overestimated the errors, we cannot unambiguously assert that CO has a vertical gradient. In that sense, our CO profile is consistent with current photochemical models prediction [Wong et al., 2002; Wilson and Atreya, 2004; Hörst et al., 2008] of a well-mixed vertical profile of CO with an abundance between 55 and 60 ppmv. However, a slight increase of the CO VMR from 50 ppmv at 200-250 km to 60 ppmv at 500 km, -right at the uncertainty level- can be appreciated in our results, with a mean gradient of about 0.05 ppm/km in the middle atmosphere. The combination of this with the well established value of 50±2 ppmv at 100-300 km measured by mm ground observation, makes that slight gradient more credible. In case this is confirmed, it would require a new unknown destruction pathway for CO around 300 km in Titan's atmosphere.

Chapter 5

Preliminary study of CH_4, HCN and C_2H_2 latitudinal and seasonal variations in Titan's middle to upper atmosphere

This chapter is dedicated to a currently on-going research that regards the retrieval of CH_4, HCN and C_2H_2 in the upper atmosphere of Titan. Preliminary results are discussed as well as the problematics encountered in the analysis.

The current knowledge of Titan's stratosphere and mesosphere is supported by observations with good latitudinal and seasonal coverage, that allowed the development of a clearer picture of the middle atmosphere dynamics, described in Section 3.2.3. Global Circulation Models have been adapted to Titan atmosphere [Rannou et al., 2004; Lebonnois et al., 2012] and are in general agreement with the observations, although more detailed processes are missing [Teanby et al., 2012; Vinatier et al., 2015]. Both CIRS measurements and current models reach 500 km or lower altitudes, thus excluding the region above. The picture in the upper atmosphere above 1000 km is currently quite confused, since the only measurements by INMS have showed a very large variability in the thermal structure, not clearly correlated with solar EUV radiation or other meaningful physical inputs [Snowden et al., 2013; Yelle et al., 2014].

The region between 500 and 1000 km lacks both observational coverage and models. This work aims to partially fill the gap through the inversion of CH_4, HCN and C_2H_2 abundances in the 500-1000 km region from VIMS measurements. VIMS spec-

tra measure the emission in the vibrational bands of CH_4, HCN and C_2H_2 in the 3 μm region, all of which are under non-LTE conditions in Titan's mesosphere and thermosphere. The signal from the three molecules is significant up to about 1000-1100 km and the coverage of VIMS is great both in latitude and time, so as to allow the study of seasonal and latitudinal variations of the molecular abundances.

HCN and CH_4 abundances in Titan's upper atmosphere from VIMS measurements have been already retrieved in the works by Adriani et al. [2011] and García-Comas et al. [2011]. Those works retrieved average HCN and CH_4 VMR profile from a subset of VIMS measurements. This work is intended as an update - with the inclusion of the non-LTE modeling of C_2H_2 - and an extension to a broader and more comprehensive dataset, for the study of latitudinal and seasonal variations.

5.1 VIMS dataset

Figure 5.1 shows a set of average VIMS measurements in the 3 μm region at different limb tangent altitudes. All spectra at solar zenith angle lower than 40° have been averaged in 50 km bins. We note various features:

- the feature centered at 3050 nm is produced by the emission of both HCN and C_2H_2, that have very similar vibrational energies. The relative contribution of the two molecules determines the shape of the feature, even if the two emissions are not resolved by VIMS.

- the emission due to CH_4 is situated between 3200 and 3500 nm, where we can clearly distinguish the P, Q and R branches. The R branch is systematically stronger than expected at high altitudes and this is due to the superimposed signal of polycyclic aromatic hydrocarbons (PAHs) that has been identified in previous studies García-Comas et al. [2011]; López-Puertas et al. [2013].

- at altitudes below 500 km a continuum signal due to aerosol scattering of sunlight can be seen.

Figure 5.2 shows the non-LTE nature of the emission measured by VIMS at a limb tangent altitude of 600 km. Measurements have been averaged in solar zenith angle bins, to show the dependence of the emission on SZA. The maximum radiance corresponds to lower SZA and therefore larger excitation. The dependence on SZA is moderate on the dayside till 80° and becomes more pronounced on the terminator (80-120°). On the nightside (SZA > 120°) a very low signal is detected compared

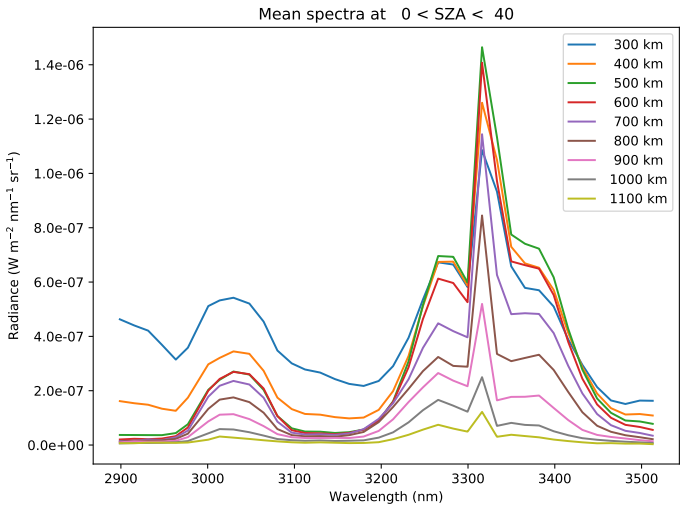

Figure 5.1: Mean spectra acquired by VIMS at SZA lower than 40° and different altitudes on Titan limb.

to the dayside, due to the missing solar forcing that pumps the molecules in their excited levels.

VIMS coverage of the region between 500 and 1000 km is quite complete and would allow the determination of seasonal trends in the middle and upper atmosphere. Figure 5.3 shows the tangent longitude and latitude of the available measurements, with the color scale indicating the SZA at the tangent point. Only measurements with SZA lower than 120° have been included, because the night side does not show a significant signal. Figure 5.4 shows the same measurements in a SZA-latitude plot, with the color scale indicating the phase angle of the measurements, that is the angle formed by the LOS and the direction of the sun (180° meaning that the sun is exactly in front of the instrument). The phase angle is of interest for the analysis in Section 5.5. More measurements exist for the subsequent years but have not yet been calibrated to date.

Apart from year 2008, in which the polar regions are missing due to the spacecraft-planet alignment, all other years show an almost complete latitudinal coverage. Again, the polar latitudes are the most problematic, since the SZA is always high. In particular, for the winter polar regions we clearly only have measurements at SZA higher than 90°, which is the less favorable configuration, but at the same time these regions are key to understand the seasonal behaviour.

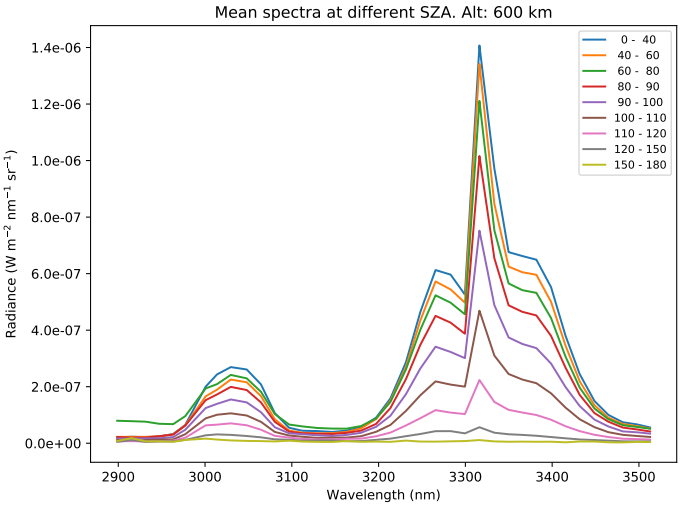

Figure 5.2: Mean spectra acquired by VIMS at 600 km limb tangent altitude for different SZA.

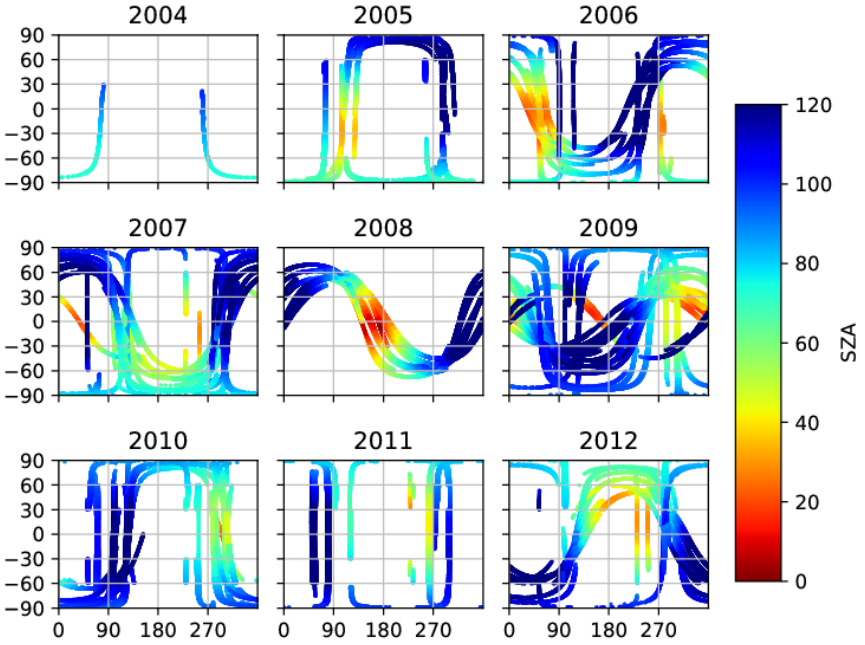

Figure 5.3: Distribution in longitude (x axis), latitude (y axis) and SZA (color scale) of available VIMS measurements in the region 500-1000 km with SZA lower than 120°.

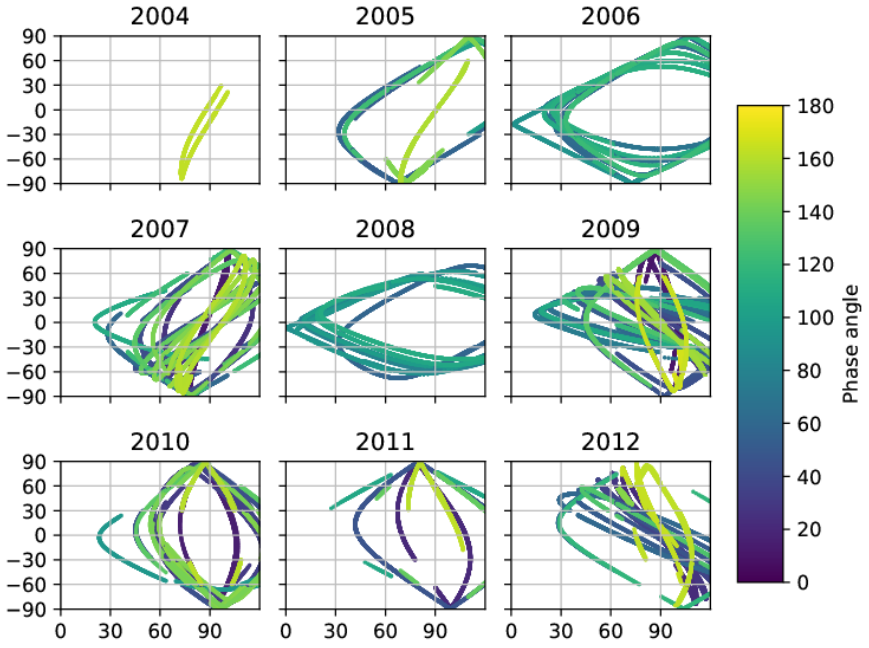

Figure 5.4: Distribution in SZA (x axis), latitude (y axis) and phase angle (color scale) of available VIMS measurements in the region 500-1000 km with SZA lower than 120°.

5.2 non-LTE behaviour of CH_4, HCN and C_2H_2 in Titan's atmosphere

As already anticipated in section above (see for example Figure 5.2), the three molecules under study show a non-LTE behaviour at least in the upper atmosphere. The excitation produced by the absorption of solar radiation is weakly contrasted by molecular collisions, which are rare due to the low density of these atmospheric regions, driving the relevant vibrational levels strongly out of equilibrium.

We summarize here the main results of the non-LTE calculations performed by the group of planetary atmospheres at the IAA of Granada, through the code GRANADA (described in Section 3.3.4). Non-LTE models have been developed for the three molecules. For CH_4 and HCN the non-LTE models had already been developed for Titan's atmosphere and published respectively in García-Comas et al. [2011] and Adriani et al. [2011], while the model for C_2H_2 has been developed specifically for this study.

The main processes controlling the population of the molecular levels for the three molecules are:

- CH_4: the absorption of solar radiation in the 3.3 μm, 2.3 μm and 1.7 μm regions

is important, primarily produced by the ν_3 band and its higher energy overtones. Fast internal redistribution of vibrational energy takes place in collisions between CH_4 molecules, transferring energy to lower levels or other quanta: the rate constants for these processes are very fast, on the order of $10^{-11}\,cm^3s^{-1}$, due to their resonance nature García-Comas et al. [2011]. Quencing of vibrationally excited CH_4 molecules happens in collisions with N_2 and CH_4, with transfer of energy to the thermal bath (rates are 4×10^{-16} and $10^{-17}\,cm^3s^{-1}$ at 175 K, representative of Titan's mesospheric temperature);

- HCN: the absorption of solar radiation in the ν_3 fundamental and hot bands, as well as in the higher energy overtone $2\nu_3$ and combination bands ($\nu_2 + \nu_3$, ..) constitute the main forcing to level populations. The quencing of the low energy ν_2 level ($713\,\mathrm{cm}^{-1}$) is efficient in collisions with the abundant N_2 with a rate of $10^{-12}\,cm^3s^{-1}$. Also the quasi-resonant transfer from the HCN ν_3 to CH_4 ν_3 is found to be efficient with a rate of $6 \times 10^{-13}\,cm^3s^{-1}$ Adriani et al. [2011].

- C_2H_2: again absorption of solar radiation in the ν_3 fundamental and quencing in N_2 collisions, which is very efficient for the low energy ν_5 level. A total of 29 levels have been considered for C_2H_2. Level $\nu_2 + \nu_4 + \nu_5$ has a very close energy to the ν_3.

Non-LTE population calculations for CH_4, HCN and C_2H_2 have been performed extensively for all years and latitudes needed for the analysis in Section 5.4. More details on the full run are given there. Figures 5.5, 5.6 and 5.7 show an example of the result obtained for equatorial latitude and 30° SZA, at the Sun-Titan distance of year 2006. The vibrational temperatures for the main levels of each molecule contributing to the 3 μm emission are shown in the figures. For CH_4 the main bands responsible of the emission are the $\nu_3 \rightarrow 0$ fundamental band, which dominates at all altitudes, and the hot band $\nu_3 + \nu_4 \rightarrow \nu_4$ which contributes significantly at lower altitudes. The ν_3 level is in LTE up to about 400 km, when it starts its departure from equilibrium which is substantially linear in the 400-800 km region. From 800 km upwards the radiative equilibrium is reached between absorption of solar radiation and spontaneous emission, making the vibrational temperature constant at 266 K. Higher energy levels containing one ν_3 quanta and one or two ν_2 or ν_4 quanta or the second excited ν_3 level are out of equilibrium in the whole atmosphere, being fairly constant above roughly 800 km and decreasing almost linearly below. The $\nu_3 + 2\nu_4$

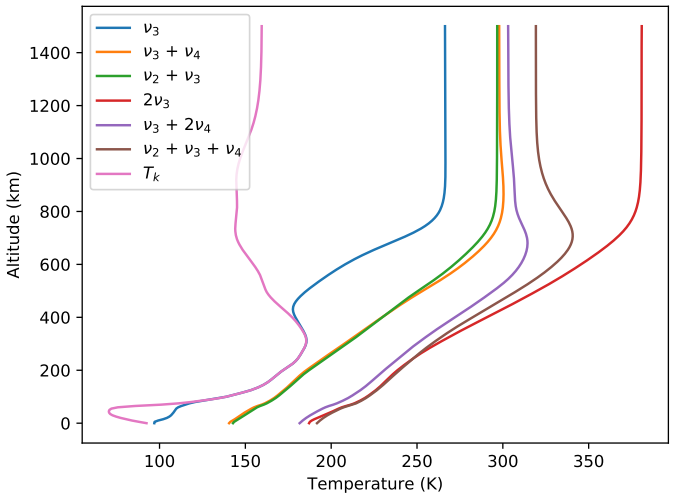

Figure 5.5: Vibrational temperatures for ν_3 level of CH_4 and higher energy level containing ν_3 quanta.

and the $\nu_3 + \nu_2 + \nu_4$ levels have a little bump of excitation around 700 km.

For HCN, the main band emitting at 3 μm is the fundamental $\nu_3 \rightarrow 0$, with the hot band $2\nu_3 \rightarrow \nu_3$ contributing to some extent at lower altitudes. The ν_3 level is in LTE up to 450 km, then its vibrational temperature steadily increases, reaching the radiative equilibrium at about 1000 km with a vibrational temperature of 232 K. The second excited $2\nu_3$ level is fully in non-LTE in the whole atmosphere and its vibrational temperature reaches 314 K above 1000 km and declines below, but is always larger than the equilibrium temperature.

The ν_3 level of C_2H_2 is much more excited than the ν_3 levels of CH_4 and HCN and never reaches LTE. This is due partially to the lower absorption in the solar ν_3 fundamental band, which keeps the vibrational temperature constantly at 285 K above 700 km, and to the less efficient thermalization.

The vibrational temperatures shown above have been obtained for a SZA of 30°. It is worth having a look at the changes in the excitation with changing SZA, at least for the main two levels of CH_4. Figure 5.8 shows the variation of the vibrational temperatures for level ν_3 (top panels) and $\nu_3 + \nu_4$ (bottom panels) for different SZA. Panels on the left show the vibrational temperatures in the region of interest, between 400 and 1000 km, while panels on the right show a zoom on the differences of each curve with the vibrational temperature obtained in a situation of maximum excitation, that is for SZA = 0°. For level ν_3, in the top panels, all curves pass from the same point at 400 km, due to efficient thermalization of the

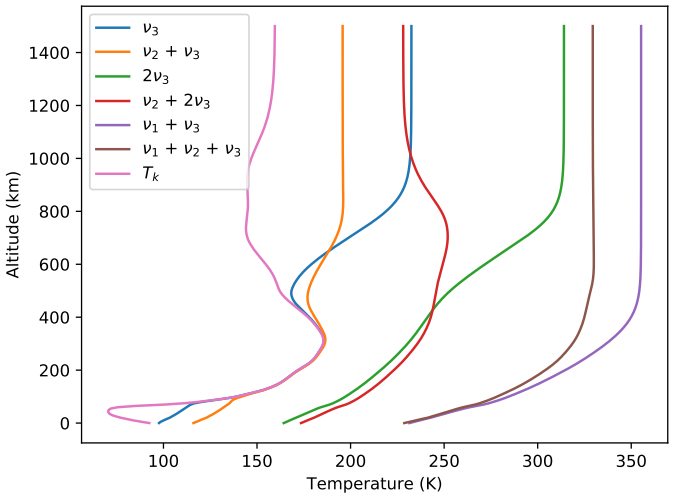

Figure 5.6: Vibrational temperatures for ν_3 level of HCN and higher energy level containing ν_3 quanta.

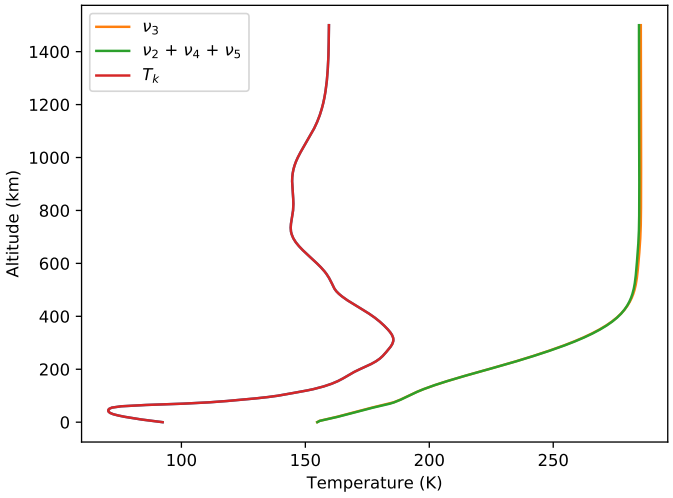

Figure 5.7: Vibrational temperatures for the ν_3 and $\nu_2 + \nu_4 + \nu_5$ levels of C_2H_2.

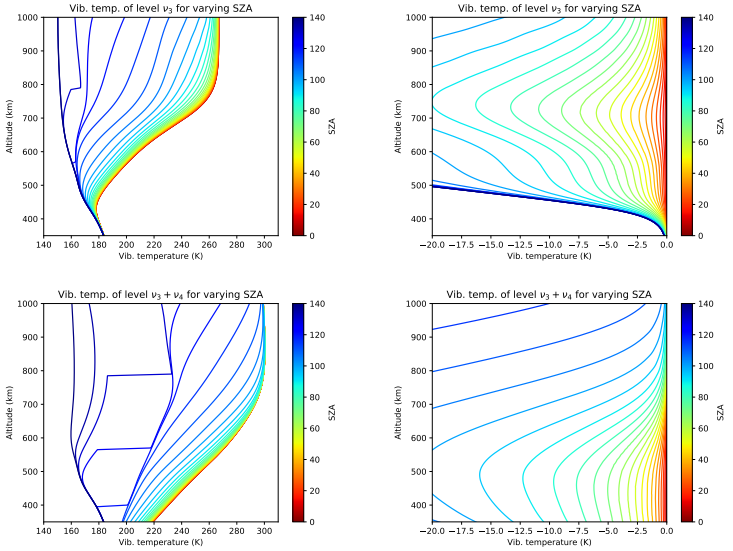

Figure 5.8: Vibrational temperatures of two CH_4 levels for varying SZA (left panel) and the differences with respect to the most excited profile (right panel). Top panels refer to the ν_3 level, bottom panels to the $\nu_3 + \nu_4$ level.

level population. The main differences are observed in the region between 600 and 900 km, with a peak at about 750 km. For SZA equal to 60°, the difference with the case of maximum excitation peaks at a value of 6 K, which grows to about 15 K for the SZA = 80° case. Higher SZA show larger differences, up to 100 K for the most extreme case. The $\nu_3 + \nu_4$ level, being the hot band more optically thin, shows differences at lower altitudes for varying SZA. Significant differences are seen below 650 km, with a shallow peak at about 500 km. Peak differences are 5 K for SZA = 60° and 7.5 K for SZA = 80°. Some curves for high SZA show steep and seemingly unphysical gradients at some altitudes: this is due to the transition between day and night conditions: due to the extended nature of Titan's atmosphere, the altitudes above 400 km are directly illuminated by the sun till SZA = 120°. This proves why we do see an excited signal also in the data above 90° as shown in Figure 5.2.

5.3 Simulated non-LTE emission

The non-LTE emission of CH_4, HCN and C_2H_2 has been simulated for a test atmosphere (equatorial latitude, SZA = 65°, year 2006) and convolved to the VIMS spectral resolution, in order to assess how the different vibrational bands contribute to build the overall spectral shape. The VMR profiles used for the three gases are shown in Figure 5.11. Figures 5.9 show the results of the simulations for the three

gases for two LOS tangent at 400 km (left panels) and 800 km (right panels). The contribution of the different bands is indicated with the upper vibrational level of the transition.

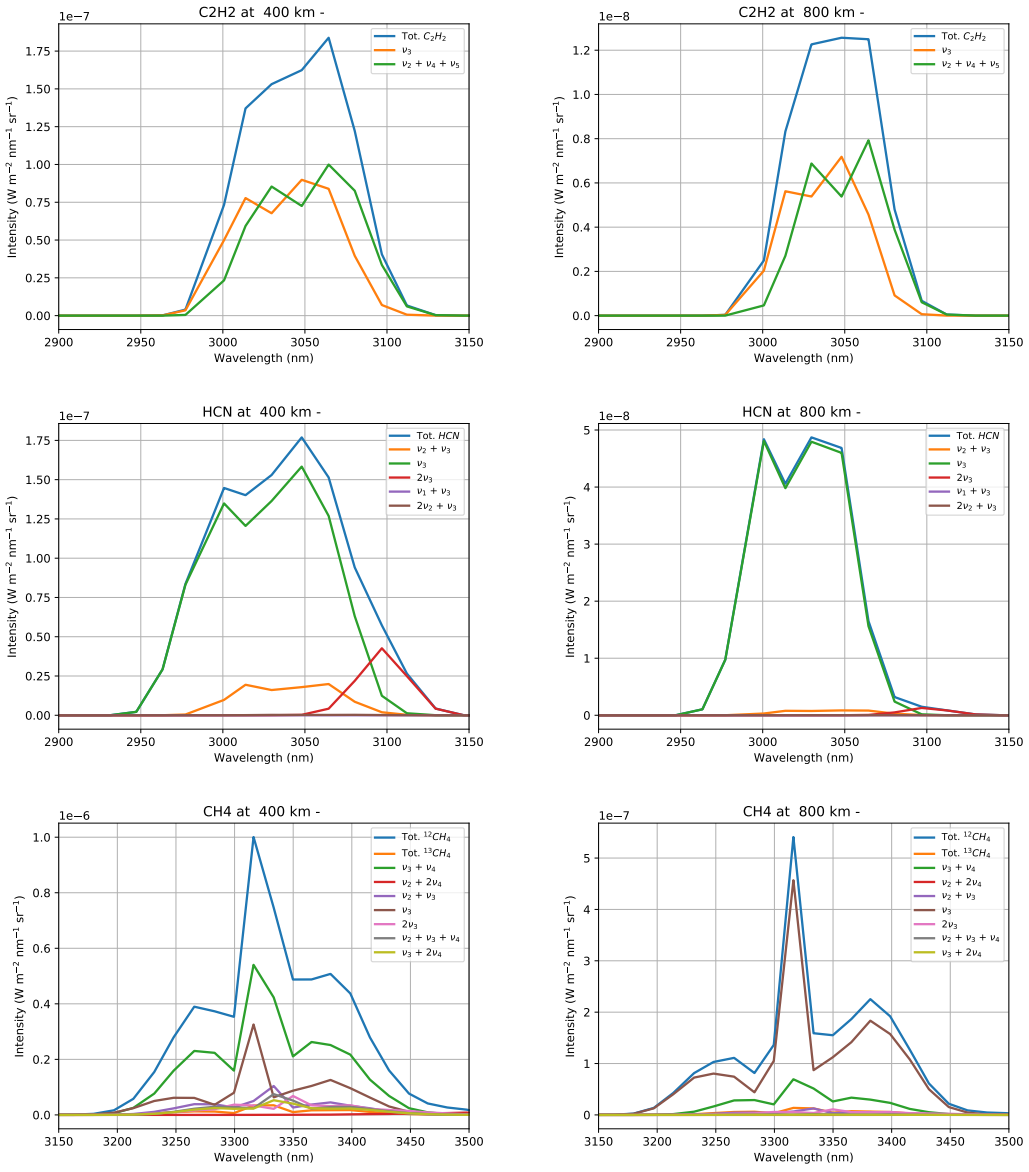

Figure 5.9: Simulations of non-LTE emission of C_2H_2 (upper panels), HCN (middle panels) and CH_4 (bottom panels) for two LOS tangent at 400 km (left panels) and 800 km (right panels), convolved to VIMS spectral resolution. The contribution of the different bands is indicated with the upper vibrational level of the transition.

Left panels of Figures 5.10 show the overall contribution (spectral integral) of each vibrational band of the three molecules for a set of 20 LOS with varying tangent altitude from 300 to 1100 km. The right panels show the relative contribution of each band normalized to the integral of the overall molecular emission. For C_2H_2

the $\nu_3 \rightarrow 0$ and $\nu_2 + \nu_4 + \nu_5 \rightarrow 0$ give similar contribution in the whole atmosphere. For HCN the main emission comes to the $\nu_3 \rightarrow 0$, with the $\nu_3 + \nu_4 \rightarrow \nu_4$ and $2\nu_3 \rightarrow \nu_3$ contributing altogether to 10-20% of the emission from 500 to 400 km, and less than 5% above 600 km. For CH_4 the $\nu_3 \rightarrow 0$ and the $\nu_3 + \nu_4 \rightarrow \nu_4$ contribute to 75-80% of the emission below 700 km, with the latter being responsible for almost 50% of the emission. The other hot and overtone bands of $^{12}CH_4$ and the ν_3 band of $^{13}CH_4$ contribute altogether to up to 25% in this altitude region. Above 800 km the fundamental ν_3 band is responsible for more than 80% of the emission.

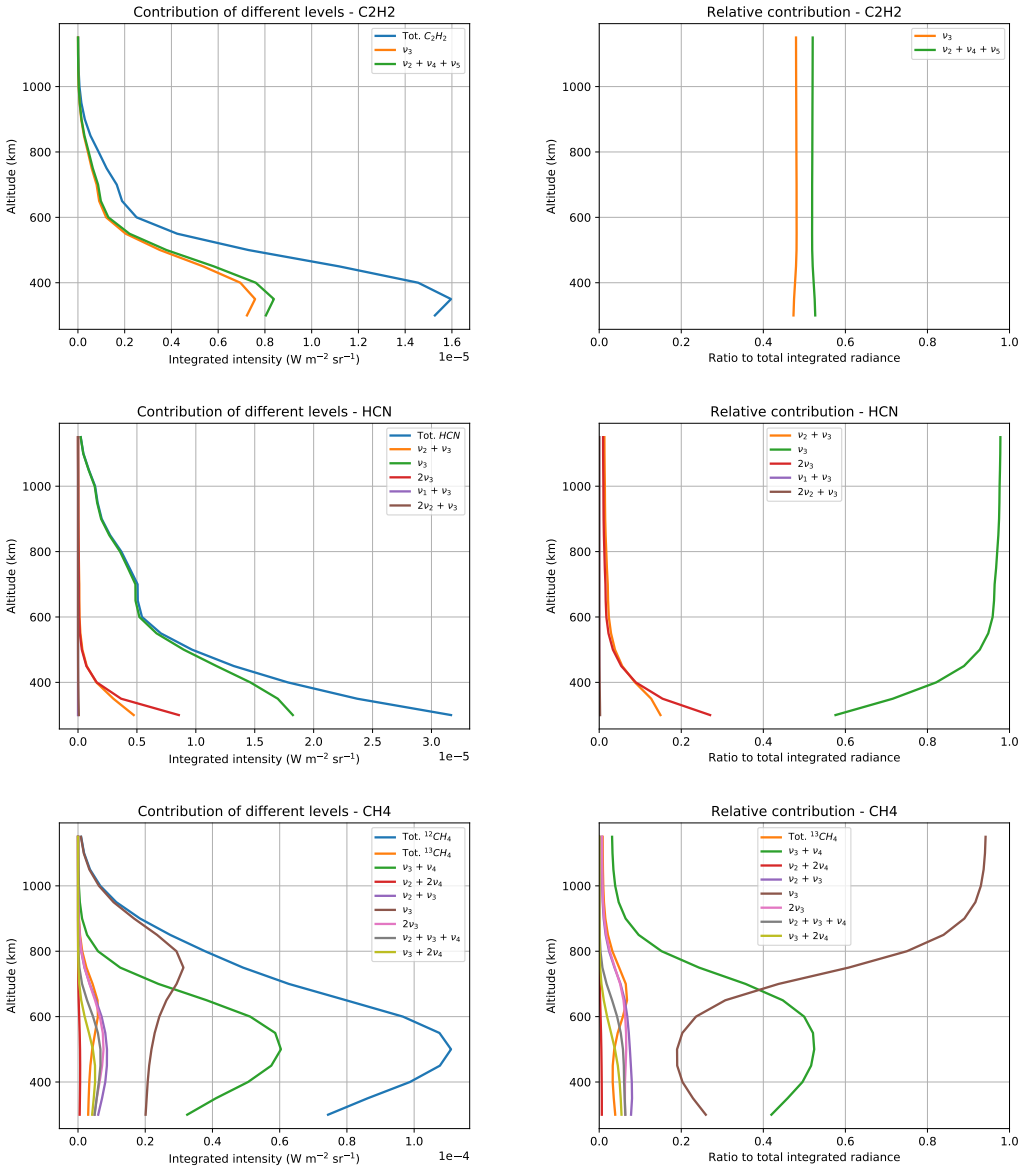

Figure 5.10: Absolute (left panels) and relative (right panels) integrated contribution of the different vibrational bands to the total integrated emission of each molecule. C_2H_2, HCN and CH_4 are shown in the top, middle and bottom panels respectively.

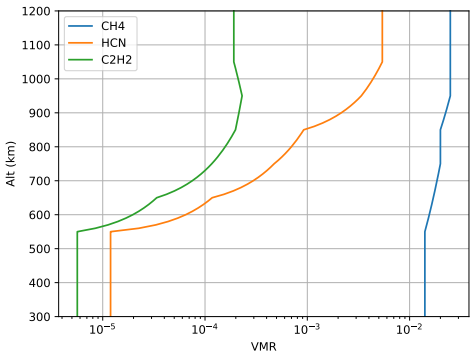

Figure 5.11: VMR profiles used for the three gases in the simulations.

5.4 Analysis on a partial dataset and preliminary results

An analysis on a partial VIMS dataset has been carried on to test the existence of significant seasonal/latitudinal variability in the retrieved VMR profiles. A set of 264 limb scanning sequences - containing about 10 limb spectra each at different tangent altitudes - has been analyzed. VIMS data cubes used are listed in Table 5.1. They were selected so as to satisfy the requirements of long integration time (larger than 600 s), SZA lower than 90° and phase angle lower than 90°.

Due to the requirement on SZA, the coverage is poor at the winter polar latitudes.

5.4.1 Analysis

For each of the 264 limb scanning sequences extracted, a set of vibrational temperatures for the main levels of the 3 molecules have been calculated, specifically for the latitude, SZA and Sun-Titan distance at the time of the observations. A different pressure-temperature (p-T) profile has been assumed for each latitude and year and used in the calculations of vibrational temperatures. The kinetic temperatures have been derived from the co-located temperature profiles measured by CIRS [Achterberg et al., 2011, 2008] and extended upwards with the temperature profile used in previous studies [García-Comas et al., 2011; Adriani et al., 2011]. Pressures have been calculated consistently assuming hydrostatic equilibrium.

The resulting set of vibrational temperatures has been assumed in the inversion of the measurements. The p-T profiles assumed for the inversions were the same as those used for the non-LTE calculations.

The emission measured by VIMS has been simulated with the code GBB, de-

Table 5.1: List of VIMS cubes used in the analysis. For each cube, the table lists the cube name, the number of spectra, the year of measurement, the mean phase angle (Pha) and the covered ranges in latitudes.

#	Cube	Year	Pha	Lat range
1	V1477459118	2004	13	70 S - 40 N
2	V1490948671	2005	57	80 S - 30 N
3	V1490955139	2005	57	80 S - 40 N
4	V1530471051	2006	61	80 S - 70 N
5	V1536397418	2006	63	70 S - 40 N
6	V1563524168	2007	60	85 S - 60 S
7	V1563524658	2007	60	80 S - 55 S
8	V1563525149	2007	26	70 S - 45 S
9	V1567269485	2007	26	80 S - 0
10	V1582444145	2008	66	60 S - 40 N
11	V1590707892	2008	89	50 S - 30 N
12	V1590616570	2008	95	50 S - 50 N
13	V1612658738	2009	70	0 - 40 N
14	V1612664166	2009	70	0 - 40 N
15	V1649210753	2010	15	60 S - 60 N
16	V1649227483	2010	18	50 S - 60 N
17	V1654449711	2010	31	50 S - 80 N
18	V1676803273	2011	31	70 S - 60 N
19	V1681937300	2011	16	50 S - 80 N
20	V1704257066	2012	58	70 S - 60 N
21	V1706671551	2012	22	20 S - 80 N

scribed in Section 1.4. As in García-Comas et al. [2011] and Adriani et al. [2011], the atmosphere is assumed horizontally homogeneous and all atmospheric quantities refer to the geolocation of the tangent points and to the SZA at the tangent point. More discussion on this approximation and on its influence on the results can be found in Section 5.5. The simulations include non-LTE emission of CH_4, $^{13}CH_4$, HCN, C_2H_2 and LTE emission from C_2H_6, C_2H_4 and CH_3D. For all these gases, spectroscopic data are taken from the HITRAN 2012 compilation [Rothman et al., 2013]. For CH_4 additional spectroscopic data relative to the $2\nu_3 \rightarrow \nu_3$, $\nu_3+2\nu_4 \rightarrow 2\nu_4$ and $\nu_2 + \nu_3 + \nu_4 \rightarrow \nu_2 + \nu_4$ bands have been considered [Boudon et al., 2003]. For HCN additional data for the bands $2\nu_3 \rightarrow \nu_3$ and $\nu_2 + \nu_3 \rightarrow \nu_2$ - not included in HITRAN - have been considered [Harris et al., 2002].

In order to properly model the narrow line shape at the low pressures of Titan's upper atmosphere, the spectra have been simulated on a wavenumber grid of $0.0005\,\mathrm{cm}^{-1}$.

The inversions have been performed with the retrieval module of the GBB code, performing optimal estimation of atmospheric quantities through a bayesian ap-

proach. The retrieval procedure minimizes the cost function (χ^2) through the Levenberg-Marquardt iterative procedure (see Section 2.3).

For each observation, two separate inversions were performed for the 2.9-3.1 μm region - including simultaneous retrieval of HCN and C_2H_2 - and for the 3.2-3.5 μm region with retrieval of CH_4. For each molecule, the retrieved quantity is a vertical profile of the abundance, discretized with a piecewise linear curve on a vertical grid from 550 to 1050 km for HCN and C_2H_2 and from 450 km to 1050 km for CH_4, at 100 km steps (5 and 6 nodes respectively).

In the inversion of CH_4, the spectral region corresponding to the R branch ($\lambda <$ 3.29 μm) has been masked out from the retrievals, due to the interfering signal from PAHs in the upper atmosphere [López-Puertas et al., 2013]. The inversion procedure is iterated for each limb scanning sequence until the relative variation of the cost function between two iterations is less than 1%.

5.4.2 Preliminary results

Average results for HCN and CH_4 from non-LTE analysis of VIMS spectra have already been published and commented in previous works [Adriani et al., 2011; García-Comas et al., 2011]. For C_2H_2, these are the first VMR profiles retrieved from VIMS spectra and the average retrieved profile is shown in Figure 5.12. A comparison can be made with the retrieval of C_2H_2 performed by UVIS [Koskinen et al., 2011]: our value at 950 and 1050 km is consistent with the value retrieved by them at 1000 km of 4×10^{-4} which retrieves a similar value (about 5×10^{-4}); also the VMR retrieved at 750 and 850 km is consistent with their value, while at 550 km and 650 km our retrieved VMR is about 3 and 2 times smaller (respectively) than their retrieved VMR at these altitudes. This discrepancy might be due to the low sensitivity of our retrieval at the lowest altitudes.

The CH_4, HCN and C_2H_2 retrieved VMR profiles for the 264 sequences have been averaged in 20° latitudinal bins from pole to pole, dividing the measurements made during northern winter - from 2004 to 2009 (included) - and those made during the early northern spring, from 2010 to 2012. The latitude-altitude contour maps for the the retrieved HCN, C_2H_2 and CH_4 are shown in Figures 5.15, 5.13 and 5.14. Left and right panels represent respectively the average VMR maps in the northern winter season and in the early spring.

The interpretation of the results is complicated due to the high variability of the retrieved profiles and the poor coverage in key regions. We first comment on the

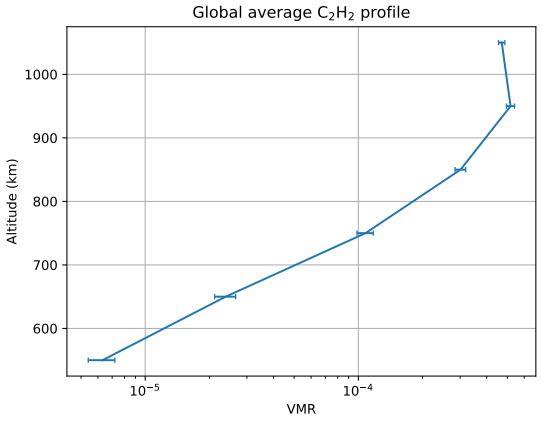

Figure 5.12: Global average of the retrieved C_2H_2 profiles for all sequences.

figures and then consider the significance of the observed patterns on the basis of the variability and coverage. Very interesting features can be noted in the figures:

HCN: in Figure 5.13, a positive trend towards the north pole can be noted at all altitudes during winter (left panel). This seems to suggest that the middle atmosphere circulation that is driving polar enhancement of HCN below 500 km [Vinatier et al., 2015; Teanby et al., 2008, 2009, 2012] extends up to higher altitudes. This is further intriguingly suggested by the map of HCN VMR during the spring season, which shows a symmetrical pattern with a pronounced enhancement both at the north and south pole up to 800 km. This may be interpreted as a signature of the circulation reversal, with subsidence taking place at the (autumn) south pole and enrichment in the polar upper mesosphere and lower thermosphere and yet with a remaining enrichment due to the winter season at the north.

C_2H_2: Figure 5.14 shows a similar pattern for C_2H_2 during spring, with strong enhancements at both poles up to 800 km. On the other side, the winter map shows no significant latitudinal variations. A pattern similar to that of HCN would have strengthen the suggestion of polar enrichment up to these altitudes. Also Vinatier et al. [2015] observed differences in the response of the two molecules to the subsidence and enrichment processes, but this would be expected to be more evident in a situation of seasonal change (then in the spring panels) rather than at the end of the winter season.

CH_4: The pattern for CH_4 is different, as expected. No significant latitudinal trend is seen in Figure 5.15 up to about 750 km, both in winter and spring. This

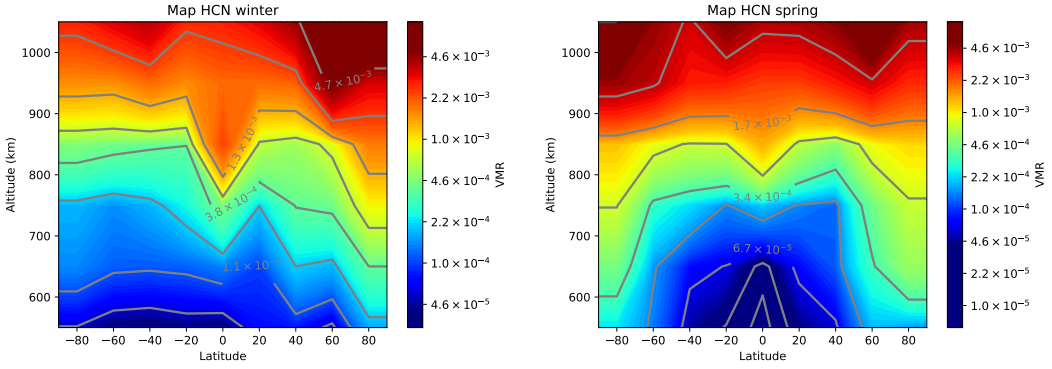

Figure 5.13: Latitude-altitude maps of the retrieved HCN VMR abundance. Left panel refers to the northern winter, right panel to early spring. The scale of the left and right panels are different, to highlight latitudinal variations.

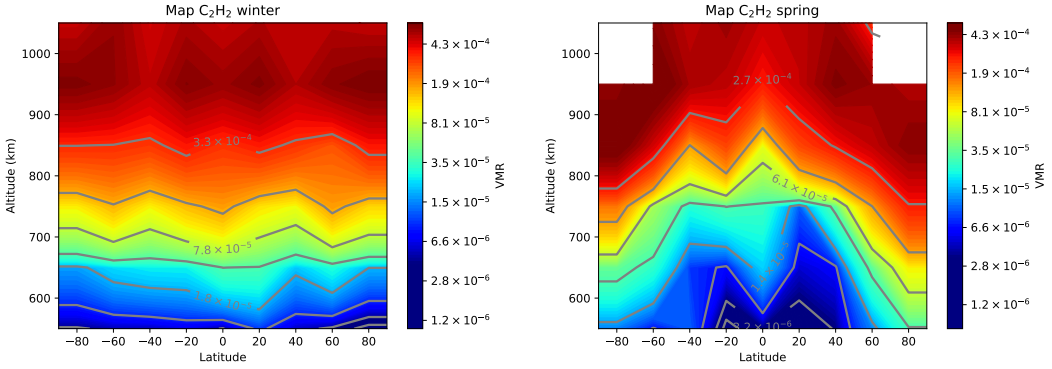

Figure 5.14: Latitude-altitude maps of the retrieved C_2H_2VMR abundance. Left panel refers to the northern winter, right panel to early spring. The scale of the left and right panels are different, to highlight latitudinal variations.

is in agreement with the photochemical models, since CH_4 is expected to be well mixed up to its homopause that is situated at about 800 km [Koskinen et al., 2011]. An unexpected feature is instead seen at higher altitudes: an enhancement at north pole during winter and a weaker enhancement at both poles during spring at altitudes above 800 km. This seems to be correlated with the (noisy) behaviour of HCN at the highest altitudes, which also shows peak abundances at the north pole during winter and at the south during spring.

5.4.3 Discussion

Figure 5.16 shows the number of retrieved profiles (left panel) and the average SZA of the retrieved profiles (right panel) for all latitudinal bins and for the two seasons.

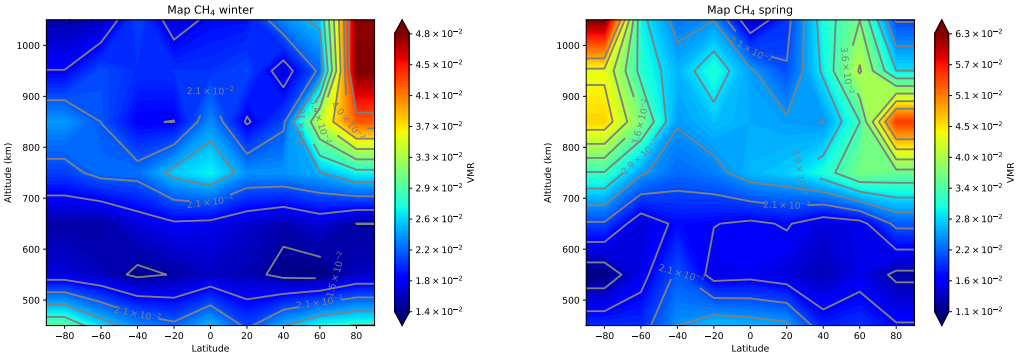

Figure 5.15: Latitude-altitude maps of the retrieved CH_4 VMR abundance. Left panel refers to the northern winter, right panel to early spring. The scale of the left and right panels are different, to highlight latitudinal variations.

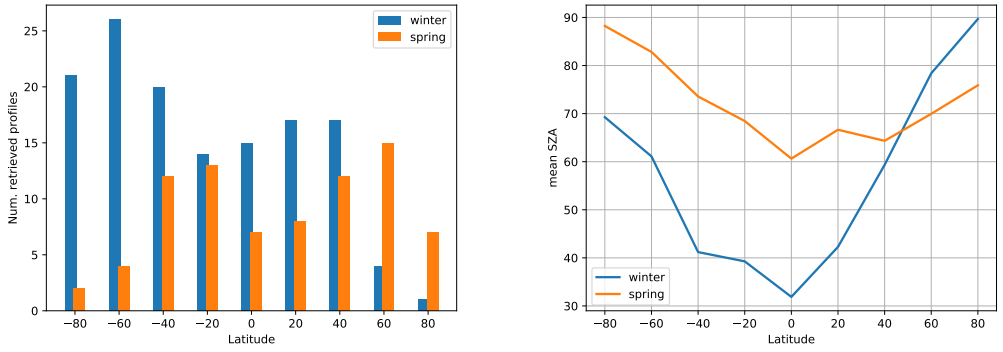

Figure 5.16: Number of retrieved profiles for the two seasons (left panel) and mean SZA of the observations (right panel) for each latitudinal bin.

As shown in the left panels, the partial dataset used has a very poor coverage at the north pole during the winter season - only one inversion above 70°N and 3 between 50° and 70° N - and the South pole during the spring, with 2 inversions south of 70°S and 3 between 50° and 70° S. Moreover, these same regions happen to have the largest average SZA, with almost 90° at the poles. Of course, this is an obvious geometrical implication of the seasons considered and requiring SZA smaller than 90° significantly limits the coverage in these key regions.

To further discuss on the results, it is worth separating the discussion about the lower and upper altitude regions:

- the lower region - from 550 km up to CH_4 homopause situated at 800 km - is most probably influenced by the global circulation pattern taking place at lower altitudes and the question to ask is up to what altitude does this circulation extend.

- the upper region - from 800 km upwards - is expected to show some of the variability seen in the upper thermosphere above 950 km by INMS. The question here is whether the are latitudinal and seasonal variations or these are hidden by the extreme variability of the region.

Teanby et al. [2012] pointed out that the top of the middle atmosphere circulation has to extend up to 600 km or more, in order to explain the observed enhancements in trace gases and the adiabatic heating seen at the polar mesosphere. This preliminary analysis of the VIMS dataset seems to suggest an extension of the middle atmospheric cell up to 750-800 km, well above the 500 km level. This is a strong implication for Titan's middle atmosphere circulation and has to be tested carefully.

Figure 5.17 shows the latitudinal averages of HCN and C_2H_2 VMR at 650 km, with the standard error of the mean μ calculated as $\epsilon = \sqrt{\sum_i (x_i - \mu)^2}/\sqrt{n(n-1)}$. For the retrieved VMR at the north pole during winter, since only one retrieved profile is available, the retrieval error is used instead. The observed latitudinal trend for HCN is significant for the spring season, while the peak at the north pole for the winter season would be also consistent with no enrichment inside 2σ. The C_2H_2 trend is weaker and is around the 2σ level for the spring season, while it is not seen at all during winter. Similar behaviours are observed at 750 km, while at 550 km the retrieval errors are generally larger and the latitudinal variations less evident (figures are not shown). In order to validate the hypothesis of extension of the middle atmosphere circulation up to these altitudes, a larger statistics is needed especially for the northern polar and subpolar latitudes during winter and for the southern polar and subpolar during spring.

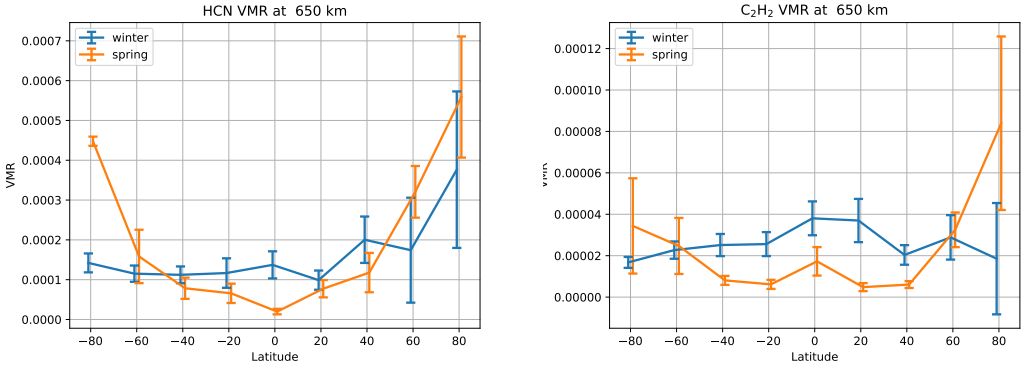

Figure 5.17: Average retrieved VMR at 650 km in each latitudinal bin for HCN (left panel) and C_2H_2 (right panel). The errorbars represent standard error, apart for the point at 80° in the winter season, where it represents retrieval error.

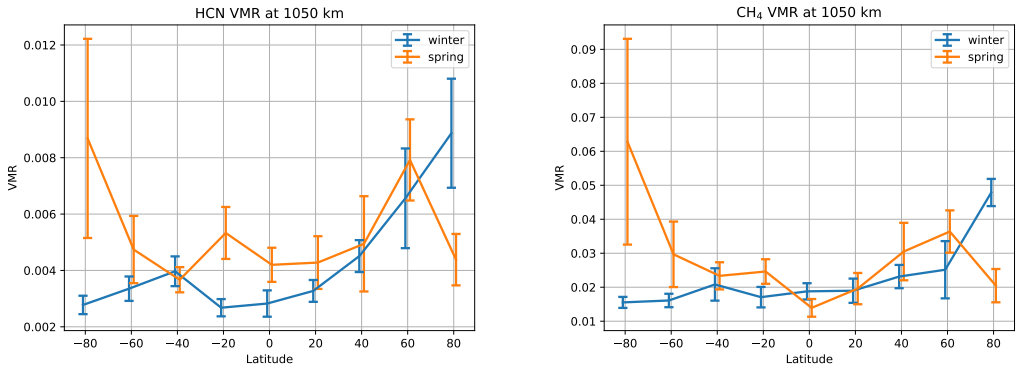

Figure 5.18: Average retrieved VMR at 1050 km in each latitudinal bin for HCN (left panel) and CH_4 (right panel). The errorbars represent standard error, apart for the point at 80° in the winter season, where it represents retrieval error.

Yelle et al. [2006] and Müller-Wodarg et al. [2008] found interesting latitudinal patterns in their empirical model of Titan's upper atmosphere, which exploits a preliminary analysis of INMS measurements taken before 2007. In particular, the strong winds predicted by the empirical model in the winter thermosphere and the pronounced oblateness of the atmosphere (with lower pressures at the poles at the same altitude) would produce an accumulation of CH_4 and HCN at the winter pole [Müller-Wodarg et al., 2008]. Figure 5.18 shows the latitudinal averages of HCN and CH_4 VMR at 1050 km, with the errors calculated as for Figure 5.17. The patterns observed for HCN and CH_4 are unexpectedly rather similar and this fact requires explanation. The trend at the north pole during winter appears to be significant despite the low statistics both for HCN and CH_4. The spring pattern is instead noisier and does not reach the 2σ level. The enhancement at the winter pole would be in line with the prediction of the empirical model in Müller-Wodarg et al. [2008]. However, the analysis in Müller-Wodarg et al. [2008] has been questioned by a subsequent reanalysis of a more complete INMS dataset by Snowden et al. [2013], which found no clear correlation of their retrieved temperatures with latitude or SZA, pointing out that the most striking feature observed is the extreme variability of the thermospheric environment due to gravity waves propagating from below. However, the retrieval of VIMS measurements gets information from signal coming from different points along the LOS, possibly smoothing the effect of waves, while INMS data are collected *in situ*.

If the enhancement at the winter pole is proved to be real with larger statistics, its cause may lie also in the larger SZA of the winter/autumn pole. For HCN this has already been noted and associated with the lower photodissociation of HCN due

to the lower EUV flux at high SZA [Cui et al., 2016; Adriani et al., 2011]. However, this is in contradiction with the model in Westlake et al. [2014], that predicts larger HCN for larger EUV flux, due to increased photodissociation of CH_4.

5.5 SZA bias and problems at the polar latitudes

The preliminary analysis in the previous section suffers mainly from the poor coverage at the polar latitudes, that does not allow an unambiguous determination of the latitudinal and seasonal trends. The geometry of the Titan-Sun alignment makes the SZA larger than 90° at winter/autumn poles. The worst situation takes place at the winter solstice with SZA equal to 116° for the winter pole and SZA larger than 96° for latitudes above 70 N. For the winter observations and early autumn that have been considered here, the SZA at the pole varies from 90° to about 110°. On the other side the signal at high altitudes is still significant also at SZA between 90° and 110°, as shown by the mean spectra in Figure 5.2.

The analysis at high SZA with the GBB code (Section 1.4) suffers of a bias, due to the approximation of assuming the SZA at the tangent point for the whole line of sight (*tangent SZA approximation*). The bias is more important for optically thick bands, as shown in Section 6.3.

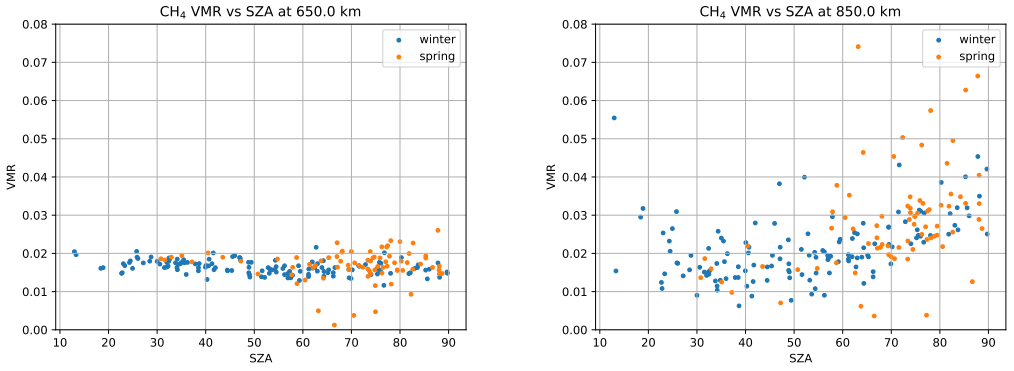

Figure 5.19: Retrieved CH_4 VMR at 650 km (left panel) and 850 km (right panel) in function of the tangent SZA of the measurement.

This bias is one of the causes of the correlation of retrieved CH_4 VMRs with SZA shown in Figure 5.19. The figure shows all retrieved CH_4 VMR at 650 km (left panel) and 850 km (right panel) in function of SZA. In the right panel there is no apparent dependence on SZA below about 60° but then a correlation is evident, with systematically larger VMRs obtained for larger SZAs. No correlation is seen at

650 km (left panel). Some real dependence on SZA of the retrieved VMR should be excluded globally, since the timescale for CH_4 enrichment due to diminished EUV photodissociation is estimated to be about 3 years at 1000 km (see Westlake et al. [2014]). Only the winter pole may satisfy the condition.

Since all analyzed measurements have phase angles lower than 90°, the sun is always found on the spacecraft side of the line of sight (LOS), and the part of the LOS closer to the observer corresponds to lower SZA and higher excitation. Assuming the tangent SZA in the simulation underestimates the actual emission and leads to overestimation of the CH_4 VMR in the inversion. The effect is larger for larger SZA and thus produces a bias that correlates with SZA. The wish to explain the observed bias and to analyze measurements at large SZA has brought to the development of a new code - SpectRobot, presented in the next chapter - that is able to perform radiative transfer simulations resolving the 3D geometrical configuration of the observation. A detailed and quantitative study of the bias, with a comparison with the 3D case, is reported in Section 6.3.

5.6 Conclusions

VIMS measurements of non-LTE emission from CH_4, HCN and C_2H_2 represent a dataset with unique coverage to study Titan's upper atmosphere in the altitude region that extends from 500 to 1000 km. This region is the key to a better understanding of the middle atmosphere circulation and the assessment of the latitudinal and seasonal variation in the distribution of HCN and C_2H_2 could give important hints, complementary to CIRS observations below 500 km. The inversion of CH_4 and HCN at the highest altitudes could help in the understanding of the complex environment observed by INMS above 1000 km.

A preliminary analysis has been carried on a subset constituted by 264 limb scanning sequences measured by VIMS between years 2004 and 2012. Non-LTE vibrational temperatures have been calculated for the three molecules in Titan's atmosphere by the group of planetary atmospheres at the IAA of Granada (Spain). These temperatures have been used in the modeling of the non-LTE emission for the inversion of the CH_4, HCN and C_2H_2 VMR with the GBB code. The results of the inversion have been averaged in latitudinal bins and in two seasons: winter (2004-2009) and early spring (2010-2012). The HCN VMR shows an enhancement at the North pole during winter at all altitudes and at both the North and South

poles during spring below 800 km. Also the average C_2H_2 abundance is larger at both poles during spring below 800 km, while no significant variation is seen for C_2H_2 during winter. For CH_4 enhancements above 800 km are seen at the North pole during winter and at both poles during spring.

These results have to be considered preliminary due to the small coverage at the polar latitudes, which affects the significance of the results. Moreover a correlation is observed between the retrieved CH_4 abundance at high altitudes and the SZA of the observation. The cause of the bias resides in the tangent SZA approximation in the GBB forward model, thoroughly analyzed in Section 5.5 and 6.3.

The will to explain the observed bias and to analyze measurements at large SZA has brought to the development of a new code - SpectRobot, presented in the next chapter - that is able to perform radiative transfer simulations resolving the 3D geometrical configuration of the observation. A new analysis on a larger VIMS dataset is currently going on with the new code developed. If the patterns observed in the preliminary results are confirmed with larger significance, these would imply that the middle atmosphere circulation on Titan does effectively extend well above the 500 km level, as expected in previous analysis [Teanby et al., 2012], but yet not observed due to lack of suitable data. At the same time, the seasonal variation in the CH_4 VMR at high altitudes, if confirmed, would give insight in the very complex upper atmospheric environment.

Chapter 6

SpectRobot: a Python framework for radiative transfer modeling and retrieval

This chapter concerns the development of SpectRobot, a Python framework for 3D radiative transfer and retrieval in planetary atmospheres. The radiative transfer module uses a line-by-line strategy suited for calculations in the infrared, that produces high resolution spectra. The code may take in input non-LTE temperatures for the molecular vibrational levels and provides the possibility of computing Look-up tables, both for LTE and non-LTE, to speed up the calculations. The ray-tracing is performed in 3D geometry and the retrieval parameters may be in a 1-, 2- or 3-dimensional space.

6.0.1 Motivation

The need for a new code arose during the study of non-LTE emission of CO and CH_4 in Titan's atmosphere, as described in Section 5.5. The non-LTE problem is indeed intrinsically three-dimensional because the molecular excitation usually depends quite strongly on SZA, which varies along the line of sight of an observation. This effect is more important for planets in which the ratio between the "thickness" of the atmosphere[1] and the planetary radius is particularly large - as it is on Titan. Moreover, also the variation of latitude along the line of sight can be important if one is interested in studying the latitudinal variation of the atmospheric composition. Figure 6.1 shows qualitatively the situation. The GBB code, described in Section 1.4

[1] To be more quantitative, we should speak in terms of the pressure scale height.

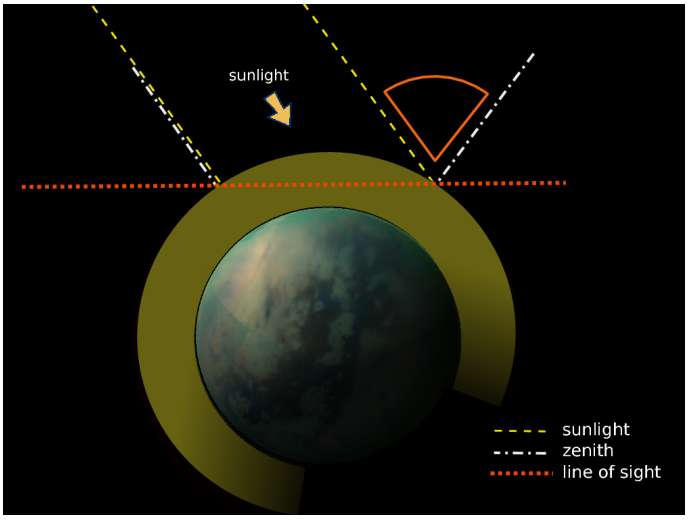

Figure 6.1: Graphical explanation of the SZA variation along the line of sight for a Titan-like planet. The left end of the line of sight is located at SZA = 0, that is here the incoming sunlight is exactly at the zenith. At the right end the SZA is instead much larger, as shown.

and used for the analyses in Chapter 4 and Chapter 5, considers a two-dimensional atmosphere with fixed SZA along the line of sight. This approximation had not yet been properly quantified for the case of Titan and is the most likely cause of the observed bias in the retrieved CH_4 at high altitudes, as described in Section 5.5.

6.0.2 Code philosophy

SpectRobot has been developed mostly in Python. Only some specific CPU-intensive functions are written in Fortran. In developing SpectRobot, I aimed at creating a flexible tool, easily adaptable to different planets and observing situations, and different problems. The choice of the Python language is motivated by the search of a flexible, readable and modular structure, with an object-oriented strategy. The objects make the code more readable (to know what it's doing) and allow to build new scripts suited for different problems with less effort.

Although being less efficient in the calculations with respect to a pure C/Fortran code, SpectRobot achieves a good efficiency with the use of Python libraries such as Numpy and Scipy for calculations on arrays and of specific Fortran functions for intensive tasks.

This Chapter is structured as follows: Section 6.1 describes the main features of SpectRobot; Section 6.2 shows comparisons with the GBB code and results of validation tests; Section 6.3 is dedicated to a quantitative study of the 3D SZA bias

(Section 5.5) through SpectRobot. A detailed description of the code, showing some examples and code snippets and explaining the usage, can be found in Appendix A.

The full code is freely accessible on GitHub and can be downloaded at `https://github.com/fedef17/SpectRobot`.

6.1 Code structure

The internal structure of SpectRobot is based on a set of objects which represent the necessary ingredients of all radiative transfer and retrieval codes. Objects are the basic concept of object-oriented programming: an object contains a set of data in the form of attributes and has specific methods that work on those data. Each object is the instantiation of a class, which is the general template for that particular object.

A more technical description of the classes developed can be found in Appendix A. Here's a list of the objects that gives an idea of the framework:

- class **Planet** represents the planet to be simulated and carries the main geometrical, orbital and stellar characteristics, as well as the information about the atmospheric structure and gases to include in the simulation (see Section A.2.1). The idea is to create a collection of child classes with standard attributes that define all solar system planets and possibly exoplanets.

- class **Coords** describes a point in space and provides painless conversions of coordinates between different reference frames (see Section A.2.2).

- class **AtmProfile** describes an atmospheric quantity and it is linked to an AtmGrid object that describes the atmospheric grid used. The flexibility of the AtmProfile and AtmGrid objects allows to describe different situations, like one- and three-dimensional problems, with the same classes and functions (see Section A.2.3).

- class **Molec**, **IsoMolec** and **Level** describe molecules, isotopologue and levels respectively and are used in the definition of the gases to be simulated. Class Level is necessary in the case of non-LTE simulations (see Section A.2.4).

- class **LineOfSight** is the fundamental class used in all radiative transfer routines, it contains all information about the line of sight (LOS) that has to

be simulated and on the value of the relevant quantities along the LOS (see Section A.2.7).

- class **SpectLine** represents a radiative transition. It is defined through a spectroscopic database and contains all methods necessary to calculate the LTE and non-LTE line strength, the Einstein coefficients and the line shape (see Section A.2.5).

- class **SpectralObject** represents a spectral distribution and is linked to a **SpectralGrid** object (Section A.2.6). These class allows to easily perform conversions, convolutions and operations between spectra and make visualization easier.

- class **LookUpTable** (Section A.2.8) contains the tabulated absorption/emission coefficients for a certain molecule. The non-LTE version contains level-specific coefficients as described in Section 1.3.5.

- classes **BayesSet**, **RetSet** and **RetParam** represent the full state vector of the bayesian inversion problem, a single retrieved profile and a single retrieved parameter respectively (see Section A.2.9).

The framework is the basis for the radiative transfer module and retrieval module of SpectRobot described in the next sections. At the same time it allows handling of atmospheric profiles and results of radiative transfer simulations and inversions for subsequent calculations, statistical analyses and visualization.

6.1.1 Radiative transfer (forward model)

The forward model of SpectRobot is a line-by-line radiative transfer routine that can work with arbitrary orientation in 3D geometry, taking into account the position of the Sun. The spectrum is simulated on a high resolution wavenumber grid (default is $5 \times 10^{-4}\,\mathrm{cm}^{-1}$) and then convolved with the instrumental spectral shape. The radiative transfer calculation works both in LTE and non-LTE, as long as vibrational temperatures are provided as input. The calculation of Look-Up tables is implemented both for LTE and non-LTE calculations.

3D ray tracing

In SpectRobot, the ray tracing is performed in 3D geometry. The line of sight (LOS) is represented by a `LineOfSight` object, described in detail in Section A.2.7. The

LineOfSight object is defined through its geometrical configuration, for which two points are required: a starting point, which is usually the spacecraft position (or generally, the observer's) and a second point, which is usually the tangent point for limb measurements and the intersection with the surface for nadir ones. From this two points, known from the instrument pointing, the LOS vector is defined, which is then used to advance along the LOS.

The calculation of the steps for the radiative transfer is performed in two subsequent operations:

A: subsequent points of the LOS are calculated at fixed length steps (default is 1 km) in a cartesian reference frame centered on the planet. This produces a set of points through which the LOS passes; at each of these points the atmospheric quantities are calculated (see Section A.2.7 for more details). Refraction has not yet been implemented but it is planned to, updating the LOS vector at each step.

B: the small steps calculated above are put together to build optimal radiative transfer steps according to user-defined thresholds, which can be of four types: maximum temperature difference in the step (default is 5 K), maximum log pressure difference (default is 1.0), maximum vibrational temperature difference (default is 5 K) and maximum optical depth (default: no threshold). When one of the thresholds is exceeded, a suitable average of the atmospheric quantities on the radiative transfer step is calculated, following the Curtis-Godson approach (defined in Equation 1.31).

The calculation of the Solar Zenith Angle (SZA) along the LOS is calculated, provided that the Sub Solar Point (SSP) at the time of the observation is known. Let us call $\hat{\boldsymbol{r}}_{\mathrm{SSP}}$ the normalized vector representing the direction of the SSP in the cartesian reference frame and $\hat{\boldsymbol{r}}_P$ the normalized vector representing the direction of the point considered along the LOS. The SZA is defined as the angle between the Sun's direction - given by vector $\hat{\boldsymbol{r}}_{\mathrm{SSP}}$ - and the Zenith direction. In the approximation that the Zenith direction is parallel to $\hat{\boldsymbol{r}}_P$, the SZA is simply the angle between $\hat{\boldsymbol{r}}_{\mathrm{SSP}}$ and $\hat{\boldsymbol{r}}_{\mathrm{P}}$, given by: $\mathrm{SZA} = \arccos \hat{\boldsymbol{r}}_{\mathrm{SSP}} \cdot \hat{\boldsymbol{r}}_{\mathrm{P}}$. This approximation is perfectly suited to Titan, given that its shape is almost perfectly spherical.

In Figure 6.2, the calculation of latitude/altitude and solar zenith angle/altitude coordinates of points along the LOS are shown, for a set of VIMS test LOSs in Titan's upper atmosphere. As expected, the solar zenith angle varies considerably along the line of sight, as shown in the sketch in Figure 6.1.

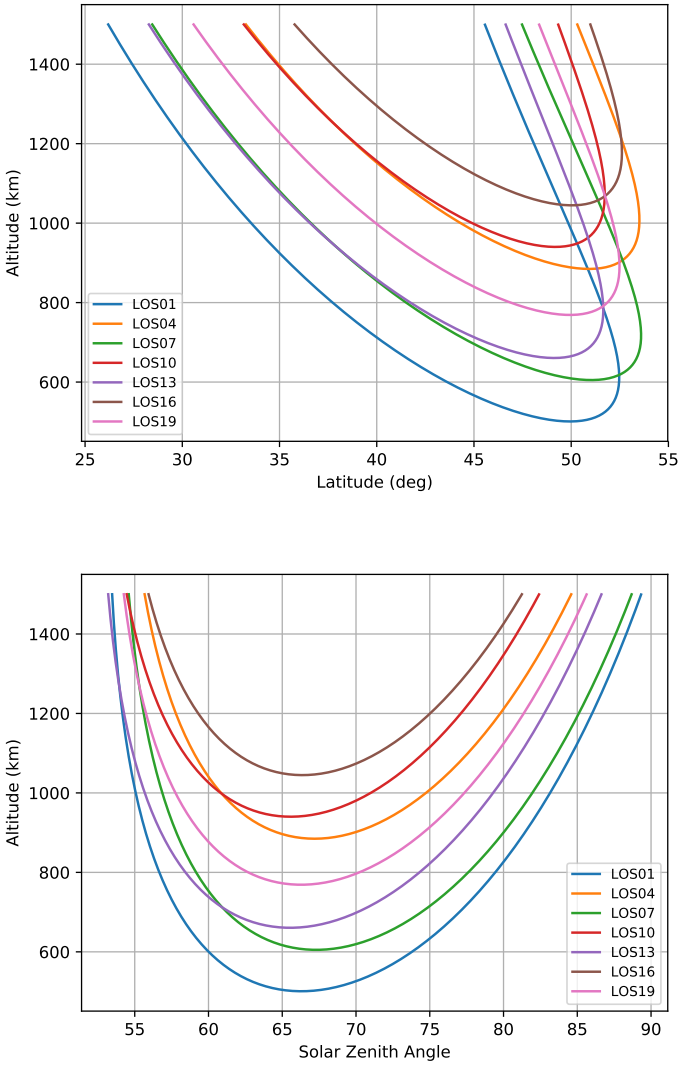

Figure 6.2: Variation of latitude (upper panel) and solar zenith angle (lower panel) for a set of limb LOSs in the upper atmosphere of Titan.

A different approach is used in the GBB code, described in Section 1.4. The ray tracing is performed there considering the intersections of the LOS with a fixed 2D atmospheric grid where atmospheric quantities are defined. In this way the number of steps in the LOS is determined by the intersections with the atmospheric grid. This same set of steps is then used in the radiative transfer, after calculation of the Curtis-Godson averages.

Figure 6.3 shows a comparison between the result of the ray tracing at fixed steps of 1 km and the CG equivalent quantities calculated at each one of the radtran steps for two different temperature thresholds.

Radiative transfer

The output of the ray tracing is a set of steps to use for the radiative transfer calculation. At each step, the emission and absorption coefficients are calculated for each molecule using the CG temperature, pressure and possibly vibrational temperatures of the step. The absorption and emission coefficients are calculated according to Eq. 1.26 and 1.27 respectively. For the non-LTE case the actual procedure is described in Section 1.3.5: level-specific coefficients are calculated first and then the overall coefficients through Eq. 1.30. The source function is calculated as the ratio of the emission to the absorption coefficient; the LTE limit correctly gives the Planck function (Eq. 1.3). No scattering contribution is taken into account in the current version of SpectRobot.

The integration of the radiative transfer equation along the LOS makes use of the standard numerical formula in Equation 1.13 (see Section 1.1.3 for more details).

Calculation of Look-Up Tables

For intensive calculations with many LOS, the absorption and emission coefficients for each gas are calculated multiple times at the same pressure and temperature. In order to shorten the computation time, a common approach is to tabulate the absorption and emission coefficients in Look-Up Tables (LUTs) and then interpolate the stored coefficients to the desired pressure and temperature.

The default setting in SpectRobot is to calculate LUTs for all the molecules considered at user-defined temperature and pressure resolution; the `LookUpTable` objects (see Section A.2.8) produced are stored in a dedicated folder with standard names that are recognized by the code at the next run. If some of the LUTs are missing or have incomplete P-T coverage, the calculation of the missing

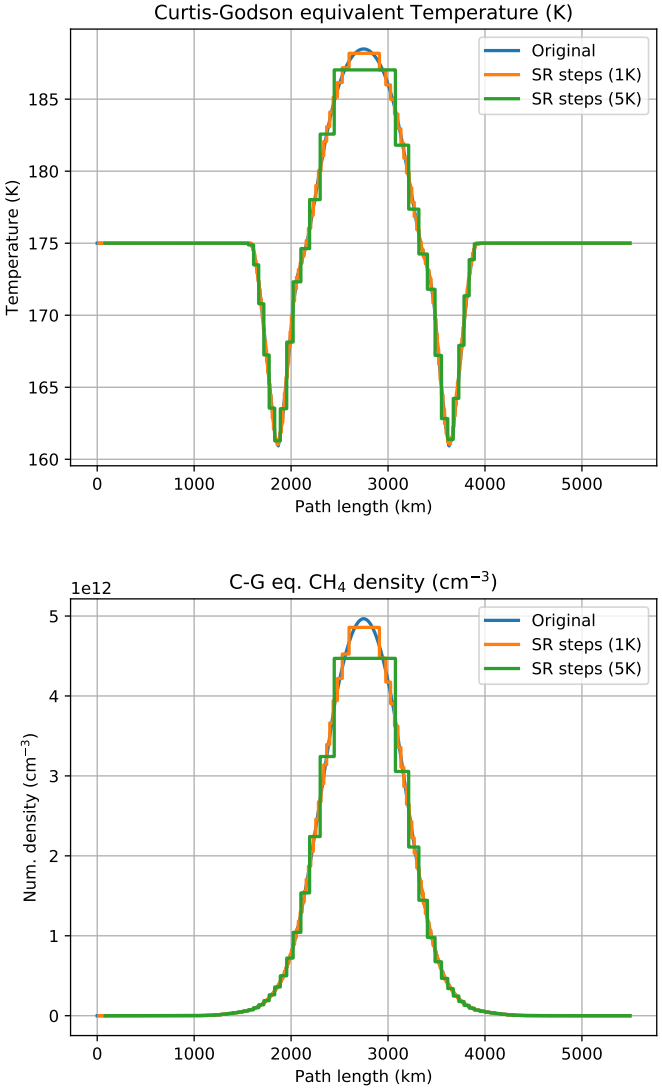

Figure 6.3: Upper panel: comparison of temperature calculated along LOS '01' of the test set at 1 km steps and two different radtran steps calculations, one with a threshold of 1 K on the temperature variation and the other with a threshold of 5 K. Lower panel: the same but for the number density of CH_4.

part is performed before the radiative transfer.

The calculation of LUTs is performed also in the non-LTE case, with the calculation of the level-specific coefficients (see Section 1.3.5) for each P-T couple needed.

Simulation of a set of observations

The forward model has been optimized for the simultaneous simulation of a set of observations. The optimal configuration assumes use of LUTs for all gases considered and parallel computing on a set of n CPUs. Given that the spectra are calculated at high resolution, the amount of memory (RAM) used by the spectral quantities is considerable. Also reading the LUTs is a time-consuming task for hard drives. The common solution to this problem consists in the calculation of the spectrum on a small wavenumber range (microwindow) at a time. SpectRobot splits the wavenumber range in a number of subranges in order to optimize the use of RAM and CPUs. For a machine with 64 Gb RAM and 8 CPUs a dimension of $100\,\mathrm{cm}^{-1}$ for the subranges assures full use of all CPUs with about 80% maximum memory usage. However, this depends on the number of molecules included and P-T couples needed in the calculation.

The results of the high resolution simulations are then convolved with the instrumental spectral response and interpolated to obtain the integrated signal over the Field of View (FOV) of the observation.

6.1.2 Inversion (retrieval module)

The inversion routine in SpectRobot follows a bayesian approach with optimal estimation of atmospheric quantities, as described in Section 2, and adopts a Levenberg-Marquardt iterative procedure (Section 2.3).

The state vector describing the atmospheric parameters that one wants to invert is represented by a BayesSet object (see Section A.2.9). In the current version of SpectRobot only inversion of gas abundances has been implemented and more gases may be inverted simultaneously. The Jacobian $\boldsymbol{K}$ is calculated analytically. The set of inversion parameters for each gas may be one-dimensional - VMR values at a set of fixed altitudes - or two-dimensional - VMR values at a set of altitudes and latitudes. The type of the inversion parameters and the information needed to calculate the Jacobian are fully contained inside the RetParam objects (Section A.2.9): further inversion strategies, such as 3D set of inversion parameters (latitude,

altitude, longitude), are planned to be implemented by creating new RetParam objects. This is particularly interesting for the problem described in Chapter 8.

6.2 Validation of forward model and inversion module

The forward model and the inversion module of SpectRobot (SR) have been validated by comparison with the GBB code (Section 1.4). The following tests have been performed:

- comparison of the spectrum and the derivatives calculated by the two codes with a uniform atmosphere and without LUTs;
- comparison of the spectrum calculated by the GBB code and by a modified SR code which assumes the radiative transfer steps and C-G quantities calculated by the GBB code;
- comparison of the spectrum and line formation for the SR and modified SR code;
- test inversion of CH_4 with GBB and SR on a set of observations used in Section 5.4.

6.2.1 Test with uniform atmosphere

The first test focuses on the simulation of the CO spectrum between 2050 and 2250 cm^{-1} assuming vertically and horizontally uniform temperature, vibrational temperatures and pressure in the whole atmosphere. This is done to avoid differences due to the interpolation and C-G calculations. The GBB code and the SR code have been run in the same conditions and the result is shown in Figure 6.4. The difference in the high-resolution ($5 \times 10^{-4}\mathrm{cm}^{-1}$) spectra has been multiplied by a factor 100 and the largest differences are of the order of 10^{-3}. Since the accuracy of the line parameters for most lines is at the 10^{-4} order, a slight difference in the line shape or in the total column of CO can explain such differences.

With the same test setting, also the derivatives of the spectrum with respect to an inversion parameter have been performed. The derivatives shown in Figures 6.5 and 6.6 are relative to the CO VMR parameter at 500 km altitude. Figure 6.5 shows

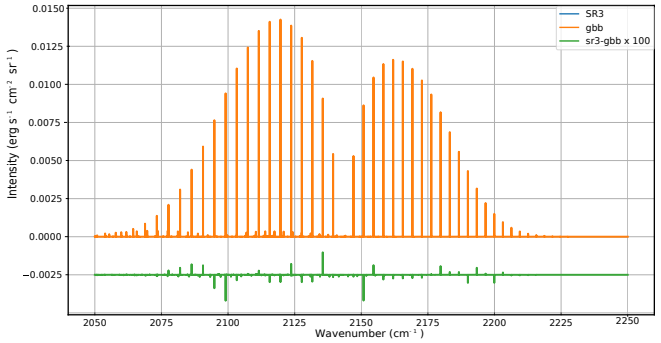

Figure 6.4: Validation: spectrum with homogeneous atmosphere. The difference has been multiplied by a factor 100.

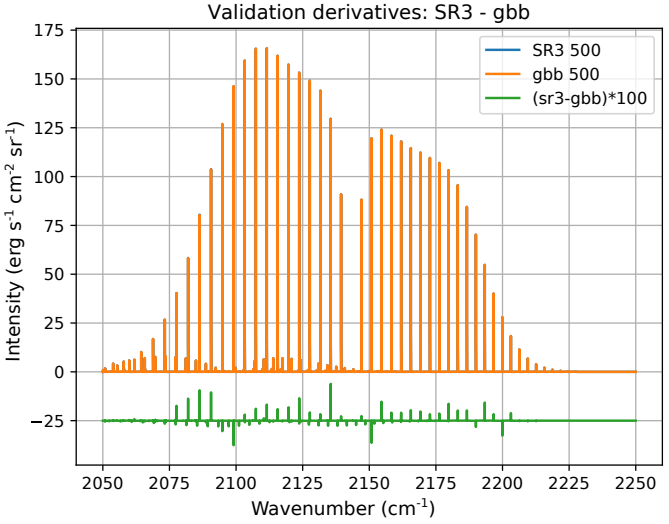

Figure 6.5: Validation: high-resolution derivative with respect of one inversion parameter.

the comparison between the high-resolution derivatives calculated with the GBB and SR codes and the difference has been multiplied by a factor 100. As for the spectrum, the largest differences are of the order of 10^{-3}. Figure 6.6 shows instead a comparison between the analytical derivative calculated with SR and the numerical version of the same derivative.In this case the differences are even smaller, proving that the analytical derivatives are correct.

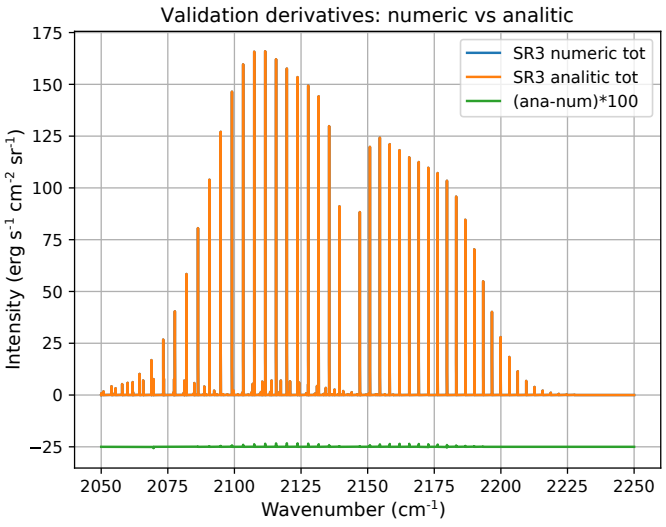

Figure 6.6: Validation: numerical and analytical derivatives

6.2.2 Test of the SR radiative transfer core with non-LTE LUTs for vertically inhomogeneous atmosphere

This test focuses on the simulation of the CH_4 spectrum between 2800 and 3200 cm^{-1} for a model Titan atmosphere which is actually used in one of the inversions of Chapter 5 and for a limb LOS tangent at 434 km. The CH_4 emission is assumed in non-LTE with a set of vibrational temperatures used in the inversion in Chapter 5. Since the aim of this test is to assure that the SR radiative transfer core is working properly, every possible difference in the ray tracing has been avoided. So the results of the GBB ray tracing in terms of arrays of the relevant quantities along the line of sight have been assumed and the same radiative transfer steps have been used in the two codes. There are two differences with the previous test:

- use of a vertically inhomogeneous atmosphere;
- use of pre-calculated non-LTE LUTs for the CH_4 spectrum calculation. Since the CH_4 has many lines in this region (about 30 thousands lines only in the HITRAN database), the calculation of LUTs improves dramatically the computing time;
- no difference in ray tracing.

This modified SR run is called "SR los gbb" in Figures 6.7, 6.8 and 6.9 below. Figure 6.7 shows the comparison of the two high resolution spectra, Figure 6.8 is

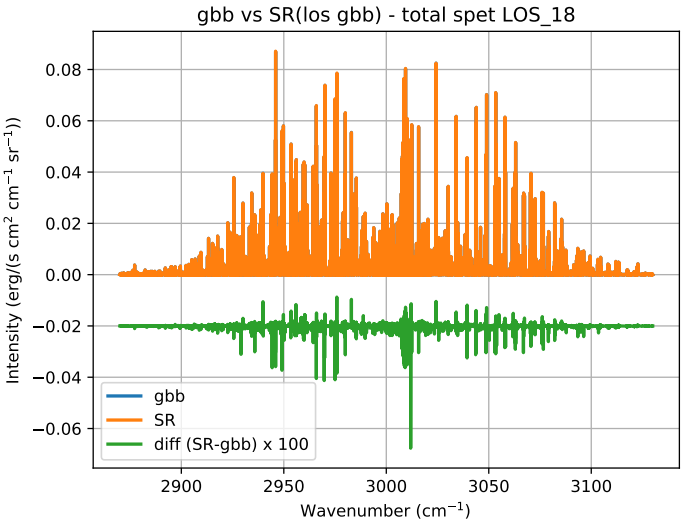

Figure 6.7: Comparison of the spectrum when assuming GBB radtran steps.

a zoom-in to better show the differences in the line shapes and Figure 6.9 is a low resolution ($5\,\mathrm{cm}^{-1}$) convolution of the spectrum. In all figures the spectral differences have been multiplied by a factor 100. Apart from one line, the largest differences are again of the order of 10^{-3}, which is satisfying if considering that the absorption and emission coefficients are calculated in the LUTs at 5 K and 1.0 log(hPa) steps and then interpolated. Figure 6.9 shows that for the low resolution spectrum differences are smaller and concentrated in the Q branch.

6.2.3 Test of the SR ray tracing for inhomogeneous atmosphere

This test is produced for the same input atmosphere of the one above and compares the spectrum produced by SR with two different ray tracing results: the run named "SR los SR" in figures uses the nominal ray tracing of SR, while "SR los gbb" stands for the modified run with GBB ray tracing described in the previous section. In Figure 6.10 the C-G equivalent temperature and CH_4 number density for the two runs are shown. The total columns of CH_4 for the two runs have been checked and their relative difference is about 10^{-4}.

The simulations shown are for the worst case, the LOS tangent at 434 km, which is the lower LOS in the test. Since the LOS is longer and crosses more atmospheric layers, the differences in the ray tracing are amplified here with respect to higher LOSs. In Figures 6.11 and 6.12 below, the high and low resolution spectra compar-

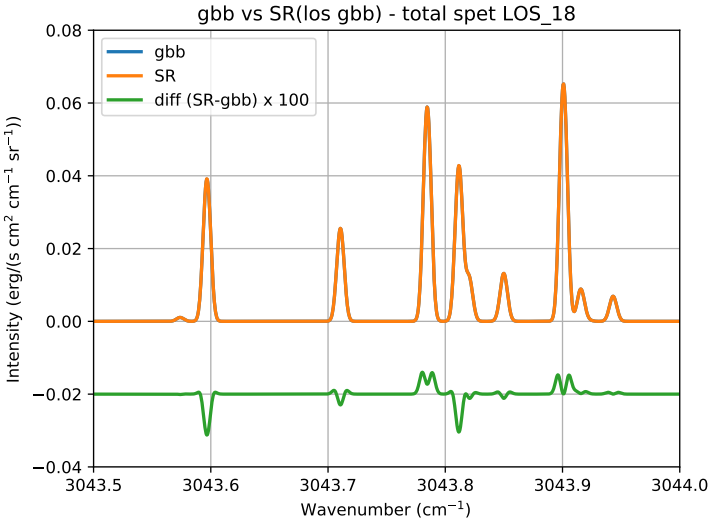

Figure 6.8: Comparison of the spectrum when assuming GBB radtran steps. ZOOM.

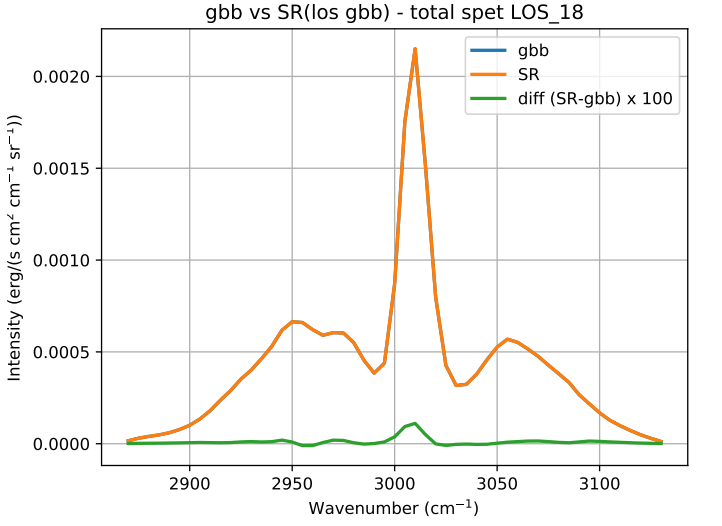

Figure 6.9: Comparison of the spectrum when assuming GBB radtran steps. Low resolution spectrum.

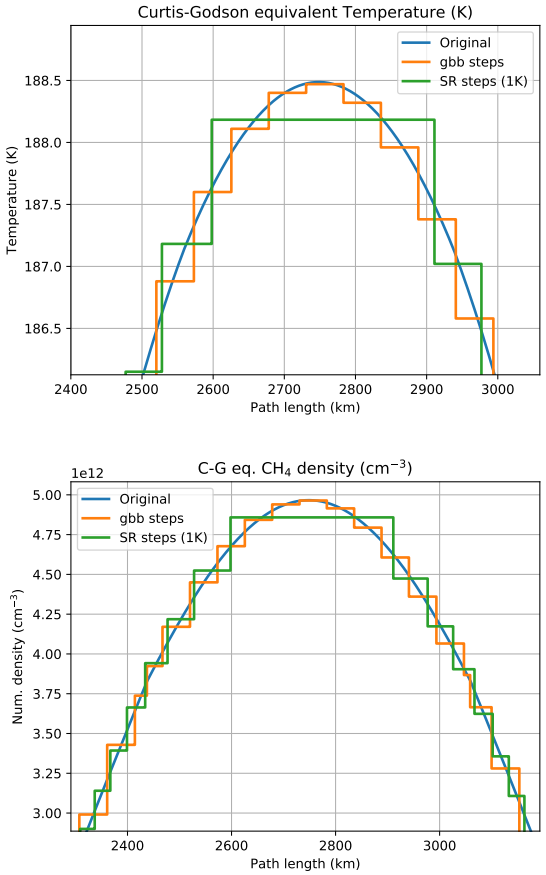

Figure 6.10: C-G equivalent temperature and CH_4 number density steps for SR and GBB ray tracing, compared with the temperature along the LOS.

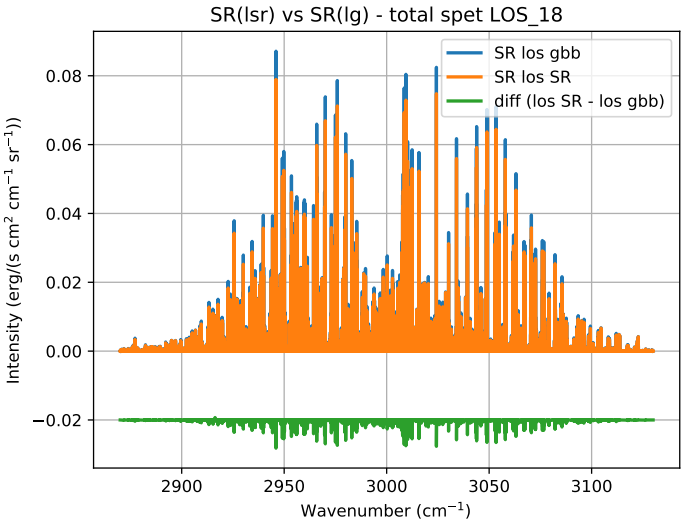

Figure 6.11: Comparison of the spectrum simulated with SR ray tracing ("SR los SR") and with GBB ray tracing ("SR los gbb").

ison are shown. Note that in those figures the differences are not multiplied by the factor 100 and are quite large, even reaching ten percent of the spectral intensity on some lines.

The differences are larger for the more excited bands of CH_4, and particularly for the $\nu_3 + \nu_4 \rightarrow \nu_4$ band. The $\nu_3 + \nu_4$ level is highly excited in the whole atmosphere but its emission is seen mainly below 700 km (see Section 5.3). Figure 6.13 shows the line formation for a transition in the band $\nu_3 + \nu_4 \rightarrow \nu_4$, for GBB and SR runs, normalized to the final value of the line peak in the GBB run. Two runs with different number of steps ("SR los" and "SR los2") are shown for SR, but the final value of the line intensity is the same for the two runs within 10^{-4}. The line intensities using the GBB LOS are instead systematically larger than the SR ones.

The source of these differences has been identified in the different interpolation scheme used for the vibrational temperatures in GBB and SR ray tracing. The GBB code converts the vibrational temperatures in non-LTE ratios on a fixed atmospheric grid and calculates the equivalent C-G average of the non-LTE ratio at each step. The SR ray tracing calculates instead equivalent C-G averages of the vibrational temperatures at each step which differ from the GBB ones by some degree for the most excited levels.

Figure 6.15 shows the differences in the intensity increment at each step for the two runs and the difference in the effective vibrational temperature of level $\nu_3 + \nu_4$ at each step. The two patterns are similar, giving a convincing hint for the cause of

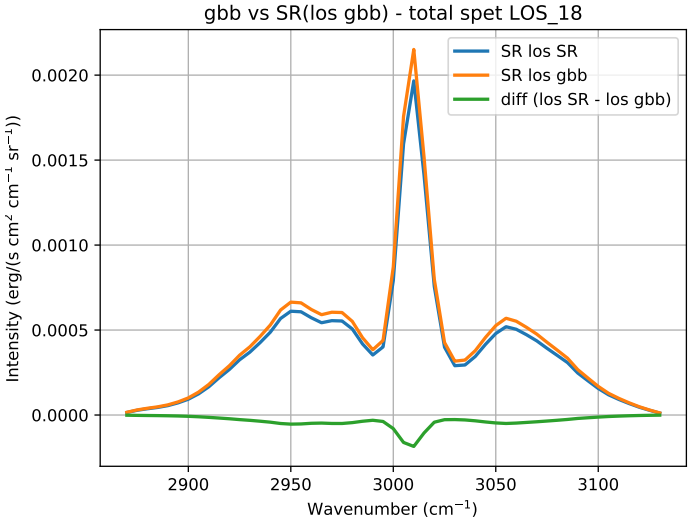

Figure 6.12: Comparison of the spectrum simulated with SR ray tracing ("SR los SR") and with GBB ray tracing ("SR los gbb"). Low resolution spectrum.

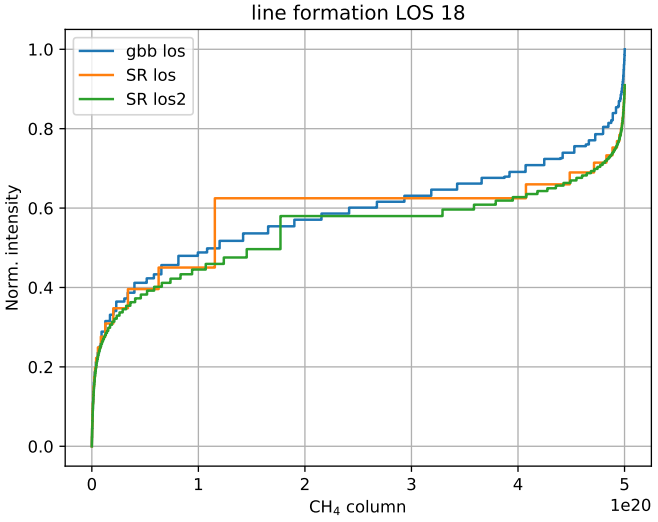

Figure 6.13: Line formation for a specific transition in the band $\nu_3 + \nu_4 \rightarrow \nu_4$ of CH_4.

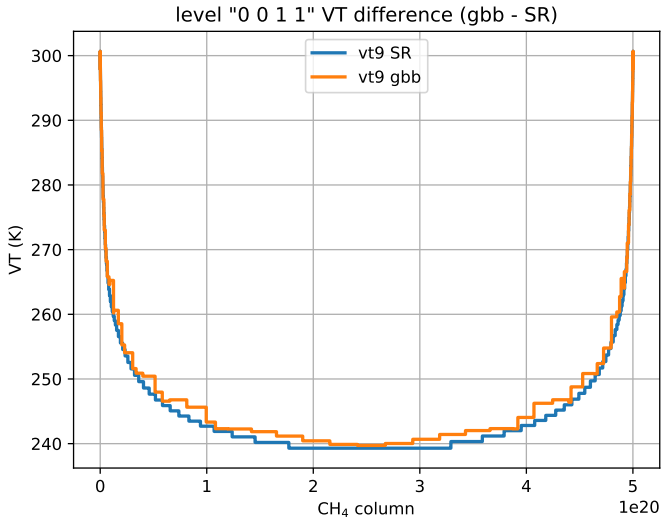

Figure 6.14: Effective vibrational temperature used for level $\nu_3 + \nu_4$ at each step by SR and GBB code.

the difference in the line formation.

6.2.4 Test of the inversion procedure

A test of the full inversion procedure has been done for a set of spectra also used for the analysis in Section 5.4. Given the many possible causes of differences, in the test only the first isotopologue of CH_4 has been included and only lines in the 2012 HITRAN database. The test consisted in a complete inversion with the GBB and SR codes, with retrieval of the CH_4 VMR profile, assuming horizontal homogeneity. Due to the fact that only the first isotopologue of CH_4 has been considered in the forward model, the fit is not perfect and the χ^2 of the simulations is large. The result of the two inversions is shown in Figure 6.16. The two retrieved profiles are consistent within the errorbars but show some differences, especially at the two lowermost points. This fact can be explained by the observed differences in the ray tracing, which produces systematically larger intensities in the GBB code compared with the SR code.

6.3 Study of the 3D SZA bias

The SZA bias discussed in Section 5.5 provided the motivation to develop the new code with 3D geometry. This section presents a test made to assess whether the 3D bias makes some significant change in the retrievals of CH_4, HCN and C_2H_2 in

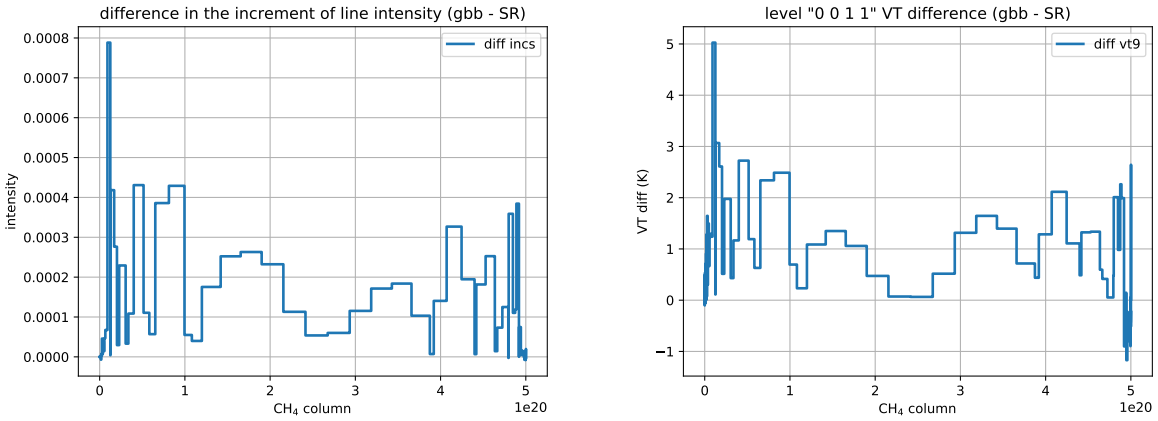

Figure 6.15: Differences in the increment of the line intensity between the GBB and SR runs (top panel) and difference in the effective vibrational temperature of level $\nu_3 + \nu_4$ at each step of the two runs (bottom panel).

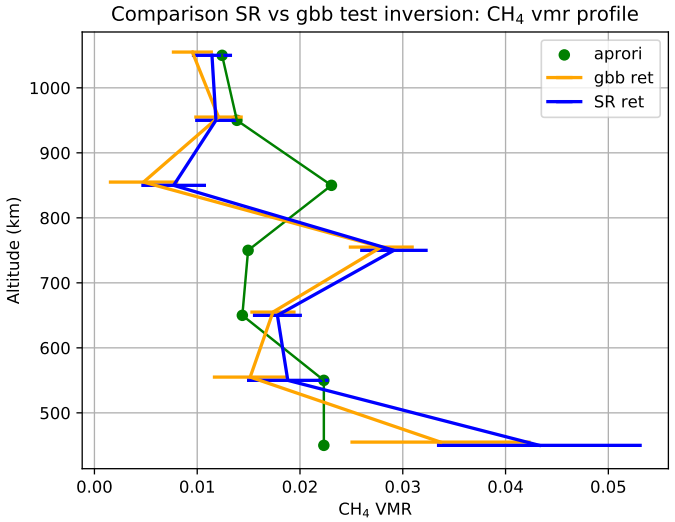

Figure 6.16: Comparison of the SR and GBB retrieved CH_4 VMR profile for the test case.

Chapter 5. Before the inversion test on two extreme cases with SZA = 30° and SZA = 80°, a study on the line formation for the two main CH_4 bands in the 3D case has been performed.

6.3.1 Study of line formation for two CH_4 bands in the 3D case

The set of real VIMS LOSs considered in this section is the same used for the validation tests, with tangent SZA around 65°. In Figure 6.17 the variation of

latitude and SZA for this set of LOSs is shown. The SZA along the LOS varies from about 55° on the inbound leg of the LOS - the region closer to the spacecraft - to 80-90° on the outbound leg. This situation is typical of an observation with phase angle lower than 90°: since the sun is situated behind the spacecraft, the inbound leg of the LOS has lower SZA and molecular levels are more excited there than on the outbound leg. For phase angles larger that 90° the situation reverses.

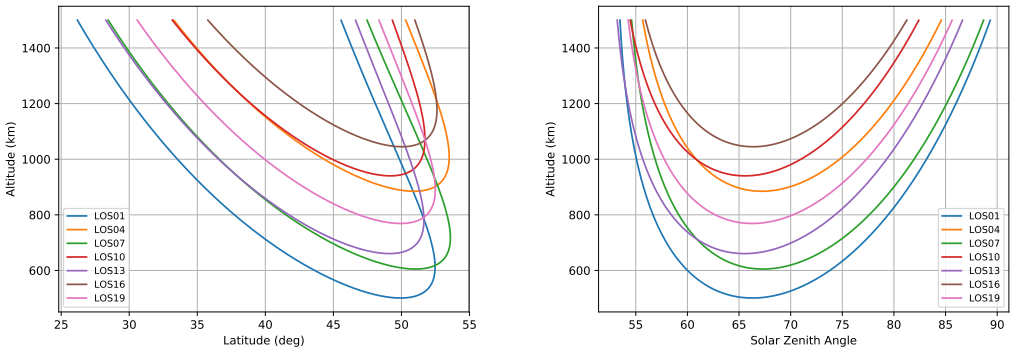

Figure 6.17: Variation of latitude (left panel) and solar zenith angle (right panel) for the set of limb LOSs.

In the following we will refer to the case with tangent SZA approximation as the 1D case and the one that calculates the change of SZA along the line of sight as the 3D case. The main levels contributing to CH_4 emission are the ν_3 and $\nu_3 + \nu_4$ levels. A significant change in the emission between the 1D and 3D case is observed if the vibrational temperature of the main levels differ substantially in the line forming part of the LOS. Figure 6.18 show the difference between the vibrational temperatures calculated in the 3D case and those in the 1D case at each point along the LOSs. LOS paths "enter" the image on the top right and "exit" on the top left. Left panel shows the differences for the ν_3 level of CH_4: in the first part of the LOS the level is more excited in the 3D case than assumed in the 1D case, while it is much less excited in the second part. Peak differences are observed at 750-800 km. The right panel of Figure 6.18 shows the vibrational temperature differences for the $\nu_3 + \nu_4$ level. The differences are much smaller in this case and significant only around 600 km. This is due to the fact that the hot $\nu_3 + \nu_4 \rightarrow \nu_4$ band is optically thin from 600 km upwards and the absorption of solar radiation does not vary steeply with SZA (see Section 5.2).

Major differences in the simulated emission are expected for the lowest LOS in the test set. The LOS path is shown in Figure 6.19 with a color scale that maps the

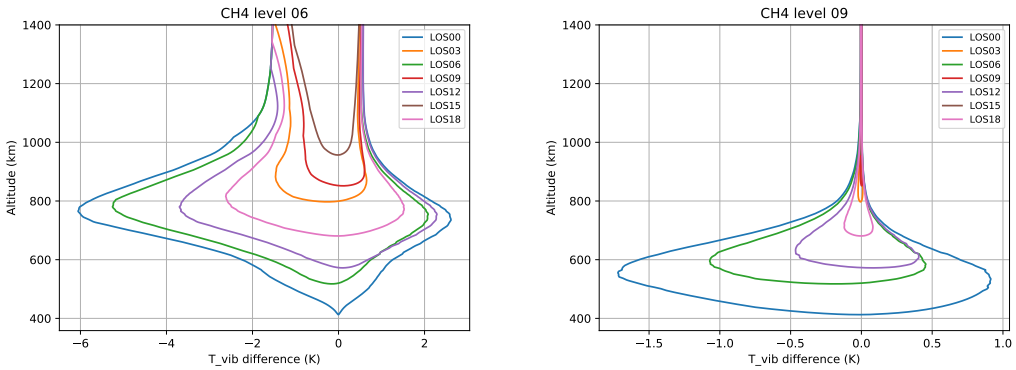

Figure 6.18: Differences of vibrational temperature for the case with and without SZA variation along the line of sight for CH_4 level ν_3 and $\nu_3 + \nu_4$ along a test set of LOSs.

steps done by the radiative transfer routine to the point along the path. A study of the line formation for a line in band $\nu_3 \rightarrow 0$ and a line in the band $\nu_3 + \nu_4 \rightarrow \nu_3$ has been performed, the results are shown respectively in Figures 6.20 and 6.21. The left panels show the intensity at a given step of the radtran routine, indicated in a color scale as a fraction of the total number of steps. The right panels show instead the increments in the line intensities at each step with respect to the previous one in logarithmic scale. For band $\nu_3 \rightarrow 0$ the line core is formed soon saturating at about 25% of the los path, corresponding to an altitude of about 750-800 km. The remaining part of the LOS changes just the sides of the line shape and the wings. Small contributions come from the tangent point - about two orders of magnitude smaller than the top value - and almost none from the second part of the LOS (3 to 4 orders of magnitude smaller). For the hot band $\nu_3 + \nu_4 \rightarrow \nu_4$ instead all the LOS contributes in a quasi-symmetric way and the main contribution - at least one order of magnitude larger - comes from the part of the LOS closest to the tangent point. These are the typical behaviours of an optically thick and optically thin regime respectively. The main changes from the 3D to the 1D case are then expected for the thick $\nu_3 \rightarrow 0$ band, whose line forming region is situated quite far from the tangent point.

6.3.2 Inversion test of 3D SZA bias

The inversion of CH_4, HCN and C_2H_2 has been run for two extreme test cases:

- a set of LOS at SZA between 80° and 90°, for which the effects of the 3D SZA bias were expected to be significant;

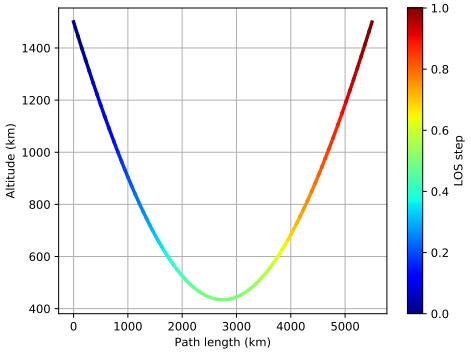

Figure 6.19: Image showing the path of the LOS at 434 km used as test case for the line formation. The color of each segment of the line gives information on the altitude at which the lines shown in Figures 6.20 and 6.21 are formed.

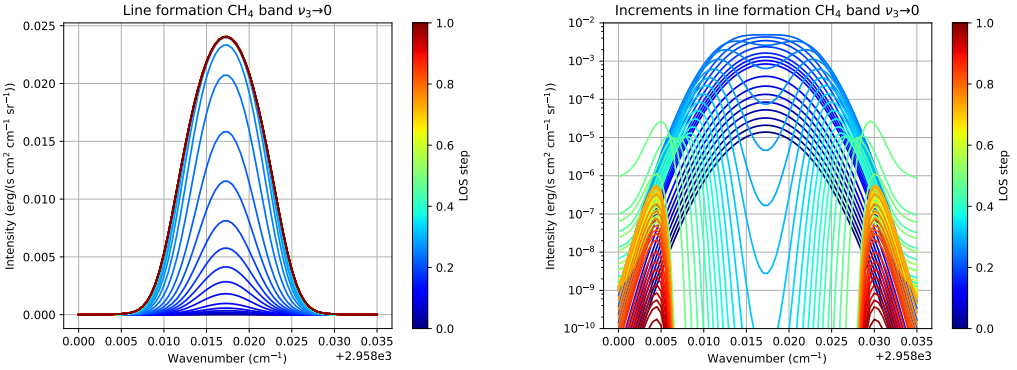

Figure 6.20: Line formation for a line of CH_4 band $\nu_3 \rightarrow 0$ along the test LOS at 434 km. Left panel: line intensity at different steps along the LOS. Right panel: increments in the line intensity at different steps.

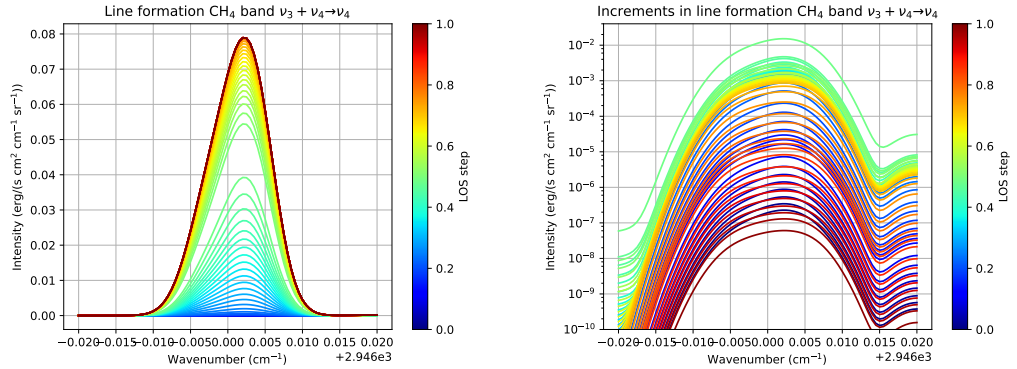

Figure 6.21: Line formation for a line of CH_4 band $\nu_3 + \nu_4 \rightarrow \nu_3$ along the test LOS at 434 km. Left panel: line intensity at different steps along the LOS. Right panel: increments in the line intensity at different steps.

- a set of LOS at SZA around 30°, for which only minor changes are expected.

The set of measurements considered belong to VIMS cube V1536397418 in year 2006, which is one of the cubes used in the analysis in Section 5.4. The phase angle of the cube is 63°, meaning that the SZA decreases in the 3D case moving from the tangent point towards the spacecraft.

Three cases have been considered for both set of LOSs:

- inversion of the measurements assuming no variation of SZA in the forward model, resembling the 1D case (*no sza var* in the panels below);
- inversion considering the real variation of SZA in the forward model (*sza var* in the panels below);
- inversion considering the variation of SZA but using the LOS in the inverse direction, simulating the case of complementary phase angle (*inverse los* in the panels below).

Simulated emission

A comparison of the spectra simulated for tangent SZA = 80° and the three cases of sza variation, no sza variation and inverse LOS is shown in Figure 6.22. The scheme of the panels in the figure is as follows: panels in the first row show the simulated emission in the fundamental $\nu_3 \rightarrow 0$ band, the second row refers to $\nu_3 + \nu_4 \rightarrow \nu_4$ band and the third to the overall CH_4 spectrum; the three columns refer to the three LOSs closer to 400, 600 and 800 km tangent altitude respectively. Figure 6.23 show the same comparison for the SZA = 30° case.

As expected, main differences are seen in the SZA = 80° case and for the thick $\nu_3 \rightarrow 0$ band. Differences are larger for the lowest tangent altitudes, since the signal in this case is formed further from the tangent point, as discussed in Section 6.3.1. The differences are much smaller for the optically thin $\nu_3+\nu_4 \rightarrow \nu_4$ band, which gives the major contribution to the overall CH_4 spectrum below 700 km. The simulations made in the *no sza var* configuration correspond to the approximation made within the GBB of assuming the tangent SZA for all the points in the LOS. Depending on the actual orientation of the LOS with respect to the Sun, the simulation considering the variation of the SZA along the LOS may fall in the *sza var* case (phase angle = 63°, corresponding to the real observations) or in the *inverse LOS* case (phase angle = 117°).

The difference between the blue and green lines shows the maximum potential error when not considering the correct orientation of the LOS with respect to the Sun.

The SZA = 30° case shows only minor differences and is shown for comparison.

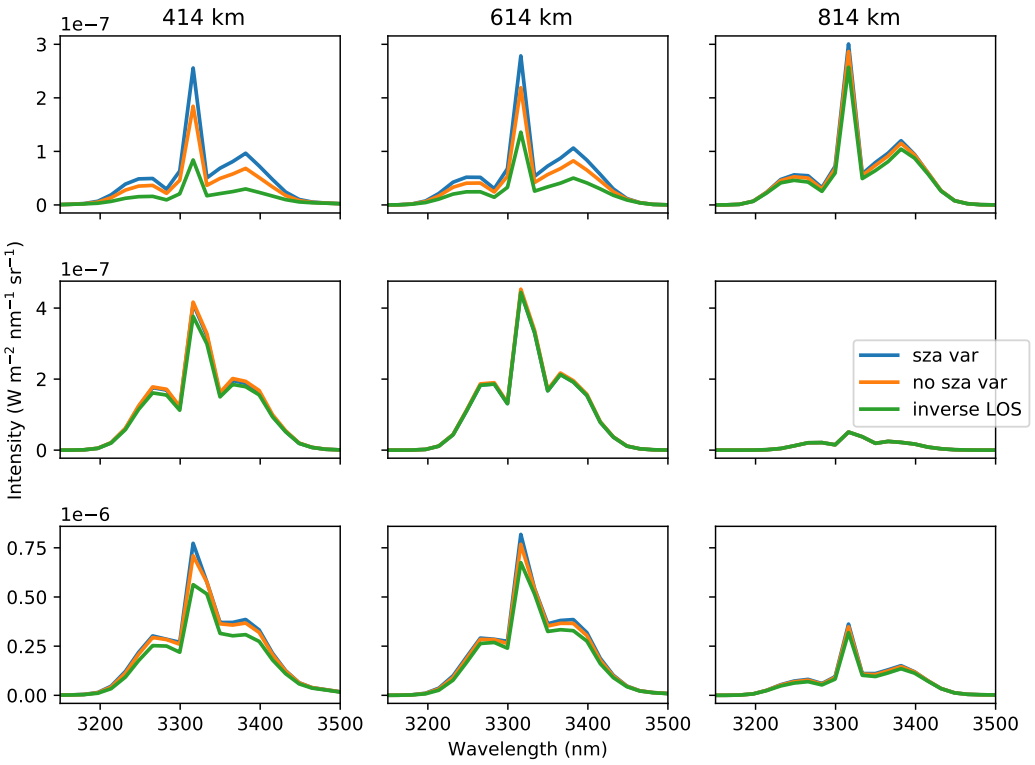

Figure 6.22: Simulated spectra for tangent SZA = 80, and the three cases: sza variation along the LOS (blue line), no sza variation along the LOS (orange line) and LOS seen from the opposite direction (green line). Legend of the panels. Columns: LOS at 399, 599 and 799 km respectively. Rows: $\nu_3 \rightarrow 0$ band (first), $\nu_3 + \nu_4 \rightarrow \nu_4$ band (second) and overall CH_4 emission (third).

Results

Figures 6.24 show the results for the case at SZA = 30° (left column) and SZA = 80° (right column). For the SZA = 30° case, almost no variation is seen in the HCN and C_2H_2 retrievals. For the CH_4 retrieval the *sza var* and *no sza var* cases show no significant variations, while the *inverse LOS* case does show a significant difference at least at 750 km, where a larger VMR is retrieved due to the smaller excitation in the first part of the LOS. The SZA = 80° case is more interesting. Differences are seen for HCN and C_2H_2 but are generally small and inside the retrieval errors. The CH_4 retrieval shows instead a significant variation at 850 km: for the true

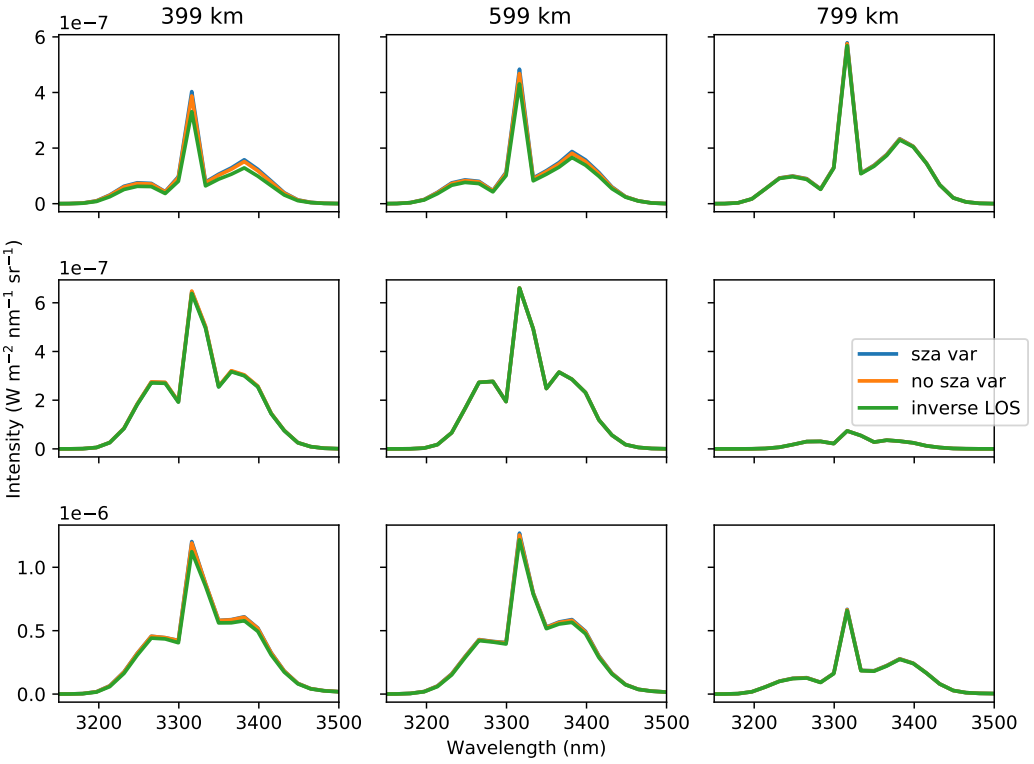

Figure 6.23: Same as Figure 6.22, for SZA = 30.

LOSs (*sza var*) a smaller VMR is retrieved, since the first part of the LOS is more excited with varying SZA; for the inverse LOSs (*inverse los*) a significantly larger VMR is retrieved instead. Although this test has been done on a single set of measurements, the observed changes go in the direction of explaining the observed correlation between CH_4 VMR and SZA observed at high altitudes in Section 5.5, whilst no correlation is seen at lower altitudes. An important point to be considered is that all observations analyzed in Section 5.4 were obtained at phase angles lower than 90°, thus the VMR retrieved under the tangent SZA approximation always overestimated the actual abundance at high altitudes for large SZA.

6.4 Conclusions

SpectRobot, a new code for radiative transfer modeling and inversion of atmospheric quantities has been developed. Written mostly in Python and partly in Fortran, SpectRobot is composed of a set of classes useful for further calculation, statistical analysis and visualization of the results. The ray tracing works in 3D geometry and takes into account the actual position of the Sun with respect to the line of

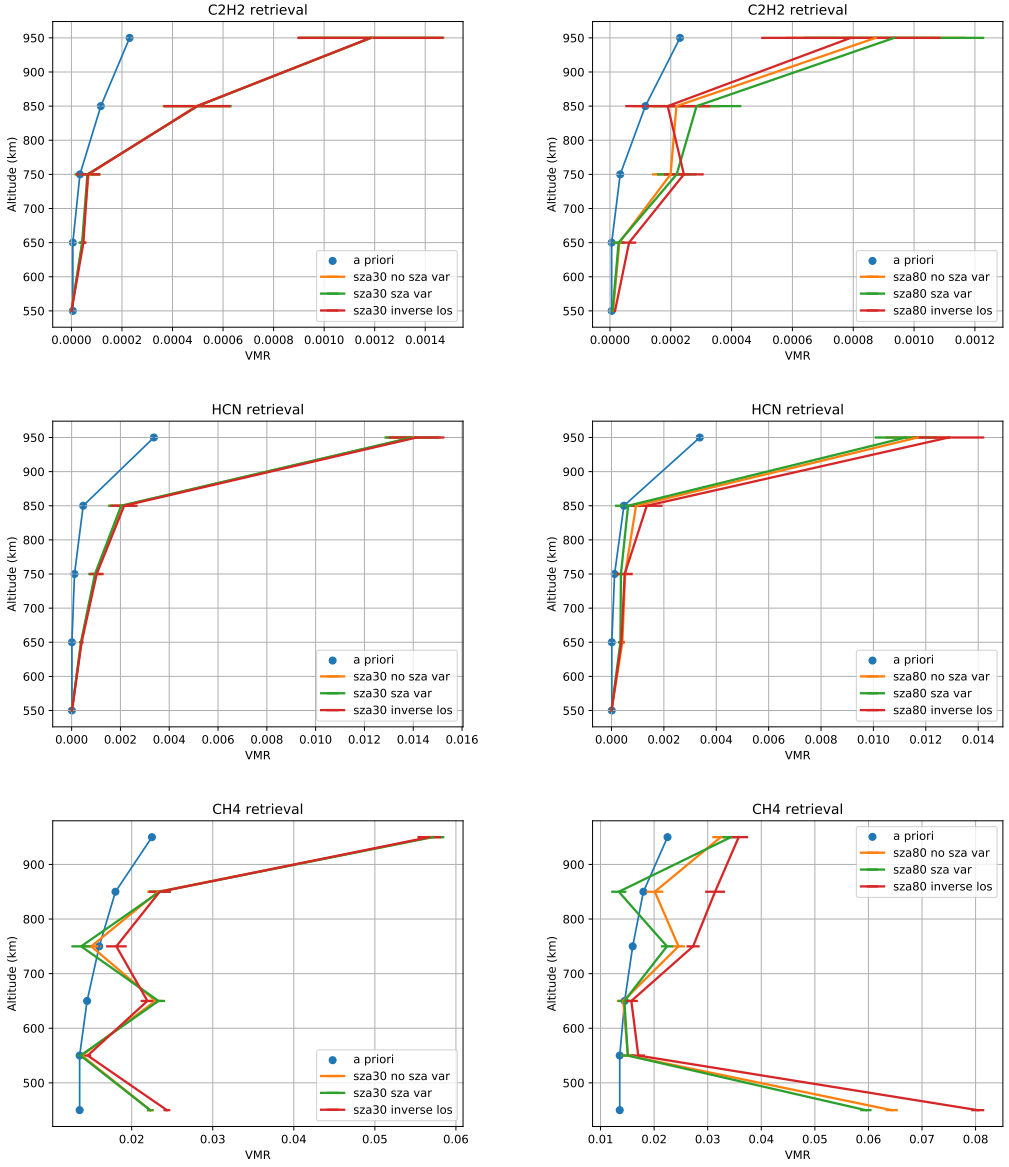

Figure 6.24: Results of the tests on the 3D sza variation. Left panels: SZA = 30°. Right panels: SZA = 80°.

sight. The radiative transfer core is a line-by-line code that can accept as input vibrational temperatures for non-LTE simulations; calculation of LUTs has been implemented both for the LTE and non-LTE case. The inversion routine exploits a bayesian inversion with optimal estimation technique, using Levenberg-Marquardt numerical procedure. The inversion parameters are flexible objects, that can be easily generalized to more complex, problem-specific configurations.

The forward model and the inversion module of SpectRobot have been validated by comparison with the GBB code. The code has then been used to quantify the error made in the inversion of CH_4, HCN and C_2H_2 abundances from VIMS measurements of non-LTE emission in Titan's atmosphere. The simulations show a significant difference for the thick $\nu_3 \rightarrow 0$ band of CH_4, especially at the lowest altitudes, while no significant difference is seen for the thin $\nu_3 + \nu_4 \rightarrow \nu_4$ band. In the test case, the error of the retrieved VMR is found to be significant for CH_4 at least at large SZA (80°) at 750 and 850 km. The variation observed in the retrieved VMR goes in the right direction to explain the observed bias in the retrieved CH_4 VMR at the highest altitudes for large SZA discussed in Section 5.5. A new analysis of the measurements in Chapter 5 is going on and is performed with SpectRobot.

Another possible application for the code developed is discussed briefly at the end of Chapter 8 and aims to the 3D inversion of H_3^+abundance in Jupiter auroras.

Part II

Jupiter's aurorae

Chapter 7

Introduction: Jupiter and its magnetosphere

Jupiter is the largest planet in the solar system and orbits the Sun at an average distance of 5.2 AU. Its mass is about one thousandth of the Sun's mass and larger than all the other planets together. Jupiter's mean radius is 71492 km (R_J), about one tenth that of the Sun. The planet rotates very fast, with a period of about 10 hours, and it's rotation axis is almost perfectly aligned with the normal to the ecliptic, with an inclination of 3°.

Jupiter is made mainly by hydrogen and helium, but a large uncertainty exists about its heavier components, which may constitute between 3 and 13% of its mass. The actual fraction of heavy components could distinguish between different scenarios of solar system formation and is currently one of the main questions regarding the planet. Jupiter's atmospheric composition is better known and is made up mainly by molecular hydrogen (~ 0.86 in volume) and helium (~ 0.136), with trace amounts of CH_4 (2×10^{-3}), NH_3 (7×10^{-4}) and H_2O (5×10^{-4}). Other constituents are found in concentrations of the order of 10^{-7} and less [Taylor et al., 2004; Bagenal et al., 2006].

Jupiter has always attracted attention for its atmospheric dynamics characterized by fast and very stable alternating jet streams and clearly observable cyclones and anticyclones, the most famous of which is the Great Red Spot, that has been known for centuries.

7.1 Jupiter's magnetosphere

Jupiter's magnetic field is the strongest in the solar system and has a dipole moment about 20 thousand times that of the Earth's. The field is generated by currents in the outer core of the planet, composed by liquid metallic hydrogen.

The outer atmospheric layer of the sun, the solar corona, expands in the interplanetary space, filling it with a magnetized hot and low density plasma called the solar wind. The solar wind plasma travels at supersonic speeds relative to the sun, reaching the outer edge of the solar system. The magnetic field is said to be frozen in the plasma flow because we are in the approximation of ideal Magnetohydrodynamics (MHD); the ideal Ohm's law $\boldsymbol{E} + \boldsymbol{v} \times \boldsymbol{B} = 0$, which descends from the limit of infinite conductivity $\sigma \to \infty$, implies that the flux of the magnetic field through a material path is conserved and so the magnetic field lines are in some sense moving with the fluid. This characteristic of the magnetized plasma gives rise to a particular configuration for the interplanetary magnetic field, the so called Parker spiral. The sun rotates with a period of about 25 days and the roots of the magnetic field lines are connected to the sun, but the magnetic field is then embedded in the radially outflowing solar wind, so that the lines have to bend in a spiral.

Jupiter's magnetic field - as for all magnetized planets - spreads into the interplanetary space, giving rise to a region called the magnetosphere that screens the planet from the solar wind plasma flow. Figure 7.1 shows the configuration of Jupiter's magnetosphere.

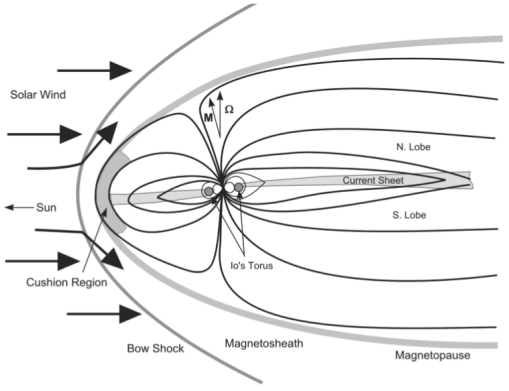

Figure 7.1: Sketch of the configuration of Jupiter's magnetosphere. After Khurana et al. [2004].

The magnetosphere is defined as the region inside which the motion of a charged particle is governed by the planetary magnetic field; seen in a large perspective, it is like a bubble in the solar wind, with a long tail in the direction opposite to the sun.

A bow shock is formed in the Sun's direction: after the shock, the supersonic flow of the plasma is converted in a subsonic flow and the plasma is heated up and compressed. The shocked gas flows around the magnetosphere in a region called the magnetosheath. Therefore it is not directly the solar wind plasma which constitutes the boundary of the magnetosphere but the strongly heated and compressed plasma behind the bow shock. The boundary between the plasma in the magnetosheath and the actual magnetosphere is called the magnetopause. It is a closed curved surface in the direction of the sun, because of the compression performed by the solar wind, and has a long tail in the opposite direction, that extends for many planetary radii.

Jupiter's magnetosphere is huge, reaching a distance of 50 to 100 planetary radii in the Sun's direction. Unlike the Earth's magnetosphere, which is driven by the solar wind, Jupiter's magnetosphere gains its energy from the planetary rotation itself and most of the plasma from the satellite Io.

7.2 The engine of Jupiter's aurora

The most evident manifestation of magnetospheric phenomena are Jupiter's aurorae, which light up the polar regions of the planet in the UV and IR images. Both the UV and IR emission patterns, shown in Figure 7.2, are characterized by a main emission feature, which is remarkably stable in position and rotates with the planet, called the *main oval* [Radioti et al., 2013; Mauk and Bagenal, 2013; Grodent, 2003; Clarke et al., 2004; Clarke, 2012].

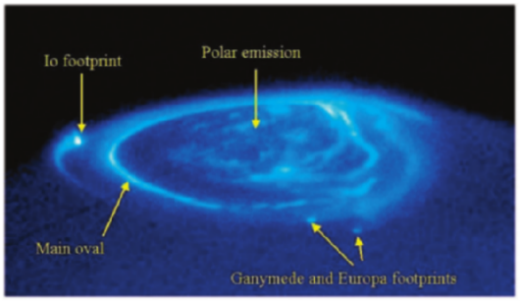

Figure 7.2: UV image of Jupiter northern aurora taken by Hubble Space Telescope. The main oval, the polar emission and the satellite footprints are indicated. After Clarke et al. [2004].

The main oval is the signature of a system of Birkeland-like magnetospheric currents. The current circuit connects a middle magnetosphere region of the equatorial plasma sheet (at about 30 R_J) with the polar ionosphere, then flows equatorward in

the ionosphere and closes again in the equatorial plasma sheet at a distance of about 20-25 R_J. A sketch of the circuit is shown in Figures 7.3: the left panel shows the result obtained with a simple dipole model of the magnetic field [Hill, 1979, 2001]; the right panel is a more realistic empirical model [Cowley and Bunce, 2001].

The currents that link Jupiter atmosphere to the equatorial plasma sheet in the magnetosphere follow the magnetic field lines. Hence a mapping exists between the observed auroral phenomena and the equatorial plasma sheet in the magnetosphere: the closer to the pole the current is situated, the further it links to the equatorial plasma sheet. The peak upward current in the ionosphere drives the precipitation of energetic electrons that are responsible for the main oval emission. The main oval is situated at about 74° magnetic latitude and maps to the middle magnetosphere Cowley and Bunce [2001].

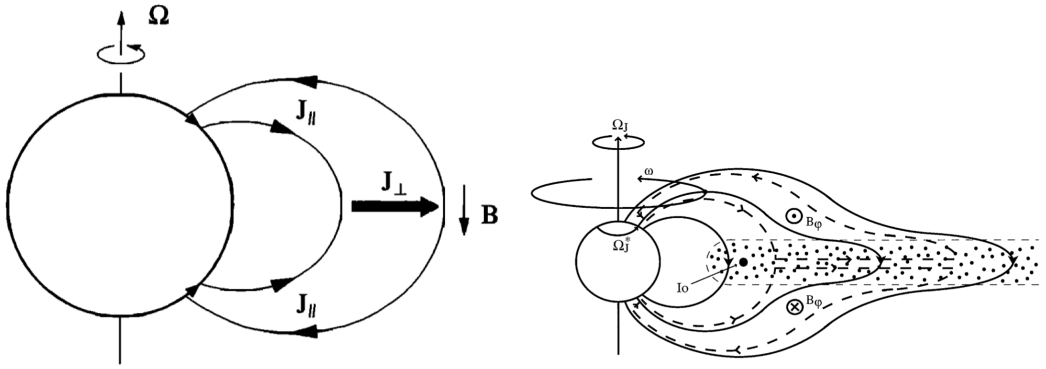

Figure 7.3: Sketch of the configuration of Jupiter's Birkeland current system in Hill's dipole model (left, after Hill [2001]) and an empirical model by Cowley et al. (right, after Cowley and Bunce [2001]).

Apart from the stable main oval, bright auroral emissions are seen at the magnetic footprints of the jovian satellites, that are situated equatorward of the main oval since they map to the satellite positions. Io's is the brightest footprint. Inside the oval, in the polar cap, a diffuse and highly variable emission is seen. The polar region is also the set of strong polar flares [Grodent, 2003; Bonfond et al., 2016], often accompanied by X-ray emission [Gladstone et al., 2002; Elsner, 2005].

The energetic electrons drive dissociation and ionization of H_2 in the upper atmosphere, which are responsible for the UV emissions. The H_2^+ molecules so produced may experience dissociative recombination in the collision with an ambient electron or react with a neutral H_2 molecule to produce H_3^+ [Miller et al., 2000, 2013].

$$\begin{aligned} H_2 + e^- &\rightarrow H_2^+ + 2e^- \\ H_2^+ + H_2 &\rightarrow H_3^+ + H \end{aligned} \tag{7.1}$$

H_3^+ is then destroyed in dissociative recombination with an ambient electron (in the upper atmosphere) or in reaction with CH_4, C_2H_2 or other hydrocarbons in the lower atmosphere.

$$\begin{aligned} H_3^+ + e^- &\rightarrow H_2 + H\ (3H) \\ H_3^+ + CH_4 &\rightarrow CH_5^+ + H_2 \end{aligned} \tag{7.2}$$

The typical lifetime for H_3^+ is estimated to be between 4 and 40 s in Jupiter's upper atmosphere considering model estimates of the electron density [Radioti et al., 2013]. H_3^+ is expected to be close to photochemical equilibrium in this region of the atmosphere and it's therefore a great tracer for electron precipitation in Jupiter's auroras [Connerney and Satoh, 2000; Satoh and Connerney, 1999; Stallard et al., 2015; Altieri et al., 2016].

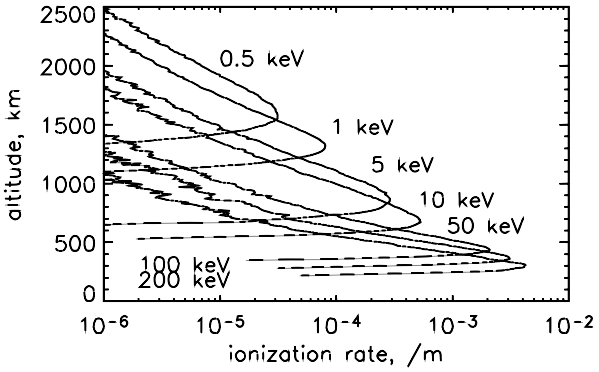

Figure 7.4: Ionization rate per electron in function of the electron energy in the model of Hiraki and Tao [2008].

Figure 7.4 shows the ionization rate per electron in function of the initial energy, in the model by Hiraki and Tao [2008]. The energy of the incoming electrons determines the altitude of the peak ionization in the auroral atmosphere and then the shape of the H_3^+ abundance profile [Tao et al., 2012].

H_3^+ is a strong IR emitter in the 3-5 μm region and is of primary importance for the cooling of Jupiter's upper atmosphere [Miller et al., 2013]. Since the peak emission of H_3^+ is situated above the hydrocarbon layer, it is not absorbed by the

abundant CH_4 and can be observed. Moreover, in the 3-4 μm region the solar radiation reflected by the lower atmospheric layers is absorbed by the CH_4 before reaching the upper atmosphere, thus preventing the contamination of the H_3^+ signal.

Chapter 8

H_3^+ and CH_4 abundance in Jupiter's auroral regions

This part of the work focuses on the upper atmosphere in the auroral region of Jupiter. JIRAM measurements analyzed in this Chapter represent a situation of chemical non-equilibrium: the H_3^+ is produced and destroyed in the auroral upper atmosphere in a time span of some tens of seconds and its local density depends both on the energy and flux of precipitating electrons. The composition of the auroral atmosphere is modified by the forcing of particle precipitation, producing a state close to photochemical equilibrium.

The work done on the Jupiter aurora through the analysis of JIRAM measurements has brought to the publication of three articles:

- B.M. Dinelli, F. Fabiano, A. Adriani, F. Altieri and 24 more (2017) - *Preliminary JIRAM results from Juno polar observations: 1. Methodology and analysis applied to the Jovian northern polar region*, Geophysical Research Letters, Wiley Online Library, 2017, 44, 4625-4632;

- A. Adriani, A. Mura, M. Moriconi, B.M. Dinelli, F. Fabiano and 23 more (2017) - *Preliminary JIRAM results from Juno polar observations: 2. Analysis of the Jupiter southern H_3^+ emissions and comparison with the north aurora*, Geophysical Research Letters, Wiley Online Library, 2017, 44, 4633-4640;

- M.L. Moriconi, A. Adriani, B.M. Dinelli, F. Fabiano and 24 more (2017) - *Preliminary JIRAM results from Juno polar observations: 3. Evidence of diffuse methane presence in the Jupiter auroral regions*, Geophysical Research Letters, Wiley Online Library, 2017, 44, 4641-4648.

This chapter follows closely the publications, describing the method used and reporting the main results. My contribution has been focused on the data analysis and on the statistical analysis and visualization of the results.

8.1 Juno and JIRAM

Juno is a scientific space probe to planet Jupiter that was launched in 2011 and reached Jupiter in July 2016. Juno carries instruments to study the planet's composition and atmospheric dynamics, as well as its gravity field, magnetic field, magnetosphere and plasma environment [Bolton, 2010].

JIRAM (Jovian InfraRed Auroral Mapper) is an imager/spectrometer onboard Juno, designed to study Jupiter's aurorae, as well as the planet's atmospheric structure, dynamics and composition [Adriani et al., 2017a]. It is composed of two IR imager channels - the M channel centered at 4.78 μm and the L channel centered at 3.45 μm - and by a spectrometer. The spectrometer sensor consists of a row of 256 pixels, with a total field of view of 3.5°. Each pixel has an instantaneous field of view of 0.25×0.25 mrad. The spectrum is sampled in 336 spectral channels in the 2–5 μm range with a mean spectral resolution of about 9 nm. Since Juno rotates on its axis in a 30 s period, JIRAM is equipped with a despinning mirror that is able to keep a stable pointing on the planet. Due to the rotation, the maximum integration time is 1 s. The geometric information on the measurements is obtained by using ad hoc algorithms based on the NAIF-SPICE tool [Acton, 1996]. JIRAM raw data are radiometrically calibrated as described by Adriani et al. [2017a]. In this work we focus on the spectrometer data in the 3–4 μm range.

8.2 JIRAM measurements from the first Juno orbit around Jupiter

The first JIRAM observations of Jupiter aurorae were acquired on 27 August 2016. Due to the particular polar orbit of Juno, the north aurora was observed first, between 8 and 12 UTC, with the spacecraft getting closer to the planet. The south aurora was then observed during the outbound leg of the orbit, from 15 to 19:45 UTC, when Juno was moving away from Jupiter.

Two typical spectra acquired by Jiram are shown in Figure 8.1, one corresponding to the dayside region and the other to the nightside. The left panel shows the entire

range of the instrument, the right panel is a zoom in the 3-4.5 μm region, where the emission from H_3^+ is clearly identified.

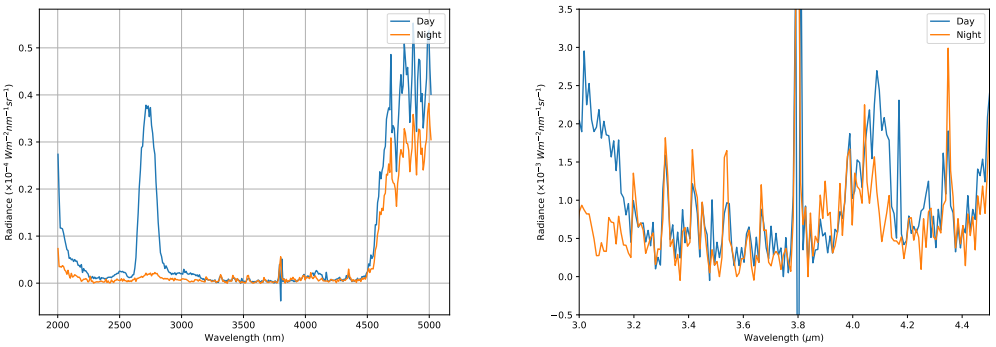

Figure 8.1: Typical spectra acquired by Jiram in the auroral region, for the day and night sides, for the full JIRAM spectral range (left panel) and the 3.0-4.5μm region (right panel).

The region below 3.2μm is affected by solar scattering from deeper layers of the atmosphere and above 4.0μm both solar scattering and thermal emission from the lower atmosphere affect the H_3^+ signal. The apparent feature at 3.8μm is an instrumental effect. In the 3.2-3.8 μm region the signal from the lower atmosphere is absorbed by the abundant CH_4, thus allowing to observe the faint signal from H_3^+, that forms in the upper atmosphere. In the analysis we focused on this spectral region, since the method described in Section 8.3 is not suited to model the more complex features observed at smaller and larger wavelengths (no solar scattering has been included).

8.2.1 Selected measurements for the North and South aurora

During the first Juno orbit, JIRAM acquired more than 100000 spectra when observing the North and South Polar regions of Jupiter. Those spectra were acquired at different times and at different distances with respect to the planet. Both the emission angle and the pixel size at Jupiter span a wide variety of values. Given the limits of the forward model - that simulates a single emission layer (see Section 8.3) - and to properly map the emission on Jupiter disk, only spectra with an emission angle smaller than 75° have been considered in the analysis.

Some of the spectra acquired over the polar regions were affected by strong spikes or showed an H_3^+ signal too weak to produce a reliable retrieval. Given the large

number of measured spectra, an automatic procedure has been designed to perform a pre-filtering of the measurements. The first step of this procedure consists in the identification of the spikes produced by energetic particles on the detector. For each spectrum, we have evaluated the maximum intensity recorded at the wavelengths of the H_3^+ lines. All the spectral points outside the H_3^+ lines whose intensity was larger than 1.5 times the maximum intensity were flagged as spikes and masked out from the retrieval. Spectra with 3 or more spikes were completely discarded. The second step, applied after the spike removal, consists in the identification of spectra where the H_3^+ integrated signal is below the detection limit. All the spectra where the integrated signal in the 3.2-3.8 μm region was below 0.0001 $\mathrm{W\,m^{-2}\,sr^{-1}}$ were discarded.

The final set of measurements that passed the pre-filtering consisted of 14131 spectra for the northern aurora and 32089 for the southern aurora.

Figures 8.2 and 8.3 show some information regarding all the analyzed measurements of the two auroral regions. The measurements are shown in orthographic projection on Jupiter North and South poles, using the planetocentric coordinates of the intercept of the Line Of Sight (LOS) of each measurement with the surface located 500 km above Jupiter 1 bar surface. The choice of the 500 km surface is motivated by the fact that the main emission of H_3^+ is expected from this altitude layer. The color of each dot indicates the value of the represented quantity, while the size of the spot represents the real projection of the instrument FOV on the 500 km surface.

The top left panel in the two Figures shows the emission angle of the measurements, that is the angle made by the LOS with the vertical to the 500 km altitude surface. As can be seen in the figures, the size of the pixel projections tends to increase with larger emission angle. This produces two effects: the first is that with larger emission angle the measurements average over a larger region, hiding finer structures; the second is that at large emission angle the mapping is poor and observed structures may appear shifted with respect to their real position (the vertical structure of the aurora has not been measured yet). The cut-off at 75° was chosen to avoid large errors in the mapping and in the retrieved quantities (see Section 8.4). In some regions measurements at very different emission angles and acquired at different times superimpose. The upper right panels show the solar incidence angle or Solar Zenith Angle (SZA) at the 500 km surface. Measurements of both the dark and illuminated regions are available.

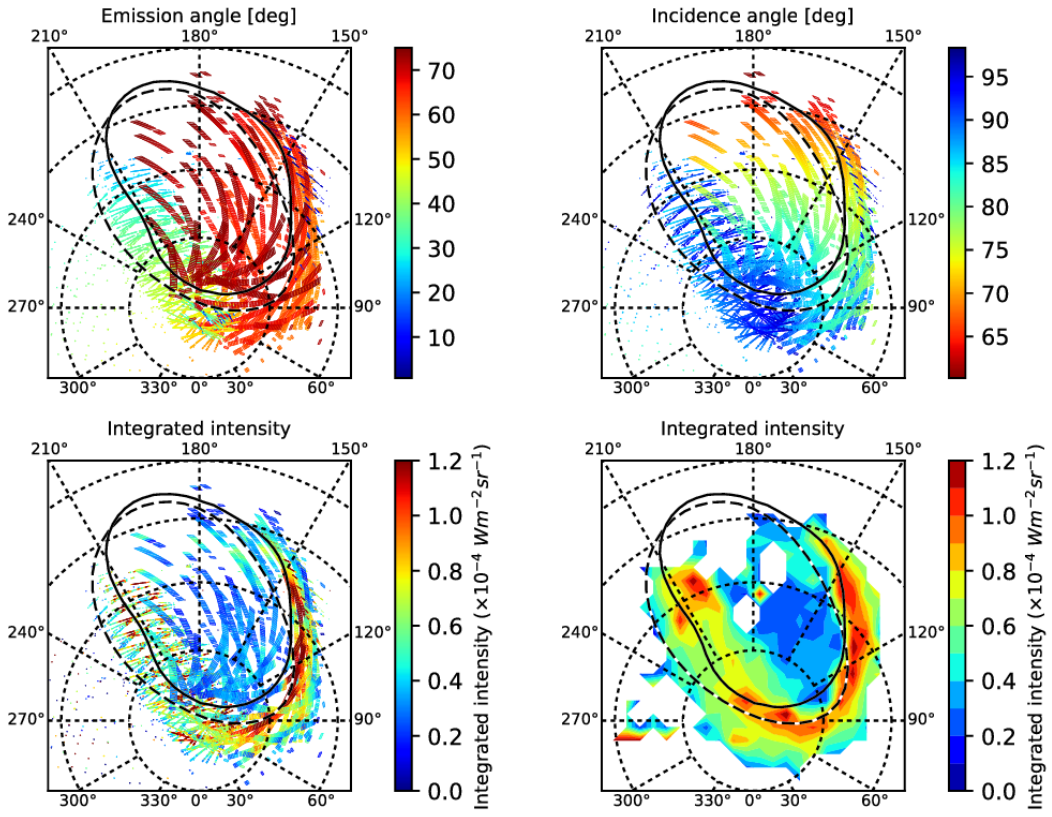

Figure 8.2: Orthographic map of Jupiter North Pole with superimposed spots at the geo-location of JIRAM observations. The longitude is indicated and dashed circles have been drawn every 10° of latitude. The color of each dot indicates the value of the represented quantity, while the size of the spot represents its spatial resolution. The black lines represent the position of the aurora from models (dashed line) and from previous observations (solid line).

Lower left panels show the integrated intensities of the analyzed measurements over the 3.35-3.75 μm spectral region, where most of H_3^+ emission is located and no interferences with other molecules are present. The integrated intensities have been corrected for the slant perspective by multiplying the integral by the cosine of the emission angle. This correction is suited for a plane-parallel atmosphere, thus an error is committed at large emission angles.

The orthographic surface shown in the panels has been divided in squared bins, obtained dividing each axis in regular intervals. The single intensities have been averaged over each bin, and bins containing less than 3 measurements have not been included in the final dataset. The dimension of the bins is different for the two

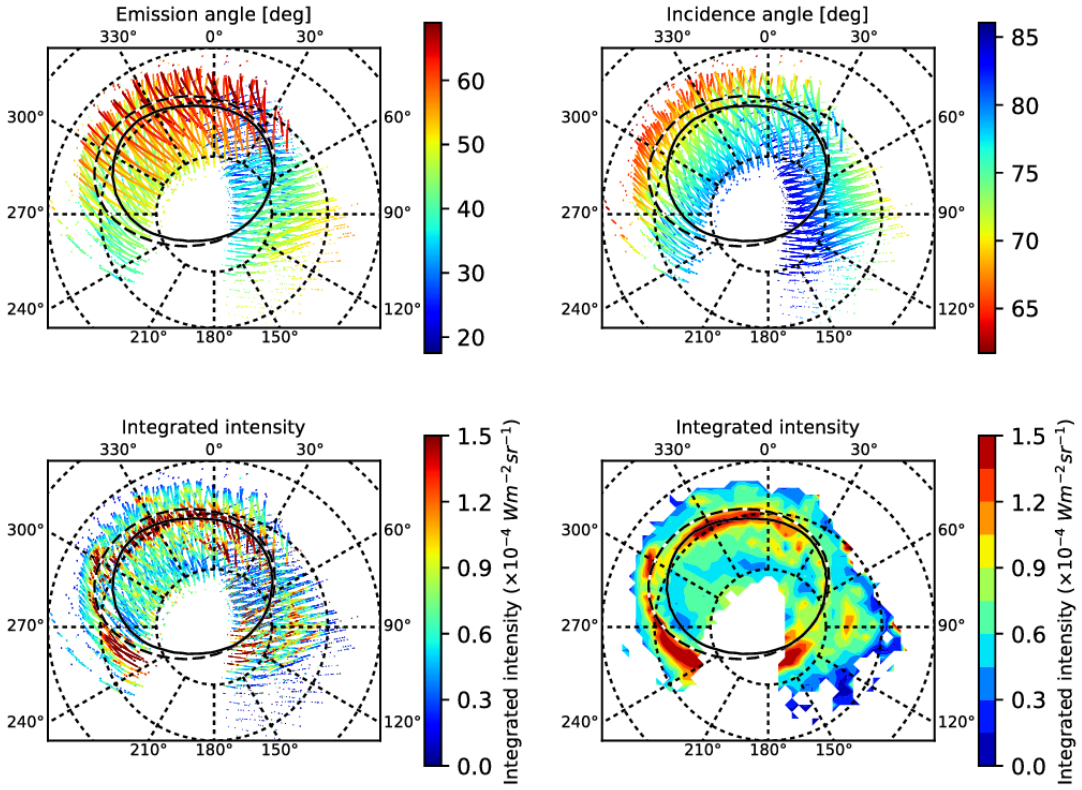

Figure 8.3: Same as Figure 8.2 but for the observations at Jupiter South Pole.

auroral regions, due to the different coverage. The side of the bins is about 2350 km for the North polar maps and 1460 km for the South polar maps, in the projection coordinates.

The lower right panels of Figures 8.2 and 8.3 represent the contour plot of the binned distribution. In all panels, the dashed line represents the geolocation of the aurora oval from existing models [Connerney et al., 1998] and the solid line is the a statistical geolocation of the aurora produced from previous observations [Bagenal et al., 2014].

In the bottom panels of Figures 8.2 and 8.3 we can identify some structures with strong H_3^+ emission that fall close to the auroral ovals.

8.3 Retrieval Code

The code used for the analysis is an update of the code previously developed for the analysis of Galileo/NIMS spectra [Altieri et al., 2016].

The code is divided into two modules, the Forward Model and the Retrieval Module. In order to analyze the large set of measurements acquired by JIRAM individually, the forward model is simpler and faster than the GBB forward model (see Section 1.4). In particular, the forward model makes the following assumptions:

- it assumes that the emission of H_3^+ in the auroral region is optically thin, which has been usually assumed in previous studies based on ground measurements;
- the pressure broadening of the spectral lines is neglected, which is justified by the fact that the linewidth is much smaller than the instrumental resolution and the re-absorption of emitted radiation is not taken into account;
- no atmospheric layering is used, but a single emission layer at an effective temperature T_e.

Moreover, the population of the vibrational levels is assumed to be in LTE or at least in Quasi-Thermal Equilibrium [Miller et al., 1991], meaning that the same temperature can be used to represent all vibrations. This assumption is justified by the fact that most of the auroral emission originates at altitudes where vibrational LTE can be assumed and may produce a maximum error of 5% in the simulated radiance [Melin et al., 2005].

The spectrum is simulated by first computing the intensity of each transition of the gases considered and then convolving the intensity with the instrumental spectral response. Since part of the JIRAM data were acquired on the dayside and show a residual solar signal also in the 3-4 μm region due to scattering from the highest layers in the atmosphere, we have introduced in the FM the possibility to add a radiometric offset to the simulated spectra. The forward model also includes the possibility to evaluate analytically the derivatives of the spectra with respect to temperature and column density of each gas.

The retrieval module is based on a Bayesian approach, that exploits the Gauss-Newton technique, as described in Section 2.3. The parameters that can be retrieved are the column density n_{col} along the instrument LOS and the effective temperature T_e of each considered gas. Moreover, to account for spectral calibration problems, we can also retrieve a wavelength shift, the width of the instrumental response function,

and a radiometric offset. At each iteration, the reduced χ^2 is evaluated and the loop is stopped when two consecutive iterations do not yield values that differ for more than 1% percent.

8.4 Analysis of the measurements from the first Juno orbit

Each spectrum in the final set of measurements described in Section 8.2.1 has been analysed with the retrieval code described in section 8.3. The measurement error has been evaluated computing the variance of a large set of deep space spectra acquired by JIRAM, giving a value of 1.5x10^{-7} W/(m^2 nm sr). Our main targets in the analysis of JIRAM measurements are the effective temperature of H_3^+ and its column density along the LOS of each observation. Since in recent studies Altieri et al. [2016] methane emission has been detected in the auroral region, along with the H_3^+ data we simultaneously retrieved an effective column density of methane along the LOS.

H_3^+ transitions and spectral properties have been downloaded from the web site `http://www.tampa.phys.ucl.ac.uk/ftp/astrodata/H3+/` [Neale et al., 1996] and the partition function has been computed using the expression of Miller et al. [2013]. CH_4 spectroscopic data have been taken from the HITRAN 2012 database [Rothman et al., 2013]. JIRAM instrumental response function is assumed to be a Gaussian function whose width has been evaluated during the on-ground calibration campaign Adriani et al. [2017a].

In the first run we considered the following retrieval parameters with the indicated a-priori errors: H_3^+ effective temperature (a-priori error: 500 K), H_3^+ column density (a-priori error: 2.0×10^{13} cm^{-2}), a wavelength shift (a-priori error: 5 nm) and an offset value (a-priori error: 10^{-3} W m^{-2} μm^{-1} sr^{-1}) for each spectrum. The results of this first run showed high χ^2 and anomalous H_3^+ temperatures on a subset of the measurements, located mainly in a region inside the auroral oval. An analysis of the average spectrum on this subset showed an anomalous high value for the intensity of the H_3^+ line at 3.32 μm in comparison to other H_3^+ lines. Considering that hot CH_4 emission has already been observed in Jupiter auroral region Altieri et al. [2016] and its ν_3 Q-branch lies very close to the position of the 3.32 μm H_3^+ line, we added the methane emission to the simulated spectra.

A second run was then performed including the CH_4 effective column density

among the retrieval parameters. The effective temperature of CH_4 was estimated on the basis of the average observed spectrum of CH_4, as described in Section 8.6, and fixed to a value of 500 K for the analysis on the north aurora and 650 K for the south aurora. For methane the approximations of the forward model described in the previous chapter may not hold, therefore the retrieved CH_4 column density is just a proxy for the abundance of CH_4 and should not be considered as a quantitative estimate.

Since the wavelength calibration of the measured spectra is expected to be dependent only from the position of the pixel on the spectrometer slit, we used the retrieved wavelength shifts of this second run to fit a second order polynomial function to the set of retrieved wavelength shift versus position of the pixel on the slit. The nominal analysis was then performed keeping fixed the new wavelengths calculated in this way. The final set of inversion parameters is then composed by H_3^+ column density, H_3^+ temperature, CH_4 column density and offset.

8.5 H_3^+ column density and effective temperature

Among the results obtained with the procedure described above, many showed a bad fit of the observed spectrum due to anomalous spikes on the H_3^+ lines or just because of the low signal from H_3^+. So the final results were further filtered keeping only the retrievals for which the final χ-test was smaller than 20 and the retrieved H_3^+ temperature had a retrieval error lower than 100 K. This filter was chosen in order to exclude from the final results the retrievals that were poorly representing the measurements or contained small information. Figure 8.4 shows a scatter plot of the individual retrieved H_3^+ temperatures and column densities for the South aurora, with the temperature retrieval error shown in color scale and the effect of the cut. The cut operates primarily on measurements with small H_3^+ column densities. The choice of the cut on the temperature error was made because, even if the column density maps were not so affected by retrievals with low information (that just indicate low H_3^+ abundance), the corresponding temperature maps were strongly affected by bad temperature retrievals, often induced by low H_3^+ abundance.

The final number of retrievals kept for the analysis is 13198 for the North aurora and 23064 for the South.

As it can be seen in the upper left panels of Figures 8.2 and 8.3, the emission angle of the analyzed observations spans a wide range of values. The retrieved H_3^+

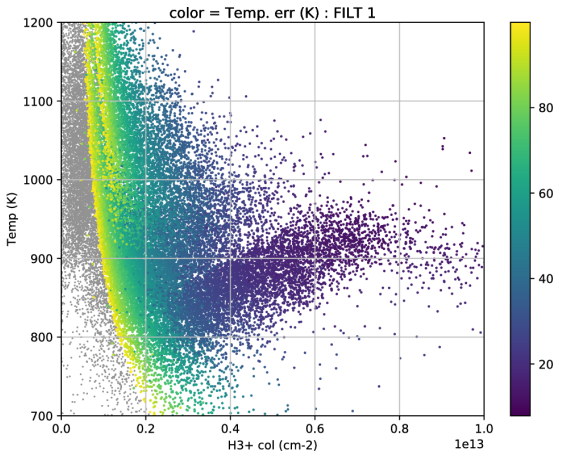

Figure 8.4: Scatter plot of the individual results obtained for the South aurora, showing H_3^+ column density (x axis) vs H_3^+ temperature (y axis) and retrieval error on temperature (color scale). The effect of the cut operated for the final results is shown, only the colored points were retained.

column density are affected by the different viewing geometry and by the effective length of the optical path. We assumed that, in first approximation, the vertical columns are obtained multiplying the slant columns by the cosine of the emission angle. Figures 8.5 show the results of the individual retrievals of H_3^+ column density for the North and South aurora (respectively in the left and right panel), corrected for the emission angle.

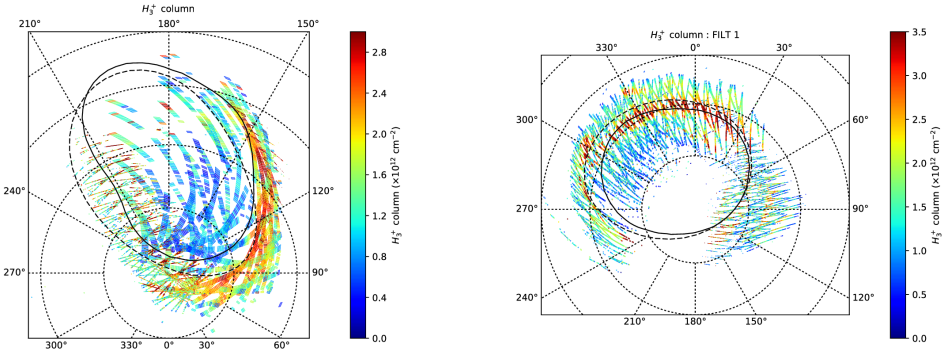

Figure 8.5: Results of H_3^+ column density for the North (left panel) and South (right panel) auroras. The column density have been corrected for the emission angle.

The corrected H_3^+ columns have values up to $2.8 \times 10^{12}\,\mathrm{cm}^{-2}$ for the North aurora and $3.5 \times 10^{12}\,\mathrm{cm}^{-2}$ for the South and show regions of evident structures close to the auroral ovals. One of the most striking features observed is the presence of very fine structures evidenced by the measurements with better spatial resolution - seen

in the region around 210° longitude for the North aurora and 60° and 150° for the South.

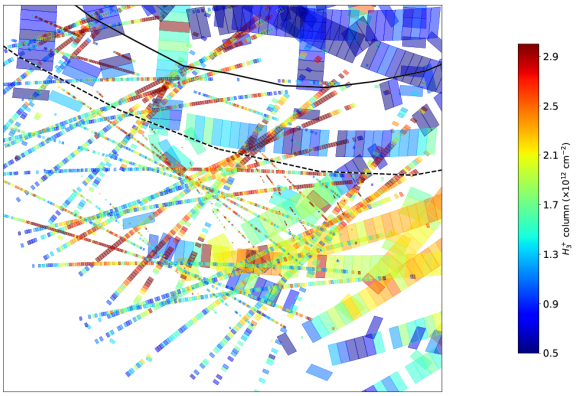

Figure 8.6: Zoom on the geographic North pole, from the left panel of Figure 8.5.

Furthermore, certain regions show both temporal and spatial variability. Figure 8.6 shows a zoom on the region of the aurora closer to the geographic North pole, at latitudes larger than 85°. As can be seen there is large variability both between adjacent pixels and between pixels mapping to the same geo-location but taken at different times (evidenced by the size of the projections).

8.5.1 H_3^+ column density and temperature maps for the North aurora

The picture given by the results is very complex and it appears that they cannot be explained through a simple model. However, in order to identify patterns and regularities in the results, we have divided the area in the orthographic projections of Figures 8.5 into bins and we have averaged all the retrieval results and their errors inside the bins (see also Section 8.2.1). The results for the North aurora, shown as contour plots of the average bin quantities, are reported in Figures 8.7 for the column densities and in Figure 8.8 for the temperatures.

The left panel of Figure 8.7 shows that the peak of H_3^+ column densities lays in part above the model oval (dashed line) and in part closer to the statistical oval (solid line). On average, the retrieval error on the column densities is below 30% (right panel). The left panel of Figure 8.8 shows that in general the highest temperatures are located on the left side of the auroral oval. The highest errors on T are located

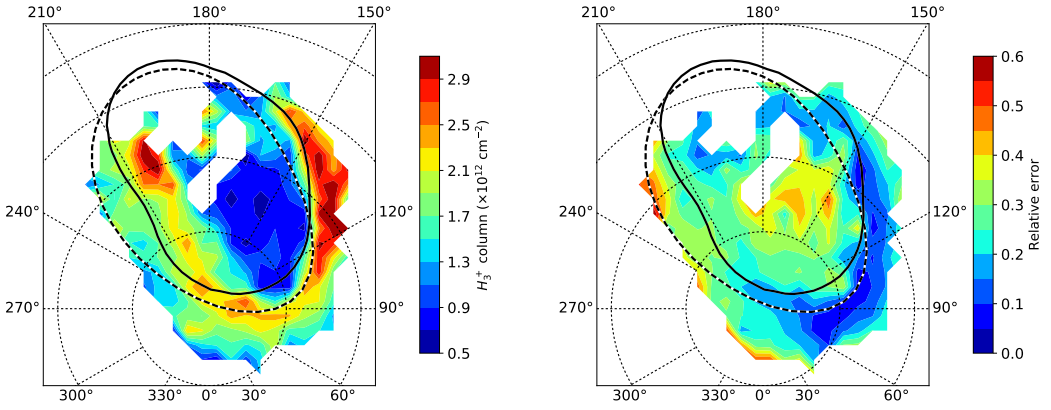

Figure 8.7: Map of the average retrieved H_3^+ column density for the North aurora (left panel) and of the relative retrieval error (right panel).

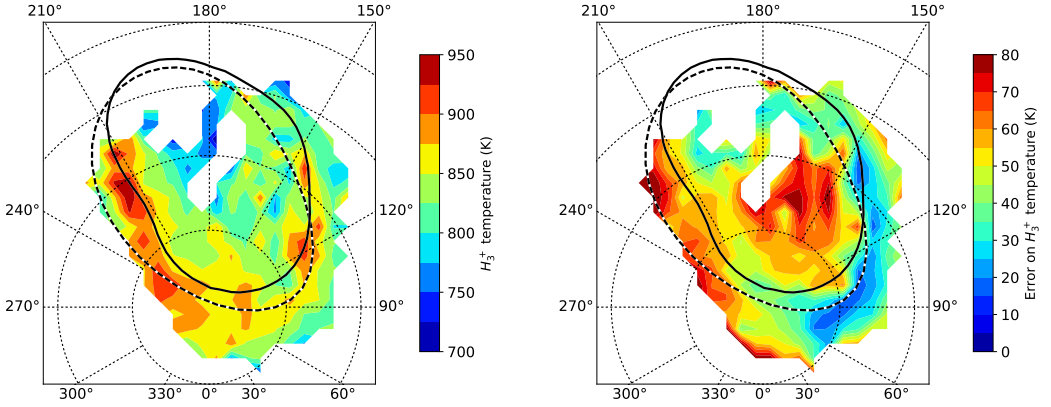

Figure 8.8: Map of the average retrieved H_3^+ temperature for the North aurora (left panel) and of the retrieval error (right panel).

in the region inside the auroral oval and in general where the H_3^+ signal is lower (right panel).

Comparing the left panels of Figure 8.7 and 8.8 we have identified 3 regions of interest, highlighted in Fig. 8.9:

A: Longitudes from 200° to 240° and latitudes from 90° to 65°N. This region of the main auroral oval is characterized by high column densities inside (poleward of) the statistical oval with a peak in the longitude range from 200° to 210°and 67°N in latitude. The corresponding temperature is about 850 K on average. However, higher values for the temperatures are retrieved equatorward, in the region located between the model and the statistical oval. The morphological

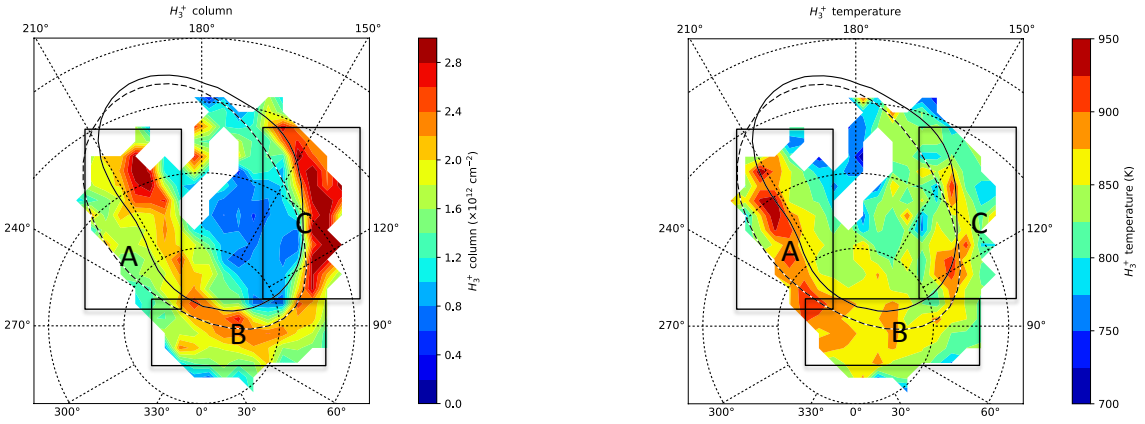

Figure 8.9: Comparison of the distribution of H_3^+ column densities (left panel) and temperature (right panel).

analysis in Mura et al. [2017] made using the imager channel of JIRAM (3.3-3.6 μm) shows that this is a region of broad emission with thin coherent features (arcs) that are visible from the main oval to 10 degrees inward.

B: Longitudes from 60° to 95°, latitudes from 90° to 75° N. On the oval arc crossing the pole, H_3^+ column densities show variation between 2 and 2.6x10^{12} cm^{-2}, with a peak on the North Pole. Temperature shows values between 800 and 850 K, with a peak eastward the North Pole of about 900 K.

C: Longitudes from 90° to 160°, latitudes from 80° to 60° N. In this region higher column densities (larger than 2.6x10^{12} cm^{-2}) are retrieved external to the statistical oval. Temperatures show high variability between 800 and 950 K, with peaks on the statistical oval. Moreover this side of the oval appears narrower than the other side. The shape of the auroral oval in this region, as seen also in the images reported by Mura et al. [2017], appears extremely sharp.

H_3^+ plays a fundamental role in the cooling of the upper atmosphere of Jupiter. A thermostat mechanism might be into play, with larger H_3^+ abundances leading to fast cooling of the atmosphere and then to lower temperatures. However, this mechanism is complicated by the concurrent heating due to the particle precipitation. The apparent anti-correlation seen for H_3^+ column densities and temperatures in the maps might suggest that this mechanism does effectively play a role in the northern aurora.

The correlation plot of the individual retrieved H_3^+ column densities (corrected) and temperature is shown in Figure 8.10. The retrieved temperatures at small column densities show a large spread, reaching up to 1100 K; the larger columns show instead a systematical lack of temperature values larger than 900 K. However, as shown by the color scale, the retrieval error on temperature is systematically larger for the high temperatures and the real situation might be more complex.

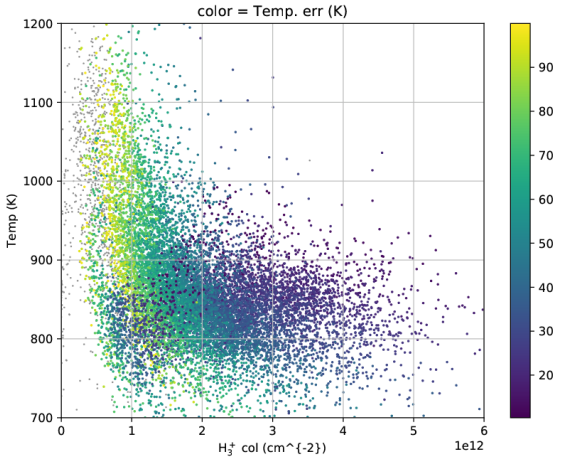

Figure 8.10: Scatter plot of the individual results obtained for the North aurora, showing corrected H_3^+ column density (x axis) vs H_3^+ temperature (y axis) and retrieval error on temperature (color scale).

8.5.2 H_3^+ column density and temperature maps for the South aurora

The study of Jupiter's South aurora through ground-based measurements has been challenging because of the very slant perspective and different morphology with respect to the North. Indeed the South auroral oval is found closer to the pole and not tilted towards one side like the North oval. JIRAM has a very favorable orientation to study the South aurora. The retrieved H_3^+ column density and temperature maps for the South aurora are reported in Figure 8.11 and 8.12 respectively.

The retrieved column densities in Figure 8.11 show a pattern of larger values that lies close to or inside the model oval (solid) between 310° and 30° longitude, and closer to or outside the statistical oval (dashed) for the remaining part. The section of the oval between 320° and 30° longitude shows average values constantly close to $3{\times}10^{12}\,\mathrm{cm}^{-2}$ or larger, while for the remaining part such large values are

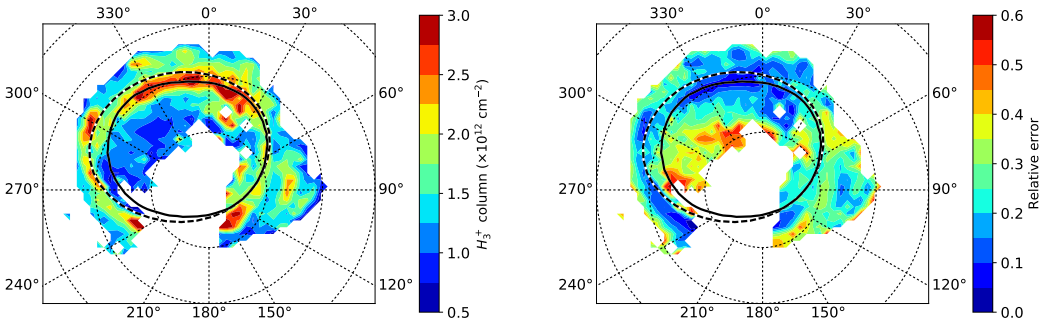

Figure 8.11: Map of the average retrieved H_3^+ column density for the South aurora (left panel) and of the relative retrieval error (right panel).

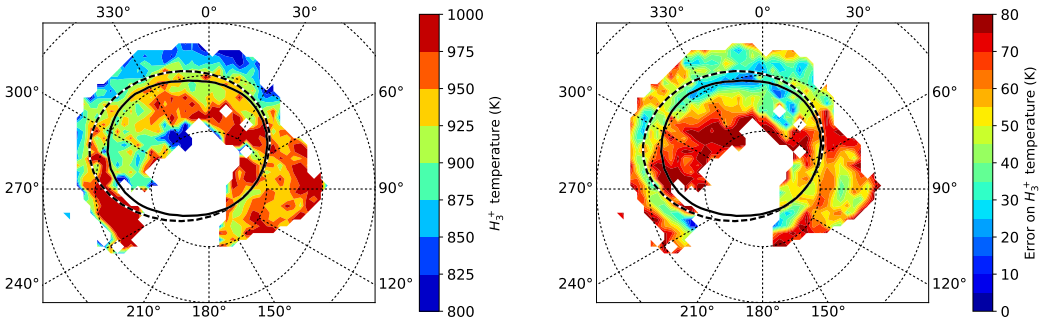

Figure 8.12: Map of the average retrieved H_3^+ temperature for the North aurora (left panel) and of the retrieval error (right panel).

seen only in three smaller spots, around 300°, 240° and 150° longitude. Significant densities outside the oval are seen equatorwards in a diffuse region at 90° longitude.

The retrieved temperature map in Figure 8.12 shows systematically larger values than for the North aurora. All points along the oval have average temperatures larger than 900 K, and many regions show values close to 1000 K or larger. The most significant region of large temperatures is seen between 240° and 270° longitude, with average values of up to 1100 K.

8.6 Retrieval of CH_4 in the auroral regions

8.6.1 Estimation of the CH_4 rotational temperature

As explained in Section 8.4, the CH_4 emission was introduced in the simulations to explain anomalous high temperatures found systematically in definite regions inside the two auroral ovals. For those measurements, the ratio between the intensities of the 3.32 μm and 3.42 μm H_3^+ lines was much larger than expected, due to the superimposed emission in the Q branch of the ν_3 band of CH_4. However, the P and R branches were below the noise level in the individual spectra, not allowing a retrieval of the CH_4 rotational temperature. Averaging over all measurements that showed large CH_4 interference and at the same time small H_3^+ columns, typical CH_4 spectra have been extracted, which are shown by the black dots in Figures 8.13 for the North (left panel) and South aurora (right panel) separately. The North auroral spectrum shows a residual contribution of H_3^+, which is almost not seen in the South. Assuming LTE, a fit of the two spectra has been performed in order to find the best estimate for the CH_4 temperature. The best fit simulations for the different temperatures are shown in the top panels of Figure 8.13, while the bottom panels show the differences with respect to the average observed.

The χ^2 values resulting from the fit are shown in Table 8.1. The best estimate for the CH_4 temperature is found to be 650 ± 100 K for the South polar region and 500 ± 150 K for the North. The χ^2 minimum for the North is shallower due to the H_3^+ contamination of the spectrum.

Table 8.1: χ^2 values obtained for the simulated CH_4 emission at different temperatures.

Temp(K)	χ^2_{North}	χ^2_{South}
200 K	2.49	17.37
350 K	1.86	9.61
500 K	1.68	4.66
650 K	1.88	2.89
800 K	2.24	3.25

The estimate of the CH_4 rotational temperature for the North polar region is in agreement with the values reported by Kim et al. [2015] for the northern bright spot at 3.3 μm; for the South, our best fit temperature of 650 K is quite lower than the value of 850 K obtained by them. Though the JIRAM observing geometry was not favorable to determine the altitude location and vertical extension of the methane distribution, we can draw some conclusion from the best-fit temperatures. A kinetic

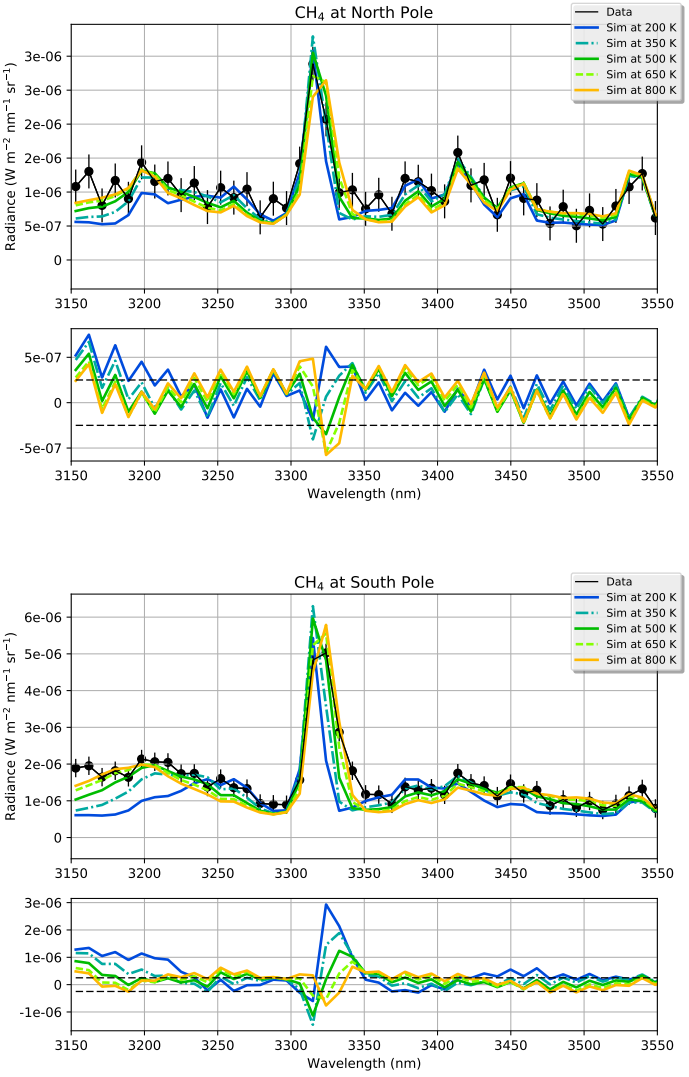

Figure 8.13: Average CH_4 spectra detected in the North (upper panel) and South (lower panel) polar regions. The fit with synthetic spectra at different temperatures is shown in the main panels, differences are shown in the smaller panels at the bottom.

temperature of 500-600 K corresponds to an altitude range between 400 and 600 km above the 1 bar level, assuming an auroral-like model atmosphere [Grodent et al., 2001]. A rotational non-LTE in this range is regarded as unlikely due to the quite large atmospheric pressure and the best-fit rotational temperatures for the CH_4 should represent the local kinetic temperature. The larger CH_4 temperature in the South would then mean either higher emission altitudes or a warmer atmospheric structure. However, the fit is poorly representing the measurements in the region of the Q branch close to the 3.35 μm spectral point. This could be produced by

a substantial contribution of the $\nu_3 + \nu_4 \rightarrow \nu_4$ hot band of CH_4 in a situation of vibrational non-LTE.

8.6.2 Distribution of hot CH_4 in the polar regions

The temperatures found with the procedure described in the previous section were assumed for CH_4 in the simulation of all measurements and in the retrieval of CH_4 column densities. Due to the approximations made in the forward model and to the large error in the fit of the CH_4 temperatures, as well as to the probable influence of vibrational non-LTE processes, the CH_4 column densities should not be taken as absolute values but just compared with respect to each other.

Therefore, to show CH_4 spatial distribution, we have normalized the column densities to the largest value, separately for each polar region. Figure 8.14 reports the distribution of the normalized column densities for the northern (left) and southern (right) regions.

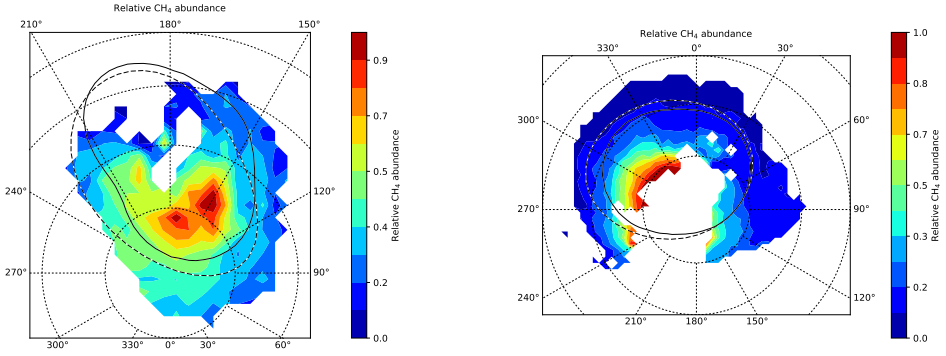

Figure 8.14: Map of the average retrieved column density of CH_4 for the North (left panel) and South (right panel) polar regions. The column densities are normalized to the peak separately for both maps.

In the Northern polar region, the CH_4 peak is located at 160°-180° longitude and 75°-85° latitude and the CH_4 hotspot diffuses also outside the oval, towards larger longitudes, although with lower abundances. This diffusion may be produced by atmospheric circulation, as already pointed out by Caldwell et al. [1983]. This is in agreement with the NIMS results [Altieri et al., 2016], but with a much better spatial resolution; the location of the CH_4 hotspot is also consistent with that of the C_2H_2 hotspot seen by CIRS at 13 μm [Sada et al., 2003]. The longitude of the 3.3 μm CH_4 hotspot is also in quite good agreement with previous Earth-based measurements at 3 μm [Kim et al., 2015] and 8 μm [Caldwell et al., 1983; Drossart

et al., 1993], although the latitudes observed previously were lower than the one reported here. Some misplacement in Earth-based observations may be due to the very slant geometry; moreover, few JIRAM data are available to date below 70° latitude, which may hide some CH_4 enhancement as well.

As for the South, unfortunately the coverage of the measurements misses much of the region poleward 80° latitude and most locations between 150° and 240° longitude. The Southern CH_4 hotspot appears much broader than the Northern one, although we are seeing just the borders of it in this first set of JIRAM data and are probably missing the peak. Most of the hotspot appears to be located inside the 80° latitude circle, shifted by some degrees towards East and we expect the peak to be well inside the auroral oval. Part of the emission seems to extend well outside the oval between 180° and 240° longitude, although no coverage is available there for now and further measurements during next JUNO orbits will clarify this specific issue.

The location of the two methane hotspot peaks well inside the auroral oval and at fixed longitudes suggests that the CH_4 excitation leading to infrared emission could be linked to the auroral ion precipitation in the polar caps [Gladstone et al., 2002; Cravens, 2003; Hui et al., 2009; Ozak et al., 2013]. The region inside the auroral oval - where the CH_4 infrared hotspot is observed along with a peak in the X-ray emission as measured by Chandra [Cravens, 2003] – maps magnetically to the outer jovian magnetosphere. As already pointed out by Gladstone et al. [2002], the same energy source may explain both X-ray, UV and IR emissions in the polar caps. Unlike the main oval, the exact mechanism and the current system behind the particle precipitation in the polar caps is still unclear. Many authors proposed that heavy positive ions coming from the outer jovian magnetosphere – mainly O^{q+}, S^{q+} [Hui et al., 2009] – precipitate well inside jovian atmosphere ionizing the local gas and giving rise to charge exchange reactions that emit X-ray photons. These same energetic ions precipitate deeper than the electrons that give rise to H_3^+ molecules and may ionize or excite the CH_4 molecules, leading to vibrational non-LTE and consequent enhanced emission in the IR. JIRAM measurements give us a picture with unprecedented detail of the two hotspots and may help understanding the actual mechanism at work in the ion aurora.

8.7 Conclusions

In this work we studied the H_3^+ abundance and effective temperature in the auroral regions of Jupiter, through analysis of the JIRAM measurements from the first Juno orbit around Jupiter. The set of observations covers most part of the North and South auroral ovals with observations of unprecedented spatial resolution. The measured spectra have been simulated through a radiative transfer code that assumes a single emission layer in optically thin conditions. H_3^+ column density and effective temperature, as well as CH_4 column density have been retrieved using a bayesian approach with optimal estimation method.

The results show an extreme variability in the H_3^+ abundance and temperature, with very thin spatial structures. Maps of average H_3^+ column density, emission temperature and CH_4 column density have been produced for the two auroral regions. The retrieved H_3^+ columns for the North aurora, corrected for the emission angle, have values up to $2.8 \times 10^{12}\,\mathrm{cm}^{-2}$ and temperatures along the main oval are in the range between 825 and 900 K. An apparent anti-correlation of temperature and column density in the map might be a signature of the H_3^+ thermostat mechanism. For the South aurora, corrected column densities reach values up to $3.5 \times 10^{12}\,\mathrm{cm}^{-2}$. The retrieved temperatures show systematically larger values than for the North aurora, with average temperatures along the oval larger than 900 K, up to 1000-1100 K in some regions. The presence of methane in two hotspots inside the auroral ovals has been detected. Methane rotational temperature is found to be about 500 K for the North hotspot and 650 K for the South. Methane emission might be due to vibrational excitation produced by auroral ion precipitation in the polar caps.

To date, more JIRAM data are available and would allow a study of the variability of the auroral environment. The inversion of a vertical profile of H_3^+ and CH_4 in the auroral region is challenging due to the very complex environment but could be tried through a 3D retrieval technique, as the one described in Chapter 6.

Chapter 9

Conclusions

The work done during my PhD regarded the inversion of infrared measurements taken by two instruments aboard space missions, VIMS on Cassini and JIRAM on Juno. Beside the analysis of the measurements, I spent considerable effort and time on the development of SpectRobot, a new 3D code for radiative transfer modeling and retrieval.

The work described in Chapter 4 and 8 has lead to the following publications in peer-reviewed journals:

- **F. Fabiano**, M. López Puertas, A. Adriani, M.L. Moriconi, E. D'Aversa, B. Funke, M.A. López-Valverde, M. Ridolfi, B.M. Dinelli, *CO concentration in the upper stratosphere and mesosphere of Titan from VIMS dayside limb observations at 4.7μm*, In Icarus, Volume 293 (2017), 119-131

- B. M. Dinelli, **F. Fabiano**, A. Adriani, F. Altieri, M.L. Moriconi, A. Mura, G. Sindoni, G. Filacchione, F. Tosi, A. Migliorini, D. Grassi, G. Piccioni, R. Noschese, A. Cicchetti, S. J. Bolton, J. E. P. Connerney, S. K. Atreya, F. Bagenal, G. R. Gladstone, C. J. Hansen, W. S. Kurth, S. M. Levin, B. H. Mauk, D. J. McComas, J.-C. Gèrard, D. Turrini, S. Stefani, M. Amoroso, A. Olivieri, *Preliminary JIRAM results from Juno polar observations: 1. Methodology and analysis applied to the Jovian northern polar region*, In Geophysical Research Letters, Volume 44, number 10 (2017), 4625-4632

- A. Adriani, A. Mura, M. L. Moriconi, B. M. Dinelli, **F. Fabiano**, F. Altieri, G. Sindoni, S. J. Bolton, J. E. P. Connerney, S. K. Atreya, F. Bagenal, J.-C. M. C. Gérard, G. Filacchione, F. Tosi, A. Migliorini, D. Grassi, G. Piccioni, R. Noschese, A. Cicchetti, G. R. Gladstone, C. Hansen, W. S. Kurth, S. M. Levin, B. H. Mauk, D. J. McComas, A. Olivieri, D. Turrini, S. Stefani, M. Amoroso, *Preliminary JIRAM results from Juno polar observations: 2. Analysis of the Jupiter southern H_3^+*

emissions and comparison with the north aurora, In Geophysical Research Letters, Volume 44, number 10 (2017), 4633-4640

- M. L. Moriconi, A. Adriani, B. M. Dinelli, **F. Fabiano**, F. Altieri, F. Tosi, G. Filacchione, A. Migliorini, J. C. Gérard, A. Mura, D. Grassi, G. Sindoni, G. Piccioni, R. Noschese, A. Cicchetti, S. J. Bolton, J. E. P. Connerney, S. K. Atreya, F. Bagenal, G. R. Gladstone, C. Hansen, W. S. Kurth, S. M. Levin, B. H. Mauk, D. J. McComas, D. Turrini, S. Stefani, A. Olivieri, M. Amoroso, *Preliminary JIRAM results from Juno polar observations: 3. Evidence of diffuse methane presence in the Jupiter auroral regions*, In Geophysical Research Letters, Volume 44, number 10 (2017), 4641-4648

I report here the main results of the different works in Chapters 4 to 8, with some perspective for future evolutions.

Chapters 4 and 5 report the analysis of day-side VIMS limb measurements of non-LTE molecular emissions in Titan's middle and upper atmosphere. For all molecules studied, non-LTE populations were calculated with the Generic RAdiative traNsfer AnD non-LTE population Algorithm (GRANADA) Funke et al. [2012] by the group of planetary atmospheres at the IAA of Granada (Spain). The results of the non-LTE modeling were used in the simulation of the observed spectra with Geofit Broad Band (GBB) radiative transfer and retrieval code.

In Chapter 4 the CO concentration in the upper stratosphere and mesosphere of Titan has been determined from the inversion of a set of day-side VIMS limb measurements around 4.7 μm in years 2006 and 2007. The atmospheric emission in this spectral region comes mainly from the fundamental and first hot bands of CO, which are in strong non-LTE conditions during day-time. The average retrieved CO VMR between 200 and 500 km represents the first measurement of the CO VMR profile in the upper stratosphere and mesosphere of Titan. The result at 200 km is compatible with previous results in the lower stratosphere Maltagliati et al. [2015]; Teanby et al. [2010]. We tried to assess whether the CO profile is uniform with altitude or not. The CO profile was found to be compatible with a uniform VMR with altitude, consistent with current photochemical models prediction Wong et al. [2002]; Wilson and Atreya [2004]; Hörst et al. [2008]. However, a slight increase of the CO VMR from 50 ppmv at 200-250 km to 60 ppmv at 500 km, -right at the uncertainty level- can be appreciated in our results, with a mean gradient of about 0.05 ppm/km in the middle atmosphere. In case this is confirmed, it would require a new unknown destruction pathway for CO around 300 km in Titan's atmosphere.

In Chapter 5 the latitudinal and seasonal variations in the distribution of CH_4, HCN and C_2H_2 in the upper atmosphere of Titan between 500 and 1000 km were studied from VIMS measurements in the 2.8-3.5 μm region. A preliminary analysis has been carried on a set of VIMS measurements between years 2004 and 2012. The results of the inversion have been averaged in latitudinal bins and in two seasons: winter (2004-2009) and early spring (2010-2012). The HCN VMR shows an enhancement at the North pole during winter at all altitudes and at both the North and South poles during spring below 800 km. Also the average C_2H_2 abundance is larger at both poles during spring below 800 km, while no significant variation is seen for C_2H_2 during winter. For CH_4, enhancements above 800 km are seen at the North pole during winter and at both poles during spring. However, these results have to be considered preliminary due to the small coverage at the polar latitudes and the observed correlation between the retrieved CH_4 VMR and SZA at high altitudes.

The wish to explain the observed bias and to build a full 3D inversion scheme has brought to the development of SpectRobot (SR), a new code for radiative transfer modeling and inversion of atmospheric quantities (Chapter 6). The ray tracing of SR works in 3D geometry and takes into account the actual position of the Sun with respect to the line of sight. The radiative transfer core is a line-by-line code that can accept as input vibrational temperatures for non-LTE simulations; calculation of LUTs has been implemented both for the LTE and non-LTE cases. The inversion routine exploits a bayesian inversion with optimal estimation technique, using Levenberg-Marquardt numerical procedure. The forward model and the inversion module of SpectRobot have been validated by comparison with the GBB code. The code has then been used to quantify the error made in the retrieval of CH_4 performed in Chapter 5. In the test case, the error of the retrieved VMR is found to be significant for CH_4 at least at large SZA (80) at 750 and 850 km. The variation observed in the retrieved VMR goes in the right direction to explain the observed bias in the retrieved CH_4 VMR at the highest altitudes for large SZA.

A new analysis of CH_4, HCN and C_2H_2 abundances on a larger VIMS dataset is currently going on with the new code. If the patterns observed in the preliminary results are confirmed with larger significance, these would imply that the middle atmosphere circulation on Titan does effectively extend well above the 500 km level, as expected in previous analysis Teanby et al. [2012], but yet not observed due to lack of suitable data. At the same time, the seasonal variation in the CH_4 VMR at high altitudes, if confirmed, would give insight in the very complex upper atmospheric

environment.

Chapter 8 reports the main results obtained from the analysis of the first JIRAM measurements at Jupiter. The observations have been calibrated and geo-referenced by the JIRAM team at IAPS-INAF in Rome. The spectra have been simulated through a radiative transfer code that assumes a single emission layer in optically thin conditions. H_3^+ column density and effective temperature, as well as CH_4 column density have been retrieved using a bayesian approach with optimal estimation method. Maps of average H_3^+ column density, emission temperature and CH_4 column density have been produced for the two auroral regions. The retrieved H_3^+ columns for the North aurora have values up to $2.8 \times 10^{12}\,\mathrm{cm}^{-2}$ and temperatures along the main oval are in the range between 825 and 900 K. An apparent anti-correlation of temperature and column density in the map might be a signature of the H_3^+ thermostat mechanism. For the South aurora, column densities reach values up to $3.5 \times 10^{12}\,\mathrm{cm}^{-2}$. The retrieved temperatures show systematically larger values than for the North aurora, with average temperatures along the oval larger than 900 K, up to 1000-1100 K in some regions. The presence of methane in two hotspots inside the auroral ovals has been detected. Methane rotational temperature is found to be about 500 K for the North hotspot and 650 K for the South. Methane emission might be due to vibrational excitation produced by auroral ion precipitation in the polar caps.

To date, more JIRAM data are available and would allow a study of the variability of the auroral environment. The inversion of a vertical profile of H_3^+ and CH_4 in the auroral region is challenging due to the complex and extremely variable environment but could be tried through the 3D retrieval technique implemented in SpectRobot.

Appendix A

SpectRobot: code description

This appendix is dedicated to a more detailed description of SpectRobot (SR), already introduced in Chapter 6. Although I hope the description gives some insight in the code, this is still far from a complete code manual.

A.1 Download and preliminaries

The full code is freely accessible on GitHub and can be downloaded at `https://github.com/fedef17/SpectRobot`. If git is installed on the computer, the git clone command can be used:

```
git clone https://github.com/fedef17/SpectRobot my-git-folder
```

SpectRobot has been developed and tested under Python 2.7.12, but should work with 3.x Python versions as well, although it has not been tested.

The following Python modules are needed: matplotlib (2.0.0), multiprocessing (0.70), numpy (1.12.1), scipy (0.19.0), cPickle (1.71). They can be installed through the python-pip package, giving in a terminal:
`pip install --user "module_name"`.

Since some key routines of the code are written in Fortran rather than in Python, the program *f2py* is needed to convert them into Python modules. These three commands have to be executed:

```
f2py -c -m fparts_mod fparts_mod.f
f2py -c -m lineshape lineshape.f
f2py -c -m curgods curgods.f
```

They produce a Python executable version of the Fortran routines, that can be called from inside SR.

To write a Python script using the SR framework, these import statements are suggested:

```
import numpy as np
import spect_base_module as sbm
import spect_main_module as smm
import spect_classes as spcl
```

A.2 Code structure: classes and methods

In order to explain how the code works, it's worth first introduce the objects that build up the framework of SR. Objects are the basic concept of object-oriented programming: an object contains a set of data in the form of attributes and has specific methods that work on those data. Each object is the instantiation of a class, which is the general template for that particular object. In this section I will describe briefly the classes developed, showing some code snippet and usage.

A.2.1 class Planet

This class describes the planet that one wants to simulate. Attributes of class planet include important data regarding the geometry - planetary radii, altitude of TOA, star-to-planet distance - as well as other characteristics of the planet like orbital period, planetary type, stellar type and others.. The idea is to create a collection of child classes with standard attributes that define all solar system planets and possibly exoplanets. Up to now only two subclasses have been created: class Titan(Planet) and class Jupiter(Planet).

Apart from the fixed attributes, the planet object contains information regarding the particular atmosphere that one wants to simulate. In particular two attributes of the planet class are fundamental inputs for the radiative transfer routine: planet.atmosphere, which is an AtmProfile object describing the temperature/pressure structure of the atmosphere, and planet.gases, which is a Python dictionary containing Molec objects which represent all the gases to be included in the simulation.

Usage

```
import spect_base_module as sbm
print('Loading planet...')

### I'm creating a Titan planet object with TOA at 1500 km.
planet = sbm.Titan(1500.)

### This adds the attribute "atmosphere" to planet. Atm is an AtmProfile
    object
planet.add_atmosphere(Atm)

### This adds gas ch4 to planet gases. ch4 is a Molec object
planet.add_gas(ch4)
```

A.2.2 class Coords

This class describes a point in space. The main reason for this class is to have painless conversions of coordinates between different reference frames: a cartesian reference frame, with its origin at the center of the planet, z axis parallel the planet rotation axis and x axis pointing in the direction of the zero meridian; a pure spherical frame described by (R,θ,ϕ); a modified spherical coordinate frame described by the triad (latitude, longitude, altitude). The cartesian frame is used for the calculation of the line of sight path, while the modified spherical is used to describe the atmospheric quantities. Default units for the cartesian coordinates and the altitude are kilometers, for latitudes and longitudes degrees are used.

Usage

```
import spect_base_module as sbm

### I'm creating a Coords object. I need to specify the radius of the
    planet to convert to the modified spherical frame.
point = sbm.Coords([0., 2360., 1362.5], s_ref='Cartesian', R =
    planet.radius)

### Converting to the modified spherical coordinates:
sph_coords = point.Spherical()
```

```
-> array([30., 90., 150.])

### Converting to the cartesian coordinates:
cart_coords = point.Cartesian()
-> array([0., 2360., 1362.5])

### I define a second point. The distance between the two points is given
    by method "distance" (in units of "km" or "cm"):
point2 = sbm.Coords([20., 120., 300.], s_ref='Spherical', R =
    planet.radius)
dist = point.distance(point2, units = 'km')
-> 1403.1672..
```

A.2.3 classes AtmProfile and AtmGrid

Class AtmProfile represents an atmospheric quantity and its dependence from the position in the atmosphere. The quantity is user-defined and can be the temperature, the pressure, the abundance of a gas or something else.

There is no fixed dimension for an AtmProfile object, which may depend on altitude, latitude, solar zenith angle, longitude or a subset of these coordinates. The information about the dimensions of the profile and the set of grid points used to define an AtmProfile object is stored in the grid attribute, which is an AtmGrid object. Class AtmGrid represents the coordinate grid used to define the atmospheric profiles. The main purpose of this class is to keep the information regarding the atmospheric grid used to define some atmospheric profile. Each dimension is accessible through a key like 'alt', 'lat' or 'sza'. The flexibility of the AtmProfile and AtmGrid objects allows to describe many different situations with the same classes and functions.

For example, if one wants to define a temperature profile which is the same for all latitudes, a one-dimensional AtmProfile object with just an altitude dimension suits the problem. To define a temperature field which varies with latitude and altitude, a two-dimensional AtmProfile object is needed. A three-dimensional AtmProfile object may be used for example to define a vibrational temperature profile, which varies with altitude, latitude and solar zenith angle. Some examples are shown in the box below.

The main methods of class AtmProfile are:

- method `AtmProfile.calc(point, sza)`: gives the interpolated value of a profile at the required point. Point is a Coords object that defines the position in the atmosphere; sza is needed if the AtmProfile depends on solar zenith angle. The interpolation on each dimension can be of three types: linear ('lin'), logarithmic ('exp') or assume the nearest value ('box').

- method `AtmProfile.plot()`: allows to visualize the profile that is being used.

- algebraic operations: two AtmProfile objects can be summed, subtracted, multiplied, divided.. Useful to construct a profile starting from components.

Usage

```
### I'm creating a 1-D AtmGrid object to construct an altitude grid
    ranging from 0 to 1500 in 10 km steps.
n_alts = 151
alt_array = np.linspace(0., 1500, n_alts)
alt_grid = sbm.AtmGrid('alt', alt_array)

### Now define a simple temperature profile, let's say a linear one,
    using the alt_grid defined above.
## Set the profile name to 'temp' and assume linear interpolation of the
    profile ('lin').
temp_array = np.linspace(200., 250., 151)
Temp_profile = sbm.AtmProfile(alt_grid, temp_array, 'temp', 'lin')

### I add a latitude grid from -90 to 90 in 20 degrees steps. I can merge
    the two grids to create a 2D grid.
n_lats = 10
lat_array = np.linspace(-90., 90, n_lats)
lat_grid = sbm.AtmGrid('lat', lat_array)
grid_2D = alt_grid.merge(lat_grid)

### I define a 2D temperature array. The dimension of the array has to be
    (n_lats*n_alts). From this I create the 2D Temp_profile object,
    setting the interpolation in latitudes to 'box' and in altitudes to
    'lin'.
temp_array_2D = np.vstack([temp_array+i for i in range(n_lats)])
```

```
Temp_profile_2D = sbm.AtmProfile(grid_2D, temp_array_2D, 'temp',
    ['box','lin'])

### I can plot the profiles to see what I've done.
pl.ion()
pl.figure(7)
Temp_profile_2D.plot()
pl.legend()

### For an arbitrary point in the atmosphere, the AtmProfile objects now
    tell the value of the interpolated temperature at point:
point = sbm.Coords([20., 120., 300.], s_ref='Spherical', R =
    planet.radius)
temp1_at_point = Temp_profile.calc(point)
-> 210.0
temp2_at_point = Temp_profile_2D.calc(point)
-> 215.5
```

A.2.4 classes Molec, IsoMolec and Level

Class Molec and class IsoMolec represent a molecule (regardless of the isotopologues) and a particular isotopologue respectively. The purpose of class Molec is just to store together the isotopologues corresponding to the same molecule - which are accessible through the attributes
`Molec.iso_1`, `Molec.iso_2`, .. - and to set quantities that regard all isotopologues. An abundance profile (an AtmProfile object) of the molecule can be set through the method `Molec.add_clim()`, which is than used in the radiative transfer routines.

Class IsoMolec can be defined both for LTE and non-LTE calculations: the switch between the two is stored in `IsoMolec.is_in_LTE` attribute. When defined for LTE, an IsoMolec object contains as attributes just the isotopic ratio, the molecular mass (MM) and isotope number. When defined for non-LTE, the IsoMolec object contains Level objects which represent all the vibrational levels that will be used for that isotopologue. Level objects are accessible through the attributes `IsoMolec.lev_00`, `IsoMolec.lev_01`,..

Class Level represents a particular vibrational level of a molecule and its main attributes are: molecule and isotope number (`Level.mol` and `Level.iso`), the level

energy (`Level.energy`), the level string in HITRAN format (`Level.lev_string`) and the vibrational temperature of the level, which is an AtmProfile object.

Since the level string of a specific vibrational level can appear in HITRAN database with different nuclear symmetries (see for example the case of CH_4), The level class contains a specific method (
`Level.equiv()`) to identify if the vibrational level of a line matches that of the level. The nuclear symmetry can either be considered or ignored. The method is consistent with HITRAN vibrational level strings of all molecules Rothman et al. [2013]. For example, if nuclear symmetry is ignored, the `0 0 1 0 1F2` and `0 0 1 0 2E` HITRAN strings for CH_4 are automatically linked to the ν_3 level.

A.2.5 class SpectLine

Class SpectLine represents a single line of the spectroscopic database. It stores all the information contained in the database using the HITRAN format. Additional formats may be specified. The following list of attributes is set for a HITRAN line with complete information, taking the value of the corresponding fields in HITRAN database: `Mol, Iso, Freq, Strength, A_coeff, Air_broad, Self_broad, E_lower, T_dep_broad, P_shift, Up_lev_str, Lo_lev_str, Q_num_up, Q_num_lo, others, g_up, g_lo`.

Apart from storing line data consistently, the SpectLine class provides methods to calculate line-specific quantities. The main methods are:

- method `SpectLine.CalcStrength()`: calculates the line strength at the given temperature for LTE conditions, using equation 1.19.

- methods `SpectLine.CalcStrength_from_Einstein()` and `SpectLine.CalcStrength_from_Strength()`: both methods calculate the line strength in non-LTE conditions given the temperature and vibrational temperatures, the first starting from the Einstein A-coefficient (using equation 1.17), the other from the line strength at reference temperature (using equation 1.20).

- method `SpectLine.MakeShapeLine()`: calculates the line shape at given temperature and pressure. Output is a SpectralObject object.

- method `SpectLine.LinkToMolec()`: identifies the correct lower and upper levels in the IsoMolec object that match the transition levels of line. This sets

additional attributes to line: `Lo_lev_id` and `Up_lev_id` which are the labels of the two vibrational levels in IsoMolec; `E_vib_lo` and `E_vib_up` that are the two vibrational energies.

- method `SpectLine.Calc_Gcoeffs()`: calculates the G-coefficients of the line as defined in equation 1.28. Before calculating the two coefficients, the line has to be correctly assigned to a couple of vibrational levels.

A.2.6 class SpectralGrid and SpectralObject

The idea regarding these two classes is to bind the spectrum to its spectral grid so as to be able to easily perform conversions, convolutions and operations between spectra and visualization of the spectrum.

Class SpectralGrid represents the spectral grid and contains only two attributes: attribute `SpectralGrid.grid` contains the vector with all spectral points, attribute `SpectralGrid.units` is a string that specifies the units used. For now, the values allowed for units are 'nm', 'cm_1' (cm^{-1}), 'mum' (μm), 'hz'. Methods for conversion to and from these units are available.

Class SpectralObject is the general object to represent a spectral distribution and contains the attributes `SpectralObject.grid`, which is a SpectralGrid object, and `SpectralObject.spectrum`, which is the spectrum array. Main methods of class SpectralObject are:

- algebraic operations between SpectralObjects, valid also between objects with different spectral grids. Restriction to a subset of the full spectral grid.
- method `SpectraObject.convolve_to_grid()`: convolves to a grid with lower sampling frequency.
- method `SpectraObject.integrate()`: integrates the full spectrum or a subset specified by a wavenumber range.
- method `SpectraObject.plot()`: plots the spectrum.
- method `SpectraObject.convert_grid_to()`: performs a conversion of both grid and spectrum according to new grid units. One can pass for example from a wavenumber spectrum to a wavelength one.
- method `SpectraObject.add_lines_to_spectrum()`: adds a large number of line-shapes at different wavenumbers to the spectrum using a Fortran routine.

Two subclasses of class SpectralObject are available:

- class SpectralIntensity, which has the additional information of units ('ergscm2' (erg s^{-1} cm^{-2}), 'nWcm2' (nW cm^{-2}), 'Wm2' (W m^{-2})) and conversion methods between these units.

- class SpectralGcoeff, which represent the level specific coefficients defined in equation 1.29 and contains the information about the molecule, the isotopologue, the level considered and the type of coefficient ('absorption', 'ind_emission', 'sp_emission'). Since these coefficients are used for the look-up tables, it also contains as attributes the temperature and pressure at which it has been calculated and possesses a method to interpolate between two coefficients at different pressure and temperature.

A.2.7 class LineOfSight

Class LineOfSight is the fundamental class used in all radiative transfer routines, which contains all information about the line of sight (LOS) that one wants to simulate. The LineOfSight object is defined through its geometrical configuration, for which two points are required: a starting point, which is usually the spacecraft position (or generally, the observer's) and a second point, which is usually the tangent point for limb measurements and the intersection with the surface for nadir ones. Once defined the LOS vector, a planet object is needed for the calculation of the path of the LOS and of all quantities needed in the radiative transfer along the LOS.

A more detailed explanation of the ray tracing is done in Section 6.1.1. Here is a list of the main methods of the class and a brief description:

- method `LineOfSight.calc_LOS_vector()`: using the starting point and the second point given in the initialization, the method calculates the normalized vector direction of the LOS used in the ray tracing.

- methods `LineOfSight.intersect_shell()`, `LineOfSight.move_along_LOS()`: these methods are used for the calculation of the intersections with any spherical surface (like the top of the atmosphere (TOA) or the surface), the movement along the LOS by a pre-determined step (default is 1 km).

- method `LineOfSight.calc_atm_intersections()`: using the methods above, this method calculates all points inside the atmosphere at the pre-determined

step. The output is a list of Coords objects which is saved in the attribute `LineOfSight.intersections`.

- methods `LineOfSight.calc_along_LOS()` and `LineOfSight.calc_abundance()`: the first method calculates the values of an AtmProfile object at each point in `LineOfSight.intersections`, using the method `AtmProfile.calc()`. The second method is used in the calculation of the number density of a molecule in `Planet.gases` along the LOS.

- method `LineOfSight.calc_SZA_along_los()`: calculates the solar zenith angle at each point along the LOS, given the position of the sub solar point (SSP). The SSP is also given in NASA PDS datasets.

- method `LineOfSight.calc_radtran_steps()`: builds up the steps for radiative transfer, calculating the Curtis-Godson averages of all quantities needed. More details in Section 6.1.1.

- methods `LineOfSight.radtran_fast()`, `LineOfSight.radtran()`, `LineOfSight.radtran_single()`: the first two methods are the routines for radiative transfer calculation along the LOS and just use a different strategy on performance. `LineOfSight.radtran_fast()` is much faster but works only with LUTs and splits the spectral range to optimize CPU and RAM usage. `LineOfSight.radtran_single()` is the implementation of the radiative transfer equation, given the set of absorption and emission coefficient along the LOS.

A.2.8 classes LookUpTable and LutSet

Class LookUpTable is used to store the look-up tables of a molecule (a specific isotopologue). The LookUpTable object is stored in a file with standard name format and contains information about the spectral grid used in the LUTs calculations, the original IsoMolec object and the pressure-temperature couples (PT couples) at which the absorption and emission coefficient have been calculated. The `LookUpTable.sets` attribute is a list of LutSet objects that effectively contain the tabulated coefficients.

LookUpTable objects can be of two types, LTE or non-LTE. When defined for non-LTE, each LutSet object is related to a single molecular level and contains the

level G-coefficients in equation 1.29 for all PT couples in form of SpectralGcoeff objects (see Subsection A.2.6 above). For the LTE case, there is no distinction of levels and the overall molecular absorption, induced emission and spontaneous emission coefficients are stored for each PT couples, always in the form of SpectralGcoeff objects.

There is a specific routine in module spect_main_module that creates and stores in memory a LookUpTable object given an IsoMolec object, a set of lines and a set of PT couples. Classes LookUpTable and LutSet possess methods to read from memory the stored values.

A.2.9 classes BayesSet, RetSet and RetParam

Class BayesSet represents the full state vector of the inverse problem (see Chapter 2), class RetParam represents a single component of the state vector and class RetSet is a collection of RetParam objects related to the same quantity. For example, to retrieve 7 altitude points for each of three gas abundance profiles, we need three RetSet objects made of 7 RetParam objects each: the resulting BayesSet is made of the three RetSet objects and 21 RetParam objects so defined. To put this in a scheme:

- state vector $\boldsymbol{x} \rightarrow$ `class BayesSet`
- retrieved VMR/temperature/.. profile $\rightarrow$ `class RetSet`
- single component of the retrieved profile $\rightarrow$ `class RetParam`

Subclasses of RetSet may be defined for different problems. To date, two subclasses of RetSet have been defined: `LinearProfile_1D` and `LinearProfile_2D`. The first one is suited to retrieve a one-dimensional VMR profile, dependent only on altitude. The second one is built for two-dimensional problems, like a vertical VMR profile with different latitudinal bands. In the first case, the VMR X_g of a molecule is decomposed in a set of triangular functions centered at the fixed altitudes z_i of the retrieval grid:

$$\begin{aligned} X_g(z) = \sum_i \alpha_i \mathcal{T}_i(z) \qquad \mathcal{T}_i(z) &= \frac{|z - z_i|}{|z_{i+1} - z_i|} \quad \text{if } z_i \leq z \leq z_{i+1} \\ &= \frac{|z - z_i|}{|z_i - z_{i-1}|} \quad \text{if } z_{i-1} \leq z \leq z_i \\ &= 0 \quad \text{otherwise} \end{aligned} \tag{A.1}$$

The first and last $\mathcal{T}_i(z)$ functions are actually defined differently, since they have just one adjacent grid point:

$$\begin{aligned}\mathcal{T}_1(z) &= \frac{|z - z_1|}{|z_2 - z_1|} \quad \text{if } z_1 \leq z \leq z_2 \\ &= 1 \quad \text{if } z \leq z_1 \\ &= 0 \quad \text{otherwise}\end{aligned}$$

$$\begin{aligned}\mathcal{T}_m(z) &= \frac{|z - z_m|}{|z_m - z_{m-1}|} \quad \text{if } z_{m-1} \leq z \leq z_m \\ &= 1 \quad \text{if } z \geq z_m \\ &= 0 \quad \text{otherwise}\end{aligned}$$

The $\mathcal{T}_i(z)$ are defined here for the 1D case but can be generalized to higher dimensions. A RetParam object contains both the mask profile $\mathcal{T}_i(z)$, which is an AtmGridMask object, and the corresponding value of the parameter α_i, which is updated at each iteration of the retrieval procedure.

The partial derivatives $\partial \boldsymbol{f}/\partial \alpha_i$ are stored at the attribute of `RetParam.derivatives`. The complete Jacobian is stored in the BayesSet object and used for subsequent calculation.

A.3 Code structure: main routines

In order to perform a radiative transfer simulation using SR, a number of preliminary steps is necessary:

- reading of the spectral database, building a set of SpectLine objects (see Section A.2.5);
- construction of the Planet object, with specification of the planet characteristics - or loading of a pre-defined Planet, like Titan() or Jupiter() - and setting the thermal structure (see Sections A.2.1 and A.2.3);
- construction of the set of Molec objects to be included in the radiative transfer, setting the vibrational temperatures for the Level objects in case of non-LTE (see Section A.2.4);

- construction of the set of LineOfSight objects to be simulated (see Section A.2.7). For non-LTE computations, the position of the Sub Solar Point on the planet is needed as well.

A.3.1 Calculation of Look-Up Tables

Given the long time required for the line-by-line calculations, it is highly recommended to perform first a calculation of the look-up tables (LUTs) for the possible P-T configurations in the atmosphere and the relevant molecules. This is done by the smm.check_and_build_allluts() function, which takes as inputs the list of molecules and the atmospheric structure. Some parameters may be defined that set the desired steps in temperature (default = 5 K) and pressure (default = 0.2 logP) and the minimum pressure after which the pressure broadening is neglected. The LUTs are stored in the location set on the hard drive, with standard names. A choice between LTE and non-LTE calculations can be set. In case of non-LTE, separate files are produced for each level.

A.3.2 Radiative transfer routine

Given the line of sight (LineOfSight object), the planet and the atmospheric structure (stored in the Planet object) the radiative transfer routine calculates the high resolution spectrum in the given spectral range. The radiative transfer routine is called through the LOS.radtran_fast() method of the LineOfSight object, which requires in input the planet object, the spectral grid and possibly the LUT objects for the molecules considered.

To perform more radiative transfer calculations on a set of LOSs, the smm.radtrans() routine is suggested, which works in parallel computing - optimizing the use of CPU and RAM - and minimizes the number of read/write operations on the hard drive.

A.3.3 Main - Inversion routine

The main routine in SR is the smm.inversion() routine, which makes use of all the other stuff inside SR. The inversion routine takes as inputs the planet to be simulated, the spectral lines and the location of the LUTs folder, the set of measurements to be simulated and the bayesian set of parameters that one wants to obtain from the inversion.

The construction of the BayesSet object is the most critical passage and requires a proper choice of the altitude steps for the parameter profiles in order to gain most information from the measurements. A faster routine, optimized for the study of a set of limb measurements, is the smm.inversion_fast_limb() routine, which adopts some approximation in the Field of View (FOV) interpolation.

Bibliography

Achterberg, R. K., B. J. Conrath, P. J. Gierasch, F. M. Flasar, and C. A. Nixon
2008. Titan's middle-atmospheric temperatures and dynamics observed by the cassini composite infrared spectrometer. *Icarus*, 194(1):263–277.

Achterberg, R. K., P. J. Gierasch, B. J. Conrath, F. M. Flasar, and C. A. Nixon
2011. Temporal variations of titan's middle-atmospheric temperatures from 2004 to 2009 observed by cassini/cirs. *Icarus*, 211(1):686–698.

Acton, C. H.
1996. Ancillary data services of nasa's navigation and ancillary information facility. *Planetary and Space Science*, 44(1):65–70.

Adriani, A., B. Dinelli, M. López-Puertas, M. García-Comas, M. Moriconi, E. D'Aversa, B. Funke, and A. Coradini
2011. Distribution of hcn in titan's upper atmosphere from cassini/vims observations at 3μm. *Icarus*, 214(2):584–595.

Adriani, A., G. Filacchione, T. Di Iorio, D. Turrini, R. Noschese, A. Cicchetti, D. Grassi, A. Mura, G. Sindoni, M. Zambelli, et al.
2017a. Jiram, the jovian infrared auroral mapper. *Space Science Reviews*, 213(1-4):393–446.

Adriani, A., A. Mura, M. L. Moriconi, B. M. Dinelli, F. Fabiano, F. Altieri, G. Sindoni, S. J. Bolton, J. E. P. Connerney, S. K. Atreya, F. Bagenal, J.-C. M. C. Gérard, G. Filacchione, F. Tosi, A. Migliorini, D. Grassi, G. Piccioni, R. Noschese, A. Cicchetti, G. R. Gladstone, C. Hansen, W. S. Kurth, S. M. Levin, B. H. Mauk, D. J. McComas, A. Olivieri, D. Turrini, S. Stefani, and M. Amoroso
2017b. Preliminary jiram results from juno polar observations: 2. analysis of the jupiter southern h3+ emissions and comparison with the north aurora. *Geophysical Research Letters*, 44(10):4633–4640. 2017GL072905.

Allen, D. and C. Simpson
1980. Vibrational energy exchange between co and the isotopes of n 2 between 300 k and 80 k. *Chemical Physics*, 45(2):203–211.

Altieri, F., B. M. Dinelli, A. Migliorini, M. L. Moriconi, G. Sindoni, A. Adriani, A. Mura, and F. Fabiano
2016. Mapping of hydrocarbons and h3+ emissions at jupiter's north pole using galileo/nims data. *Geophysical Research Letters*, 43(22):11,558–11,566. 2016GL070787.

Bagenal, F., A. Adriani, F. Allegrini, S. J. Bolton, B. Bonfond, E. J. Bunce, J. E. P. Connerney, S. W. H. Cowley, R. W. Ebert, G. R. Gladstone, C. J. Hansen, W. S. Kurth, S. M. Levin, B. H. Mauk, D. J. McComas, C. P. Paranicas, D. Santos-Costa, R. M. Thorne, P. Valek, J. H. Waite, and P. Zarka
2014. Magnetospheric science objectives of the juno mission. *Space Science Reviews*, 213(1-4):219–287.

Bagenal, F., T. E. Dowling, and W. B. McKinnon
2006. *Jupiter: the planet, satellites and magnetosphere*, volume 1. Cambridge University Press.

Baines, K. H., P. Drossart, M. A. Lopez-Valverde, S. K. Atreya, C. Sotin, T. W. Momary, R. H. Brown, B. J. Buratti, R. N. Clark, and P. D. Nicholson
2006. On the discovery of co nighttime emissions on titan by cassini/vims: Derived stratospheric abundances and geological implications. *Planetary and Space Science*, 54(15):1552–1562.

Bellucci, A., B. Sicardy, P. Drossart, P. Rannou, P. Nicholson, M. Hedman, K. Baines, and B. Burrati
2009. Titan solar occultation observed by cassini/vims: Gas absorption and constraints on aerosol composition. *Icarus*, 201(1):198–216.

Bohren, C. and D. Huffman
1983. *Absorption and Scattering of Light by Small Particles*. Wiley.

Bolton, S.
2010. The juno mission. volume 6, Pp. 92–100. Cambridge University Press.

Bonfond, B., D. Grodent, S. V. Badman, J.-C. Gérard, and A. Radioti
2016. Dynamics of the flares in the active polar region of jupiter. *Geophysical Research Letters*, 43(23):11,963–11,970.

Boudon, V., J.-P. Champion, T. Gabard, G. Pierre, M. Loëte, and C. Wenger
2003. Spectroscopic tools for remote sensing of greenhouse gases ch4, cf4 and sf6. *Environmental Chemistry Letters*, 1(1):86–91.

Boursier, C., J. Menard, L. Doyennette, and F. Menard-Bourcin
2003. Rovibrational relaxation of methane in ch4-n2 mixtures: Time-resolved ir-ir double-resonance measurements at 193 k and kinetic modeling. *The Journal of Physical Chemistry A*, 107(27):5280–5290.

Brown, R., K. Baines, G. Bellucci, J.-P. Bibring, B. Buratti, F. Capaccioni, P. Cerroni, R. Clark, A. Coradini, D. Cruikshank, et al.
2004. The cassini visual and infrared mapping spectrometer (vims) investigation. In *The Cassini-Huygens Mission*, Pp. 111–168. Springer.

Caldwell, J., A. T. Tokunaga, and G. S. Orton
1983. Further observations of 8 μm polar brightenings of jupiter. *Icarus*, 53(1):133–140.

Capalbo, F. J., Y. Bénilan, R. V. Yelle, and T. T. Koskinen
2015. Titan's upper atmosphere fromcassini/uvis solar occultations. *The Astrophysical Journal*, 814(2):86.

Carlotti, M., G. Brizzi, E. Papandrea, M. Prevedelli, M. Ridolfi, B. M. Dinelli, and L. Magnani
2006. Gmtr: Two-dimensional geo-fit multitarget retrieval model for michelson interferometer for passive atmospheric sounding/environmental satellite observations. *Applied optics*, 45(4):716–727.

Clarke, J. T.
2012. Auroral processes on jupiter and saturn. In *Auroral Phenomenology and Magnetospheric Processes: Earth and Other Planets*, Pp. 113–121. American Geophysical Union.

Clarke, J. T., D. Grodent, S. W. Cowley, E. J. Bunce, P. Zarka, J. E. Connerney, and T. Satoh
2004. *Jupiter's aurora*, volume 1, Pp. 639–670.

Connerney, J. E. P., M. H. Acuña, N. F. Ness, and T. Satoh
1998. New models of jupiter's magnetic field constrained by the io flux tube footprint. *Journal of Geophysical Research: Space Physics*, 103(A6):11929–11939.

Connerney, J. E. P. and T. Satoh
2000. The h_3^+ ion: a remote diagnostic of the jovian magnetosphere. *Philosophical Transactions of the Royal Society A: Mathematical, Physical and Engineering Sciences*, 358(1774):2471–2483.

Coustenis, A., R. K. Achterberg, B. J. Conrath, D. E. Jennings, A. Marten, D. Gautier, C. A. Nixon, F. M. Flasar, N. A. Teanby, B. Bézard, et al.
2007. The composition of titan's stratosphere from cassini/cirs mid-infrared spectra. *Icarus*, 189(1):35–62.

Cowley, S. and E. Bunce
2001. Origin of the main auroral oval in jupiter's coupled magnetosphere–ionosphere system. *Planetary and Space Science*, 49(10):1067 – 1088. Magnetosphere of the Outer Planets Part II.

Cravens, T. E.
2003. Implications of jovian x-ray emission for magnetosphere-ionosphere coupling. *Journal of Geophysical Research*, 108(A12).

Cui, J., Y.-T. Cao, P. P. Lavvas, and T. T. Koskinen
2016. The variability of hcn in titan's upper atmosphere as implied by thecassiniion-neutral mass spectrometer measurements. *The Astrophysical Journal*, 826(1):L5.

Cui, J., R. Yelle, V. Vuitton, J. Waite, W. Kasprzak, D. Gell, H. Niemann, I. Müller-Wodarg, N. Borggren, G. Fletcher, E. Patrick, E. Raaen, and B. Magee
2009. Analysis of titan's neutral upper atmosphere from cassini ion neutral mass spectrometer measurements. *Icarus*, 200(2):581 – 615.

De Kok, R., P. Irwin, N. Teanby, E. Lellouch, B. Bézard, S. Vinatier, C. Nixon, L. Fletcher, C. Howett, S. Calcutt, et al.
2007. Oxygen compounds in titan's stratosphere as observed by cassini cirs. *Icarus*, 186(2):354–363.

Dinelli, B. M., F. Fabiano, A. Adriani, F. Altieri, M. L. Moriconi, A. Mura, G. Sindoni, G. Filacchione, F. Tosi, A. Migliorini, D. Grassi, G. Piccioni, R. Noschese,

A. Cicchetti, S. J. Bolton, J. E. P. Connerney, S. K. Atreya, F. Bagenal, G. R. Gladstone, C. J. Hansen, W. S. Kurth, S. M. Levin, B. H. Mauk, D. J. McComas, J.-C. Gèrard, D. Turrini, S. Stefani, M. Amoroso, and A. Olivieri
2017. Preliminary jiram results from juno polar observations: 1. methodology and analysis applied to the jovian northern polar region. *Geophysical Research Letters*, 44(10):4625–4632. 2017GL072929.

Dobrijevic, M., E. Hébrard, J. Loison, and K. Hickson
2014. Coupling of oxygen, nitrogen, and hydrocarbon species in the photochemistry of titan's atmosphere. *Icarus*, 228:324–346.

Drossart, P., B. Bézard, S. K. Atreya, J. Bishop, J. H. Waite, and D. Boice
1993. Thermal profiles in the auroral regions of jupiter. *Journal of Geophysical Research: Planets*, 98(E10):18803–18811.

Edwards, D. P., M. Lopez-Puertas, and R. Gamache
1998. The non-lte correction to the vibrational component of the internal partition sum for atmospheric calculations. *Journal of Quantitative Spectroscopy and Radiative Transfer*, 59(3-5):423–436.

Edwards, D. P., M. López-Puertas, and M. A. López-Valverde
1993. Non-local thermodynamic equilibrium studies of the 15-μm bands of co2 for atmospheric remote sensing. *Journal of Geophysical Research: Atmospheres (1984–2012)*, 98(D8):14955–14977.

Elsner, R. F.
2005. Simultaneous chandra x ray, hubble space telescope ultraviolet, and ulysses radio observations of jupiter's aurora. *Journal of Geophysical Research*, 110(A1).

Esposito, L. W., C. A. Barth, J. E. Colwell, G. M. Lawrence, W. E. McClintock, A. I. F. Stewart, H. U. Keller, A. Korth, H. Lauche, M. C. Festou, et al.
2004. The cassini ultraviolet imaging spectrograph investigation. *Space science reviews*, 115(1-4):299–361.

Fabiano, F., M. L. Puertas, A. Adriani, M. Moriconi, E. D'Aversa, B. Funke, M. López-Valverde, M. Ridolfi, and B. Dinelli
2017. CO concentration in the upper stratosphere and mesosphere of titan from VIMS dayside limb observations at 4.7 μm. *Icarus*, 293:119–131.

Flasar, F., R. Achterberg, B. Conrath, P. Gierasch, V. Kunde, C. Nixon, G. Bjoraker, D. Jennings, P. Romani, A. Simon-Miller, et al.
2005. Titan's atmospheric temperatures, winds, and composition. *Science*, 308(5724):975–978.

Flasar, F., R. Achterberg, and P. Schinder
2014. *Thermal Structure of Titan's Troposphere and Middle Atmosphere*, P. 322. Cambridge University Press.

Flasar, F. M., V. G. Kunde, M. M. Abbas, R. K. Achterberg, P. Ade, A. Barucci, B. Bézard, G. L. Bjoraker, J. C. Brasunas, S. Calcutt, R. Carlson, C. J. Césarsky, B. Conrath, A. Coradini, R. Courtin, A. Coustenis, S. Edberg, S. Edgington, C. Ferrari, T. Fouchet, D. Gautier, P. J. Gierasch, K. Grossman, P. Irwin, D. E. Jennings, E. Lellouch, A. A. Mamoutkine, A. Marten, J. P. Meyer, C. A. Nixon, G. S. Orton, T. C. Owen, J. C. Pearl, R. Prangé, F. Raulin, P. L. Read, P. N. Romani, R. E. Samuelson, M. E. Segura, M. R. Showalter, A. A. Simon-Miller, M. D. Smith, J. R. Spencer, L. J. Spilker, and F. W. Taylor
2004. *Exploring the Saturn System in the Thermal Infrared: The Composite Infrared Spectrometer*, Pp. 169–297. Dordrecht: Springer Netherlands.

Fulchignoni, M., F. Ferri, F. Angrilli, A. Ball, A. Bar-Nun, M. Barucci, C. Bettanini, G. Bianchini, W. Borucki, G. Colombatti, et al.
2005. In situ measurements of the physical characteristics of titan's environment. *Nature*, 438(7069):785–791.

Funke, B., M. López-Puertas, , D. Bermejo-Pantaleón, T. von Clarmann, G. P. Stiller, M. Höpfner, U. Grabowski, and M. Kaufmann
2007. Analysis of nonlocal thermodynamic equilibrium CO 4.7 μm fundamental, isotopic and hot band emissions measured by the Michelson Interferometer for Passive Atmospheric Sounding on Envisat. *J. Geophys. Res.*, 112(D11).

Funke, B., M. López-Puertas, M. García-Comas, M. Kaufmann, M. Höpfner, and G. Stiller
2012. Granada: A generic radiative transfer and non-lte population algorithm. *Journal of Quantitative Spectroscopy and Radiative Transfer*, 113(14):1771–1817.

Funke, B., M. López-Puertas, M. García-Comas, G. P. Stiller, T. von Clarmann, M. Höpfner, N. Glatthor, U. Grabowski, S. Kellmann, and A. Linden
2009. Carbon monoxide distributions from the upper troposphere to the meso-

sphere inferred from 4.7 μm non-local thermal equilibrium emissions measured by mipas on envisat. *Atmospheric Chemistry and Physics*, 9(7):2387–2411.

García-Comas, M., M. López-Puertas, B. Funke, B. M. Dinelli, M. L. Moriconi, A. Adriani, A. Molina, and A. Coradini
2011. Analysis of titan ch 4 3.3 μm upper atmospheric emission as measured by cassini/vims. *Icarus*, 214(2):571–583.

Gladstone, G. R., J. H. Waite, D. Grodent, W. S. Lewis, F. J. Crary, R. F. Elsner, M. C. Weisskopf, T. Majeed, J.-M. Jahn, A. Bhardwaj, J. T. Clarke, D. T. Young, M. K. Dougherty, S. A. Espinosa, and T. E. Cravens
2002. A pulsating auroral x-ray hot spot on jupiter. *Nature*, 415(6875):1000–1003.

Goody, R. and Y. Yung
1989. *Atmospheric Radiation*. Oxford University Press (OUP).

Gregory, E. A., M. M. Maricq, R. M. Siddles, C. Wickham-Jones, and C. Simpson
1983. Vibrational relaxation of gaseous co (v= 1) and n2 (v= 1) from 300 k to liquid temperatures: A comparison with liquid state relaxation. *The Journal of Chemical Physics*, 78(6):3881–3892.

Grodent, D.
2003. Jupiter's polar auroral emissions. *Journal of Geophysical Research*, 108(A10).

Grodent, D., J. H. Waite, and J.-C. Gérard
2001. A self-consistent model of the jovian auroral thermal structure. *Journal of Geophysical Research: Space Physics*, 106(A7):12933–12952.

Guelachvili, G., D. D. Villeneuve, R. F. R, W. Urban, and J. Verges
1983. Dunham coefficients for seven isotopic species of CO. *J. Mol. Spectrosc.*, 98:64–79.

Gurwell, M. A.
2004. Submillimeter Observations of Titan: Global Measures of Stratospheric Temperature, CO, HCN, HC_3N, and the Isotopic Ratios $^{12}C/^{13}C$ and $^{14}N/^{15}N$. *The Astrophysical Journal Letters*, 616(1):L7.

Gurwell, M. A. and D. O. Muhleman
1995. CO on Titan: Evidence for a Well-Mixed Vertical Profile. *Icarus*, 117(2):375 – 382.

Gurwell, M. A. and D. O. Muhleman

2000. Co on titan: More evidence for a well-mixed vertical profile. *Icarus*, 145(2):653–656.

Harris, G. J., O. L. Polyansky, and J. Tennyson

2002. Opacity data for hcn and hnc from a new ab initio line list. *The Astrophysical Journal*, 578(1):657.

Hartle, R., E. Sittler, F. Neubauer, R. Johnson, H. Smith, F. Crary, D. McComas, D. Young, A. Coates, D. Simpson, et al.

2006. Preliminary interpretation of titan plasma interaction as observed by the cassini plasma spectrometer: Comparisons with voyager 1. *Geophysical research letters*, 33(8).

Hase, F., P. Demoulin, A. J. Sauval, G. C. Toon, P. F. Bernath, A. Goldman, J. W. Hannigan, and C. P. Rinsland

2006. An empirical line–by–line model for the infrared solar transmittance spectrum from 700 to 5000 cm^{-1}. *J. Quant. Spectrosc. Radiat. Transfer*, 102(3):450–463.

Hidayat, T., A. Marten, B. Bezard, D. Gautier, T. Owen, H. Matthews, and G. Paubert

1998. Millimeter and submillimeter heterodyne observations of titan: The vertical profile of carbon monoxide in its stratosphere. *Icarus*, 133(1):109–133.

Hill, T.

1979. Inertial limit on corotation. *Journal of Geophysical Research: Space Physics*, 84(A11):6554–6558.

Hill, T. W.

2001. The jovian auroral oval. *Journal of Geophysical Research: Space Physics*, 106(A5):8101–8107.

Hiraki, Y. and C. Tao

2008. Parameterization of ionization rate by auroral electron precipitation in jupiter. In *Annales geophysicae: atmospheres, hydrospheres and space sciences*, volume 26, P. 77.

Hörst, S. M., V. Vuitton, and R. V. Yelle
2008. Origin of oxygen species in titan's atmosphere. *Journal of Geophysical Research: Planets (1991–2012)*, 113(E10).

Hui, Y., D. R. Schultz, V. A. Kharchenko, P. C. Stancil, T. E. Cravens, C. M. Lisse, and A. Dalgarno
2009. The ion-induced charge-exchange x-ray emission of the jovian auroras: Magnetospheric or solar wind origin? *The Astrophysical Journal*, 702(2):L158–L162.

Humlicek, J.
1982. Optimized computation of the voigt and complex probability functions. *Journal of Quantitative Spectroscopy and Radiative Transfer*, 27(4):437–444.

Jurado-Navarro, Á. A., M. López-Puertas, B. Funke, M. García-Comas, A. Gardini, G. P. Stiller, and T. v. Clarmann
2015. Vibrational-vibrational and vibrational-thermal energy transfers of co2 with n2 from mipas high-resolution limb spectra. *Journal of Geophysical Research: Atmospheres*, 120(15):8002–8022. 2015JD023429.

Khurana, K. K., M. G. Kivelson, V. M. Vasyliunas, N. Krupp, J. Woch, A. Lagg, B. H. Mauk, and W. S. Kurth
2004. *The configuration of Jupiter's magnetosphere*, volume 1, Pp. 593–616. Cambridge University Press, New York.

Kim, S. J., C. K. Sim, J. Ho, T. R. Geballe, Y. L. Yung, S. Miller, and Y. H. Kim
2015. Hot ch4 in the polar regions of jupiter. *Icarus*, 257(Supplement C):217 – 220.

Koskinen, T., R. Yelle, D. Snowden, P. Lavvas, B. Sandel, F. Capalbo, Y. Benilan, and R. West
2011. The mesosphere and lower thermosphere of titan revealed by cassini/uvis stellar occultations. *Icarus*, 216(2):507–534.

Krasnopolsky, V. A.
2009. A photochemical model of titan's atmosphere and ionosphere. *Icarus*, 201(1):226–256.

Lara, L., E. Lellouch, M. González, R. Moreno, and M. Rengel
2014. A time-dependent photochemical model for titan's atmosphere and the origin of h2o. *Astronomy & Astrophysics*, 566:A143.

Lavvas, P., A. Coustenis, and I. Vardavas
2008a. Coupling photochemistry with haze formation in titan's atmosphere, part i: Model description. *Planetary and Space Science*, 56(1):27–66.

Lavvas, P., A. Coustenis, and I. Vardavas
2008b. Coupling photochemistry with haze formation in titan's atmosphere, part ii: Results and validation with cassini/huygens data. *Planetary and Space Science*, 56(1):67–99.

Lavvas, P., R. Yelle, and C. Griffith
2010. Titan's vertical aerosol structure at the huygens landing site: Constraints on particle size, density, charge, and refractive index. *Icarus*, 210(2):832–842.

Lebonnois, S., J. Burgalat, P. Rannou, and B. Charnay
2012. Titan global climate model: A new 3-dimensional version of the IPSL titan GCM. *Icarus*, 218(1):707–722.

Lebonnois, S., F. M. Flasar, T. Tokano, and C. Newman
2014. *The General Circulation of Titan's Lower and Middle Atmosphere*, P. 322. Cambridge University Press.

Lellouch, E., A. Coustenis, B. Sebag, J.-G. Cuby, M. López-Valverde, B. Schmitt, T. Fouchet, and J. Crovisier
2003. Titan's 5-μm window: Observations with the very large telescope. *Icarus*, 162(1):125–142.

López-Valverde, M., E. Lellouch, and A. Coustenis
2005. Carbon monoxide fluorescence from titan's atmosphere. *Icarus*, 175(2):503–521.

Lutz, B., C. De Bergh, and T. Owen
1983. Titan: Discovery of carbon monoxide in its atmosphere. *Science*, 220:1374–1375.

López-Puertas, M., B. M. Dinelli, A. Adriani, B. Funke, M. García-Comas, M. L. Moriconi, E. D'Aversa, C. Boersma, and L. J. Allamandola
2013. Large abundance of polycyclic aromatic hydrocarbons in titan's upper atmosphere. *The Astrophysical Journal*, 770(2):132.

López-Puertas, M. and F. Taylor
2001. *Non-LTE Radiative Transfer in the Atmosphere*. World Scientific.

Maltagliati, L., B. Bézard, S. Vinatier, M. M. Hedman, E. Lellouch, P. D. Nicholson, C. Sotin, R. J. de Kok, and B. Sicardy
2015. Titan's atmosphere as observed by cassini/vims solar occultations: Ch 4, co and evidence for c 2 h 6 absorption. *Icarus*, 248:1–24.

Mauk, B. and F. Bagenal
2013. *Comparative auroral physics: Earth and other planets*, Pp. 3–26. Wiley Online Library.

McCord, T., A. Coradini, C. Hibbitts, F. Capaccioni, G. Hansen, G. Filacchione, R. Clark, P. Cerroni, R. Brown, K. Baines, et al.
2004. Cassini vims observations of the galilean satellites including the vims calibration procedure. *Icarus*, 172(1):104–126.

Melin, H., S. Miller, T. Stallard, and D. Grodent
2005. Non-lte effects on h3+ emission in the jovian upper atmosphere. *Icarus*, 178(1):97–103.

Mihalas, D. and B. Weibel
1999. *Foundations of Radiation Hydrodynamics*.

Miller, S., N. Achilleos, G. E. Ballester, T. R. Geballe, R. D. Joseph, R. Prange, D. Rego, T. Stallard, J. Tennyson, L. M. Trafton, and J. H. Waite
2000. The role of h_3^+ in planetary atmospheres. *Philosophical Transactions of the Royal Society A: Mathematical, Physical and Engineering Sciences*, 358(1774):2485–2502.

Miller, S., R. D. Joseph, and J. Tennyson
1991. Infrared emissions of h_3^+ in the atmosphere of jupiter in the 2.1 and 4.0 micron region. *The Astrophysical Journal*, 367:L37.

Miller, S., T. Stallard, J. Tennyson, and H. Melin
2013. Cooling by h_3^+ emission. *The Journal of Physical Chemistry A*, 117(39):9770–9777.

Moriconi, M. L., A. Adriani, B. M. Dinelli, F. Fabiano, F. Altieri, F. Tosi, G. Filacchione, A. Migliorini, J. C. Gérard, A. Mura, D. Grassi, G. Sindoni, G. Piccioni, R. Noschese, A. Cicchetti, S. J. Bolton, J. E. P. Connerney, S. K. Atreya, F. Bagenal, G. R. Gladstone, C. Hansen, W. S. Kurth, S. M. Levin, B. H. Mauk, D. J.

McComas, D. Turrini, S. Stefani, A. Olivieri, and M. Amoroso
2017. Preliminary jiram results from juno polar observations: 3. evidence of diffuse methane presence in the jupiter auroral regions. *Geophysical Research Letters*, 44(10):4641–4648. 2017GL073592.

Muhleman, D. O., G. L. Berge, and R. T. Clancy
1984. Microwave measurements of carbon monoxide on titan. *Science*, 223:393–396.

Müller-Wodarg, I., C. A. Griffith, E. Lellouch, and T. E. Cravens
2014. *Titan: Interior, surface, atmosphere, and space environment*, volume 14. Cambridge University Press.

Müller-Wodarg, I., R. Yelle, M. Mendillo, and A. Aylward
2003. On the global distribution of neutral gases in titan's upper atmosphere and its effect on the thermal structure. *Journal of Geophysical Research: Space Physics*, 108(A12).

Mura, A., A. Adriani, F. Altieri, J. E. P. Connerney, S. J. Bolton, M. L. Moriconi, J.-C. Gérard, W. S. Kurth, B. M. Dinelli, F. Fabiano, F. Tosi, S. K. Atreya, F. Bagenal, G. R. Gladstone, C. Hansen, S. M. Levin, B. H. Mauk, D. J. McComas, G. Sindoni, G. Filacchione, A. Migliorini, D. Grassi, G. Piccioni, R. Noschese, A. Cicchetti, D. Turrini, S. Stefani, M. Amoroso, and A. Olivieri
2017. Infrared observations of jovian aurora from juno's first orbits: Main oval and satellite footprints. *Geophysical Research Letters*, 44(11):5308–5316.

Müller-Wodarg, I. C. F., R. V. Yelle, J. Cui, and J. H. Waite
2008. Horizontal structures and dynamics of titan's thermosphere. *Journal of Geophysical Research*, 113(E10).

Neale, L., S. Miller, and J. Tennyson
1996. Spectroscopic properties of the h 3+ molecule: a new calculated line list. *The Astrophysical Journal*, 464:516.

Niemann, H., S. Atreya, S. Bauer, G. Carignan, J. Demick, R. Frost, D. Gautier, J. Haberman, D. Harpold, D. Hunten, et al.
2005. The abundances of constituents of titan's atmosphere from the gcms instrument on the huygens probe. *Nature*, 438(7069):779–784.

Noll, K. S., T. R. Geballe, R. F. Knacke, and Y. J. Pendleton
1996. Titan's 5 μm spectral window: Carbon monoxide and the albedo of the surface. *Icarus*, 124(2):625–631.

Ozak, N., T. E. Cravens, and D. R. Schultz
2013. Auroral ion precipitation at jupiter: Predictions for juno. *Geophysical Research Letters*, 40(16):4144–4148.

Radioti, A., M. Lystrup, B. Bonfond, D. Grodent, and J.-C. Gérard
2013. Jupiter's aurora in ultraviolet and infrared: Simultaneous observations with the hubble space telescope and the nasa infrared telescope facility. *Journal of Geophysical Research: Space Physics*, 118(5):2286–2295.

Rannou, P., F. Hourdin, C. McKay, and D. Luz
2004. A coupled dynamics-microphysics model of titan's atmosphere. *Icarus*, 170(2):443–462.

Rodgers, C. D. et al.
2000. *Inverse methods for atmospheric sounding: theory and practice*, volume 2. World scientific Singapore.

Rothman, L., I. Gordon, Y. Babikov, A. Barbe, D. C. Benner, P. Bernath, M. Birk, L. Bizzocchi, V. Boudon, L. Brown, A. Campargue, K. Chance, E. Cohen, L. Coudert, V. Devi, B. Drouin, A. Fayt, J.-M. Flaud, R. Gamache, J. Harrison, J.-M. Hartmann, C. Hill, J. Hodges, D. Jacquemart, A. Jolly, J. Lamouroux, R. L. Roy, G. Li, D. Long, O. Lyulin, C. Mackie, S. Massie, S. Mikhailenko, H. Müller, O. Naumenko, A. Nikitin, J. Orphal, V. Perevalov, A. Perrin, E. Polovtseva, C. Richard, M. Smith, E. Starikova, K. Sung, S. Tashkun, J. Tennyson, G. Toon, V. Tyuterev, and G. Wagner
2013. The HITRAN2012 molecular spectroscopic database. *Journal of Quantitative Spectroscopy and Radiative Transfer*, 130:4–50.

Sada, P., D. Jennings, P. Romani, G. Bjoraker, F. Flasar, V. Kunde, C. Nixon, R. Carlson, and G. McCabe
2003. Transient ir phenomena observed by cassini/cirs in jupiter's auroral regions. In *Bulletin of the American Astronomical Society*, volume 35, P. 998.

Satoh, T. and J. Connerney
1999. Jupiter's h_3^+ emissions viewed in corrected jovimagnetic coordinates. *Icarus*, 141(2):236 – 252.

Serigano, J., C. A. Nixon, M. A. Cordiner, P. G. J. Irwin, N. A. Teanby, S. B. Charnley, and J. E. Lindberg
2016. Isotopic ratios of carbon and oxygen in titan's co using alma. *The Astrophysical Journal Letters*, 821(1):L8.

Shin, H.
1981. Temperature dependence of the vibrational relaxation rate coefficient of n2 (1)+ n2 (0). *The Journal of Chemical Physics*, 74(5):2866–2868.

Siddles, R., G. Wilson, and C. Simpson
1994. The vibrational deactivation of the bending modes of cd 4 and ch 4 measured down to 90 k. *Chemical physics*, 188(1):99–105.

Simeckova, M., D. Jacquemart, L. S. Rothman, R. R. Gamache, and A. Goldman
2006. Einstein a-coefficients and statistical weights for molecular absorption transitions in the hitran database. *Journal of Quantitative Spectroscopy and Radiative Transfer*, 98(1):130–155.

Snowden, D. and R. Yelle
2014. The thermal structure of titan's upper atmosphere, II: Energetics. *Icarus*, 228:64–77.

Snowden, D., R. Yelle, J. Cui, J.-E. Wahlund, N. Edberg, and K. Ågren
2013. The thermal structure of titan's upper atmosphere, i: Temperature profiles from cassini INMS observations. *Icarus*, 226(1):552–582.

Sromovsky, L., K. Baines, and P. Fry
2013. Saturn's great storm of 2010–2011: Evidence for ammonia and water ices from analysis of vims spectra. *Icarus*, 226(1):402–418.

Stallard, T.
2002. On the dynamics of the jovian ionosphere and thermosphere ii. the measurement of h3+ vibrational temperature, column density, and total emission. *Icarus*, 156(2):498–514.

Stallard, T. S., H. Melin, S. Miller, S. V. Badman, K. H. Baines, R. H. Brown, J. S. D. Blake, J. O'Donoghue, R. E. Johnson, B. Bools, N. M. Pilkington, O. T. East, and M. Fletcher
2015. Cassini vims observations of h_3^+ emission on the nightside of jupiter. *Journal of Geophysical Research: Space Physics*, 120(8):6948–6973.

Stephenson, J. C. and E. R. Mosburg Jr
1974. Vibrational energy transfer in co from 100 to 300 k. *The Journal of Chemical Physics*, 60(9):3562–3566.

Stiller, G. P., T. von Clarmann, B. Funke, N. Glatthor, F. Hase, M. Höpfner, and A. Linden
2002. Sensitivity of trace gas abundances retrievals from infrared limb emission spectra to simplifying approximations in radiative transfer modelling. *Journal of Quantitative Spectroscopy and Radiative Transfer*, 72(3):249–280.

Tao, C., S. V. Badman, T. Uno, and M. Fujimoto
2012. On the feasibility of characterizing jovian auroral electrons via h_3^+ infrared line-emission analysis. *Icarus*, 221(1):236–247.

Taylor, F., S. Atreya, T. Encrenaz, D. Hunten, P. Irwin, and T. Owen
2004. *The composition of the atmosphere of Jupiter*, Pp. 59–78.

Teanby, N., R. de Kok, P. Irwin, S. Osprey, S. Vinatier, P. Gierasch, P. Read, F. Flasar, B. Conrath, R. Achterberg, et al.
2008. Titan's winter polar vortex structure revealed by chemical tracers. *Journal of Geophysical Research: Planets (1991–2012)*, 113(E12).

Teanby, N., P. Irwin, R. De Kok, and C. Nixon
2010. Mapping titan's hcn in the far infra-red: implications for photochemistry. *Faraday discussions*, 147:51–64.

Teanby, N. A., P. G. Irwin, R. de Kok, and C. A. Nixon
2009. Dynamical implications of seasonal and spatial variations in titan's stratospheric composition. *Philosophical Transactions of the Royal Society A: Mathematical, Physical and Engineering Sciences*, 367(1889):697–711.

Teanby, N. A., P. G. Irwin, C. A. Nixon, R. de Kok, S. Vinatier, A. Coustenis, E. Sefton-Nash, S. B. Calcutt, and F. M. Flasar
2012. Active upper-atmosphere chemistry and dynamics from polar circulation reversal on titan. *Nature*, 491(7426):732–735.

Tran, H., N. Ngo, and J.-M. Hartmann
2013. Efficient computation of some speed-dependent isolated line profiles. *Journal of Quantitative Spectroscopy and Radiative Transfer*, 129(Supplement C):199 – 203.

Vardavas, I. and F. Taylor
2007. *Radiation and Climate*. Oxford University Press (OUP).

Vinatier, S., B. Bézard, S. Lebonnois, N. A. Teanby, R. K. Achterberg, N. Gorius, A. Mamoutkine, E. Guandique, A. Jolly, D. E. Jennings, and F. M. Flasar
2015. Seasonal variations in titan's middle atmosphere during the northern spring derived from cassini/cirs observations. *Icarus*, 250(Supplement C):95 – 115.

Vuitton, V., O. Dutuit, M. Smith, and N. Balucani
2014. *Chemistry of Titan's atmosphere*, P. 322. Cambridge University Press.

Waite, J. H., W. S. Lewis, W. T. Kasprzak, V. G. Anicich, B. P. Block, T. E. Cravens, G. G. Fletcher, W.-H. Ip, J. G. Luhmann, R. L. Mcnutt, H. B. Niemann, J. K. Parejko, J. E. Richards, R. L. Thorpe, E. M. Walter, and R. V. Yelle
2004. The cassini ion and neutral mass spectrometer (inms) investigation. *Space Science Reviews*, 114(1):113–231.

Westlake, J. H., J. H. Waite, J. M. Bell, and R. Perryman
2014. Observed decline in titan's thermospheric methane due to solar cycle drivers. *Journal of Geophysical Research: Space Physics*, 119(10):8586–8599. 2014JA020394.

Wilson, E. H. and S. Atreya
2004. Current state of modeling the photochemistry of titan's mutually dependent atmosphere and ionosphere. *Journal of Geophysical Research: Planets (1991–2012)*, 109(E6).

Wong, A.-S., C. G. Morgan, Y. L. Yung, and T. Owen
2002. Evolution of co on titan. *Icarus*, 155(2):382–392.

Yelle, R., D. Snowden, and I. Müller-Wodarg
2014. *Titan's upper atmosphere: thermal structure, dynamics, and energetics*, P. 322. Cambridge University Press.

Yelle, R., D. Strobel, E. Lellouch, and D. Gautier
1997. Engineering models for titan's atmosphere. *Huygens: Science, Payload and Mission*, Pp. 243–256.

Yelle, R. V., N. Borggren, V. de la Haye, W. Kasprzak, H. Niemann, I. Müller-Wodarg, and J. Waite
2006. The vertical structure of titan's upper atmosphere from cassini ion neutral

mass spectrometer measurements. *Icarus*, 182(2):567 – 576. Results from the Mars Express ASPERA-3 Investigation.

Zebker, H. A., B. Stiles, S. Hensley, R. Lorenz, R. L. Kirk, and J. Lunine 2009. Size and shape of saturn's moon titan. *Science*, 324(5929):921–923.